In-situ Electrochemical Spectroscopy and Imaging for Reaction Monitoring

Scott Keith Richardson

Swansea University

Submitted to Swansea University in fulfilment of the requirements for the Degree of PhD

September 2025

DECLARATIONS

This work has not previously been accepted in substance for any degree and is not being concurrently submitted in candidature for any degree.

Signed...**SCOTT.KEITH.RICHARDSON**.. ....

Date....**23/09/2025**... ....

This thesis is the result of my own investigations, except where otherwise stated. Other sources are acknowledged by footnotes giving explicit references. A bibliography is appended.

Signed...**SCOTT.KEITH.RICHARDSON**.. ....

Date......**23/09/2025**... .....

I hereby give consent for my thesis, if accepted, to be available for electronic sharing

Signed......**SCOTT.KEITH.RICHARDSON**... ....

Date......**23/09/2025**... .....

The University's ethical procedures have been followed and, where appropriate, that ethical approval has been granted.

Signed......**SCOTT.KEITH.RICHARDSON**... ....

Date.......**23/09/2025**...

ABSTRACT

The focus of the thesis is on the development and validation of in-situ characterisation techniques for advanced nanoscaled materials such as 2D molybdenum disulphide (MoS_2) and methylammonium lead bromide ($MAPbBr_3$) perovskite. The thesis provides three case studies, the third of which involves the detection of intermediate formation from a Density Functional Theory (DFT) calculated reaction pathway. All case studies involve the use of an in-house designed polyether ether ketone (PEEK) electrochemical cell.

The first case study examines the excitonic properties from the transition metal chalcogenides (TMD) compound MoS_2. This compound has gained significant importance in catalysis due to the efficient electron transfer facilitated by excitons and trions, particularly in reactions such as the hydrogen evolution reaction (HER). In the study, a demonstration is made of the visualization of trion distributions and their dynamics in electrochemically exfoliated MoS_2, within a typical electrochemical cell setup. The measurements consisted of the asymmetric characteristics of trion photoluminescence (PL), its variation with applied voltage, and the influence of the electrical layer during a voltage scan. The forward and reverse voltage scans highlighted that the PL intensity is increasing from the negative to the positive potentials and that a higher concentration of trions is observed at more positive potentials indicating more activity toward the HER. The hyperspectral images (HSI) used for monitoring the trion signal, exhibited significant spatial variations and a strong dependence on the voltage, highlighting the influence of electrical layer formation on the PL from excitons and trions.

The second case study is an investigation into the effects of moisture on degradation and the effects of pH on the water-induced degradation of perovskite compound $MAPbBr_3$; conducted using Fluorescence Microscopy and HSI methods. Initial studies had shown and confirmed that moisture in Relative Humidity (RH) environments had little effect on degradation due to the stability of the perovskite lattice to these environments. The application of water in an electrochemical cell environment was then used to determine if the onset of degradation would take place. Experimental observation confirmed this was the case, which then prompted investigation on other environments in the cell that could help alleviate, slow down and retard the rate of the degradation process. Acidic and basic environments were created using a pH range of 3-9 and PL measurements conducted in-situ using HSI methods were made to monitor the degradation process. The measurements showed that basic environments (pH 8-9) lead to rapid degradation of the perovskite, and the lower the pH number, the slower the rate of degradation. Analysis of the PL spectra from the hyperspectral image, demonstrated that the spectral contribution from the thicker region reduced whereas that from the thinner regions remained unchanged which signified preferential degradation of the thicker regions of the perovskite nanoplatelets (NPLs).

The third and final case study involved an in situ electrochemical-Raman method that was developed and used to monitor, identify and validate the reaction pathway of amine nitrosations using DFT calculations. All intermediate species formed have been detected using Raman spectra and correlate with the calculated DFT spectra expected in the reaction pathway to the formation of N-nitrosamine products. Sodium nitrite is used as an affordable and readily available nitrosating reagent, which also serves as an electrolyte in the reaction. A different cell setup was used in this study as graphite is used as the working electrode. In conclusion, the three case studies all demonstrated that the use of electrochemical spectroscopy and imaging methods can be used to monitor reactions using an electrochemical cell setup.

Contents

ACKNOWLEDGEMENTS

I am extremely grateful to Dr D. Roy, Dr C. Klinke and Post Doctoral Research Fellow Himanshu Tyagi in the Chemistry Department, Singleton Campus, Swansea University for their assistance, support and advice throughout my research project.

Thanks goes to Professor Matthew Davies and his Postdoctoral Research Fellow Rodrigo Garcia Rodriguez in the Engineering faculty at Bay Campus, Swansea University for permitting and aiding in the use of their instrumentation in carrying out experiments applicable to this thesis.

I am also extremely thankful to the Engineering workshop staff at Bay Campus, Rhys Jones and Gary Jones for the construction of the electrochemical cell which was a vital part of the project.

And finally, much thanks and appreciation go to the Physics workshop staff at Singleton Campus, Phil Hopkins and Kevin Morgan who assisted with technical modifications to the PEEK electrochemical cell and other equipment throughout the research project.

LIST OF ABBREVIATIONS

Ag/AgCl – Silver/silver chloride
ALD – Atomic Layer Deposition
Bpy – bipyridine
CCD – Charge Coupled Detector
CVD – Chemical Vapour Deposition
DFT – Density Functional Theory
DOS – Density of States
Dppz – dipyridophenazine
ECDL– Electrochemical Double Layer
eq. – equivalents
FL – few layer
FTO – fluorine-doped tin oxide
FWHM – full width half maximum
HER – Hydrogen Evolution Reaction
HSI – Hyperspectral Imaging
ITO – Indium Tin Oxide
KOH – potassium hydroxide
LDH – Layered Double Hydroxide
LED – Light Emitting Diode
LPE – Liquid Phase Exfoliation
LUMO – Lowest unoccupied molecular orbital
MALPE – Microwave Assisted Liquid Phase Exfoliation
$MAPbBr_3$ – Methyl ammonium lead bromide
$MaPbI_3$ – Methyl ammonium lead iodide
MLCT – Metal to Ligand Charge Transfer
MoS_2 – Molybdenum disulphide
N_2O_4 – Dinitrogen tetroxide
NA – Numerical Aperture
Na_2SO_4 – sodium sulphate
NaCl – sodium chloride
$NaNO_2$ – sodium nitrite
NMP – N-methyl-pyrrolidone
NPL – Nanoplatelet
OER – Oxygen Evolution Reaction
PbBr(OH) – Lead bromide hydroxide
PBS – Phosphate buffer solution
PECVD – Plasma Enhance Chemical Vapour Deposition
PEEK – polyether ether ketone
PHE – Photocatalytic hydrogen evolution
PL– Photoluminescence
PSC – Perovskite Solar Cell

Pt – Platinum
PT – Pulse-Tip
PTFE – polytetrafluoroethylene
PV – Photovoltaic
QY – Quantum Yield
ReS_2 – rhenium disulphide
RH – Relative Humidity
SEM – Scanning Electron Microscopy
$TBAPF_6$ – Tetra butyl hexafluorophosphate
TCD – Trinity College Dublin
TMD – Transition metal dichalcogenide
TTL – Time – to -live
UHV – Ultra-High-Vacuum
UV-Vis – Ultraviolet – Visible
VdW – van der Waals

LIST OF FIGURES

CHAPTER–2

CHAPTER–3

CHAPTER–4

CHAPTER–5

CHAPTER– 6

CHAPTER–7

CHAPTER– 8

LIST OF TABLES

CHAPTER–7

CHAPTER–8

CHAPTER–1

Introduction

The focus of the thesis is on the development and validation of in-situ characterisation techniques for advanced nanoscaled materials, and contains three case studies, (Chapters 6-8). Two-dimensional layered nanomaterials such as the transition metal dichalcogenides (TMDs) introduced in Chapter 2 and trihalide perovskite compounds (Chapter 3) are the focus of this research. The compounds being investigated in this research thesis are molybdenum disulphide (MoS_2) and methylammonium lead bromide ($MAPbBr_3$). MoS_2 has electron confinement in two dimensions giving rise to intriguing electronic properties compared to bulk MoS_2. and this necessitates the need for further research and development on in-situ characterisation techniques to further probe the distribution and density of the catalytic active sites using high spatial and spectral resolution in terms of activity toward the Hydrogen Evolution Reaction (HER). There is renewed interest in the HER, as hydrogen is the cleanest fuel available to the modern world and represents one of the most promising energy sources.[1] MoS_2 does show potential as an electrocatalyst in the HER reaction and the challenges are making the surface sites more catalytically active toward it. It is relatively inexpensive and earth abundant in comparison to the platinum catalysts, as the high price and limited resource of noble metals largely prevent their utilization in practice. Hence why more focus and attention to research and development is afforded to MoS_2 with regard to a future hydrogen economy, and thus developing effective HER electrocatalysts with low cost and high abundance still remains urgent. Scalability is currently another issue for catalysis applications of MoS_2 as the methods used to produce monolayer material are either physically impractical to scale up such as the Scotch tape method,[2] and other preparation methods involve environmentally unfriendly organic solvents that are hazardous and toxic to certain environments. Since the drive is now on for greener more environmentally friendly processes, it is vital that these solvents are replaced with greener alternatives that are aqueous based. In-situ characterizations by means of electrochemical spectroscopy and hyperspectral imaging (HSI) techniques have potential to contribute to understanding the catalytic nature of materials such as MoS_2. Certain material properties such as photoluminescence (PL) can be used as a descriptive guide to highlight potential active sites based on the enhanced intensity produced when applying a varying potential when using an electrochemical setup. Previous measurements on MoS_2 using an electrochemical cell required fabricating electrodes that connect only to the flake being probed,[3] this process is time-consuming and requires elaborate sample fabrication. This has led to a focus on exfoliation methods as a way forward in allowing measurements to be made on multiple flakes of monolayer produced material. Theoretical simulations combined with the development of appropriate preparation technology; means it will not be long until real catalytic applications are achieved in terms of the HER contribution to the hydrogen economy. Raman spectroscopy has been shown to be a powerful tool to determine the exact number of layers of exfoliated MoS_2. The energy, width, and amplitude of the vibrational modes are strongly influenced by the thickness of the flakes. For bulk MoS_2 both the in-plane E^1_{2g} mode and the out-of-plane A_{1g} mode can be observed. The in-plane E^1_{2g} mode results from the opposite vibration of two S atoms with respect to the Mo atom within the layer and the A_{1g} mode results from the out-of-plane vibration of only the S atoms in opposite directions.[4] The separation between the two modes decreases with decreasing thickness of the material, which is an excellent indicator for the number of layers in MoS_2.[5] UV-Vis absorption spectroscopy can be used to measure exciton absorbance in MoS_2 by analysing the light absorbed by the material as a function of wavelength, revealing characteristic peaks corresponding to excitonic transitions.[6] In MoS_2, excitons are formed when an electron and a hole are bound together, and they can absorb light at specific wavelengths corresponding to their energy levels. The characteristic peaks, notably the A and B excitonic peaks, are indicative of direct band gap transitions at the K-point in the Brillouin zone, and can further indicate the thickness of the material after exfoliation.[6]

Perovskite compounds such as $MAPbBr_3$ that possess 2D stacking structures have shown promise in optoelectronic applications, as well as perovskite solar cells (PSCs) in recent years.[7] Despite their improving performance over the years, they still lag behind the conventional silicon technology in terms of longevity and durability. Environmental factors like moisture, water ingress, heat, and light can all adversely affect PSC performance and limit device lifetime.[7] Systematically elucidating and eliminating PSC degradation pathways will be critical to the success of this technology in commercial applications. In-situ techniques such as hyperspectral imaging provide powerful tools to this end, as they allow structural, compositional, morphological, and optoelectronic changes to be tracked in real-time.[8] As they follow a single film, or nanoplatelet over the course of the degradation process, they can help eliminate the statistical variation that negatively affects many studies; as there can be a number of competing processes occurring at the same time giving rise to variation of the fluorescence maximum intensity. Additionally the high stability of the system and high spectral resolution based on single-pixel technology further limits any statistical variation of the imaging.[8] Raman spectroscopy is a valuable tool for characterizing perovskite materials, providing insights into their crystallinity, composition, and structural changes, including degradation. Raman spectra can reveal information about the crystallinity of perovskite films, which is crucial for their performance, especially in solar cells.[9] Many studies on the Raman spectra of Methylammonium lead iodide ($MAPbI_3$) show features also attributable to the Raman spectrum of PbI_2 suggesting that severe sample degradation might have taken place before or during the Raman measurements.[10-12] Grancini et al. have published a fundamental work on the vibrational modes of $MAPbI_3$ single crystals observing two very broad bands at approximately 110 cm^{-1} and 250 cm^{-1} under 532 nm laser excitation.[13] UV-Vis spectroscopy is another crucial technique for characterizing perovskite materials, particularly in the context of perovskite solar cells, as it allows for the determination of their optical properties, including light absorption characteristics and bandgap, which are vital for photovoltaic performance. UV-vis spectroscopy measures the amount of ultraviolet and visible light absorbed by a material as a function of wavelength. By analysing the absorption spectrum, researchers can determine the bandgap of the perovskite material, which is the energy required to excite an electron from the valence band to the conduction band. The technique can be used to monitor the degradation of perovskite materials over time, providing insights into their stability.[14, 15] Photoluminescence (PL) spectroscopy is another valuable tool for monitoring the degradation of perovskite materials, as it can detect changes in material properties like bandgap, electronic defects, and phase distribution, which are indicative of degradation processes.[16] PL spectroscopy measures the light emitted by a material after it has been excited by light of a specific wavelength. Changes in the PL spectrum (e.g., shifts in peak position, intensity, or broadening) can reveal information about the material's degradation.[16] This research on $MAPbBr_3$ will utilize these techniques to provide an overview of perovskite degradation processes, with an emphasis on in-situ studies under varying conditions.

Another focus of this research is on electrochemical-Raman techniques. This research focuses on the application of this technique to ruthenium complexes used in anti-cancer treatments with different complexes exhibiting good anti-tumour and anti-metastatic properties.[17] As part of this research, electrochemical-Raman was able to detect the redox changes that occur on the ruthenium metal centre when a change in potential is applied, and therefore it is expected that this could be applied to other metal complexes such as MoS_2. Resonance Raman spectroscopy has been shown to produce Raman bands for the Ru complexes and so offers potential for electrochemical-Raman characterisation of these compounds.[18-20] The detection of intermediate formation during N-nitrosation reactions is another focus of the research using electrosynthesis and electrochemical-Raman techniques (Chapters 4 & 8). Detection and monitoring of intermediates in a chemical process is highly important. This is to prevent their occurrence, especially for *N*-nitrosamines which may enter as impurities in products made for human consumption, such as in pharmaceuticals and food products.[17, 21] Raman spectroscopy has produced spectra of $HNO_3 \cdot NO_2$ that have been detected on liquid and solid surfaces in the presence of concentrated nitric acid and nitrogen dioxide gas. The Raman spectrum of HNO_3 solutions containing N_2O_4 has been partly reinterpreted in terms of contributions from $HNO_3 \cdot N_2O_4$ and $N_2O_4 \cdot NO_3$. Solutions of N_2O_4 and N_2O_5 in anhydrous and aqueous nitric acid were examined by Raman spectroscopy to gain a more detailed knowledge of the species present in these solutions and to assess the applicability of Raman spectroscopy as an analytical measurement technique.[22, 23] It is expected that as Raman bands were detected in these studies that this can be extended into Electrochemical-Raman studies of nitroso intermediates formed in the production of *N*-nitrosamines. Modern industrial organic chemistry has evolved to efficiently exploit fossil fuel-based hydrocarbon feedstocks and turn them into chemical products using classical organic chemistry. However, the carbon toll from the chemical sector, makes it one of the largest industrial emitters of carbon dioxide. This legacy of polluting waste is leading chemists to search for greener processes such as electrosynthesis, using an electric current to facilitate chemical reactions instead of chemical redox agents.[24] The latest resurgence comes with the challenge to decarbonise the chemical industry and the hope that cheaper renewable electricity can be used to fuel these reactions. The hope is also that electrosynthesis may provide access to new chemistries via the free radical intermediate species that are produced in an electrochemical cell and when coupled with Raman spectroscopy, can be used to identify the intermediates formed during a reaction.[24, 25] There are also safety advantages in using electrosynthesis as it could offer more direct routes, cutting out many synthesis steps and if there is a problem, just cutting the electrical supply could prevent a runaway reaction or something more dangerous happening such as high temperature ignitions that could lead to a fire or explosion hazard.[26] The other safety advantage is the removal of toxic reagents currently used in many conventional organic syntheses, including noble metal catalysts.[24-28]

Finally, electrode material and design is one of the crucial factors in electrosynthesis in getting the right mix of products that you would want, and therefore much research into looking at advanced materials that might improve electrode performance is key for future application.[27, 28]

CHAPTER–2

Two-dimensional MoS_2

2.0 – Introduction and background

MoS_2 is one of the Two-dimensional (2D) materials that are the focus of the research. The potential of this material as an electrocatalyst for the HER will be investigated. MoS_2 in monolayer form in high yield is one of the objectives of the research, as this will maximise catalytic efficiency providing easier access to surface active sites. Various liquid phase exfoliation methods will be used to hopefully produce the monolayer material in high yield. Characterisation techniques such as Raman/PL spectroscopy and UV-vis spectroscopy will be used to monitor monolayer yields. If a high enough yield can be produced, a validated CV curve will be produced to confirm and determine redox properties from which, electrochemical-Raman techniques will be used to characterise the structural changes formed under an applied voltage range upon application of an electrochemical cell. The use of dopants and the creation of defects are potential routes that can be used to maximize the surface-active sites. If, however, a low yield of monolayer is obtained from LPE methods, then electrochemical exfoliation on an MoS_2 crystal will be used to produce a higher yield of monolayer material with larger flake size that can be examined using HSI methods. HSI can be used to monitor the PL emission signals that produce exciton and trion emissions. The trion hotspots formed can be used as an indicator of the few-layer (FL) regions of the flake where potential active sites occur, and a visual image is produced using HSI methods for catalytic efficiency toward the HER.

2D nanomaterials are substances made up of layers of atoms, a few nano-meters thick, where the electrons are able to move freely within the layers.[29] Layer–layer interactions in 2D materials can result in unusual material properties and provide excellent platforms to study fundamental physics. An example of a 2D nanomaterial is graphene, which is a single layer of graphite (see Fig. 2.1) that contains carbon atoms arranged in a hexagonal lattice structure being atomically thin.[30]

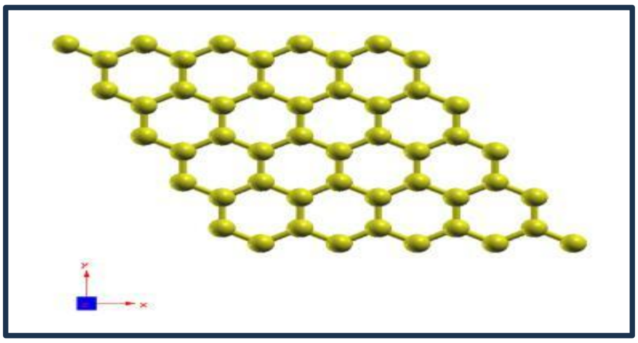

Figure 2.1: Top-down view of graphene[31]

2D nanomaterials have come to the fore in recent years as they have electron confinement in two dimensions giving them intriguing electronic properties compared to bulk MoS_2. The bulk MoS_2 crystal is an indirect band gap semiconductor with an energy gap of 1.29 eV, due to the weak van der Waals interaction between S−Mo−S layers, it is possible to exfoliate the crystal into individual layers that exhibit properties that are dramatically different from the bulk material as a direct bandgap is then formed. This increases the potential for many different applications of MoS_2[1] Another reason being is that MoS_2 in nanostructure form exposes the catalytically active edge sites which correlates with the Hydrogen Evolution Reaction (HER) activity of MoS_2[32] In addition, the large specific surface area of 2D nanomaterials motivates their use in surface-active applications, such as catalysis due to the ease of accessibility to the surface properties and active sites.[31]

There is significant interest on the use of scalable 2D nanomaterials beyond graphene, as the two-dimensional transition metal dichalcogenide (TMD) compounds[33] and naturally occurring materials such as zeolites,[34] layered double hydroxide (LDH) compounds[35] and mineral compounds,[36] all show potential for catalysis applications. The reason being and most importantly is that they offer scalable, low-cost, environmentally friendly alternatives to the more conventional precious metal catalysts for practical applications. TMD compounds have been thoroughly investigated over the last couple of decades due to their unique properties. However, much more investigation is needed to determine how efficient these materials can become as electrocatalysts for the HER in place of the expensive noble metals such as platinum. This class of materials have the formula MX_2 where M represents a transition metal such as Molybdenum (Mo) and Tungsten (W) and X represents chalcogens such as Sulphur (S), Selenium (S) and Tellurium (Te).[33] (See Fig. 2.2). Unlike graphene the TMD compounds possess band gaps which can be tuned and modified accordingly, and mono- or few-layered TMDs — obtained either through exfoliation of bulk materials or bottom-up syntheses — are direct-gap semiconductors whose bandgap energy, as well as carrier type (n- or p-type), varies between compounds depending on their composition, structure, number of layers and dimensionality, leading to promising properties such as structure-dependent electronic energy bands.[33] Their electronic structures and surface properties can be further altered by methods such as chemical doping,[37] the addition of strains to the lattice,[38] van der Waals heterostructures (stacks of several 2D crystals).[39,2, 40] defect engineering[32, 41] and phase changes.[42] These are all demonstrated to be efficient ways of manipulating their electronic features. These methods must be developed for the scalable preparation of 2D nanomaterials and 2D heterostructures of high quality and low cost; and with the TMDs having the ability to form a wide range of nanostructures, makes them good candidates for electro and photocatalysis applications for such reactions as hydrogen evolution reaction (HER), carbon dioxide reduction reaction (CO_2RR) and nitrogen reduction reaction (N_2RR), as well as electrically active materials in opto-electronics.[33]

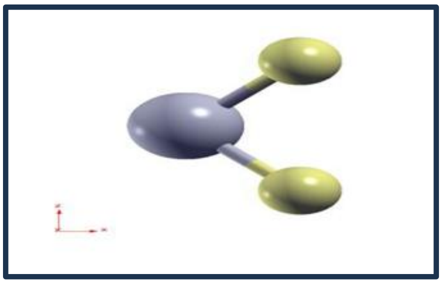

Figure 2.2: Side view of MX_2 molecule consisting of a transition metal element (grey) sandwiched between two chalcogen atoms (yellow)[31]

Since the surface of these two-dimensional nanocrystals are atomically flat, they can be aligned with other layered-structured materials such as (carbon nitrides, metal oxides) through van der Waals interactions forming complex architectural heterostructures.

The synthesis and fabrication techniques towards 2D TMD nanomaterials have evolved over the last few decades and can generally be divided into two categories, which are physical methods and wet chemical methods. Colloidal based methods have come to the fore in the last 25 years since they offer advantages in synthesis technique in controlling crystal growth.[43]

Hydrogen (H_2) production through electrochemical and photoelectrochemical water splitting is emerging as a sustainable energy source, recognized for its environmentally friendly nature in renewable energy technologies.[44-48] A key component for efficient H_2 production is a catalyst that promotes charge transfer and reduces overpotential.[45,49,50] Although noble metals like platinum (Pt) are highly effective catalysts for the HER due to their low hydrogen absorption free energy (ΔG_H), their high cost and the risks of limiting availability due to geopolitical reasons necessitate the search for alternative affordable materials.[45,1, 46, 51, 52]

Excitonic nanomaterials from the chalcogenide family, such as few-layer MoS_2, $MoSe_2$, and ReS_2, have been shown to enhance the photocatalytic hydrogen evolution (PHE) efficiency in two-dimensional (2D) monolayer-like structures, facilitated by electron transfer via trions. A trion is a bound state of three charged particles, such as two electrons and one hole (negative trion) or two holes and one electron (positive trion).[53-55] In recent years, studies have demonstrated that electron-hole pairs in transition metal dichalcogenide (TMD) monolayers exhibit significantly enhanced Coulombic interactions, forming tightly bound excitons.[45,56,57] Excitation with light on the surface of TMD compounds in a process known as photoexcitation leads to the formation of excitons, which are bound electron-hole pairs, that can also drive photoredox reactions, influencing phase transitions and charge transfer.[58] These excitons can capture free electrons or holes to create negative or positive trions (charged excitons).[57] Negative trions, which consist of two electrons and one hole, enable two-electron catalytic reactions such as $2H^+ + 2e^- \rightarrow H_2$ on the surface of TMD compounds to drive a chemical reaction that produces hydrogen gas from water.[59] A bandgap is needed to drive reactions on the surface of a TMD material as it determines the material's ability to absorb light and generate these electron-hole pairs, which are essential for initiating and sustaining the surface reactions.[59] Despite behaving as free charged particles with increased effective mass and lower carrier mobility, their extended Auger recombination lifetimes can mitigate these drawbacks.[60-62] However, individual TMD monolayers still face challenges with electron-hole recombination due to insufficient hydrogen-evolving sites for disposing of the electrons for the reaction, preventing a significant increase in PHE efficiency.[53,60] To overcome this, a TMD compound with abundant active sites and a high concentration of trions is needed, though this requires suitable imaging tools with timescale imaging (exposure time) in the tens of milliseconds range, sufficient spectral information and high spatial resolution imaging down to hundreds of nanometres to assess the active sites and electrochemistry and to measure their distribution and density.[63]

Exciton and trion concentrations in 2D TMD semiconductor catalysts are modulated by electrolyte gating during electrocatalytic reactions, which also depends on the doping type.[64] For instance, n-type semiconductors favour cathodic reactions such as HER, while p-type semiconductors favour anodic reactions such as the oxygen evolution reaction (OER).[30, 51,65] 2D TMD semiconductor catalysts typically consist of a mix of "active" (defects or edges) and "inert" sites,[66-68] and the effects of electrolyte gating on these sites during electrocatalytic reactions are not fully understood. Therefore, it is crucial to study the spatially resolved catalytic activity of 2D TMD semiconductors under self-gating conditions to comprehend their fundamental operational mechanisms. In addition, the adsorption and desorption of hydrogen or electrolyte ions during HER can significantly modulate the carrier density or type on the surface of MoS_2 catalysts.[69] Consequently, electrolyte gating caused by ion build-up across the nanometre-scale electrochemical double layer (ECDL) may also lead to exciton and trion accumulation at ML-MoS_2 catalysts.[70,71] The ECDL is when an electrode (a conductor) comes into contact with an electrolyte (a substance that can conduct electricity through ions), and an interface forms. This interface is characterized by a separation of charges, with the electrode accumulating a certain charge and the electrolyte ions (cations and anions) arranging themselves to form a layer of opposite charge near the electrode surface. This results in two layers of opposite charge, hence the name "double layer". It is important in electrochemical science as the properties of the ECDL (like its capacitance and potential drop) directly influence the rate and mechanism of electrochemical reactions occurring at the electrode-electrolyte interface.[72, 73] Additionally, in terms of energy storage, electrochemical capacitors offer advantages over traditional capacitors and batteries, such as high-power density, fast charging/discharging times, and long cycle life.[74-76]

Given their unique carrier dynamics, excitons and trions, which are highly sensitive to changes in local charge due to ion adsorption and desorption, can serve as sensitive "descriptors" to monitor the catalytic activity of MoS_2 in situ during HER.[70] However, this requires in-situ real-time imaging with spatial resolution down to $<$ 500 nm resolution that is sufficient to resolve these sites.

The rate of hydrogen evolution depends primarily on two factors: the density of available electrons via trions and the binding of the reactants and products onto the trion-hotspots.[45,46,77] The binding energies need to be strong enough for the reactants to receive the electrons and weak enough for the products to vacate the site for new reactants to occupy. Both of these conditions must be met for the catalytic reaction to go to completion.

Previous approaches on exciton and trion research have used temperature-dependent PL response to measure the trion size and the temperature dependence of the band gap. This was done by measuring the long low-energy tail of the trion PL spectra on MoS_2 over a wide range of temperatures. Temperature and thickness-dependent behaviors of exciton and trion PL for FL MoS_2 have been studied, and despite the shifting of exciton and trion PL bands with temperature due to thermal quenching, other characteristics did not vary with the thickness from ML to FL MoS_2.[78] Monolayer $MoSe_2$ has shown to be an ideal nanomaterial for exploring excitonic physics in the ultimate 2D limit. It has a true 2D excitonic system, which exhibits strong electrostatic tuning of exciton charging via a standard back-gated voltage via PL.[79] Optical absorption spectroscopy methods have also been used to measure the exciton and trion radii on MoS_2 in comparison with theoretical prediction, and it is predicted from the literature that trion binding energy and tail length could be measured as a function of gate voltage.[80-82] A custom broadband femtosecond pump–probe optical microscope is another technique used to measure the ultrafast dynamics of neutral and charged excitons in high-quality hBN-encapsulated monolayer MoS_2 at 8 K. This focuses on the fundamental mechanisms that determine exciton formation, dissociation, and decay processes; and investigation of samples with lateral size of few micrometers, performing transient reflectivity measurements with high spatial and temporal resolution and static optical characterizations on the same sample spot.[83] Trion formation dynamics in $MoSe_2$ has been reported when trions are generated on a picosecond timescale through exciton-electron interaction when resonantly pumping the exciton transition. As the pump energy is tuned from the high energy to low energy side of the inhomogeneously broadened exciton resonance, the trion formation time increases by ~ 50%. This feature can be explained by the existence of both localized and delocalized excitons in a disordered potential and suggests the existence of an exciton mobility edge in transition metal dichalcogenides.[84]

Doping and PL enhancement behaviour of seven p-type aromatic dopant molecules (salicylic acid, phenol, benzoic acid, methyl salicylate, nitrobenzene, aniline, melamine) on 1L MoS_2 have been investigated. The total PL intensity can be enhanced up to nine times using salicylic acid as dopant molecule. With strong enhancement of neutral exciton, some molecules, such as salicylic acid, phenol and melamine, can strongly enhance the intensity of trions up to 3.5 times. The enhancement with dominant intensity of trion and along with strong intensity of neutral exciton is explained by exciton dynamic equations with defect state involved. Therefore, defect dominated exciton process may be an essential factor governing the light-emitting capability of 1L MoS_2.[85]

The dielectric permittivity of the medium that surrounds the MoS_2 quantum dots (QDs) has a significant influence on the emission properties of the QDs. It is observed that the surrounding medium donates electrons to the QDs, which in effect causes destabilized exciton recombination by an increased formation of A^- trions. Also, the PL peak energies of A^- trions shift faster than those of A exciton with respect to the increase in the dielectric constant. And the radiative recombination rate of A exciton changes more quickly with dielectric permittivity than that of the A^- trions. Moreover, control of the generation of A^- by properly tuning and selecting the surrounding environment was achieved. This will provide valuable information for tuning the emission properties of TMDC QDs for various optoelectronics and valleytronics applications.[86]

2.1 – Synthesis and fabrication methods for TMD compounds

In general, 2D materials can be prepared by two strategies, i.e., top-down-based exfoliation methods and bottom-up-based growth methods.[40] The most common physical methods used involve chemical vapour deposition (CVD),[40,87] epitaxial growth[88,89] and mechanical/liquid exfoliation methods.[90-94] The following sections 2.2 to 2.5 give an overview of these methods from literature to enable a better understanding of each method in terms of advantages, disadvantages and drawbacks as well as scalability potential for the synthesis and fabrication of TMD materials such as MoS_2. The main reasons for the decision to use certain methods for the experimental preparations for exfoliation are also given.

2.2 – Chemical Vapour Deposition

CVD is a bottom-up synthetic route that provides a scalable and controllable way to grow high quality and large area 2D materials with a reasonable cost. It is a process in which gaseous materials react in the vapour phase or on the surface of substrates, forming a solid product that can be deposited on the substrate.[40] In forming the material, growth parameters such as temperature, chamber pressure, carrier gas flow rate, precursor, and source−substrate distance, can be used to control the number of layers, their size, phases, morphology, orientation, and the introduction of any dopants or defects into the structure.[40] These same parameters can also affect mass and heat transport which can further affect the growth of these materials. Plasma-enhanced CVD (PECVD) is a powerful tool to enable many film deposition processes that are impossible or very difficult to achieve by solely adjusting temperatures and other parameters in a typical thermal CVD reaction.[95] For example, Kim et al. used the PECVD approach and achieved the growth of MoS_2 films at temperatures from 423K to 473K using a Mo thin film and H_2S gas as precursors.[96] In another example Lu et al. used ICP (Inductively-Coupled-Plasma)-CVD to strip the top-layer S atoms from an as-grown MoS_2 monolayer and obtained intermediate MoSH, and followed this with thermal selenization to grow Janus MoSSe monolayer TMD materials.[97] PECVD has advantages such as low temperature, transfer-free process, and industrial compatibility, which enables facile, scalable, and low-cost preparation of 2D materials with clean surfaces and interfaces directly on noncatalytic substrates. In comparison CVD is the most successful method for low-cost scalable preparation. However, when it comes to practical applications, disadvantages such as high operating temperature (∼1000 °C), probable usage of metal catalysts, contamination, defects, and interstices introduced by postgrowth transfer are not negligible. These are the reasons why plasma-enhanced CVD (PECVD), a method that enables catalyst-free in situ preparation at low temperature, is imperatively desirable.[98, 99]

Overall, the CVD technique shows promise to generate high-quality TMD layers with scalable size, controllable thickness and excellent electronic properties. The obtained TMD monolayers or films can be used as the active components for nanoelectronics and as the building blocks for constructing layered heterostructures.[87] However, the need for interdigitated electrodes to connect to the flake electrochemically and the above disadvantages ruled out using this method as part of this research.

2.3 – Epitaxial Growth

Epitaxial growth is another bottom-up method and the three primary growth modes most commonly known for thin-film epitaxy are: the Volmer−Weber, Frank Van der Merwe, and Stranski−Krastanov modes.[88] The 2D TMDs van der Waals epitaxial growth commonly follows the Stranski−Krastanov or Frank Van der Merwe growth modes. For Stranski−Krastanov growth mode, also known as “layer-plus island growth”, monolayer TMD domains initially gather and interconnect with each other until the full coverage of the monolayer is completed.[88] The growth continues through the nucleation and coalescence of TMD nanoparticles or few-layer islands, leading to few-layer epitaxy and multilayer growth.[88] The Frank Van der Merwe mode is an “island growth” mode, where the TMDs layers are formed in isolated islands with different layer thicknesses and then stitched to form a complete thin film. It can produce TMDs with abundant structural edges, which is desirable in catalytic applications.[88] The epitaxial growth approach to minimize grain boundaries uses single crystalline substrates, such as sapphire and mica, in order to enable growth of the 2D materials.[89] The crystal symmetry of the substrate is used to control the crystallographic orientation of the film to ideally obtain single crystal (single domain) films with minimal dislocations and other defects. Layered materials present an opportunity for epitaxy to occur due to the lack of out-of-plane chemical bonding, nevertheless, film-substrate interactions are sufficiently strong to cause in-plane alignment resulting in "epitaxy" despite lattice mismatch.[100] Other substrate properties include the lattice constant, miscut angle and surface energy which are important factors to control the film orientation and surface coverage.[100] The aforementioned properties along with the substrate symmetry/lattice match, size, availability, thermal and chemical stability are all major contributors to the scalability potential for epitaxial growth of TMD compounds.[100] The use of a mica substrate has been inspired by molecular beam epitaxy (MBE) growth of TMDs under ultra-high vacuum (UHV) conditions pioneered by Koma[101] in the 1980s and termed van der Waals (vdW) epitaxy.[89] For vdW epitaxy to occur both the film and the substrate have to be inert 2D surfaces. The presence of weak van der Waals interactions between the film and the substrate instead of strong covalent or ionic bonding enables growth of epitaxial films of materials with dissimilar lattice constants.[89] Epitaxial nuclei that share the same orientation can stitch together to effectively form a wafer-scale single crystal. However, as outlined above, vdW epitaxy has been mostly limited to UHV (MBE) or high temperature (CVD) conditions, which are difficult or costly to integrate into existing process flows.[89] However despite this, vdW epitaxial growth on 2D materials, has been achieved on metal sulphides HfS_2,[102] MoS_2,[103] ReS_2,[104] SnS_2,[3] and ZrS_2[102] as well as a 2D metal halide PbI_2,[105] by ALD (Atomic Layer Deposition) method using previously reported processes that operate at relatively low temperatures of 348K to 673K. ALD is a specially modified chemical vapor deposition method to grow thin films by self-limiting chemical reactions.

ALD involves the formation of thin films by pulsed alternating passes of gas-phase precursors into a reactor and chemisorbing and reacting on a substrate. Individual atomic layers are deposited by supplying inert gases (Ar, N_2, etc.) to separate the various reactants, and the thickness is controlled by repeated deposition, ensuring precise layer-by-layer film growth. In other words, ALD is not deposited by a gas phase reaction, but rather one reactant is adsorbed onto a substrate, and then a second or third gas enters and chemisorbs with the substrate to form a film. This reaction is called a self-limiting reaction.[106] In comparison CVD processes involve a continuous chemical reaction with all reactants present simultaneously, leading to less control over film thickness and conformality on complex surfaces.[106] The self-limiting reaction and high-temperature conditions again ruled out this method for producing monolayer and scalable MoS_2 as part of this research thesis.

2.4 – Exfoliation Methods

Exfoliation is a top-down method and can generally be categorised into mechanical or liquid phase exfoliation.[90-94] A classic example of mechanical exfoliation is the exfoliation of graphite to give graphene,[107] the mechanism involved in this process involves peeling graphene from the bulk graphite layer by layer. There are two kinds of mechanical routes to exfoliate graphite into graphene, i.e. normal force and lateral force; one can exert normal force to overcome the Van der Waals attraction when peeling two graphite layers apart, such as micromechanical cleavage by Scotch tape.[108] Through graphite self-lubricating ability in the lateral direction, one can also exert lateral force to promote the relative motion between two graphite layers.[107] Other mechanical methods used for the production of graphene over the last decade have included sonication, ball milling, fluid dynamics and supercritical fluid methods to name but a few.[107] One example of mechanical exfoliation is by Higashitaramizu et al. They oxygen-annealed mechanically taped-exfoliated bulk SnS under a reduced pressure at 10 Pa, where surface oxidation and SnS sublimation proceed simultaneously, resulting in a monolayer-thick SnS layer with a SnOx passivation layer.[93] Layered materials such as MoS_2 can be exfoliated by ion intercalation while layered oxides and hydroxides are generally exfoliated by ion exchange.[109, 110] Liquid phase exfoliation (LPE) methods result in 2D nanosheets with lateral sizes in the range 100 nm-100 µm and thicknesses ranging from 1-10 monolayers.[90] This method involves the production of few-layer nanosheets by applying high shear or ultrasound to layered crystals in certain stabilizing liquids (i.e. appropriate solvents and surfactant or polymer solutions).[90] LPE has been applied to a wide range of 2D materials including graphene, boron nitride, TMDs, phosphorene, $Ni(OH)_2$, transition metal oxides (TMOs), and MXenes.[90] Balan et al. report that the naturally occurring hematite with highly oriented, large crystals can act as an excellent precursor for the liquid exfoliation of novel 2D materials such as hematene.[91] Works by Coleman et al. demonstrated that TMD compounds that undergo liquid exfoliation are efficiently dispersed in common solvents that can be deposited as individual flakes or formed into films as they are exfoliated into individual layers.[92] Nicolosi et al. discovered that after liquid exfoliation electrons are constrained to adopt a 2D wave function, thus modifying the electronic band structure of materials. They observed the bandgap of MoS_2 changes on exfoliation from 1.3 eV for the bulk crystal to 1.9 eV for an exfoliated layered nanosheet.[94] The main liquid exfoliation mechanisms are shown in figure 2.3.

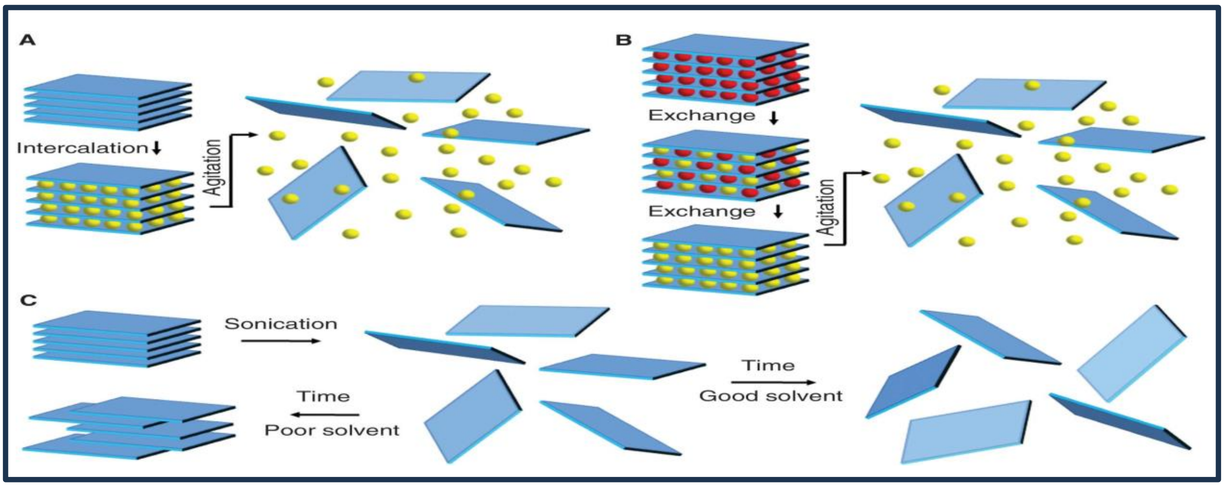

Figure 2.3: Schematic description of the main liquid exfoliation mechanisms. (A) Ion intercalation. Ions (yellow spheres) are intercalated between the layers in a liquid environment, swelling the crystal and weakening the interlayer attraction. Then, agitation (such as shear, ultrasonication, or thermal) can separate the layers, resulting in an exfoliated dispersion. (B) Ion exchange. Some layered compounds contain ions between the layers to balance surface charge on the layers. These ions (red spheres) can be exchanged in a liquid environment for other, often larger ions (yellow spheres). As above, agitation results in an exfoliated dispersion. (C) Sonication assisted exfoliation. The layered crystal is sonicated in a solvent, resulting in exfoliation and nanosheet formation. In "good" solvents—those with appropriate surface energy—the exfoliated nanosheets are stabilized against reaggregation. Otherwise, for "bad" solvents reaggregation and sedimentation will occur. This mechanism also describes the dispersion of graphene oxide in polar solvents, such as water.[94]

Chemical lithium intercalation/extraction exfoliation is still the most effective route to obtain the 1T (trigonal)-phase MoS_2 monolayer with high crystallinity.[94]

Finally, work by Fang et al.[111] used electrochemical exfoliation to produce high-quality 2D sheets via cathodic exfoliation and functionalized 2D sheets via anodic exfoliation. These materials were found to possess large size, high crystallinity, and a pure phase structure, comparable with the products from the CVD method.[111] The mechanism of electrochemical exfoliation of bulk MoS_2 crystals is described in Figure 2.4. First, by applying a positive bias to the working electrode, the oxidation of water produces •OH and •O radicals assembled around the bulk MoS_2 crystal. The •OH and •O radicals and/or SO_4^{2-} anions insert themselves between the MoS_2 layers and weaken the van der Waals interactions between the layers. Second, oxidation of the radicals and/or anions leads to a release of O_2 and/or SO_2, which causes the MoS_2 interlayers to greatly expand.[111] Finally, MoS_2 flakes are detached from the bulk MoS_2 crystal by the erupting gas and are then suspended in the solution. The surface of the bulk MoS_2 crystal should be oxidized during electrochemical exfoliation, and this is directly related to the quality and degree of oxidation of the exfoliated MoS_2 nanosheets. By optimizing the experimental conditions, a bulk MoS_2 crystal with a barely oxidized surface can be obtained.

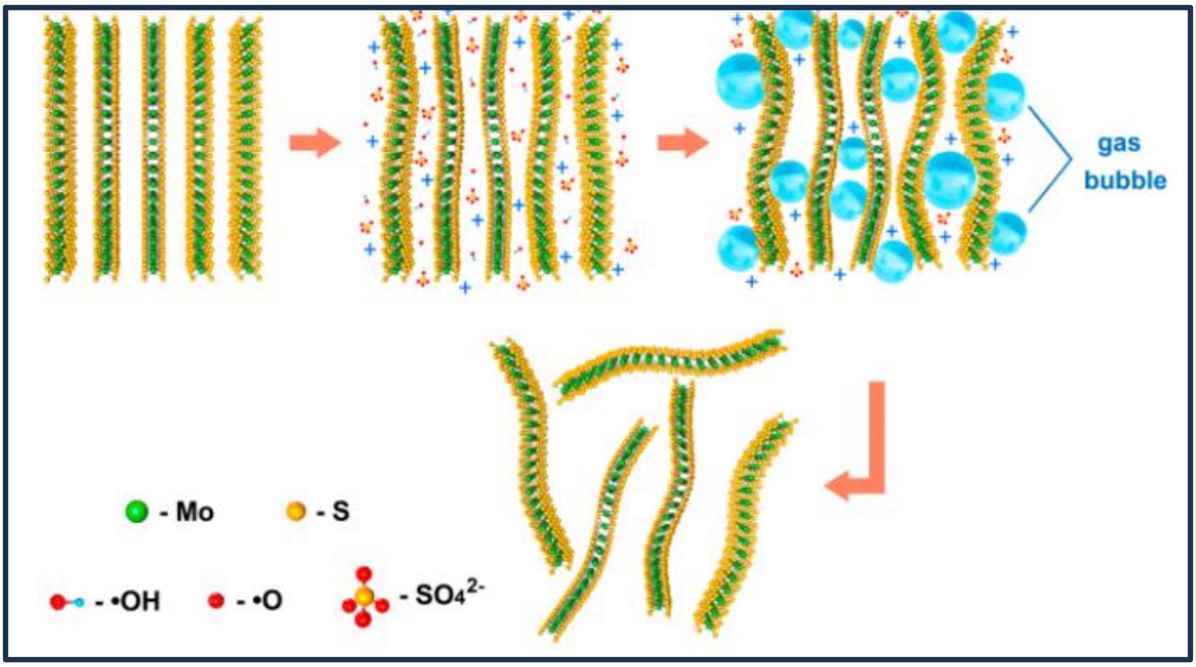

Figure 2.4: Schematic illustration for mechanism of electrochemical exfoliation of bulk MoS_2 crystal in Na_2SO_4 solution.[111]

In conclusion the LPE and electrochemical methods of exfoliation involve less harsh conditions with no high temperatures and metal catalysts involved in producing exfoliated monolayer MoS_2 material in comparison with CVD and epitaxial methods. The potential to use greener solvents and surfactants as the dispersion medium in the exfoliation process further provides improved potential for scalability purposes. The larger flake size produced in electrochemical exfoliation will enable easier mapping measurements on the flake. It was therefore decided that these methods would be suitable experimentally in producing monolayer/FL MoS_2 material.

2.5 – Microwave Assisted Liquid Phase Exfoliation (MALPE) Methods

As methods of liquid phase exfoliation techniques have been shown to be unsatisfactory in terms of achieving short processing times, high yields, chemical stability, ultrathin thicknesses and large lateral sizes of the nanosheets, microwave assisted methods have shown more rapid times, higher efficiency and a potentially scalable approach to exfoliate 2D nanomaterials into mono- and few-layer nanosheets of superior chemical stability and large lateral size.[112] The microwave exfoliation of graphene oxide into large monolayer sheets and flakes of graphene is one recent example of where this has been successfully achieved with a high yield obtained.[113]

The MALPE process is split into two main steps: wet-grinding and microwave irradiation as depicted in Figure 2.5. The wet-grinding procedure has traditionally been done using high-affinity polar organic solvents and ionic liquids with varying experimental parameters such as power, temperature and time.[112] The dielectric constants of the solvents and ionic liquids allow for efficient absorption of the electromagnetic energy due to the polarization effects of dipole rotation and in the case of ionic liquids, ionic conduction as they have abundant anion−cation pairs, and thus a high density of strong dipoles.[114]

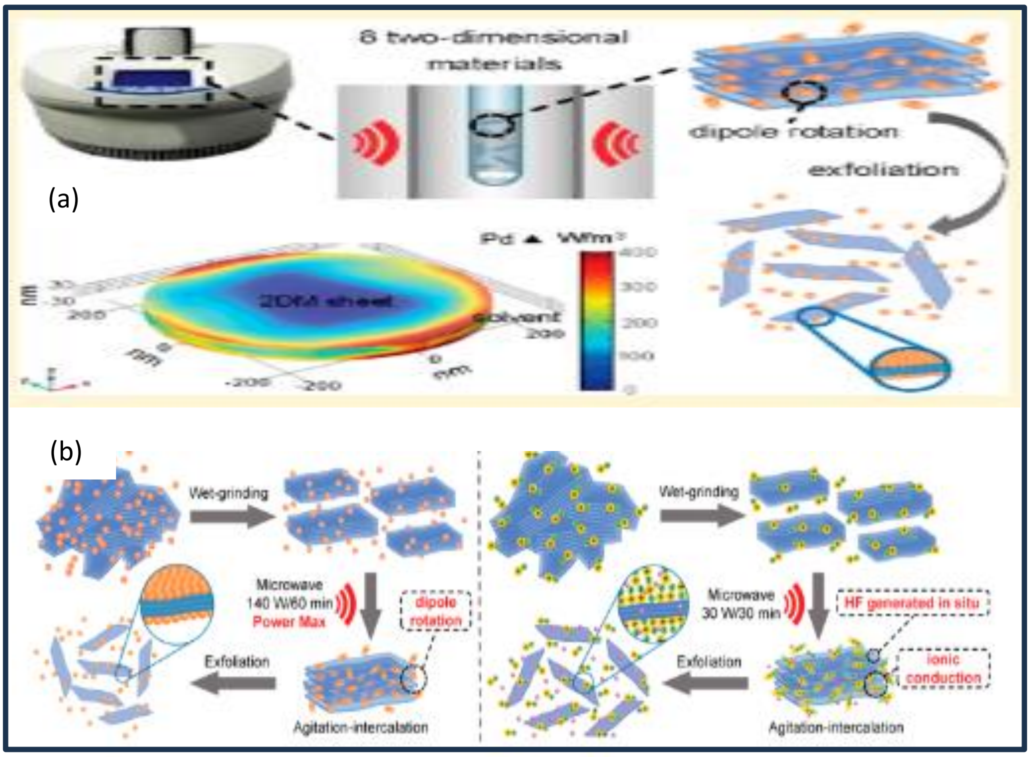

Figure 2.5: (a) Pathway for the efficient liquid exfoliation of 2D nanomaterials Using microwave assisted (MALPE) methods.[112] (b) Schematic diagram of the MALPE process with organic solvents and ionic liquids as fluid media.[112]

In terms of yields, organic solvents generally achieve higher yields than ionic liquids, likely originating from the longer-lasting strong molecular dipole rotation of microwave-durable organic solvents under prolonged higher-power irradiation as well as sterically less demanding organic solvent molecules facilitating intercalation and exfoliation.[112]

In terms of green chemistry, microwave synthesis offers potential for a more environmentally benign method for the fabrication of 2D nanomaterials such as MoS_2, when using more aqueous media such as surfactant solution or water/ethanol solvent to perform exfoliation with shorter reaction time, lower energy consumption and higher product yield, and the scope of this research will investigate such possibilities. Coleman and co-workers reported the first liquid phase exfoliation of MoS_2 in N-methyl pyrrolidone (NMP),[92] and various other organic solvents have also been used for successful exfoliation of MoS_2. However, the solvents used are highly toxic and have a high boiling point which makes them difficult to remove. The microwave-assisted preparation of inorganic nanostructured materials in liquid phase is currently a fast-growing area of research; and it is expected that related research activities will continue to grow rapidly in the coming years due to the involvement of low-cost solvents making it a very cost-effective process. Although most research on microwave assisted synthesis is still performed on a laboratory (ml) scale, it is expected that this novel technology will soon be used on a larger, perhaps even production, scale.[115]

An example of the absorption data from literature for a microwave treated MoS_2 sample (plot in blue) in the wavelength range of 200–800 nm is shown in Figure 2.6.[116]

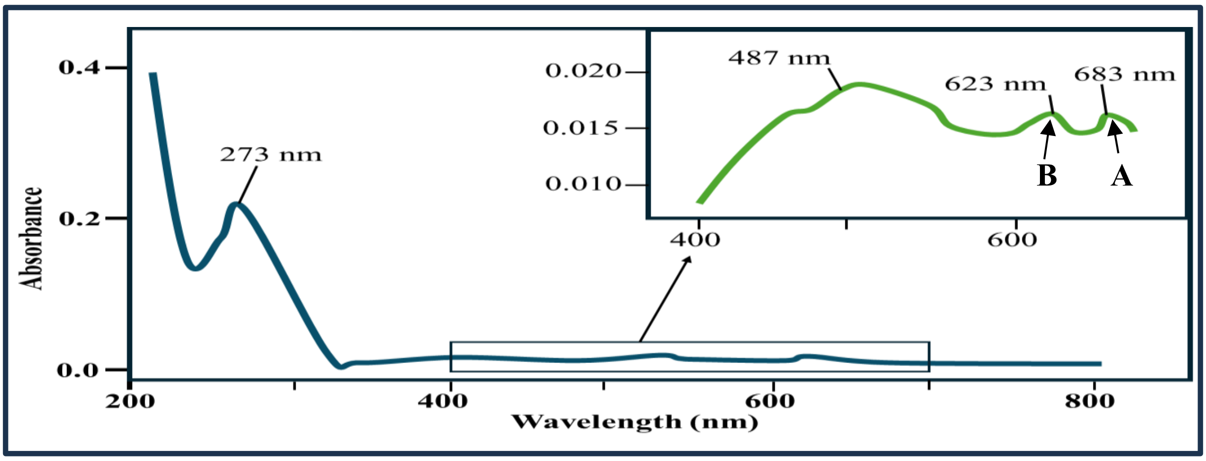

Figure 2.6: UV–vis absorption spectrum of a microwave treated MoS_2 sample. A prominent peak at 273nm is seen in the spectrum which we associate with the high energy excitonic transitions corresponding to the 2H phase of MoS_2. Inset in green shows the enlarged region from 400–700nm. Peak features at 487, 623 and 683nm are shown as inset; these peak features are assigned due to quantum confinement effects and the A, B excitonic transitions respectively.[116] The exciton absorption bands are known to originate from the direct band-gap transition at the K point, with the energy split arising due to the valence band spin-orbital coupling.[4]

From Fig. 2.6, the characteristic peak featured at 273 nm in the absorption data corroborates the existence of mainly the 2H phase of MoS_2 which comprises the nanosheets and the nanostructures of a microwave treated sample. The A exciton (683 nm) and B exciton (623 nm) peaks shown as inset are of interest as they might shift or change in intensity depending on the microwave treatment parameters and the resulting changes in the material's structure and electronic properties. The other preparation techniques cannot be compared spectrally by UV-vis as they are in solid form on a substrate.

With the successful microwave exfoliation of graphene oxide using microwave irradiation to rapidly and efficiently separate the layers of graphite, to produce graphene sheets or flakes with high yield, high quality and large size.[113] It was decided to use this approach experimentally for the exfoliation of MoS_2 in this research thesis, as there was also availability of a microwave within the Swansea University chemistry department.

2.6 – Conclusion

Opportunities for research in the area of 2D MoS_2 have come in the direction of LPE and electrochemical exfoliation methods in terms of preparation of exfoliated material. MoS_2 in monolayer form in high yield is one of the objectives of the research, as this will maximise catalytic efficiency providing easier access to surface active sites. Various liquid phase exfoliation methods will be used to hopefully produce the monolayer material in high yield. Characterisation techniques such as Raman/PL spectroscopy and UV-vis spectroscopy will be used to monitor monolayer yields. If a high enough yield can be formed, a validated CV curve will be produced to confirm and determine redox properties from which, electrochemical-Raman techniques will be used to characterise the structural changes formed under an applied voltage range upon application of an electrochemical cell. The use of dopants and the creation of defects are potential routes that can be used to maximize the surface-active sites. If, however, a low yield of monolayer is obtained from LPE methods, then electrochemical exfoliation on an MoS_2 crystal will be used to produce a higher yield of monolayer material with larger flake size that can be examined using HSI methods. HSI can be used to monitor the PL emission signals that produce exciton and trion emissions. The trion hotspots formed can be used as an indicator of the few-layer (FL) regions of the flake where potential active sites occur and produce an image of catalytic efficiency toward the HER.

CHAPTER–3

2D perovskites

2.0 – Introduction

2D perovskite compounds are a class of material that have gained increasing attention in recent years, as they have found applications in solar cells (PSCs), light-emitting diodes (LEDs), photodetectors, lasers, and photocatalysis. [117, 118] The compound $MAPbBr_3$ is the focus of this work, with stability and degradation of the perovskite structure being investigated. A review of 2D and 3D bulk perovskite structure is given for comparison purposes, and perovskite catalysis and the degradation mechanism are also reviewed.

3D bulk perovskites have a general formula of ABX_3, where smaller transition metal ions on the B site reside in corner-sharing octahedra of X anions, and larger A-site cations have 12-fold coordination with X (Fig. 3.1).

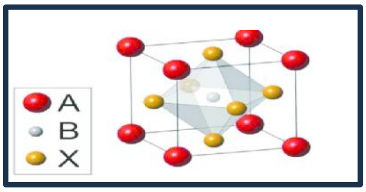

Figure 3.1: ABX_3 perovskite general (3D) crystal structure.[119]

In comparison, 2D perovskites are perovskite materials with a layered crystal structure. They are made up of metal halide ($[BX_6]$) octahedral layers (where B is a divalent heavy metal, usually Pb, and X are halide ions) interspaced by large organic cations called spacers. They have the general chemical structure $RA_{n-1}B_nX_{3n+1}$ where:

- R is an organic spacer cation
- A is a smaller, monovalent A-cation
- M is a divalent metal cation (commonly lead (Pb) or tin (Sn))
- X are halide ions
- n is the number of inorganic perovskite layers between spacer layers

This layered 2D structure changes the optical and electronic properties of the material compared to the bulk (3D) perovskite. This gives the layered and bulk perovskites very different material properties that are used for different applications. 2D perovskites can form colloidal nanoplatelets or sheets, which can be incredibly useful for controlling charge properties within devices (LEDs, PV, photodetectors, etc).[117, 118] An image of the 2D perovskite structure is shown in Fig. 3.2.

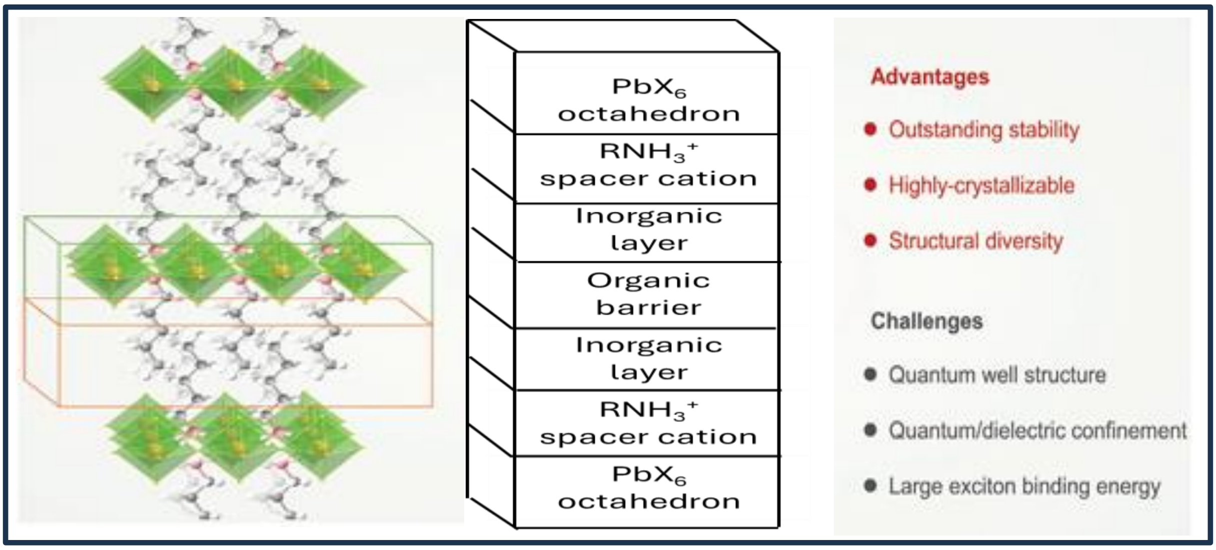

Figure 3.2: Schematic illustration of the 2D perovskite structure, clearly distinguishing the roles of the organic and inorganic layers. Specifically, the organic layer functions as a barrier, while the inorganic layer acts as a potential well. This layered crystal structure exhibits significant advantages in device applications, although it also encounters certain challenges.[120]

These bulky organic RNH_3^+ spacer cations perform a similar role to organic A-cations in 3D perovskite structures. They balance out charge within the crystal structure and therefore create stability. However, their larger molecular radius creates separation between their metal halide layers, which is instrumental in defining the 2D structure. You can tune the electrical and optical properties of the perovskite material by changing the type of spacer cation used, as well as the layers of dimensionality, n, and the metal halide composition. This separation significantly affects the electronic and optical properties of the material, leading to enhanced stability and tunable properties compared to their 3D counterparts. The dimensionality of a perovskite is defined by the number of metal-halide layers between spacer layers, n:

- For 2D perovskite materials, $n=1$ so there is only 1 layer of $[BX_6]$ octahedra between spacer layers.
- For a 3D perovskite crystal, $n \rightarrow \infty$. There are no spacer molecules at all.
- Perovskites where $n=2,3,4...$ are known as quasi-2D perovskites. These have a few $[BX_6]$ octahedral layers between spacer layers.[117, 118]

2D perovskite layered surfaces can potentially catalyse several reactions including oxidation of small molecules such as CO, hydrocarbons and NOx, (photo)electrochemical splitting of H_2O, and reduction of CO_2, N_2, and O_2. The flexibility of the electronic and crystal structure and chemical versatility of 2D perovskites can be used to establish design principles for highly active, selective, and stable catalysts.[119] In addition, 2D layered perovskites have generated wide interest due to their enhanced stability in ambient conditions. The optoelectronic properties of 2D perovskites are tunable with n, as n decreases, confinement increases, leading to a rise in binding energy much higher than in their 3D counterparts.[121] Bulk 3D perovskites with the above formula of ABX_3 have had limited success, however, they do possess chemical versatility and flexibility of the electronic and crystal structure. In terms of structure, the A is an organic ammonium cation or Cs^+, B is Pb^{2+}, and X is a halide anion such as iodide, bromide or chloride. These perovskite nanosheets can be prepared through various approaches. Micron-sized sheets were obtained via a chemical vapor deposition growth method.[122] However, bulk 3D perovskite commercial usage is challenging due to their low long-term chemical stability in moist environments.[121] They also suffer from high defect densities, low carrier mobilities, and higher charge recombination due to grain boundaries.[121] Colloidally stable $MAPbBr_3$ and $MAPbI_3$ nanosheets, up to 500 nm in size, can be prepared via exfoliation of bulk crystals with long chained ligands[123] or via instantaneous crystallization of precursor salts in an antisolvent.[124] The perovskite structures are prepared either as single crystal 2D particles or as stacked sheets consisting of the aforementioned repeatable $MA_{n-1}Pb_nX_{3n+1}$ layers separated by long chain alkyl ligands. In the case of $MAPbBr_3$, the long chain alkyl ligands are the larger A site methylammonium cations that act as stabilisers as they form a dense shell on the outside of the crystal lattice as shown in Fig. 3.1. The layered structures, which are more stable due to the dense ligand shell,[125] exhibit quantum confinement, as confirmed by UV-vis absorption and photoluminescent (PL) spectroscopy.[126] However, on the whole, development work on perovskite catalysis is at a very early stage and practical uses are limited due to environmental stability issues. An improved understanding is required of 2D perovskite electronic structure and how it can rationalize surface energetics, catalytic activity trends, and mechanistic insights into the degradation process. This can involve carbon, nitrogen, and oxygen chemistries of which this study will primarily focus using initially electrochemical-Raman techniques on the $MAPbBr_3$ perovskite compound.[126-128]

Perovskite solar cells have improved enormously in terms of power efficiency in recent years however, they still lag behind the more conventional silicon technology as their performance suffers due to environmental factors such as moisture, heat and light which adversely affect the lifetime of these kind of devices.[7, 126, 127] Research into the elucidation and elimination of these degradation pathways is critical to the future success of PSCs and other similar devices and technologies. If these types of devices are to be successful in the future and become viable then the key requirements are high performance, a long lifetime and low cost.[7]

3.2 – Perovskite Degradation

As humidity has the largest impact on PSC performance, groups such as Yang et al and Leguy et al, have shown that with prolonged exposure to water vapour and a high relative humidity (RH) of (80 – 100%), the perovskite lattice can undergo extreme adverse effects and undergo complete decomposition after only ~6 hours.[126,127] The interaction between $MAPbI_3$ and H_2O vapor was investigated by Christians et al.[129] These undertakings revealed that H_2O exposure does not simply cause $MAPbI_3$ to revert to PbI_2. It was shown that, in the dark, H_2O is able to complex with the perovskite, forming a hydrate product similar to $(MA)_4PbI_6{\cdot}2H_2O$. This causes a decrease in absorption across the visible region of the spectrum and a distinct change in the crystal structure of the material. The decomposition to PbI_2 was monitored using UV-vis and XRD measurements over varying Relative Humidity (RH) conditions and timescales.[129] Femtosecond transient absorption spectroscopy (TAS) experiments, were used to detect small quantities of PbI_2 formed that were not observable with XRD.[129] A study led by Bryant et al, demonstrated that light and oxygen-induced degradation is the main reason for the low operational stability of $MAPbI_3$ perovskite solar cells exposed to ambient conditions.[130] When exposed to both light and dry air, unencapsulated $MAPbI_3$ solar cells rapidly degrade on timescales of minutes to a few hours. This rapid degradation is also observed under electrically bias driven current flow in the dark in the presence of O_2. In contrast, significantly slower degradation is observed when the $MAPbI_3$ devices are exposed to moisture alone (e.g. 85% relative humidity in N_2). They showed that the light and oxygen induced degradation can be slowed down by the use of interlayers that are able to remove electrons from the perovskite film before they can react with oxygen to form O_2. These observations demonstrate that the operational stability of electronic and optoelectronic devices that exploit the electron transporting properties of $MAPbI_3$ will be critically dependent upon the use of suitable barrier layers and device configurations to mitigate the oxygen sensitivity of this material.[130] Certain tools such as UV-vis spectroscopy have been used to show visually the colorimetric transformation that takes place upon the decomposition of the perovskite when changing from a black to yellow colour in the case of $MAPbI_3$.[7, 126, 127] Additionally, in situ and time-resolved methods can also provide important information about decomposition kinetics and can detect transient intermediates in degradation pathways.[126]

Finally, a study by Liu et al, found that the PL quantum yield (QY) of bromide-based perovskites can be increased from 2.5% to 71.54% by introducing water, and the PL QY of a sample in aqueous solution decreases minimally over 1 year. The enhanced stability and PL QY are attributed to the formation of the water-induced methylammonium lead bromide perovskite ($MAPbBr_3$)@PbBr(OH).[131] In terms of in-situ spatial resolution, the literature has achieved resolution down to 1 µm images of $MAPbI_3$ films using SEM,[132] and down to 10 nm scale for AFM (Atomic Force Microscopy) thickness measurements on PbI_2 nano platelets.[10] TEM images of $MAPbBr_3$ have achieved 20 nm spatial resolution.[131]

3.3 – Conclusion

Opportunities for research in the area of 2D perovskites from literature would appear to show that the 2D perovskite layered structure offers more potential for longer term stability under certain conditions. The 2D structure enables and facilitates easier tuning of their properties in comparison with the 3D bulk perovskite structure. Hence, it is for this reason that the $MAPbBr_3$ compound will be investigated further as it is shown from literature that it possesses high optical absorption, high carrier mobility, long diffusion lengths, and unique charge transport properties.[128, 133] Further investigation into moisture and water-induced degradation is needed to determine the mechanism of degradation and develop a more stable perovskite to water and oxygen environments. It is proposed that electrochemical-Raman techniques can be used to characterise this material if a valid CV curve is produced, and Raman spectroscopy can be used to monitor the degradation process in real-time under various conditions (e.g., humidity, light exposure) by using the electrochemical cell in-situ setup. Raman spectroscopy can help to understand the mechanisms of perovskite degradation, leading to the development of more stable perovskite materials. If an electrochemical response is not observed and a valid CV curve not produced, then a combination of fluorescence microscopy, PL spectroscopy and HSI imaging techniques will be used to produce a sequence of images during in-situ real-time experiments under varied RH conditions as well as aqueous acidic and alkaline conditions to further characterise the degradation process.

CHAPTER–4

Raman studies on electrochemical *N*-nitrosation reactions and nitroso species.

4.0 – Introduction

The *N*-Nitrosamines are compounds with carcinogenic[134-137] and mutagenic properties,[17,138] and can be found in our environment as contaminants in the air, soil, water, drinks, drugs, and diet.[137] The primary sources are industrial chemical processes or from incomplete combustion. Therefore, detection and monitoring of those contaminants in a chemical process is highly important. This is to prevent their occurrence, especially for the *N*-nitrosamines which may enter as impurities in products made for human consumption, such as pharmaceutical compounds. The dimer of NO_2, dinitrogen tetroxide (N_2O_4) is a known reagent which can be generated in situ or utilised directly as NO_2 for the synthesis of *N*-nitrosamines.[21, 139-146] Infrared (IR) spectroscopy has been used to study N_2O_4 and the presence of its different isomers.[147-155] Nitrogen oxides are known to be Raman active, and have all been fully characterised using this technique. They can also be quantified in solutions provided the experiments are calibrated.[156-159] Electrochemical-Raman spectroscopy can be used to study the nature of intermediates formed during the course of a reaction. It is proposed from this study that the combination of Cyclic Voltammetry and electrochemical Raman spectroscopy could be a powerful tool that will provide a greater understanding of the redox reactions and the formation of intermediates occurring in nitrosations. With the combination of these techniques, it is possible to see structural changes in the compounds when a range of bias potentials and currents are applied. Cyclic Voltammetry is unable to show structural changes alone, however in combination with Raman spectroscopy this becomes possible as was observed in the preliminary study on ruthenium complexes in Chapter 6. Vibrational Raman spectroscopy has the potential to reveal the identity of many of the redox products, although not surprisingly, the documented vibrational spectra from these experiments are very complex due to the large number of possible products. In this study, we focus on the spectroscopic investigation of the electrochemical nitrosation of amines in an aqueous solution. When the technique is refined in future studies, it will allow for the electrosynthesis, testing and characterization of many other similar compounds, including nitro derivatives To date, there are several studies of N_2O_4, N_2O_5 and their compounds in the gas and solid phase.[23] but there have been few investigations that have dealt with these compounds in solution. Work by Brooksby and McQuillan.[160] on $NaNO_2$ under methanolic non-aqueous conditions demonstrated the formation of electrochemical products that are different to those from other nonaqueous solvents. Infrared spectra show that methanol reacts directly with the electrooxidation products of nitrite, and the presence of water also influences the product formation indicating that the solvent plays an important role in determining the fate of the intermediates that are formed in the absence of water. The oxidation of NO_2^- - generates NO_2 (eq 4.1) that quickly dimerizes to dinitrogen tetroxide, N_2O_4 (eq 4.2), which is a highly favoured reaction.

$$NO_2^- \rightarrow NO_2 + e^- \tag{4.1}$$

$$2NO_2 \leftrightarrow N_2O_4 \tag{4.2}$$

NO_2 is in the form of equilibrium between its zwitterionic form ($O{=}N^+{-}O^-$) and the NO_2 radical. The radical monomer $^{\cdot}NO_2$ can dimerise and form N_2O_4 at temperatures below dinitrogen tetroxide's boiling point of 21.1 °C.[161] However, the enthalpy of the dissociation-association reaction ($\Delta_f H^o_{(g)} = 57.12$ kJ. mol^{-1}) is in between that of a typical covalently bound molecule and a van der Waals complex, so this bond is relatively weak.[160,161]

In addition to NO_2 and N_2O_4, the generation of N_2O_3, NO_3^-, NO, and NO^+ are also postulated from chemical reactions involving nitrite and its oxidation products.[162]

4.1– Raman Spectroscopy

Harrar et al also studied solutions of N_2O_4 and N_2O_5 in anhydrous and aqueous nitric acid using Raman spectroscopy to gain a more detailed knowledge of the species present in these solutions and to assess the applicability of Raman spectroscopy as an analytical measurement technique.[23,160] The spectra of solutions of N_2O_4 in HNO_3 displayed evidence of the presence of the associated species, ($3NO^+ \bullet NO_3^-$), which had been identifed previously in a solid compound.[163,164] The effects of water on the spectra of these solutions were examined as there is an incomplete knowledge of the association of the species and how these compounds may interact with the solvent. It was confirmed that the nitronium cation, NO_2^+ is the dominant species in solutions of N_2O_5 in anhydrous HNO_3, and the spectra of concentrated solutions of

N_2O_5 exhibit a band that has not been reported previously; as Raman spectroscopy is the only technique that directly measures N_2O_5 and NO_2^+.[23] This weak band, has been attributed to a second vibrational mode of the molecule indicating a nonlinear conformation of the NO_2^+ ion which suggests that it is strongly associated with other species in solution. As the nitronium cation is known to be the primary reactant in solutions of N_2O_5 in HNO_3, the intensity of its Raman band at 1400 cm^{-1} is a good indicator of its concentration.[23] The Raman data indicated that N_2O_5 in HNO_3 is completely ionized into NO_2^+, and NO_3^- (with a strong band at 1050 cm^{-1}) at concentrations up to at least 3.0 mol l^{-1} (21 wt%).[23] In solvents of high dielectric constant, such as anhydrous HNO_3, N_2O_5 behaves as a strong electrolyte, and ionizes as follows:[165]

$$N_2O_5 \rightarrow NO_2^+ + NO_3^- \tag{4.3}$$

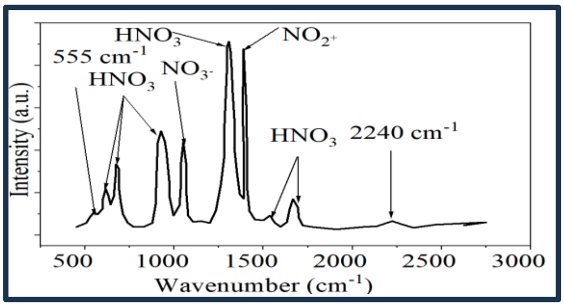

Figure 4.1: Raman spectrum of 3.0 mol l^{-1} N_2O_5 (21 wt%) in anhydrous nitric acid.[23] The spectrum shows the strong bands of both NO_3^- (at 1050 cm^{-1}) and NO_2^+ (at 1400 cm^{-1}), the ions which are present at high concentrations in this solution.

N_2O_4 also ionizes to NO^+ and NO_3^- when dissolved in HNO_3 and there is evidence of the presence of an associated species ($3NO^+ \bullet NO_3^-$) in addition to the well-known nitrosonium cation, NO^+.

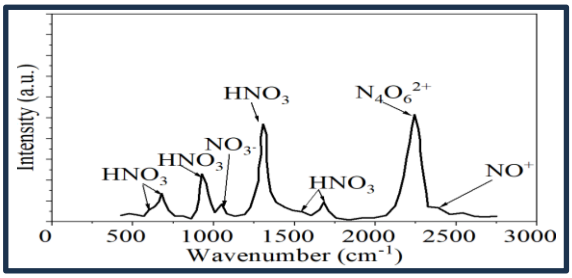

Figure 4.2: Raman spectrum of 4.0 mol l^{-1} N_2O_4 (24 wt%) in anhydrous nitric acid.[23]

The equilibria in these solutions are strongly influenced by the concentration of water, because it influences the degree of dissociation of HNO_3 and hence the concentration of NO_3^- ion.[23] Finally, the products of these reactions can be easily transformed into a variety of diverse functionalities. For example, *N*-nitrosamines (*N*- NO) are a class of carcinogenic, mutagenic and teratogenic compounds of biological interest and are used as 'trans-nitrosating agents', i. e., NO-donor drugs, the closely related N-nitramines (*N*-NO_2) are substances that exist widely in azo dyes and energetic materials. Other areas of research include the discovery of new NO donors, finding novel applications for NO donors, development of NO-drug hybrids, and development of NO donors with good tissue specificity.[23]

4.2– Conclusion

Opportunites for research in electrochemical *N*-nitrosation reactions arise from the fact that previous Raman spectroscopy studies on nitroso compounds in solution have produced Raman bands for N_2O_4, N_2O_5 and NO_2^+ species.[23, 160] This paved the way for further electrochemical research using an electrochemical cell setup into nitrosation reactions such as the formation of *N*-nitrosamine compounds from a secondary amine substrate and sodium nitrite reagent in solution form. This investigation continues on from previous research from Cardiff University Chemistry Department in work by Ali et al,[21] who investigated various secondary amine substrates in reaction with sodium nitrite reagent in producing *N*-nitrosamine products under flow electrolysis conditions. This collaboration will continue to investigate further this same reaction but this time using Electrochemical-Raman techniques by combining Cyclic Voltammetry with Raman Spectroscopy to identify and detect the formation of intermediates produced from a Density Functional Theory (DFT) calculated reaction pathway. A valid CV cuve will be produced to show the redox properties, and Raman spectra will be produced and matched up against the calculated spectra from DFT calculations. The electrochemical cell is modified for the reaction as a graphite working electrode is used.

CHAPTER–5

Instrumentation setups - background and theory

5.1 – Background and theory of UV – Vis Spectroscopy

UV-vis spectroscopy is a quantitative technique that is used to measure the amount of light that a compound absorbs. It uses light in the visible region, and the measurement is done by measuring the intensity of light that passes through a sample with respect to the intensity of the light through a reference sample. The light absorption process occurs when a molecule absorbs energy from UV or visible light, this causes the bonding and non-bonding electrons to jump from the lower energy levels (ground state) to higher energy levels that contain anti-bonding orbitals (excited state).[166] This absorption will affect the perceived colours of the chemicals that are involved in the measurement. Light emission happens when the excited electron returns to the ground state, releasing the absorbed energy as a photon of light at a specific wavelength. The wavelength is determined by the energy gap between its highest occupied molecular orbital (HOMO) and lowest unoccupied molecular orbital (LUMO).[166] Figure 5.1 displays a photo and schematic of a UV-visible spectrophotometer, and the Perkin Elmer Lambda 265 instrument used to perform the UV –vis absorbance measurement.

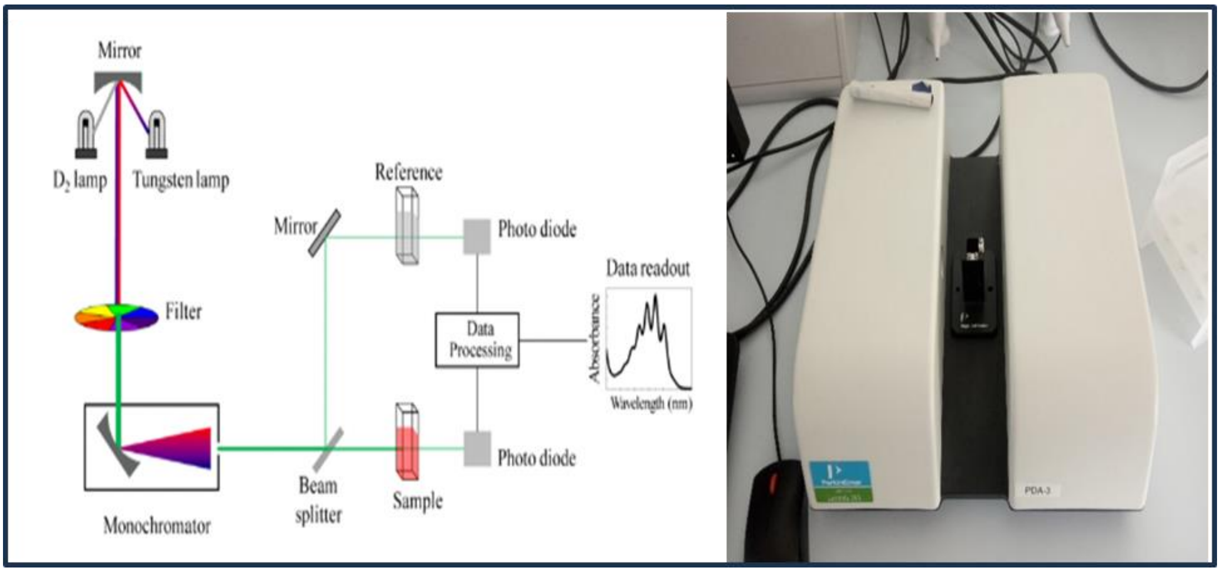

Figure 5.1: Photo and Schematic of a UV-Visible spectrophotometer.[166]

The main components of the UV-Vis spectrophotometer are the light source, a holder for the sample, a prism to separate the different wavelengths and a photodiode array (PDA) detector. The radiation source used for UV – Vis is normally a Tungsten filament (300 – 2000 nm) and deuterium lamp (180 – 300 nm). In a single – beam instrument, the cuvette that contains the blank solution needs to be measured first. The cuvettes used are rectangular, transparent and have an internal width of 1 cm. The Beer – Lambert law states that the absorbance is proportional to the concentration of the sample and the path length. It has a linear relationship between the absorbance and the concentration.[166]

$$A = \varepsilon cl \qquad (5.1)$$

Where **A** – is the absorbance, **ε** – is the molar absorption coefficient, **c** – is the molar concentration and **l**– optical path length.

The Beer – Lambert Law is useful for characterizing compounds, but there are assumptions that must be met experimentally for the law to fully apply, as the chemical and physical makeup of the sample can alter the extinction coefficient. In liquids, the extinction coefficient is wavelength dependent, and measurements are made at the peak maxima to minimize errors produced by the instrument, as at this point the absorbance is most sensitive to concentration changes resulting in more accurate data. At high concentrations, the absorption bands will saturate and show flattening of the peak. This flattening happens because the absorption peak is close to 100% due to the light that is already absorbed, solutions that are non–homogeneous exhibit this flattening effect and similarly homogeneous solutions of high concentration cause saturation of the signal and thus the same flattening effect.[166]

5.2 – Photoluminescence (PL) Theory

The Jablonski diagram (Figure 5.2) offers a convenient representation of the excited state structure, and the relevant transitions involved in the photoluminescence (PL) process.[167] Photoluminescence is light emission from any form of compound after they absorb electromagnetic radiation; and the technique can be used for characterisation of the electronic and optical properties of molecules. It is instrumental to 2D nanomaterial investigations since it enables effective detection of the exciton and phonon dynamics and uses these to display the electronic structure.[30] Similar to absorption spectra, photoluminescence can be applied to determine various changes occurring on the 2D nanocrystal, such as growth and size distribution, changes in thickness of the material and electronic properties such as the bandgap structure and surface defects are all areas of characterization. Quantitative PL measurements on 2D nanocrystals in general can be challenging as the PL signal can vary dramatically depending on the surface states and degree of quantum confinement. Additionally, the PL origin and its performance further complicate quantification due to potential bandgap transitions between direct and indirect behaviour.[30,31] A strong PL emission signal is caused by the transition from an indirect band gap semiconductor of bulk material to a direct band gap semiconductor in thin layer form.[31] PL emission is observed on monolayer MoS_2, which has a direct bandgap, and the quantum yield of the monolayer PL is much higher than for bilayer and bulk MoS_2.[30] The trihalide perovskite compounds also exhibit photoluminescent properties due to their microstructure and composition.[168]

JABLONSKI DIAGRAM

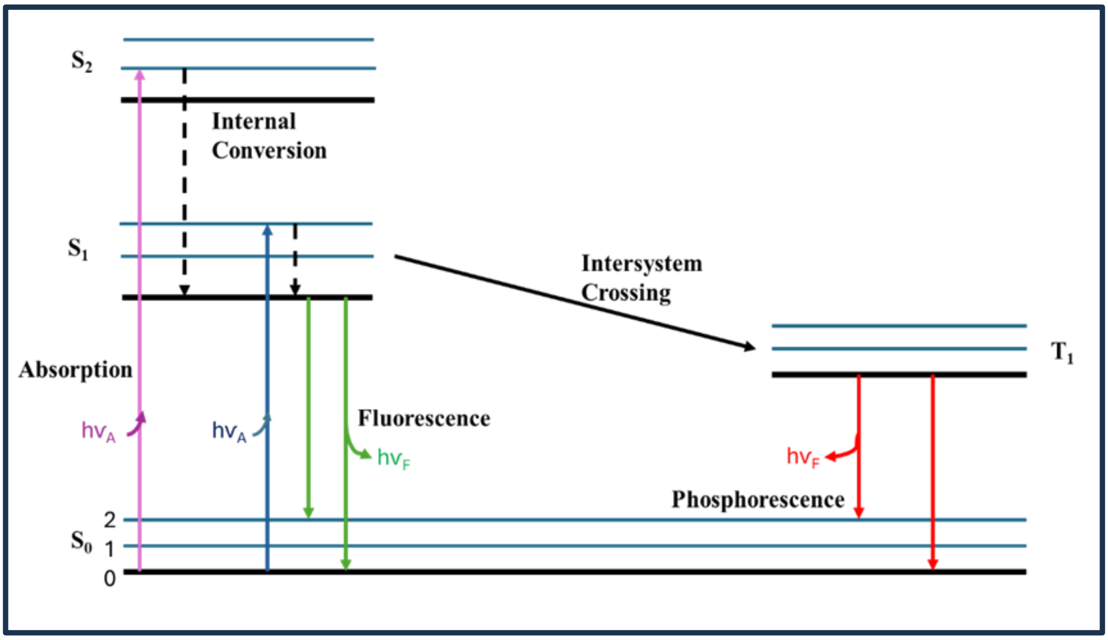

Figure 5.2: Jablonski Diagram: S0, S1, S2 are the singlet ground, first and second electronic states respectively.0,1,2, etc, are the different vibrational levels within each electronic energy level. T1 is the first triplet excited state.[169]

When light is absorbed, the molecule is usually excited from S0 to a higher vibrational level of either S1 or S2. Internal conversion takes place releasing non–radiative energy as the molecule itself relaxes to the S1 lowest vibrational levels. This is the most likely transition to occur in a molecule as it involves relaxation of the excited electron to the lowest vibrational level within the same electronic state before further transitions occur. No photons are emitted during this process, and hence no fluorescence or phosphorescence can take place. Therefore, it is a faster transition, and more likely to happen as determined by selection rules. Fluorescence can then occur emitting radiation as the molecule transitions back to S0 and typically to an excited vibrational level of S0. The loss of non–radiative energy through vibrational relaxation explains why the wavelength of fluorescent light emitted is always longer or of a lower energy than that of the light absorbed. This is the Stokes shift that occurs also with Raman, the difference in PL being that it is a radiative relaxation of an already electronically excited state.[13,14.]

Equally the tendency to relax to the lowest vibrational level is the concept of Kasha's rule which states that the emitting level of a given multiplicity is the lowest level of that multiplicity.[170] In essence this means that fluorescence only occurs with an appreciable yield from the lowest excited state of a given multiplicity: the lowest vibrational level of S1 in this case. Intersystem crossing is an isoenergetic radiationless process involving a transition between the two electronic states with different spin multiplicity and occurs when the electron in the molecule in the S1 state changes its direction of spin (spin conversion) and moves to the first triplet excited state T1. A change in spin is always required as the triplet state is lower in energy and because of conservation of (electron spin) angular momentum, it is not possible to excite directly from a singlet ground state to a triplet excited state with a photon. The molecule has to undertake a spin orbit coupling process which allows for a mixing of the electronic states involved, to undergo intersystem crossing into the lower energy triplet state.[171] Radiative emission from T1 or phosphorescence then returns the molecule to S0 once more. Phosphorescence usually involves the emission of longer wavelengths of light than fluorescence and because transitions from T1 to S0 are forbidden due to the spin forbidden nature of the transition. If it is based strictly on electronic selection rules it should not happen, therefore it is slower (milliseconds or seconds as opposed to nanoseconds). However, by coupling vibrational factors into the selection rules, the transition becomes weakly allowed and able to compete with the time scale of fluorescence.[172] The luminescence in ruthenium complexes is actually phosphorescence as it is due to transitions from T1 to S0.[171]

During the PL process, a semiconductor material such as MoS_2 is excited using a light source that provides photons, the photons are then absorbed, and electrons are then excited from the valence band to the conduction band, leaving behind a "hole" in the valence band. The combination of the excited electron in the conduction band and the hole in the valence band is called an electron-hole pair.[173] The excitations then undergo energy and momentum relaxations and the electrons then recombine with the holes under the emission of photons in a process called radiative recombination. However, electron-hole pairs can also recombine through non-radiative pathways, where the energy is transferred to lattice vibrations (phonons) and may dissipate as heat instead of being emitted as light. This can occur due to impurities within the material. Other factors affecting radiative recombination are material properties such as bandgap and defect density.[173] Photoluminescence affects the Raman signal, as a strong PL will show a weak Raman signal and vice versa. Both the Raman and PL information can be captured in one spectrum using the same laser. The Raman peaks occur at the beginning of the spectrum, with the PL peaks occurring enough of a distance away from the Raman so there is no overlap. The intensity of the PL band decreases with increasing layer number and bulk MoS_2 produces no PL signal at all. This effect is due to the indirect to direct band gap transition which occurs as we go from bulk MoS_2 to few-layer MoS_2.[78, 174, 175] The Raman and PL intensity maps should therefore be opposites of one another when comparing areas of monolayer and multilayer MoS_2.[78, 174, 175] In bulk MoS_2, the reason no PL is observed, and the Raman signal is weak is due to the local field effect, as for high refractive index materials such as MoS_2, the local electric field is weaker than the incident electrical field.[15]

5.3 – Fluorescence Microscope and Fluorescence Spectrometer setups for perovskite PL measurements

The Olympus BX51 Fluorescence Microscope, consisted of a Light source: (Olympus U-LH100HG) and a Blue Excitation bandpass filter: MF475-35 (475 nm) used. The Objectives used are: 20x, 50x and 160x magnifications respectively.

The FS5 Edinburgh Instruments Fluorescence Spectrometer consisted of Excitation wavelength: 455 nm Excitation bandpass filter: 455 nm Emission long pass filter: 496 nm Range: 500 -700 nm, Dwell time: 0.2 seconds. (sample exposure time). Step Size: 0.25 nm, and a Bandwidth of 1.5 nm. Fig 5.3 (a and b) displays photos of the fluorescence microscope and the fluorescence spectrometer.

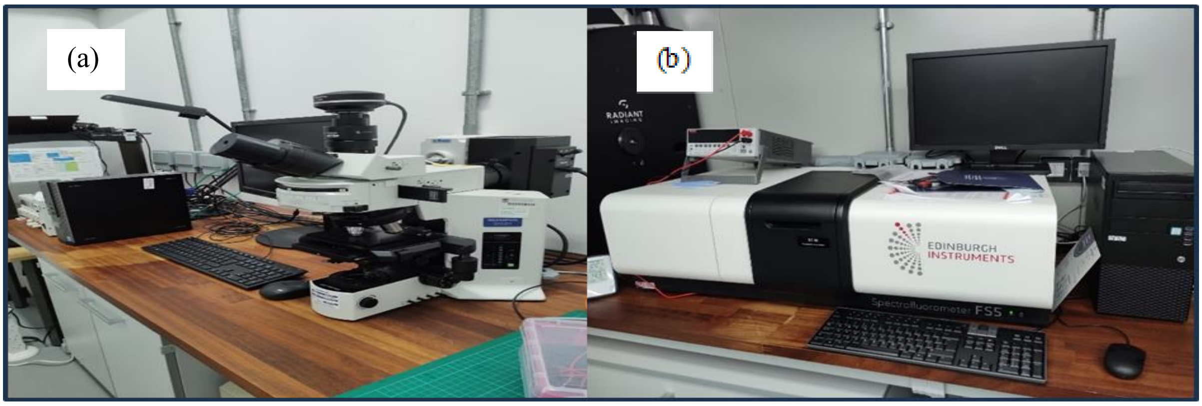

Figure 5.3: (a) Olympus BX51 Fluorescence Microscope. (b) FS5 Edinburgh Instruments Fluorescence Spectrometer.

5.4 – Background and theory of Raman spectroscopy

In 1962 as technology and instrumentation became more advanced, laser sources were developed for use with Raman spectroscopy.[176-178] Eventually, the Ar^+ (351.1-514.5 nm) and the Kr^+ (337.4-676.4 nm) lasers became available, and more recently the Nd-YAG laser (1.064 nm) has been used for Raman spectroscopy. Developments in Raman instrumentation brought commercial Raman instruments to the present state of the art for Raman measurements. Figure 5.4 represents the differences in Raman and IR with respect to mechanism.

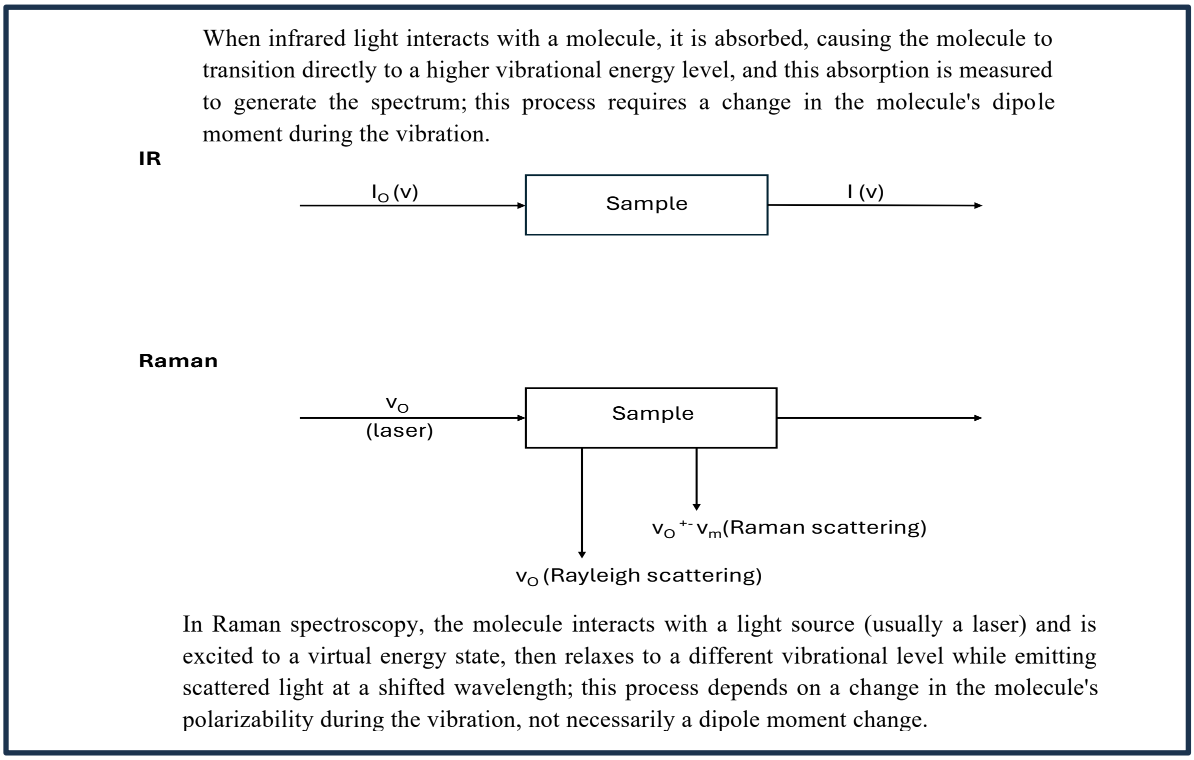
When infrared light interacts with a molecule, it is absorbed, causing the molecule to transition directly to a higher vibrational energy level, and this absorption is measured to generate the spectrum; this process requires a change in the molecule's dipole moment during the vibration.

In Raman spectroscopy, the molecule interacts with a light source (usually a laser) and is excited to a virtual energy state, then relaxes to a different vibrational level while emitting scattered light at a shifted wavelength; this process depends on a change in the molecule's polarizability during the vibration, not necessarily a dipole moment change.

Figure 5.4: Differences in mechanism of Raman vs IR.[177]

In Raman spectroscopy, we measure the vibrational frequency (v_m) as a shift from the incident beam frequency (v_o). In IR spectroscopy, we measure the absorption of infrared light by the sample as a function of frequency. The molecule absorbs $\Delta E = hv$ from the IR source at each vibrational transition. The intensity of IR absorption is governed by the Beer-Lambert law:

$$I = I_o e^{-\varepsilon cl} \tag{5.2}$$

Here, I_o and I denote the intensities of the incident and transmitted beams, respectively, ε is the molecular absorption coefficient, and c and l are the concentration of the sample and the cell length, respectively.[176] In contrast to IR spectra, Raman spectra are measured in the UV-visible region where the excitation as well as Raman lines appear. In terms of the light source, IR spectroscopy uses broad-band infrared radiation, while Raman spectroscopy uses a monochromatic laser light source. [179] IR spectroscopy only detects vibrations that cause a change in the molecule's dipole moment, whereas Raman can detect vibrations that change polarizability, even if there's no dipole moment change. This change in polarizability occurs because the electron cloud of the molecule is distorted by the electric field of the incident light.[177] In terms of anisotropic polarizability requirements, the polarization of the incident and scattered light can affect the intensity of Raman peaks, providing information about the crystal orientation and anisotropy of the material. For certain materials such as $ReSe_2$, the intensity of certain Raman modes is strongly influenced by the polarization angle of the laser beam.[180] The strength of a Raman transition is determined by a transition integral, which essentially calculates the overlap between the initial (ground state) and final (excited state) vibrational wavefunctions.[180] For a mode to be Raman active, this integral must be non-zero, meaning that the molecule can transition to a higher vibrational energy level.[180] Recent investigations using more advanced Raman techniques have pushed the studies of phonon modes in 2D layered materials to the atomically thin regime, down to monolayers.[177] Raman scattering is a process in which incident light is inelastically scattered by phonons,[177, 178] a sample undergoes a light-induced transition between vibrational states and the Raman scattering can be divided into Stokes and anti-Stokes scattering. [178] Stokes scattering occurs when the energy of the final vibrational state is higher than that of the initial state, implying that the scattered photons have lower energy than the incident photons. The energy difference between the incident and scattered photons is usually known as the Raman shift in the Raman spectroscopy literature and is reported in the units of cm^{-1}. Similarly, anti-Stokes scattering occurs when the scattered photons have higher energy than the incident photons, yielding a negative Raman shift.[177] Rayleigh scattering is the elastic scattering of light by a sample, where the scattered light has the same frequency and energy as the incident light. A Jablonski diagram highlighting these Raman transitions in an MoS_2 molecule is shown in Fig. 5.5.

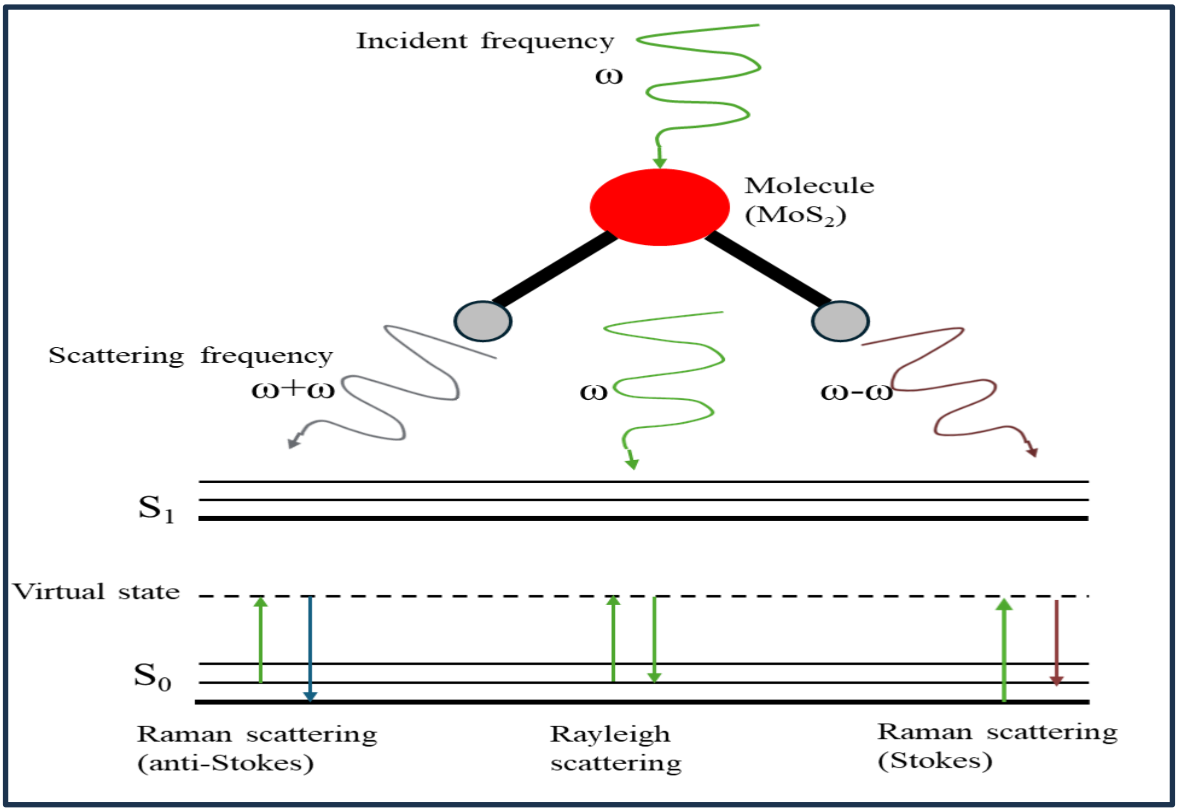

Figure 5.5: Scheme and Jablonski diagram illustrating the Raman transitions in an MoS_2 molecule.[182]

The study of Raman scattering in layered materials other than graphene has been occurring for more than a decade, and now that individual monolayers and multilayers are available in TMD compounds such as MoS_2, there is a resurgence of Raman studies on them. Thus far, MoS_2 is one of the most studied materials by Raman spectroscopy as a means of probing phonon and electron interactions in these 2D nanomaterials. Fig 5.6 represents the room-temperature Raman studies of bulk MoS_2 and exfoliated MoS_2 nanostructures.[116] Two prominent peaks are observed: The in-plane (E^1_{2g}) mode corresponds to the two S atoms vibrating in the same direction and Mo atoms in the opposite direction, whereas, in the out-of-plane (A^1_g) mode, the two S atoms vibrate in the opposite way out of the plane and Mo is stationary.[116]

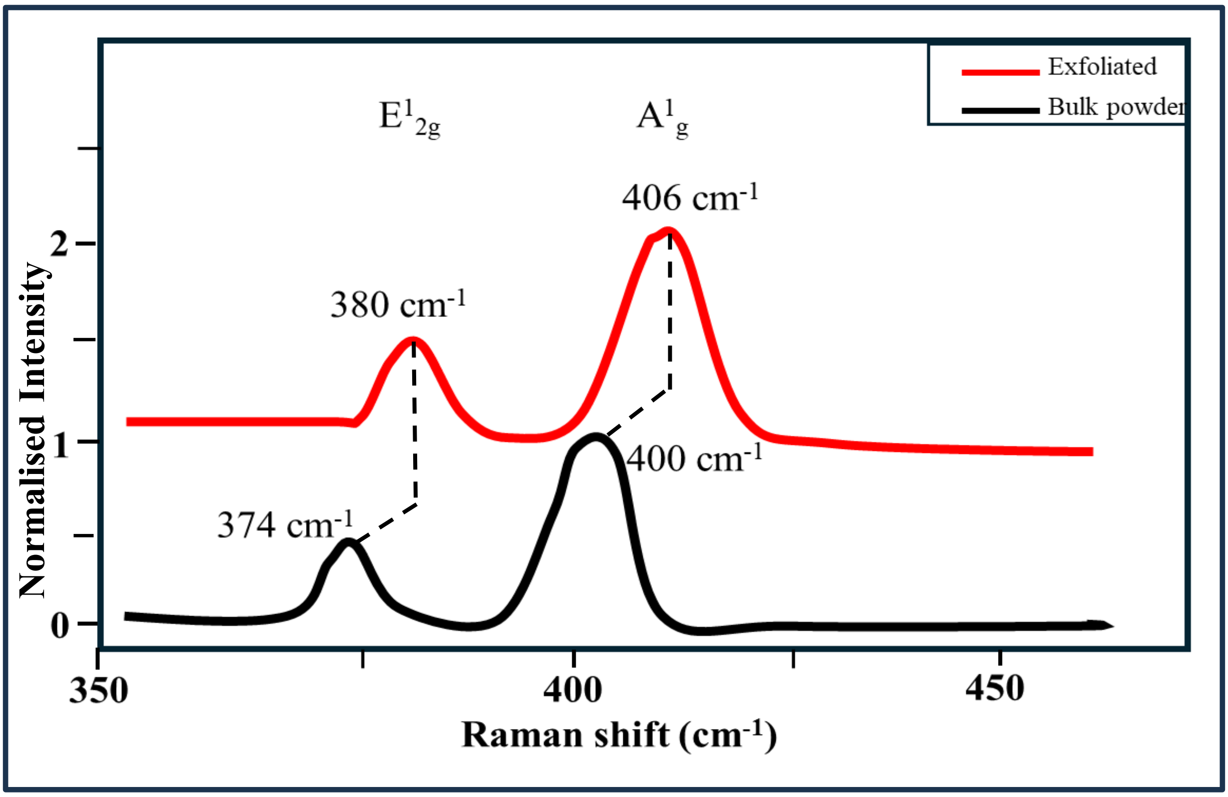

Figure 5.6: Normalised Raman spectra from bulk MoS_2 powder (black) and from exfoliated (red) MoS_2 taken with a laser excitation of 532nm.[116]

In the bulk powder sample, the prominent characteristic E^1_{2g} and A^1_g Raman bands appear at 374cm^{-1} and 400cm^{-1} respectively. Both of these two bands in the Raman spectrum correspond to the optical phonon modes. On the other hand, for the exfoliated sample, these characteristic peaks are blue shifted to 380cm^{-1} and 406cm^{-1} respectively. The Raman shift observed between bulk and exfoliated MoS_2 arises from changes in the material's structure and vibrational modes as the number of layers decreases. Specifically, the E^1_{2g} and A^1_g Raman modes, shift to different energies as the layer number changes. These shifts are due to changes in the strength of the interlayer van der Waals (vdW) interactions and the increased influence of intralayer interactions in ultrathin layers.[183] Bulk MoS_2 is a layered material held together by weak van der Waals forces between the layers, while exfoliated MoS_2, particularly at the monolayer level, is a two-dimensional material with a direct band gap. This difference in structure leads to a change in electronic properties, including a transition from an indirect band gap in bulk MoS_2 to a direct band gap in monolayer exfoliated MoS_2.[184] According to the symmetry considerations and a lattice-dynamical calculation, the strong 380cm^{-1} Raman peak indicates a crystalline 2H MoS_2.[116]

5.5 – Theory of Resonance Raman spectroscopy

Resonance Raman spectroscopy is a Raman spectroscopy technique, in which the incident photon energy is close in energy to an electronic transition of a compound.[185] With resonance Raman spectroscopy it is possible to study reactions that take place at the surface of electrodes, allowing the study of the electronic properties of the molecules and their relationships to their structure and the physical properties of their environment.[34] This technique can also be used to determine changes in the molecular conformation; and in resonance Raman the intensity of bands can be increased by several orders of magnitude.[35] This provides increased sensitivity to specific compounds that are present in low concentrations in complexes containing a mixture of compounds. Resonance enhancement of the Raman scattering requires the incident wavelength to be close to an electronic transition of the molecule.[37]

5.6 – Background and theory of Hyperspectral Imaging (HSI) methods

Hyperspectral imaging (HSI) techniques are used to measure PL to understand the electronic properties and band structure of 2D nanomaterials. This is a non-destructive technique used in many applications for medical science and in food quality control and biological sample analysis.[186,187] It has enormous potential and can be extended for use as a powerful tool in spectral imaging of 2D nanomaterials to monitor effects of PL on the surface of these kind of materials. The application of a hyperspectral camera, can provide quick and robust acquisition of hyperspectral data in the visible spectral range with high spectral resolution from PL imaging, this then provides us with information on the PL profile of the sample under investigation, indicating the regions where the PL intensity is enhanced due to the edges and kinks on the surface of the imaged needle or flake, however, if degradation is occurring there should be a decrease in intensity over time.[8] A complete spectrum is formed at any image point with a spectral resolution of up to 1 nm or single-pixel resolution, this essentially creates a "spectral cube" where each pixel contains its own unique spectrum.[186] The spectral resolution for the system used was 50 µm. This detailed spectral information for each pixel captured in an image, allows for more precise identification of materials and objects than traditional imaging methods. The quality of the acquired data for spectral resolution, is adequate for a reliable and highly differentiating analysis of the PL surface area whether in transmittance or reflected mode.[186] Analysis of PL intensity requires an appropriate excitation wavelength to achieve an emission spectrum, with the former having a shorter wavelength and substantially higher energy. Shorter wavelengths correspond to higher energy photons, thus giving a higher energy level. The energy can be calculated from the equation: $E = hc/\lambda$ where "E" is the energy, "h" is Planck's constant, "c" is the speed of light, and "λ" is the wavelength of your excitation light. The quality of the fluorescent image generally reflects a combination of contrast and brightness, and the contrast depends on the ratio of emission intensity to background light.[186] As a consequence, the use of filters to block the excitation wavelength and prevent it from overwhelming the field is critical for providing high contrast in the detection of PL.[186] Schultz et al. have developed a prototype hyperspectral imaging microscope capable of collecting the complete emission spectrum from a microscope slide,[188] and this is the expected outcome of this study on 2D nanomaterials. The hyperspectral imaging microscopy system used for this study is based on Fourier-transform imaging. In this case, a continuum of spectra is taken, and deconvolution is based on two steps: collection of light passed by a filter with a Michelson interferometer followed by an inverse Fourier transform with the relevant software to acquire the spectra from the collected data. The interferometer consists of a moving mirror, a fixed mirror, and a beam splitter. To ensure high stability and precision, piezoelectric ceramic actuators are used to drive the moving mirror. As the voltage increases, the mirror moves at a nanometre scale, with movements expected to be consistent. This could be checked by making measurements of the voltage signal at many discrete positions of the moving mirror and observing a linear response.[8] The system used in this research consisted of a Gemini interferometer supplied by Nireos Inc. This makes use of a coherent light source that is split into two arms using a beam splitter, the light beams are reflected back toward the beam splitter which then combines their amplitudes using the superposition principle. The resulting interference pattern that is not directed back toward the source is typically directed to the camera. Analysing the variations in the interference pattern created when light from a laser source is split and recombined within the interferometer are the key means of gaining spectral and spatial information. A Fourier transform is applied to the measured interference pattern, which allows for the separation of the spatial and spectral components. In conclusion, HSI is an emerging technology that offers huge potential and the possibility of extracting both spectral and spatial information about each pixel from a PL image.[188]

5.6.1 – HSI experimental setup for MoS_2 measurements

An Olympus Microscope setup fitted with Gemini interferometer and white light control using an LED source with a range of wavelengths, is attached to a Hamamatsu camera (ORCA-Fusion Digital CMOS camera C14440-20UP) for imaging purposes and is used for focusing the sample for the measurements. A 100x 1.35 NA oil immersion objective lens is used for focusing the electro-exfoliated MoS_2 samples in wide-field imaging mode to capture more than one flake at a time. HSImage software is used to capture the images. The Labview software is used to setup the various parameters such as frame count, wavelength range and sample exposure time. MATLAB software is used to collect, process and extract the data. A schematic of the setup is shown in Fig. 5.7. The electrochemical cell setup is shown in Fig. 5.8.

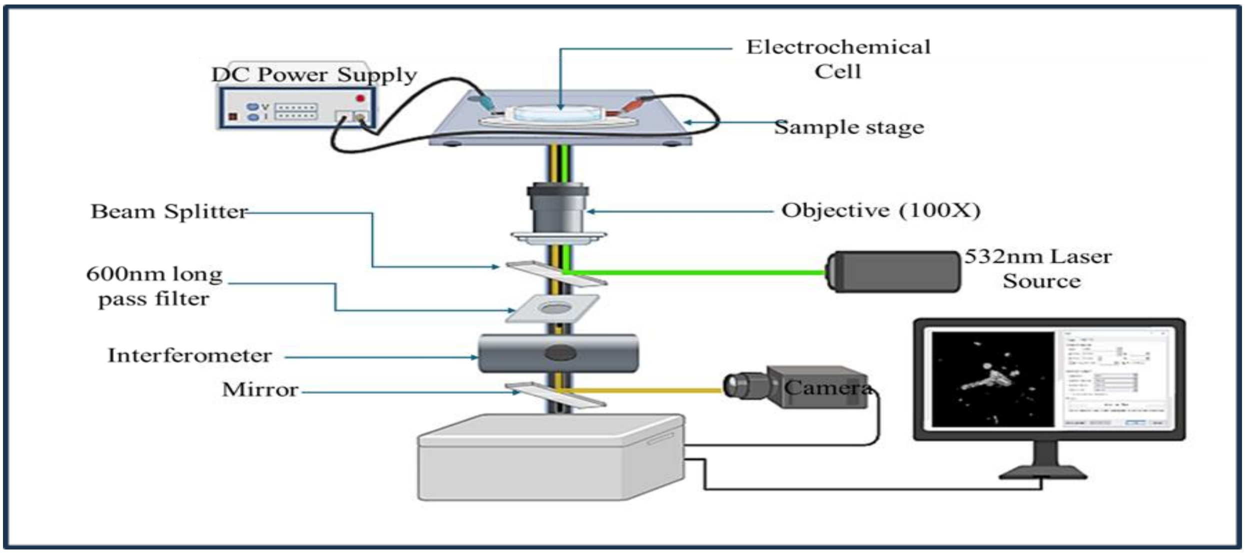

Figure 5.7: Schematic of the optical set up for hyperspectral imaging on MoS_2 using tungsten filament as the light source with 450 nm bandpass filter and 600 nm long pass filter. Hyperspectral images were obtained using an interferometric method followed by Fourier transformation using a Gemini 2D interferometer supplied by Nireos.

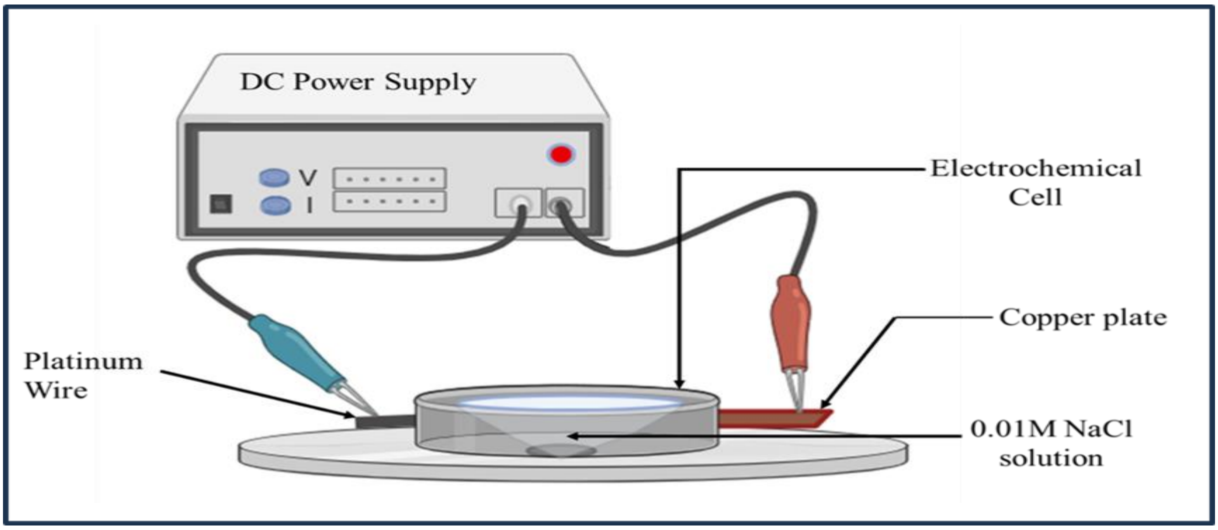

Figure 5.8: Schematic of the two-electrode electrochemical cell setup.

5.6.2 – HSI Experimental setup for perovskite measurements

The experimental setup consisted of an Olympus fluorescence microscope with a 2-dimension Fourier-transform interferometer attached to the Hamamatsu camera for image acquisition using HSImaging software. LabView software is used to setup the frame number for images collected depending on the area being measured, and PL spectra are then collected over the range of 400 to 700 nm using MatLab software. An LED 470 nm excitation source is used to generate the PL and a 100x 1.5 NA oil immersion objective lens is used to focus the light on the sample. A band pass filter of 450 nm is used to filter off the excitation source and enable the emission source to pass through to the CCD detector. A schematic of the optical setup used for time lapse and HSI imaging is shown in Figure 5.9.

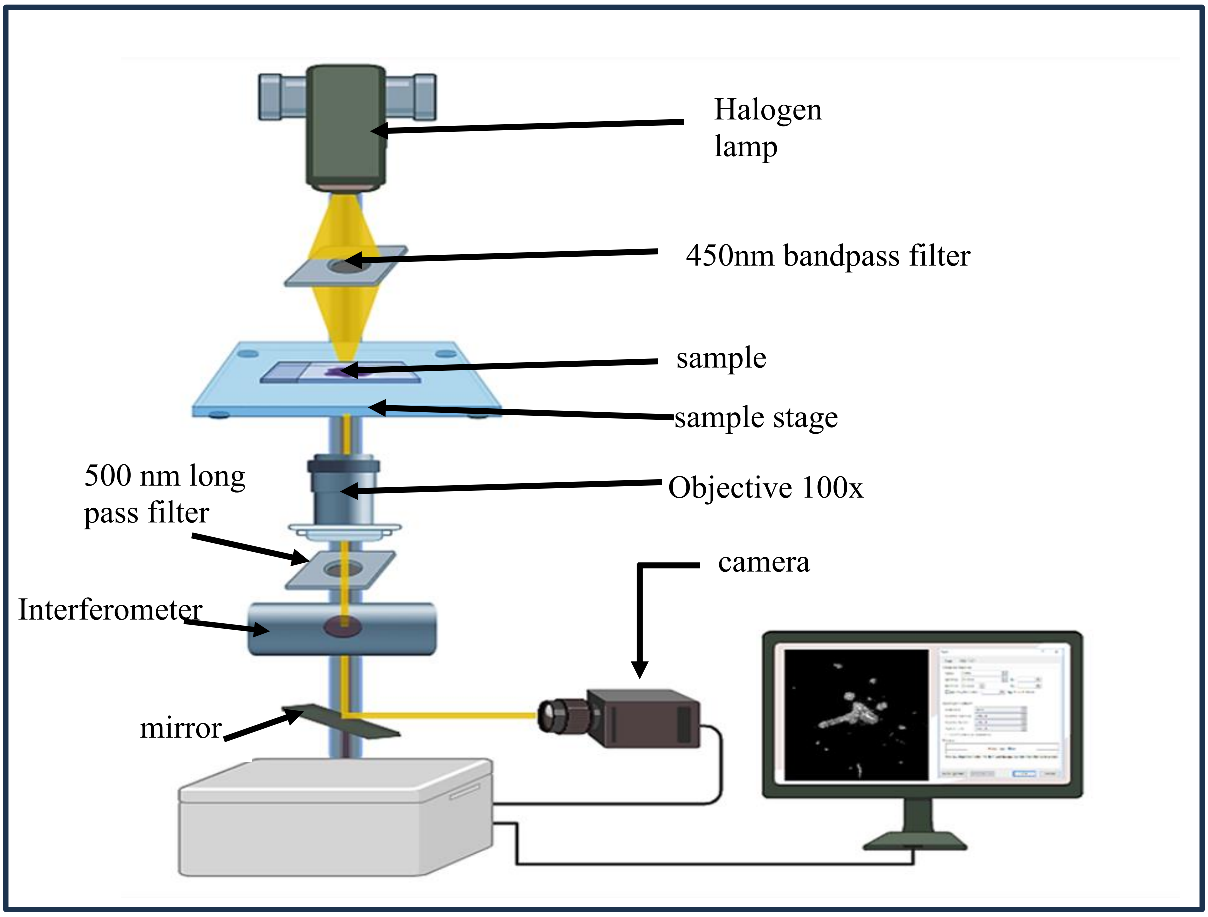

Figure 5.9: Schematic of the optical set up for hyperspectral imaging on $MAPbBr_3$ perovskite using tungsten filament as the light source with 450 nm bandpass filter and 500 nm long pass filter. Hyperspectral images were obtained using interferometric method followed by Fourier transformation using a 2D interferometer supplied by Nireos.

5.7 – Background and theory of Cyclic Voltammetry

Cyclic voltammetry (CV) is a powerful tool to probe reactions involving electron transfers; and is one of the most versatile electroanalytical techniques for studying electroactive species. A standard CV experiment employs a cell fitted with three electrodes: reference electrode, working electrode, and counter electrode, in what is commonly referred to as a three-electrode setup. Most modern equipment uses a three-electrode cell in which a counter or auxiliary electrode provides the current that is needed at the working electrode. Therefore, virtually no current flows through the reference electrode and its potential remains constant.[189] The electrochemistry relates the flow of electrons to chemical changes that take place in the molecule of interest. Diffusion is the principal means of moving the reactant to the surface of the electrode.[190] It is a simple and direct method for measuring the formal potential of a half reaction under certain solution conditions when both the oxidized and reduced forms are stable during the time required to obtain a voltammogram. The formal potential is the non-standard electrode potential when the ratio of analytical concentrations of reactants and products of a half reaction are exactly 1.00 and the molar concentrations of any other solutes are specified.[191] A cyclic voltammogram is obtained by measuring the current at the working electrode which is immersed in an unstirred solution during the potential scan; and the current is considered to be the response signal to the potential excitation signal. The voltammogram is a display of current (vertical axis) versus potential (horizontal axis).[190] In cyclic voltammetry, the use of an external power source such as a potentiostat, where voltage can be applied to the electrode to modulate the energy of the electrons in, and this energy can be increased until electron transfer becomes favourable.[191] The potential of a working electrode that is stationary is changed linearly with time, beginning with a starting potential where no electrode reaction takes place, or the zero point and then applying incremental potentials to where reduction or oxidation of the solute occurs.[190] The potential of this stationary working electrode is measured against a reference electrode such as silver/silver chloride. This type of electrode is most commonly used in electrochemistry applications as it provides a consistent reference potential, crucial for accurate potential measurements; and has low electrical resistance, allowing for accurate measurements with minimal interference. Additionally, it is easy to fabricate, is non-toxic and has wide applicability to various aqueous electrolytes and non-aqueous solvent environments.[192] When the set potential is reached for the measurement run by the Autolab potentiostat system, the initial positive potential value is +1.5V, this value is set for the forward sweep, and the working electrode's potential is ramped to go in the opposite direction for the reverse sweep until it reaches the negative set potential of -2V and then returns to zero to complete the scan. These cycles can be repeated any number of times as needed with each repetition improving upon the initial scan.[190] This potential range is chosen for the chapter 6 experiments as it is known from experiment (Chapter 6, Section 6.61) that the Ru complex displays redox peaks around -1.3 V and 0.4 V which are within this potential window to be scanned. This window can be used to control the reactivity and biological activity, particularly in applications like cancer treatment. By tuning the redox potential, researchers can target specific cellular environments and mechanisms, ensuring the complex is activated or deactivated under desired conditions.[193] Other parameters such as the solvent, electrolyte, and material composition of the working electrode will further determine the potential range that can be accessed during the experiment.[190]

Cyclic voltammetry satisfies the conditions of Eq. (5.3), i.e. linear dependence of potential on time. The relationship between the current, I and potential, E, is called the polarisation curve (5.4).[194]

$$E(t) = E(0) \pm vt \tag{5.3}$$

$$I = f(E) \tag{5.4}$$

Where E(t) is the potential at time t, E (0) is the potential at time t = 0 and v is the scan rate for eq. (5.3). I is the current, f is the frequency and (E) is the potential for eq. (5.4).[194]

The cyclic voltammogram shows the representation of the polarisation curve from eq. (5.4). Fig. 5.10 shows an example of a cyclic voltammogram obtained from a solution phase redox couple in a three-electrode setup consisting of working, counter and reference electrodes.

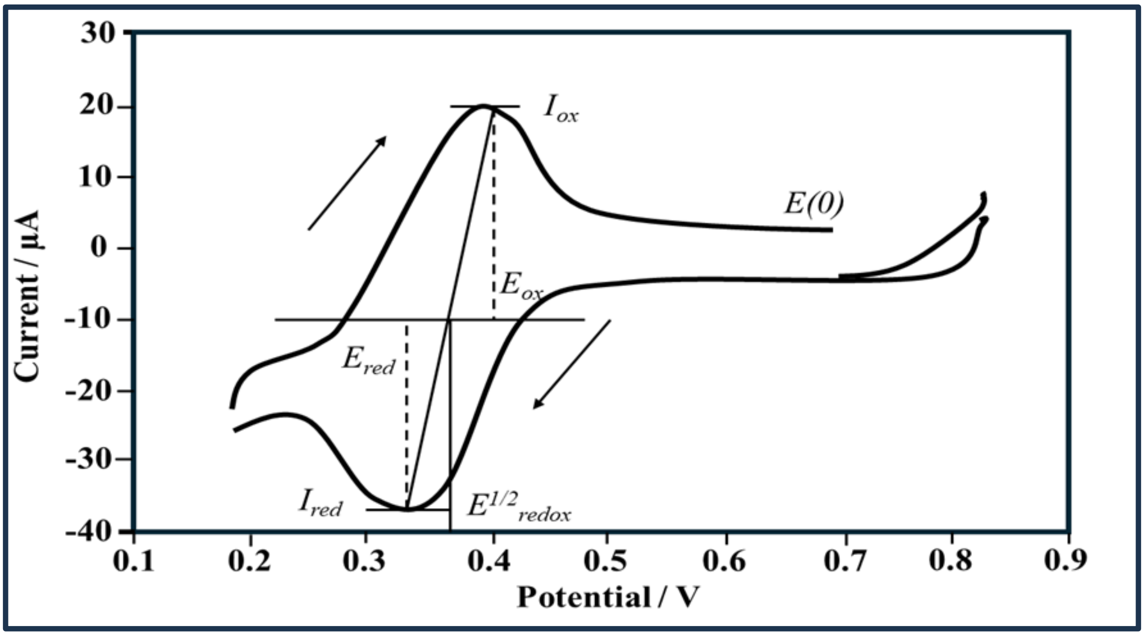

Figure 5.10: Schematic of a cyclic voltammogram in a redox couple system.[194]

Fig. 5.10 shows the two characteristic peaks which correspond to the diffusion of the reduced and oxidised forms of a redox couple. The half – wave potential $E^{1/2}$ redox (which is an average of the oxidation and reduction peak potentials, E_{ox} and E_{red}) is specific to the redox species and the oxidation of the sample that is studied. Depending on the potential applied to the working electrode, the sample undergoes a series of redox reactions that take place at the metal centre, where essentially electrons are gained or lost at the electrode surface. This causes a measurable current to flow between the working electrode and counter electrode as the potential is swept through a range and then reversed back to the starting potential from the reference electrode.[195] The peak currents I_{ox} and I_{red} provide information about the quantity of the analyte, as in the CV scan, they are directly proportional to analyte concentration.[194]

5.8 – Theory of Staircase Voltammetry (SCV)

Staircase voltammetry is a potentiostatic method that is a derivative of linear sweep voltammetry, where the potential sweep, is a series of stair steps.[194] It involves sweeping the potential linearly with time at rates faster than cyclic voltammetry, the difference being that the size and duration of each potential step can be selected according to the experimental setup. Staircase voltammetry is capable of much higher sweep rates compared to basic cyclic voltammetry, and unlike cyclic voltammetry, it is determined by the ratio of step amplitude and period as:

$$\frac{dE}{dT} = \frac{EA1SCV}{TP1SCV} = \upsilon = \frac{\Delta \mathrm{E}}{\mathrm{T}} \tag{5.5}$$

Where dE – is the change in the potential, dT – is the change in period, $EA1$ – is the first potential amplitude step when running a scan and $TP1$ – is the first period on the staircase voltammogram. This in turn is equal to the sweep rate υ, which is equal to the change in potential ΔE divided by the period T. In the staircase voltammetry setup, the step height and duration can be controlled, allowing for larger sweep rates if required.[194]

5.8.1 – Cyclic voltammetry setup for Ru complex measurements

Cyclic voltammetry measurements are performed using the quartz Spectro electrochemical thin layer cell setup shown in Fig. 5.11.

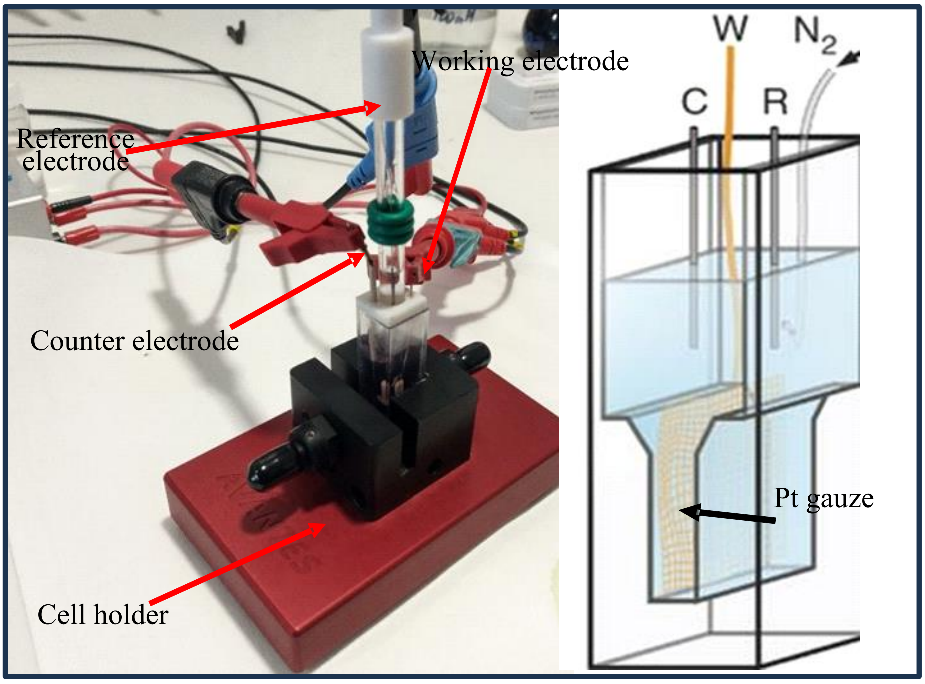

Figure 5.11: Experimental setup used for Cyclic voltammetry measurements on the Ruthenium complex $[Ru(bpy)^2dppz]^{2+}Cl_2$. With C – counter electrode, W – working electrode, R – reference electrode.

The electrochemical workstation Autolab PGstat10 potentiostat is used and controlled by the Nova software to produce the CV curves. The measurements are carried out in a three – electrode cell set up, platinum gauze is used as the working electrode, Ag/AgCl is used as the reference electrode and a Platinum counter electrode completing the setup for electrochemical activity. Upon validation of this setup for the Ru complex measurements, a similar electrode configuration can be applied to the final version of electrochemical Raman cell used in the exfoliation stage to study MoS_2 material in Chapter 6.

5.8.2–Aqueous and Non-aqueous electrolytes used in Ru CV measurements setup

Different aqueous electrolytes such as: KOH (potassium hydroxide), PBS (phosphate buffer solution) and a non–aqueous electrolyte such as $TBAPF_6$ (Tetra-butyl ammonium hexafluorophosphate), each having a concentration of 0.1M can be used for Ru CV scans. A literature comparison was made between the aqueous (0.1M PBS and 0.1M KOH, 1mM Ru in ACN) and non-aqueous electrolytes (0.1M $TBAPF_6$, 4 mM Ru in Ethanol) in terms of the Ru complex CV scans produced.

The electrolytes are added to ensure conductivity between the unstirred solution and the electrodes during the measurements. The unstirred solution allows for diffusion–controlled peaks, as then only parts of the analyte will remain after the oxidation or reduction in order to display further redox activity. The 0.1 M non–aqueous electrolyte $TBAPF_6$ is chosen for cyclic voltametric measurements made on Ru complex in Chapter 6, section 6.6.1, as from literature it has shown an electrochemical stability that can exceed 4V and has a high operating potential of 2.5V.[195] The non-aqueous electrolyte displays redox peaks as shown in Chapter 6 (Fig. 6.11, p. 70) whereas the aqueous electrolytes KOH and PBS are observed to display no redox peaks at all with an ohmic curve response observed. This can be explained by a kinetic improvement due to enhanced surface diffusion and transport of ions for the Ru^{2+} to Ru^{3+} electron transfer, that enables the redox reactions to take place. [195] The redox chemistry being probed in ruthenium complexes focuses on understanding how the metal centre's oxidation state changes upon electron transfer and how these changes affect the complex's properties and reactivity.[195] A higher concentration 4 mM of non-aqueous compared to 1 mM aqueous electrolyte increases the ion concentration and therefore the ionic transport between the electrodes. Concentrated saline solutions such as 0.1M PBS and 0.1M KOH electrolytes do not facilitate the transfer of ruthenium ions between electrodes that enable the electron transfer and redox reactions to take place.

Non-aqueous electrolyte solutions such as $TBAPF_6$ contain more ion conductors compared to the aqueous versions and so this improves the kinetic transport of ions for electron transfer and redox reactions; in addition, the extent of ion-ion and ion-solvent interactions can affect mobilities as ACN and ethanol are different solvents compared to water.[191]

Non-aqueous electrolytes are also more stable, possess greater solubility than aqueous solutions and offer wider liquid temperature ranges (down to −150 °C and up to about 300 °C) and an appreciably larger voltage window, also called electro-inactivity range (up to about >4 V vs. about 1.2 V for aqueous systems).[191] Both the large liquid temperature range and the large voltage window not only extend the range of accessible investigations of dissolved materials in fundamental research but also offer applications for processes and devices that would not be possible with aqueous electrolyte solutions.[9] For the addition of ruthenium ions, the electrochemical reaction kinetics of the active redox couple is enhanced as the diffusion coefficient of active ions increases,.and the charge transfer resistance decreases. This allows for minimal solution resistance, and it is considered to be resistant to reduction itself.[191] The ions present in the electrolyte increase the rate of reaction as the carbon chain length in the electrolyte is increased from the methyl to the butyl moiety and thus the electrochemical stability increases, this then allows for conductivity increase. The electron transfer then occurs at the electrodes, and the supporting electrolyte then migrates to balance the charge and complete the electrical circuit, this is more probable to occur with a higher concentration of electrolyte compared to concentration of the analyte used. Large supporting electrolyte concentrations are also necessary to limit analyte migration.[191]

The working electrode used is the platinum gauze and is where the electrochemical reaction takes place, the surface of the gauze is cleaned after each use and the surface area is kept well defined using polishing methods. The cleaning is done using a mixture of nitric acid and deionised water, with the gauze being placed inside this mixture for 10 minutes, the gauze electrode is then sonicated in ultrapure water. The final cleaning step involves a large potential range scan being performed multiple times to remove any adsorbed species left over from the polishing process, as the working electrode is very sensitive and can produce inaccurate data if effective cleaning is not carried out.[191]

Electrolyte compositions:

The 0.1M aqueous electrolyte phosphate buffer solution (PBS) consisted of 1.461 g of NaCl, 1.852 g of KCl, 3.5496 g of Na_2HPO_4 and 3.340 g of KH_3PO_4 dissolved in 250 mL DI water and stored at 40 ̊C for 24 hours before use.

The 0.1M non–aqueous electrolyte consisted of 2.579g Tetra-butyl ammonium hexafluorophosphate salt (Nbu_4PF_6) $TBAPF_6$, made up of a white powder dissolved in 50 mL of acetonitrile solvent and stored at 40 ̊C for 24 hours before use.

5.8.3 – Cyclic Voltammetry setup for exfoliated MoS_2

5.8.3.1 – Autolab Potentiostat

An Autolab potentiostat PGSTAT204 (Metrohm plc.) is used to plot CV scans over a range of potentials, and scan rates. Nova software is used to design a procedure to record signals and measurements from the three-electrode cell arrangement. A TTL trigger is used to send a pulse to the camera, which then takes an image of the sample flakes for each potential applied for PL measurements. A plot of PL intensity is made using Labview software.

The Autolab instrument includes a base potentiostat/galvanostat with a compliance voltage of 20 V and a maximum current of 400 mA or 10 A. The cables and wires are connected to leads to which these are attached to crocodile clips. The clips are then used to connect up the reference, counter and working electrodes in the electrochemical cell.

5.9 –Raman Spectroscopic –Microscopic in-situ methods

5.9.1 – Raman spectrometer setup

A Raman spectrometer (Renishaw plc) with double beam Class 3B laser, 488 nm and 532 nm is used to produce spectra of the MoS_2 samples using an Olympus 40 x 0.5NA objective lens and Wire version 5.1 software. The Leica microscope is inverted and can only be used in transmission mode with ITO (Indium Tin Oxide) coated glass as the substrate. This system was used to measure the Raman and PL signals from the liquid phase and microwave preparations. The 532 nm laser is used for excitation of the MoS_2 samples as it falls near the absorption edge, giving a strong resonance Raman effect that enhances the signal and allows for detailed analysis of the vibrational modes. Figure 5.12 shows a schematic of the working components inside the Raman spectrometer.

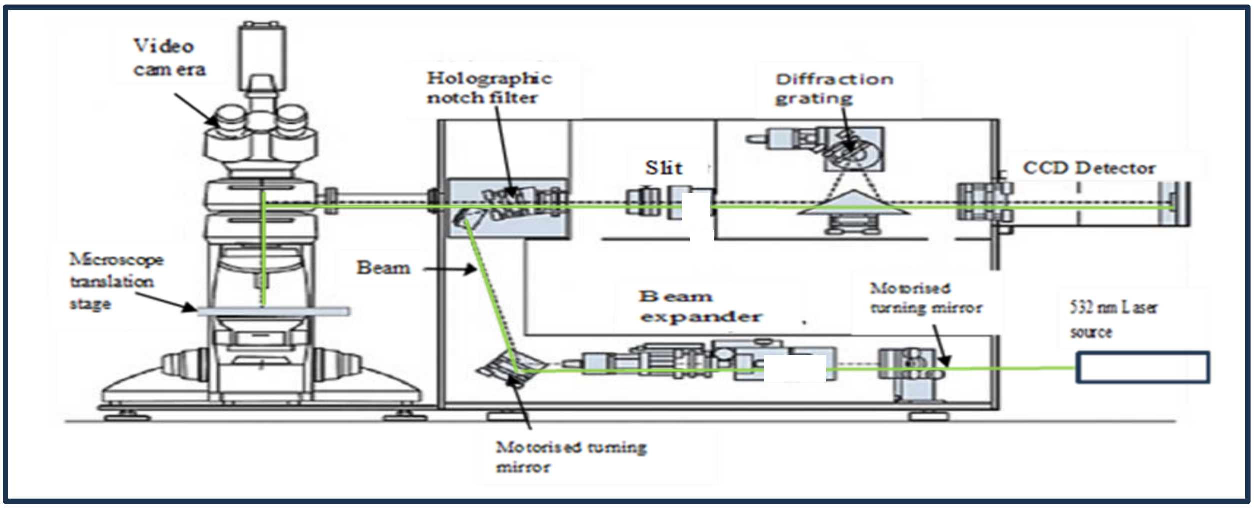

Figure 5.12: Schematic diagram of a Renishaw Raman microscope.[196]

The laser source is needed to excite the target species. The filter collects the Raman scattered light (Stokes) and filters out the Rayleigh and Anti Stokes light. A diffraction grating bends the Raman shifted light according to wavelength, and gratings range from 1200-lines mm^{-1} (medium resolution) to 2400-lines mm^{-1} (high resolution) for spectral resolution purposes. The CCD (Charge Coupled Detector) records the signal and passes the signal to a computer for decoding. The addition of an iHR320 Horiba spectrometer with class 3B laser, 532 nm excitation wavelength, 450 nm cut-off or bandpass filter, a 540 nm long pass filter to remove Rayleigh scattering and equipped with a Synapse CCD was used to produce the Raman and PL spectra for the electrochemical-exfoliated MoS_2 samples. This is shown in Figure 5.13.

Figure 5.13: Photo of Horiba iHR320 Raman spectrometer.

5.10 – In-situ Electrochemical-Raman setup

In-situ electrochemical-Raman measurements are made using the Raman class 3B laser system interfaced with the Autolab potentiostat PGSTAT204 using .NET functionality Master-Slave triggering between the Wire and Nova software. The Nova software acts as the Master in sending a prompt to the Wire software that is the slave in the relationship, the Wire software then produces a spectrum for each potential. The in-house built PEEK electrochemical cell is placed on the microscope stage in transmission mode with the laser beam being focused up through the transparent substrate and sample surface. An image of the electrochemical cell is shown in Fig. 5.14.

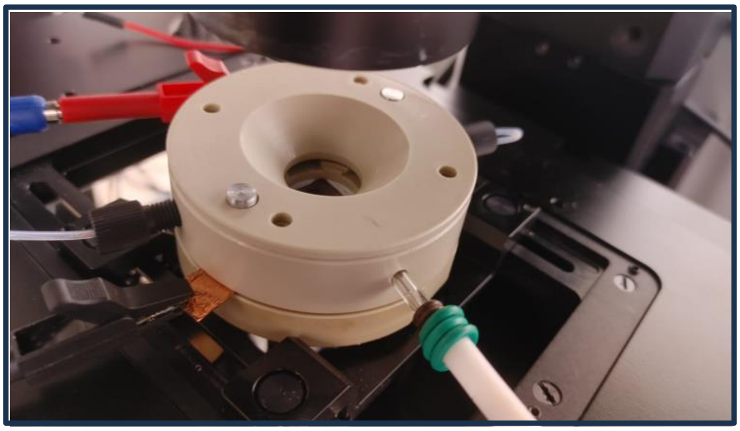

Figure 5.14: Photo of in-house designed electrochemical cell positioned on microscope stage.

5.11 – Resonance Raman and Electrochemical-Raman setup for Ru complex measurements

Resonance Raman measurements are carried out on the ruthenium complex using a 457 nm laser excitation wavelength Raman spectrometer based in ESRI laboratory at Bay Campus in Swansea University. The reason for using a lower wavelength excitation of 457 nm, is the ligand peaks do not appear using a higher excitation wavelength due to the metal to ligand charge transfer (MLCT) not fully taking place. Extended scans are produced after focusing the beam on the Ru sample using a 40x/0.75 D P/N Olympus objective lens and a 30 s exposure time is used for each scan. The laser power is kept low (~5 mW) to avoid damaging or burning the sample. The sample is prepared by drop-casting 50 microlitres of the homogeneous sample solution of uniform concentration (4 mM) onto a glass coverslip and leaving to dry in air. Electrochemical-Raman single-point measurements are performed with the InVia Renishaw instrument using a 40x/0.75 D P/N Olympus objective lens. An argon – ion laser is used consisting of excitation wavelengths of 488 nm and 532 nm. A silicon standard (520.5 cm^{-1}) is used as a reference to calibrate the wavenumber and laser intensity of all Raman instruments before measurements. The Si peak produced ensures the accuracy of the wavenumber (x-axis) that is more critical for comparison than the intensity (y-axis) of the instruments. The same Raman system was used throughout for the Ru measurements. The software used to obtain the Raman spectra is Wire 5.1, and the potential bias is supplied using the AutoLab potentiostat PGSTAT204; and a TTL (Time -to-live) trigger is sent from Nova to Wire software to produce the relevant spectra at each potential. The experiment is carried out at room temperature (300 K) with a 25 s exposure time for each spectra. The in-situ measurements are made by focusing the 40x objective lens onto the Pt gauze using an extension adapter as shown in Figure 5.15. The 488 nm laser is used to make the measurements in this case to capture Ru complex peak maxima, as the 532 nm excitation laser has lower energy and is unable to excite the higher energy electronic transitions within the Ru complex molecule. This results in any additional peaks in the emission spectrum not being visible at the higher 532 nm wavelength excitation.

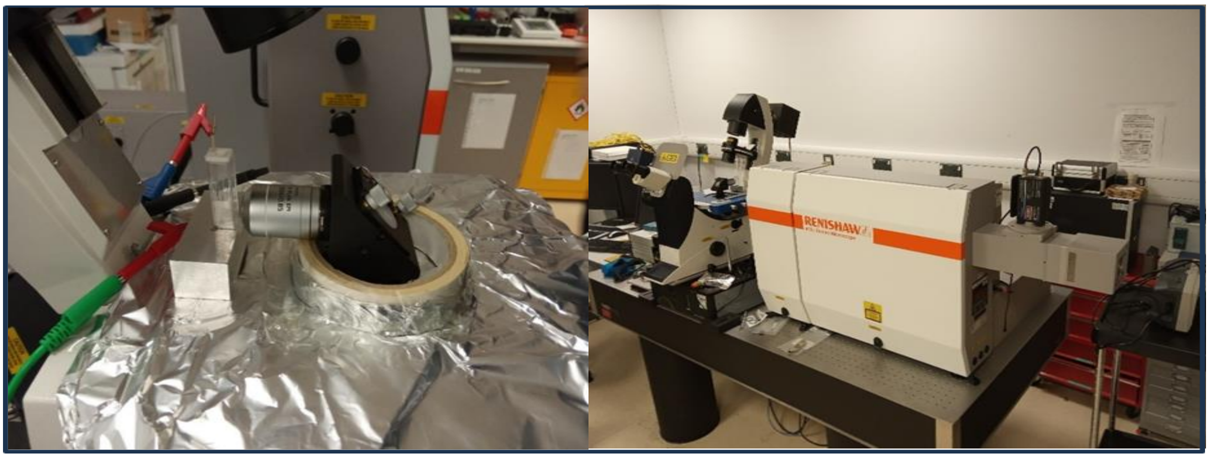

Figure 5.15: Experimental setup used for electrochemical-Raman measurements on the ruthenium complex $[Ru(bpy)^2dppz]^{2+}Cl_2$ using extension adaptor for Olympus 40x objective lens to focus on Pt gauze inside the quartz Spectro-electrochemical cell.

5.12 – Sonication setups

The sonication methods used for the LPE methods involved Pulse-Tip (PT) sonication and bath sonication techniques. The setup for PT sonication was a Q500 model sonicator (QSonica plc) shown as a photo in Fig. 5.16

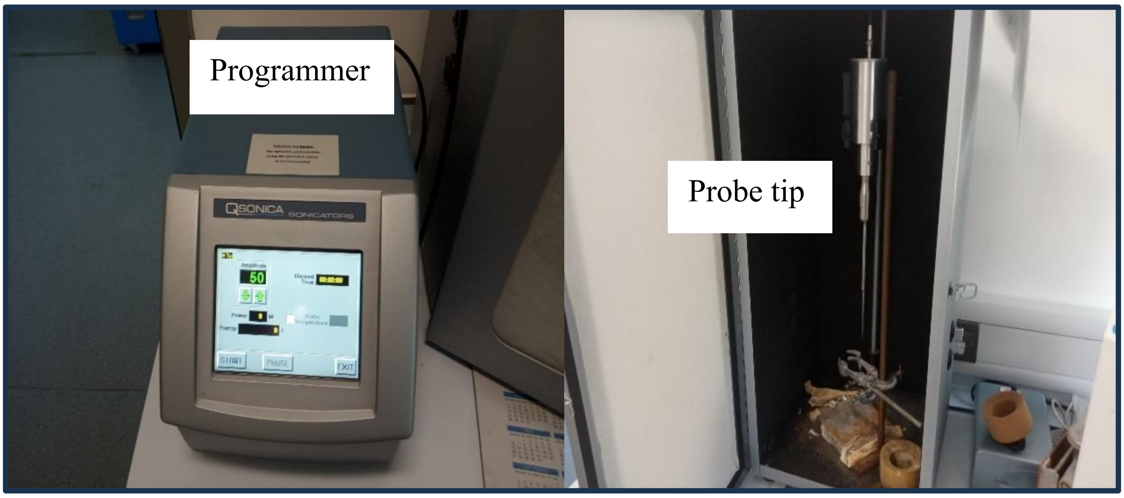

Figure 5.16: Photo of a PT Q500 sonicator with sound enclosure. (QSonica plc).

The PT sonicator was used inside a sound enclosure as pulsing can create excessive noise that can potentially cause loss of hearing. Its main uses are in nanoparticle dispersion, emulsification and particle size reduction. It features 500 watts of power, 20 kHz frequency and a programmer that sets adjustable pulse on and off times, amplitude and run times depending on the experiment you are running and sample preparation. It comes with various probe tips and for experimental purposes a ½” diameter pointed tip was used and immersed in the liquid samples.

Bath sonication was carried out using an RS Pro model sonicator. This is a more basic less powerful version of sonicator and much simpler to use. Samples are simply placed in the basket and placed in the bath filled with DI water, the bath was then set to run on full power for as long as the sample preparation required. If the run time was longer than 20 mins, ice is added to the bath to prevent overheating and to maintain room temperature conditions.

5.13 – Microwave Synthesizer Setup

The microwave synthesis setup for MALPE methods consisted of a CEM-Discover 2.0 model instrument. A photo and schematic of the instrument is shown in Fig. 5.17.

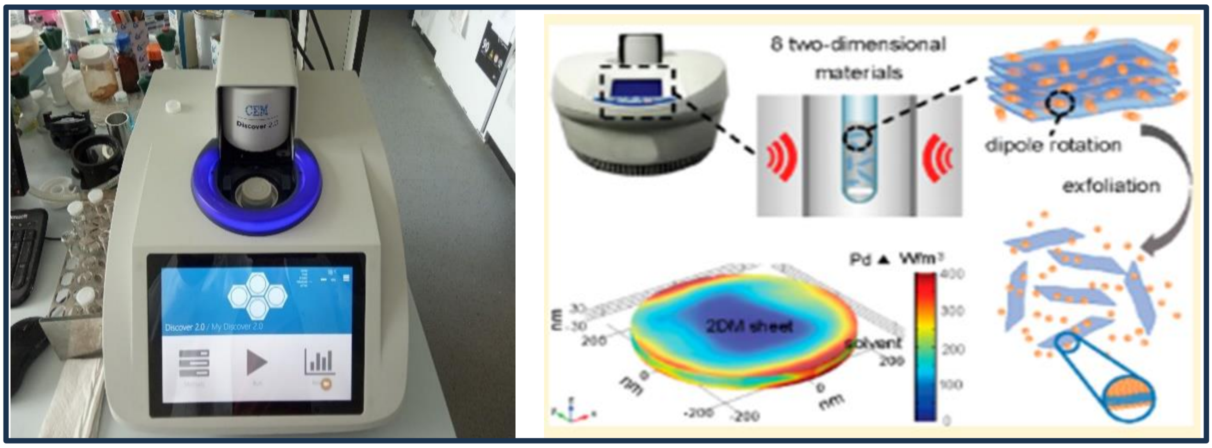

Figure 5.17: Photo and Schematic of a microwave synthesizer (Discover 2.0 – CEM Inc.)[112]

The Microwave synthesizer provides unique benefits for synthetic chemistry and MALPE methods in terms of speed, reaction efficiency, and promotion of green chemistry principles. This faster, greener, and more efficient technology has enabled shorter reaction times and improved yields. These benefits arise from the unique ability of microwaves to directly heat polar/ionic species in a reaction. It was proposed that the selective heating capability of microwave irradiation could further enhance the LPE process in terms of producing a higher yield of monolayer MoS_2 material from surfactant and solvent based preparations, as it is designed for use in nanotechnology and materials science applications.

5.14 – DFT Computational details

This was carried out by a team from the department of Chemistry from Cardiff University. Gaussian 09, Revision D.01,[197] was employed to optimize the structures discussed in chapter 8 of this thesis using the B3LYP-D3 level[198-203] of density functional theory (DFT) in combination with the SMD[204] solvation model in acetonitrile. A 6-31G(d) basis set[205] was utilized for all atoms during this process. Frequency calculations were conducted at the same theoretical level as the optimizations. Transition states were identified using the Berny algorithm. To refine the energy calculations further, single-point energy calculations were performed with the ωB97X-D[206] functional and a larger def2-tzvp basis set[207] in the SMD solvation model. All thermodynamic properties were determined at standard conditions (298.15 K and 1 atm). The free energy of each species was calculated using the formula:

$$G = E_{(SMD/\omega B97X\text{-}D/def2\text{-}tzvp)} + G_{(SMD/B3LYP\text{-}D3/6\text{-}31G(d))} - E_{(SMD/B3LYP\text{-}D3/6\text{-}31G(d))} + \Delta G^{1atm\rightarrow 1M} \quad (5.6)$$

where $\Delta G^{1atm\rightarrow 1M}$ = 1.89 kcal/mol is the free energy change for compression of 1 mol of an ideal gas from 1 atm to 1 M solution phase standard state.[208] In a simple word, a correction of -1.89 (or 1.89) kcal/mol is employed to estimate relative free energies for a 2-to-1 (or a 1-to-2) transformation. The 3D molecular structure $\mathbf{TS_{nitrosation}}$ was visualized using CYLview.[209]

CHAPTER–6

Electro-Spectrochemical Study on Exfoliated MoS_2

6.1 –Introduction

The primary objectives of the electro-spectrochemical study are to investigate and evaluate various exfoliation methods used in the preparation of monolayer MoS_2. If sufficient monolayer/few- layer yield is produced with a large enough flake size, then electrochemical-Raman and PL measurements using *in-situ* Hyperspectral Imaging (HSI) techniques will then be performed on the relevant flakes. This technique can be used to simultaneously image exciton and trion dynamics with applied potential as a practical descriptor of catalytic activity in HER. The methods of preparation investigated are Liquid Phase Exfoliation (LPE) in different solvent mediums, Microwave-assisted Liquid Phase Exfoliation (MALPE) and electrochemical exfoliation.

A preliminary study was made on $[Ru(bpy)^2dppz]^{2+}Cl_2$ as the leading well established ruthenium complex for anticancer treatment.[210] The Ru complex was used to validate the setup of Raman spectroscopy and cyclic voltammetry methods, and to determine if it is possible to apply these techniques as a combination to learn more about the ruthenium structural changes when different voltage potentials are applied. Both systems have their own disadvantages, as Raman spectroscopy is not able to supply the voltage potential increments to the ruthenium complexes for measurements and cyclic voltammetry is not able to show structural changes but only the oxidation and reduction potentials from the CV scans that are produced. The literature gives varied results with regard to Ru oxidation and reduction potentials, peak potentials ranging from -1.5V to – 1.8V have been reported but, reduction peaks as high as -0.5V have also been reported and proving which result is more probable will form part of this study.[211-213]

The preliminary measurements are made on the ruthenium complex using a three – electrode Spectro-electrochemical cell set up shown in Chapter 5, Fig, 5.11 to determine the range in which the reduction peaks occur. It is hoped this study will lead the way in determining other compounds that could be studied using the combination of both Cyclic Voltammetry and

Raman spectroscopy. To test and show the validity for electrochemical-Raman measurements, the quartz Spectro-electrochemical cell is tested for electrochemical activity with a three-electrode setup consisting of platinum gauze as Working electrode, Pt wire as Counter electrode and Ag/AgCl as Reference electrode. A 5mM ferrocene solution is used as a calibration standard along with 0.1M tetra-butyl hexafluorophosphate ($TBAPF_6$) electrolyte. Once calibrated, this is then subjected to staircase voltammetry to determine if the configuration can be applied to the final PEEK (polyether ether ketone) version of the electrochemical-Raman cell used in the exfoliation stage of the project if found to produce valid CV scans and electrochemical-Raman spectra.

6.2 – Electrochemical cell design

The electrochemical flow cell design is originally designed using Perspex material for the prototype versions and the final design made with PEEK material. Fig. 6.1 shows the component parts of the cell that consists of three parts (a) lid, (b) chamber and (c) sample holder.

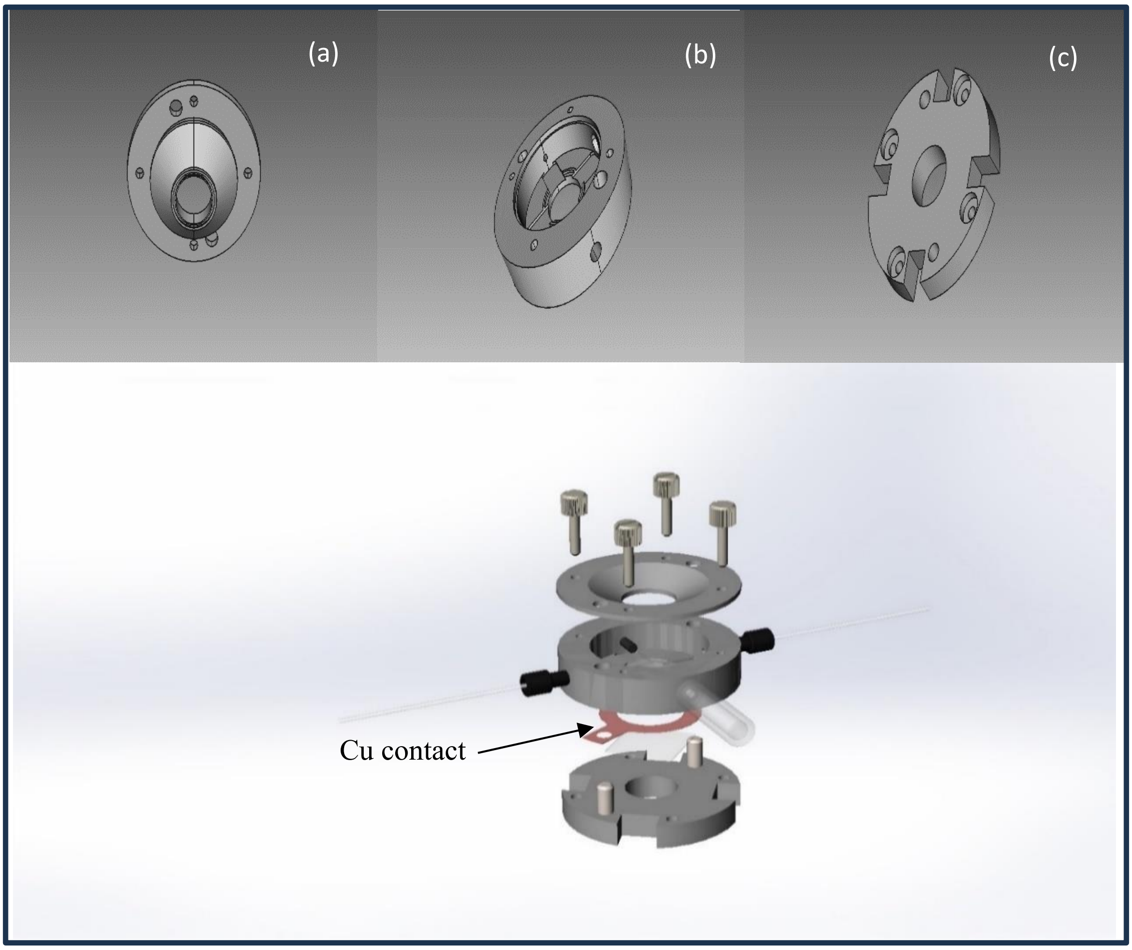

Figure 6.1: Schematic diagram of the electrochemical cell setup

The cell lid, chamber and sample holder are bolted together using stainless steel supports and magnets to form the complete cell, as shown in the diagram. The chamber consists of holes for the Ag/AgCl Reference electrode and the Platinum counter electrode to insert into and inlet and outlet holes for the electrolyte to enter into and exit out from the cell. The platinum counter electrode consists of a 150 mm long platinum wire carrying < 1mA of current that is inserted into a groove around the inside of the chamber. Any magnetic fields generated from the current passing through the wire would be insignificant and would not affect the measurements as the flow of current is of such a low value. A quartz optical window sits on the central hole in the chamber to accommodate the laser beam from the Raman spectrometer. A copper contact sits on top of the sample-holder, and this then contacts the sample substrate, e.g. ITO coated glass or glassy carbon to act as the working electrode and thus to complete the cell circuit. Fig 6.2 shows the final PEEK version, and the copper contact used for the working electrode.

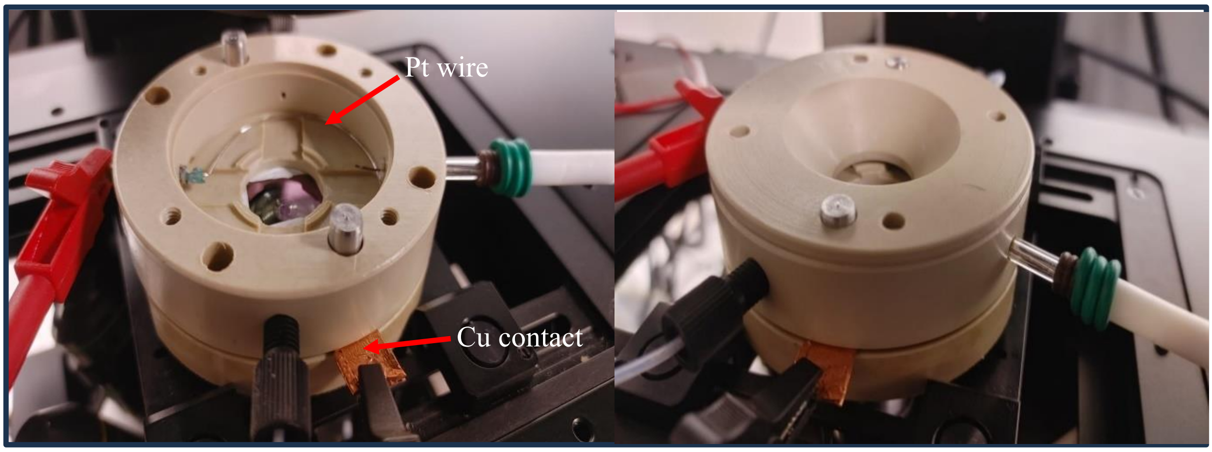

Figure 6.2: Photographs of the final PEEK version of the electrochemical cell.

6.3 –Exfoliation of MoS_2

The Liquid phase exfoliation methods in both solvent mediums (EtOH-40%:H_2O-60%) and the aqueous surfactant solution using sodium cholate were found to give a very low yield of the monolayer material as determined by Raman and UV-vis spectroscopies. Both of these preparations underwent pulse tip and bath sonication methods at room temperature in which centrifugation followed. The microwave samples were prepared by wet-grinding the sodium cholate aqueous surfactant solution with a mortar and pestle, they did not undergo sonication but were microwaved with varying time and temperature conditions and then centrifuged at the highest rate possible.

6.4 – Liquid Phase Exfoliation (LPE) methods

6.4.1 – Ethanol/water dispersions

Ethanol/water MoS_2 dispersion samples are prepared for pulse tip and bath sonication methods. For the pulse tip preparation, a 50 ml sample was prepared in 40% ethanol : 60% water solvent medium. 0.5 g of MoS_2 powder is placed into a vial and the 50 ml solvent then added, this solution is then pulse-tip sonicated for 4 hours at an amplitude setting of 40. The solution is then centrifuged for 1 hr at 5000 rpm (Rotina 380 – Hettick Zentrifugen) after which 20 ml of supernatant is pipetted into a fresh vial, the sediment is discarded. The sample is then drop-casted (100 µl) by micro-pipette or spray deposited on to a substrate such as ITO coated glass, glassy carbon or Si for Raman/PL measurements.

The bath sonicated sample is prepared by adding 0.5 g of MoS_2 powder to 50 ml of solvent medium (40% Ethanol/water) and bath sonicated for ~ 8 hrs controlling the temperature in an ice bath to ~23° C. This is then centrifuged for 1 hr at 5000 rpm after which 20 ml of supernatant is pipetted into a fresh vial. The sample is then drop-casted (100 µl) by micro-pipette or spray deposited on to a substrate such as ITO coated glass, glassy carbon or Si for Raman/PL measurements. Drop-casting is the preferred method as spray deposition is observed to produce a lower PL signal indicating more bulky material is present.

6.4.2 – Aqueous surfactant dispersions

Aqueous surfactant MoS_2 dispersion samples are prepared for pulse tip (PT) and bath sonication methods. For the PT preparation, a 100 ml sample was prepared in water solvent medium. 0.15 g of sodium cholate powder and 1 g of MoS_2 powder are placed into a vial and the 100 ml solvent then added, this solution is then PT sonicated for 30 mins using an amplitude setting of 40. Sodium cholate surfactant is chosen ahead of sodium dodecyl sulphate and sodium stearate, as previous work by Smith et al,[214] demonstrated a higher yield of monolayer formation. PT sonication for longer timeframes was shown to produce thicker flake-size from UV-Vis, absorbance measurements. The solution is then centrifuged for 90 mins at 1500 rpm after which 20 ml of supernatant is pipetted into a fresh vial. The sample is then drop-casted (100 µl) by micro-pipette or spray deposited on to a substrate such as ITO coated glass, glassy carbon or Si for Raman/PL measurements. The bath sonicated sample is prepared by adding 0.15 g of sodium cholate powder and 1 g of MoS_2 powder to 100 ml of water solvent medium and bath sonicated for~8 hrs controlling the temperature in an ice bath to~23° C. This is then centrifuged for 3 hrs at 5000 rpm after which 20 ml of supernatant is pipetted into a fresh vial. The sample is then drop-casted (100 μl) by micro-pipette or spray deposited on to a substrate such as ITO coated glass, glassy carbon or Si for Raman/PL measurements. Again drop-casting is the preferred method as previously mentioned for similar reasons. The typical Raman and PL spectra are shown in Figures 6.3 – 6.6 respectively to highlight the low monolayer yields obtained from both LPE method preparations. The PL signals are shown to be relatively weak in intensity and display the expected broad emission peaks. A broad and low-intensity PL peak might indicate the presence of defects, non-radiative recombination centres (which quench the PL signal), or most likely a higher layer number MoS_2 which indicates the low monolayer yield.[5]

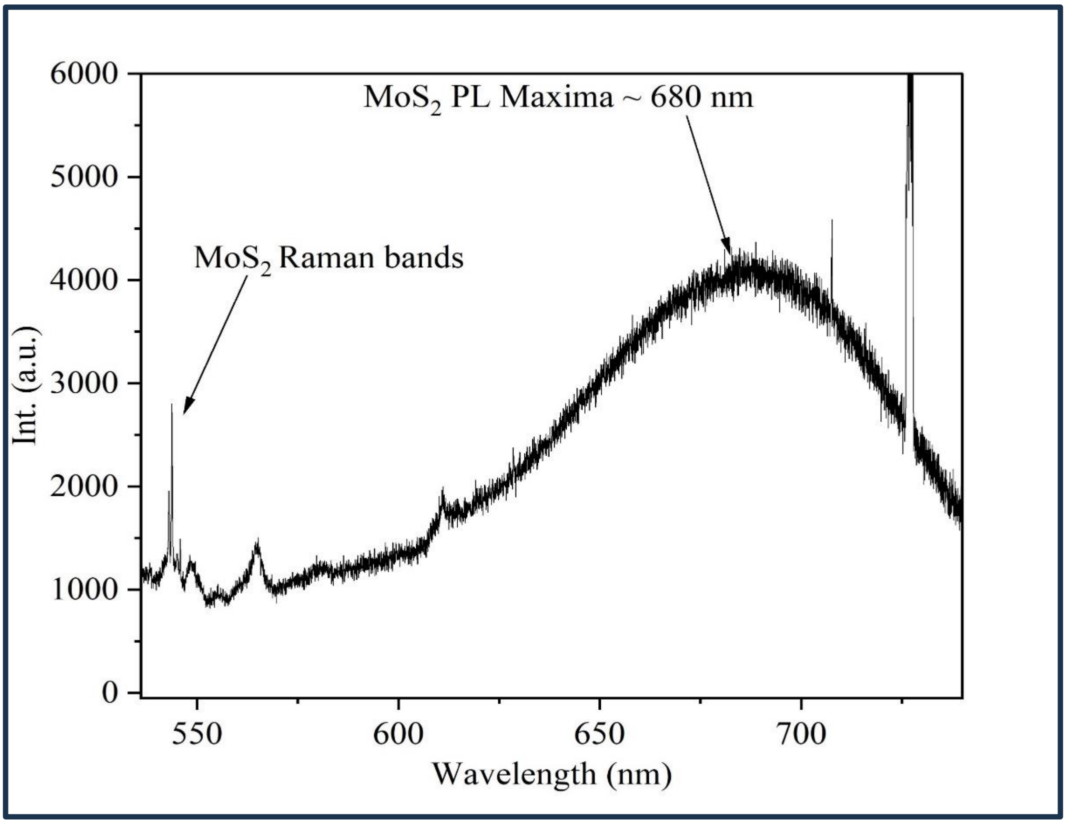

Figure 6.3: PL spectra of the MoS_2 Ethanol/H_2O PT sonicated sample. Generated using a monochromator with 1200 lines/mm grating, Olympus 40x 0.75 NA objective. Source Renishaw Plc.The PL peak maxima is observed to be approximately 1.5 x the intensity of the Raman bands indicating MoS_2 is mainly in bulk form and has a low yield in monolayer/few-layer material (PL count < 6000).

in comparison with the Raman spectra and display low intensity counts. SEM imaging further highlighted and confirmed the low monolayer yields obtained from the LPE preparations as only particles are observed with no presence of monolayer material

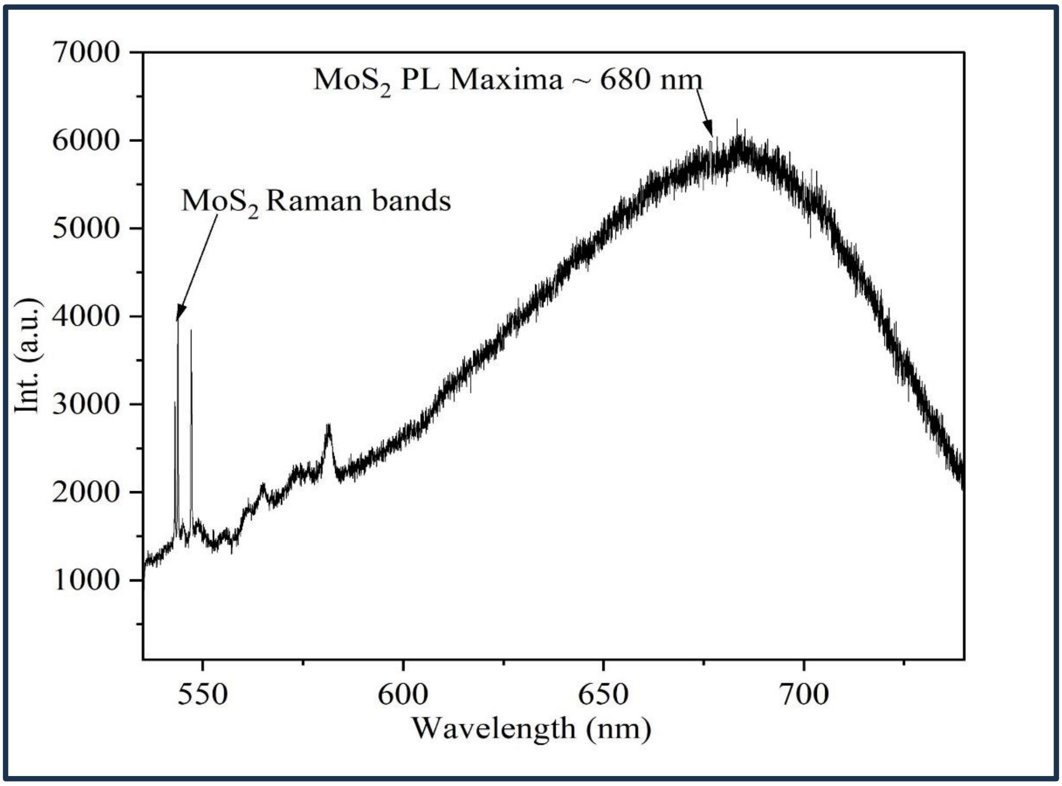

Figure 6.4: PL spectra of the MoS_2 aqueous surfactant sample. Generated using a monochromator with 1200 lines/mm grating, Olympus 40x 0.75 NA Objective. Source Renishaw Plc. The PL peak maximum is again observed to be approximately 1.5 x the intensity of the Raman bands indicating MoS_2 is again high in bulk form and has a low yield in monolayer/few layers material. (PL count < 5000).

The bath sonicated samples displayed similar spectra with a low intensity count PL signal and therefore a low yield in monolayer/few layer MoS_2 material. After a substantial amount of time was spent optimising various parameters such as sonication times, centrifugation speeds, microwave times and temperature conditions; both the LPE and MALPE exfoliation methods were found to produce low yields of monolayer material. Subsequently a sample of MoS_2 monolayer material was sourced from Trinity College Dublin (TCD) prepared using centrifugal cascading techniques in isopropyl alcohol (IPA) solvent.[215] The strength of this sample is 10 mg/ml containing small flakes of MoS_2 in an ink form. The PL signal was found to be significantly stronger reaching 15000 counts indicating a larger monolayer yield as shown in Fig. 6.5. The corresponding Raman spectra shown in Fig. 6.6 further indicated that the monolayer yield has increased significantly as the average peak separation was around 20 cm^{-1} (1-2 layers). However, with the flake size being very small (< 500 nm), this meant that further electrochemical measurements could not be made on this sample, as mapping of this flake size would not be possible.

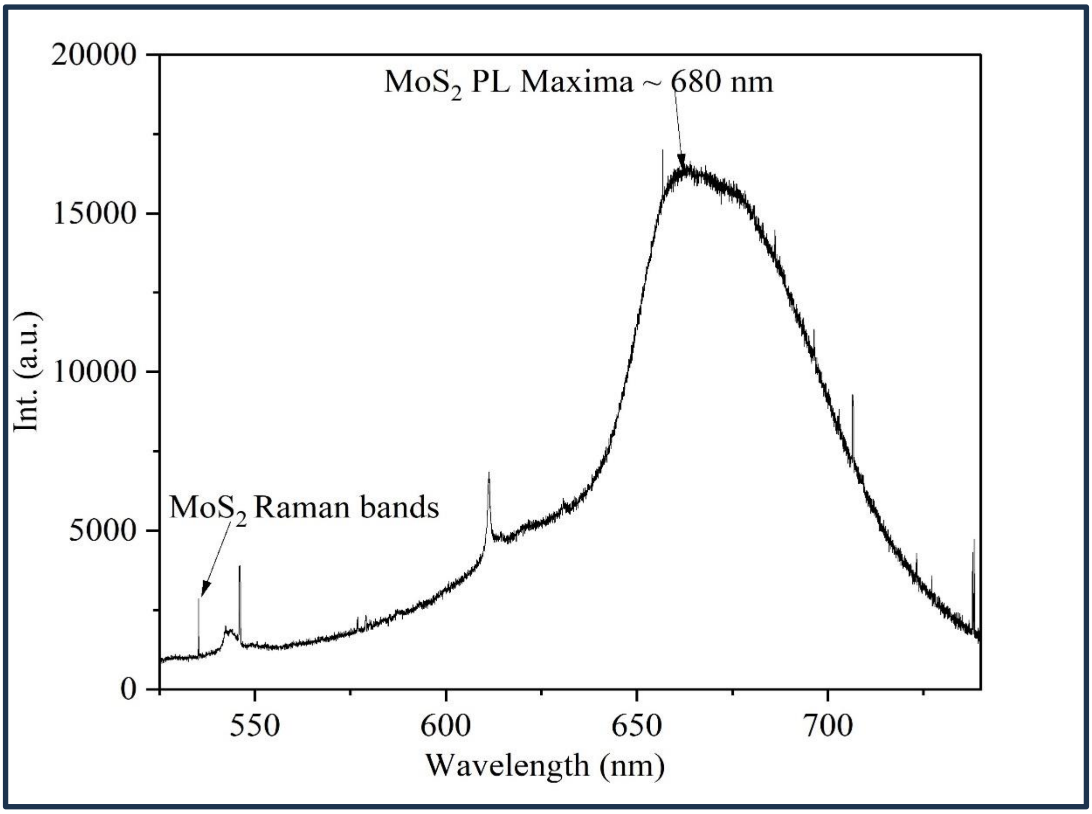

Figure 6.5: PL spectra of the TCD MoS$_2$ sample. Generated using a monochromator with 1200 lines/mm grating, Olympus 40x 0,75 NA Objective. Source Renishaw Plc. The PL peak maximum is observed to be approximately 5 x the intensity of the Raman bands indicating MoS$_2$ is displaying a higher yield in monolayer/few-layer material. (PL count ~ 15000).

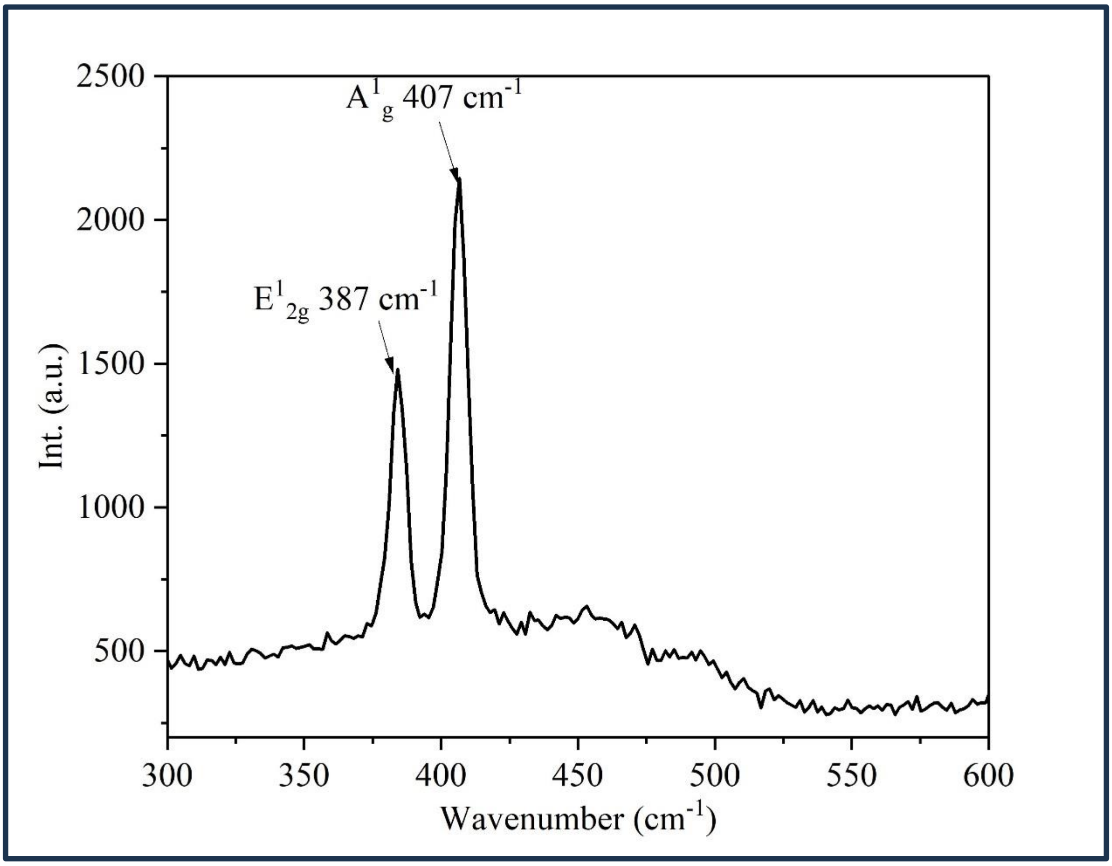

Figure 6.6: Raman spectra of the TCD MoS_2 sample. Generated using a monochromator with 1200 lines/mm grating, Olympus 40x 0.75 NA Objective. Source Renishaw Plc. The average peak separation of the Raman bands E^1_{2g} (387 cm^{-1}) and A^1_g (407 cm^{-1}) giving 20 cm^{-1} indicates the MoS_2 is high in monolayer yield and mostly 1-2 layers in thickness.

SEM (Scanning Electron Microscopy) imaging was also carried out on 50% dispersions of MoS_2 in EtOH/H_2O and sodium cholate and the images are shown in Fig. 6.7 (a-c). The images in Fig. 6.7 show the µm scale bulky particles that are indicative of the multilayered material formed from LPE methods. These images showed repeatedly the MoS_2 sample consisting of bulk-like particle material, with no monolayer material observed. Even though spatial resolution of the SEM instrument is very high, the imaging was discontinued due to limitations of the instrument. The MoS_2 is beam-sensitive and the high-energy electrons from beam irradiation can cause damage by modulating the structure of the MoS_2.[216] Additionally, the interaction volume of the electron beam with the sample can be large, particularly at higher accelerating voltages, leading to a blurring of the image and a loss of fine detail at the nanoscale.[217] Subsequently Raman and UV-vis spectroscopy were used as a means of reliably monitoring and characterizing the thickness (no. of layers) and yield of monolayer material formed from the spectra produced on further preparations.

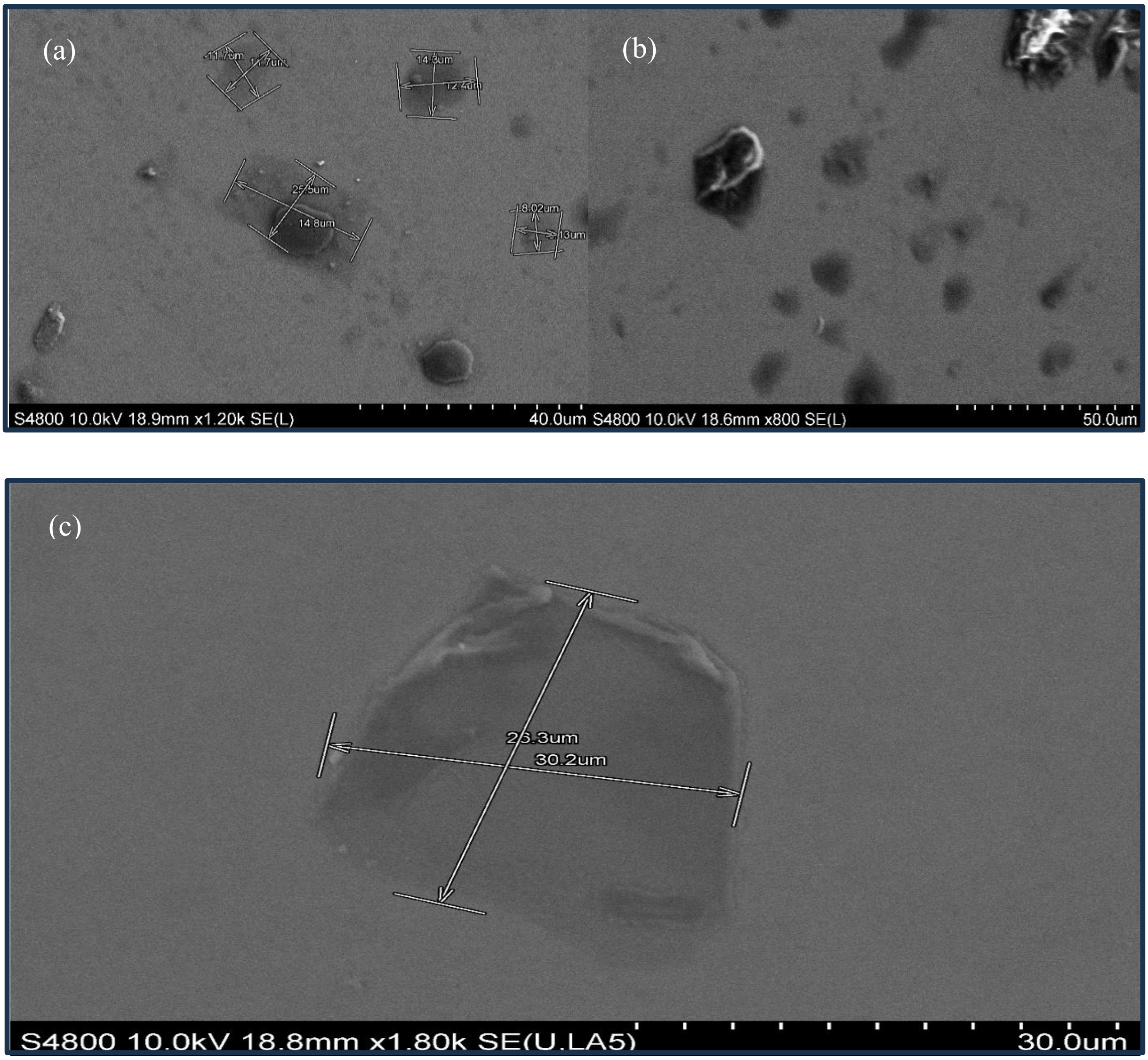

Figure 6.7: SEM (Hitachi S4800, Accelerating Voltage 10kV, magnification 20k) images of 50%dispersions of MoS_2 in (a) EtOH/H_2O and (b) sodium cholate (c) Image of a large flake of MoS_2 showing multilayered material at µm scale.

6.4.3 –Exfoliation by Microwave Assisted Liquid Phase exfoliation (MALPE) experimental methods.

The microwave exfoliated samples are prepared by adding 50 mg of MoS_2 powder to 1 ml of a solution containing 15mg of sodium cholate surfactant in 10 ml de-ionised water. This solution is then placed in a mortar and pestle and wet -grinded for ~10 mins to form a slurry, the wet-ground material or slurry is then added to a 200 ml volumetric flask and made to volume in de-ionised water. This solution is then placed in the microwave (CEM Inc. Discover 2.0), 140 W at temperatures of 40, 50, 60, 70, 80 and 90° C and 300 psi pressure for initially 1 hr, and then 3 hrs, after which the time is increased to 6 hrs and then the sample is allowed to cool to room temperature. A 50 ml portion of this sample is then centrifuged at 4000 rpm for 1 hr keeping the supernatant and increasing the centrifugation rate to 13300 rpm (17000g, VWR-Micro Star 17R) on this same supernatant and spinning for 1 hr again, with this sample placed in Eppendorf tubes. The final supernatant is then taken out to remove the surfactant, and the remaining precipitate or sediment is collected in 6ml of ethanol. The ethanol precipitate is then spray deposited onto an ITO glass plate, using 100 µl at a time, drying each time until 1ml is applied and then dried. Each prepared sample is checked for UV absorption using the UV-Vis spectrometer to determine the layers and the thickness of material present in solution. The PL signal after each preparation was checked using a fluorometer instrument (Perkin Elmer LS55). Strong photoluminescence was not observed at the direct excitonic transition energies from the MoS_2; and if such luminescence is absent, then the sample is bulk MoS_2.[218] A Raman spectra of the sample was also used to determine the layers present as the peak separation distance between the Raman bands indicates this as shown in Fig. 6.6. If monolayer material is being produced, the peak distance should decrease, and the PL signal should increase. The UV-Vis plots from the experiments are shown in Fig. 6.8. They are shown for the different rates of centrifugation against the size or thickness of the flakes produced.

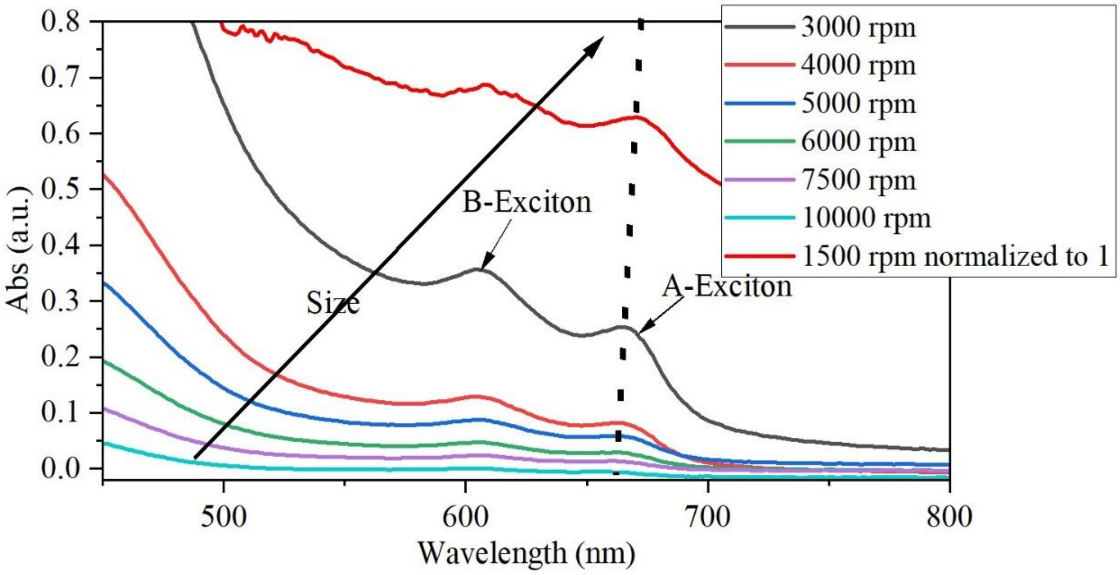

Figure 6.8: Normalized UV–vis absorption spectra of microwave treated samples, taken at different rates of centrifugation. The prominent peak at 273nm that is not fully observed in the spectrum is associated with the high energy excitonic transitions corresponding to the 2H phase of MoS_2. In the region from 600–700nm, the main peak features are at 623 (B-Exciton) and 683 nm (A-Exciton). The B-exciton PL peak is higher in energy than the A-exciton PL peak.[116]

The plots show how the flake size and thickness, decreases with the increase in centrifugation rate, as the UV absorbance B-exciton backgrounds are observed to decrease in absorbance indicating monolayer formation. The A-exciton is also observed to blue shift slightly with increasing centrifugation rate. In MoS_2, the A and B excitons are two distinct exciton states associated with different energy transitions. The A exciton is the lowest energy direct exciton (ground state exciton), while the B exciton arises from a higher-energy valence band splitting due to spin-orbit coupling (higher spin-orbit split state). These excitons exhibit different optical properties, including emission wavelengths, intensity ratios, and response to external stimuli like electric fields.[219, 220] It was discovered that above 70° C the UV absorbance signal started to disappear, and the average Raman peak distance at different locations on the sample was around 25 cm^{-1} at each temperature, indicating that monolayer formation is not taking place. This suggested that the optimum conditions for microwaving the MoS_2 aqueous surfactant preps are 60 mins, 70° C, 140 W and 300 psi. Even under these conditions and with an increase in time and centrifugation rate, this did not improve the UV absorbance, and the average peak separation remained at 25 cm^{-1}. This experimental preparation was then discontinued as it was deemed unsuccessful. The main reasons proposed for this are the microwave radiation can unevenly heat the sample, leading to localized hot spots that might damage the MoS_2 flakes or cause excessive aggregation, preventing efficient exfoliation. The rapid evaporation of the solvent during microwave heating can create pressure gradients between the MoS_2 layers, potentially causing incomplete separation and restacking of the flakes. Finally, the initial size and morphology of the bulk MoS_2 powder can significantly affect the exfoliation efficiency, with larger particles being more difficult to separate into monolayers.[112, 114] Further experimentation could possibly make it a success given more time.

Microwave preparations using toluene solvent were also examined by adding 50 mg of MoS_2 and sodium cholate solution (15 mg in 10 ml DI water) to 10 ml of toluene in a round-bottomed flask with no wet-grinding and performing the experiment using a reflux condenser attached to the flask on the microwave to prevent flammability hazards. The microwaving procedure was carried out five times at 40° C for 15-minute time intervals. The PL measurements made on the fluorometer, and the UV-Vis measurements made after each microwave interval showed no PL signal and no exciton peaks are observed in UV. Changing the method to wet-grinding for 10 mins, increased temperatures of 60 -80 °C and increasing the centrifugation rate, lead to the disappearance of the UV absorption and the PL signal and so this experimental preparation was discontinued.

Microwave preparations using NMP (N-methylpyrrolidone) solvent were prepared the same way as the toluene preparation with wet-grinding and carried out using a reflux condenser. The microwaving procedure was carried out five times at 120 ̊C for 15-minute time intervals at 140 W and 300 psi pressure and high-speed stirring used to prevent oxidation and loss of material. The sample is then centrifuged at 3000 rpm for 1 hr. The PL and UV absorbance were measured accordingly between each interval. Initially no UV absorbance or PL signals are observed under these conditions, and so the time was increased to 1 hr for each cycle with no pressure being applied and the same centrifugation rate used. UV and Raman are then used to monitor the sample each time and UV absorbance is observed but the Raman spectra show 25 cm^{-1} peak separation and therefore monolayer material was not forming. After increasing the centrifugation rate to 5000 rpm the Raman and UV signals are no longer observed and so the experimental preparation was discontinued.

The typical Raman and PL spectra are shown in Figure 6.9 respectively to highlight the low monolayer yields obtained from the MALPE method preparation. The PL signals are shown to be relatively weak in comparison with the Raman spectra and display low intensity counts.

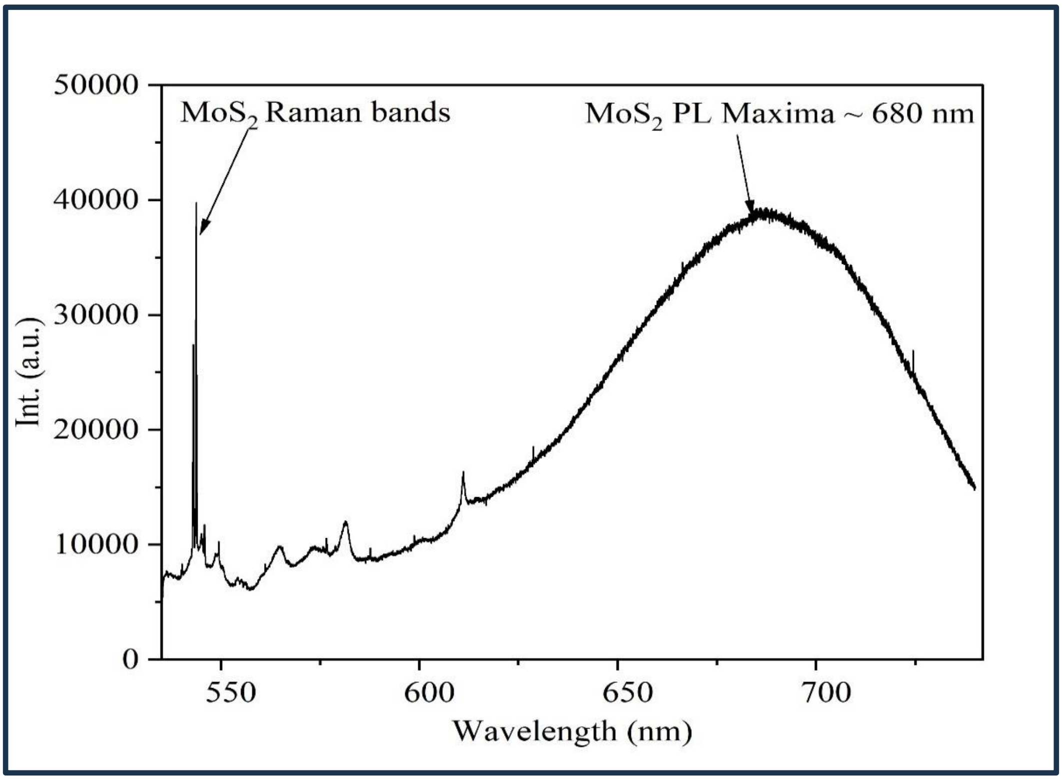

Figure 6.9: PL spectra of the MoS_2 microwave aqueous surfactant sample. Generated using a monochromator with 1200 lines/mm grating, Olympus 40x 0.75 NA Objective. Source Renishaw Plc. The PL peak maxima are observed to be approximately similar in intensity to the Raman bands, indicating MoS_2 is high in bulk form and has a low yield in monolayer/few-layer material. (PL count – 40000).

6.5–Exfoliation by Electrochemical Method

Natural, single-crystalline bulk MoS_2 (SPI Supplies, 429MM-AB) is used as the working electrode and source for the electrochemical exfoliation method.[221] The bulk MoS_2 crystal is clamped to a Pt clip and the MoS_2 crystal alone is immersed in the 0.5 M Na_2SO_4 ionic solution. A grounded Pt wire is used as the counter electrode and is placed 2 cm away from, and parallel to, the bulk MoS_2 crystal. The 0.5 M Na_2SO_4 solution is prepared by mixing 4.0 g of sodium hydroxide (Duksan) and 5.2 g of sulphuric acid (95%) dilute solutions, then adding DI water to obtain 100 mL of the combined solution. The electrochemical exfoliation process is carried out by applying a positive bias on the working electrode. A low positive bias of +2 V is initially applied to the working electrode for 10 min to wet the bulk MoS_2 crystal. The bias is then increased to +10V for 0.5-2 h to exfoliate the crystal. As a result, many MoS_2 flakes dissociated from the bulk crystal and became suspended in the solution., the successful exfoliation and the presence of MoS_2 flakes was evident by the appearance of pale-yellow colour of the solution. The intensity of the electrochemical reaction could be estimated by the amount of gas bubbles produced on the MoS_2 bulk surface. After the electrochemical-exfoliation efficiency is optimized, the bulk MoS_2 crystal developed a barely oxidized surface when the Pt clip is 0.5 cm above the liquid level. In the exfoliation process, electrolysis of water released O_2 and H_2, which led to a drawdown of the liquid level. This caused the current passing through two electrodes to decrease with increasing time. To eliminate the effect of current variation on experimental results, a tube is connected to the experimental setup (shown in Figure 6.10) with a large beaker that also contained the 0.5 M Na_2SO_4 solution. The beaker is large enough to allow us to ignore the lower liquid-level drawdown because of water electrolysis. As a result, the current remained stable during the exfoliation process. The exfoliated MoS_2 flakes are collected using porous membranes (0.2 µm, JGWP, Millipore), washed with DI water using vacuum filtration and then dried at room temperature for 1 h. After that, the MoS_2 nanosheets are carefully washed with DI water and dried again. These samples are found to be high in monolayer/few layer yield and produced much larger flake size than the previously mentioned exfoliation methods; therefore, electrochemical PL measurements could be made on them.

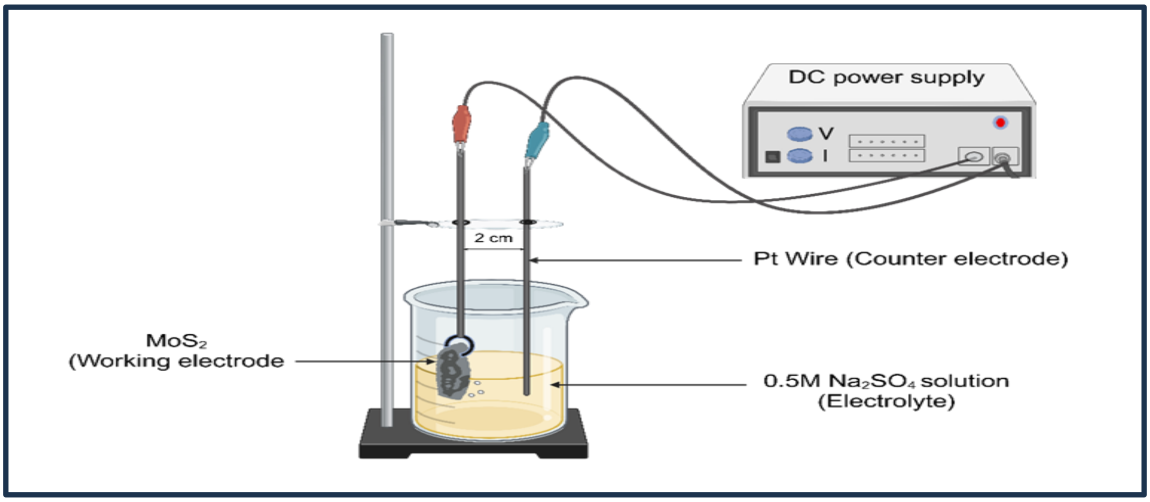

Figure 6.10: Electrochemical exfoliation set up assembled in-house using the MoS$_2$ crystal as the working electrode.

6.6 –Electrochemical CV Measurements

6.6.1– CV measurement of ruthenium complex

The redox properties of the [Ru(bpy)$_2$dppz]$^{2+}$Cl$_2$ complex were determined and the electrochemical configuration validated using cyclic voltammetry, where Ag/AgCl is used as the reference electrode, and the scan rate used was 50 mV/sec. The cyclic voltammogram is shown in Fig. 6.11. The setup is shown in Chapter 5 Figure 5.11.

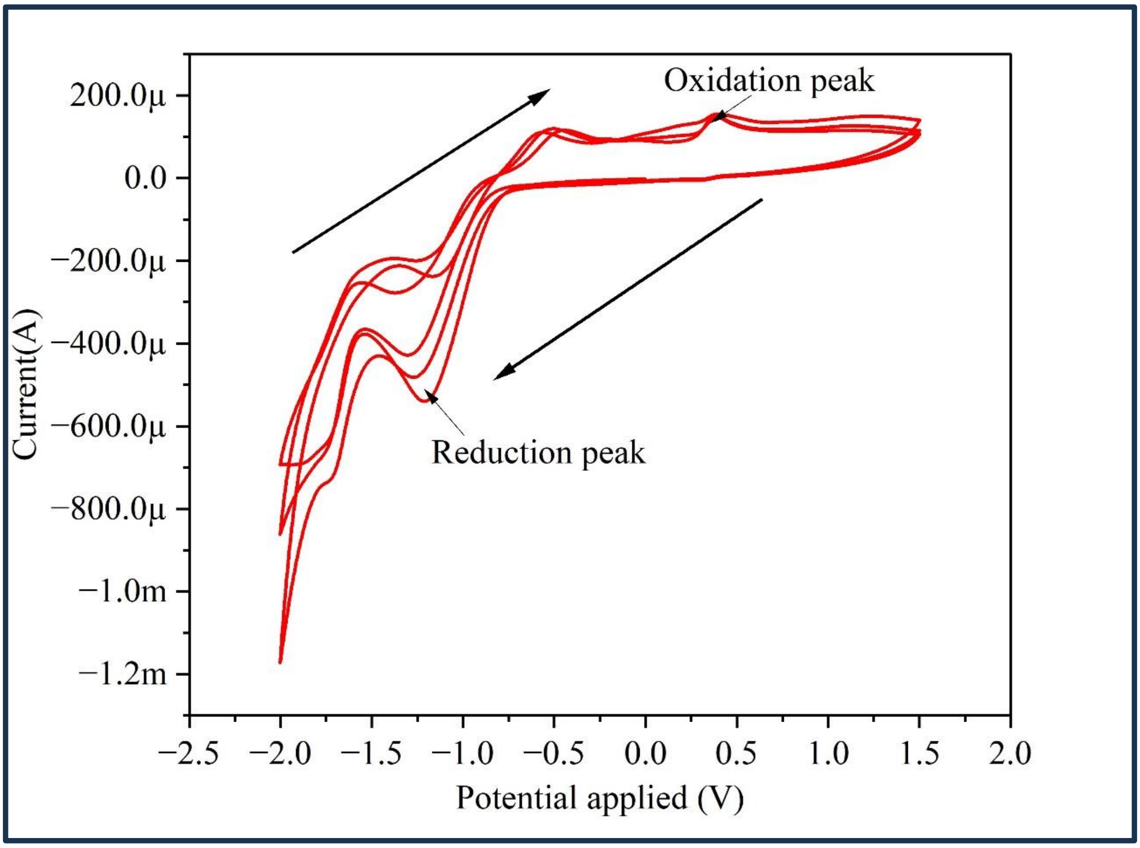

Figure 6.11: Validation of the Cyclic voltammogram of Ru complex obtained using 50 mV/s scan rate. The scan was performed three times.

The oxidation process that occurs in this complex is a one transfer process, from Ru^{2+} to Ru^{3+}. The peaks obtained from Figure 6.11 show redox peaks around -1.3 V and 0.4 V. The peak at -1.3 V is the reduction of Ru, which gains an electron to form Ru^{3+} and the peak at around 0.4 V shows the oxidation of Ru which loses an electron to form the Ru^{2+}. The reduction peak is consistent with other literature data.[18, 20, 222, 223] The 0.1 M non – aqueous electrolyte $TBAPF_6$ was chosen for cyclic voltammetry measurements because it has an electrochemical stability that can exceed 4V and has a higher operating potential of 2.5 V. This allows for minimal solution resistance, and it is considered to be resistant to reduction itself. The ions present in the electrolyte increase the rate of reaction as the carbon chain length from the methyl to butyl moiety decreases and thus the electrochemical stability increases. The electrochemical stability then allows for conductivity increase as shown in (Figure 6.11). The voltammogram shows the high degree of reversibility of the Ru II/III redox process even under the high scan rate examined. The scans differ each time due to system noise as the data from each scan is typically averaged together, which can smooth out random noise components. The electron releasing tendency of 2,2' – bipyridyl ligand has a high electron rich environment in the metal centre and causes the redox value to be lower. There are some other irreversible peaks on the cyclic voltammogram, which are due to both metal oxidation and ligand centred reduction. The reduction peak at ~ -1.75 V appears to be ligand-based $Ru(bpy)_2(dppz)_2^{2+}/Ru(bpy^{-}\cdot)(bpy)(dppz)_2^{+}$.[224] The oxidation peak ~ -0.4 V is due to the oxidation of Ru^{2+} to Ru^{+}.[222]

6.6.2– CV measurement of exfoliated MoS_2

Electrochemical CV curves were produced for exfoliated MoS_2 using the PEEK three-electrode cell arrangement with NOVA software interfaced with the Autolab PGStat204 for acquiring the CV curve. These are recorded for the liquid phase exfoliated (EtOH/H_2O) MoS_2 in 0.1 M PBS electrolyte for multilayer material. A CV curve is also produced for the monolayer/few layer TCD sample in 0.1M PBS. These are shown in Figs 6.12 to 6.14.

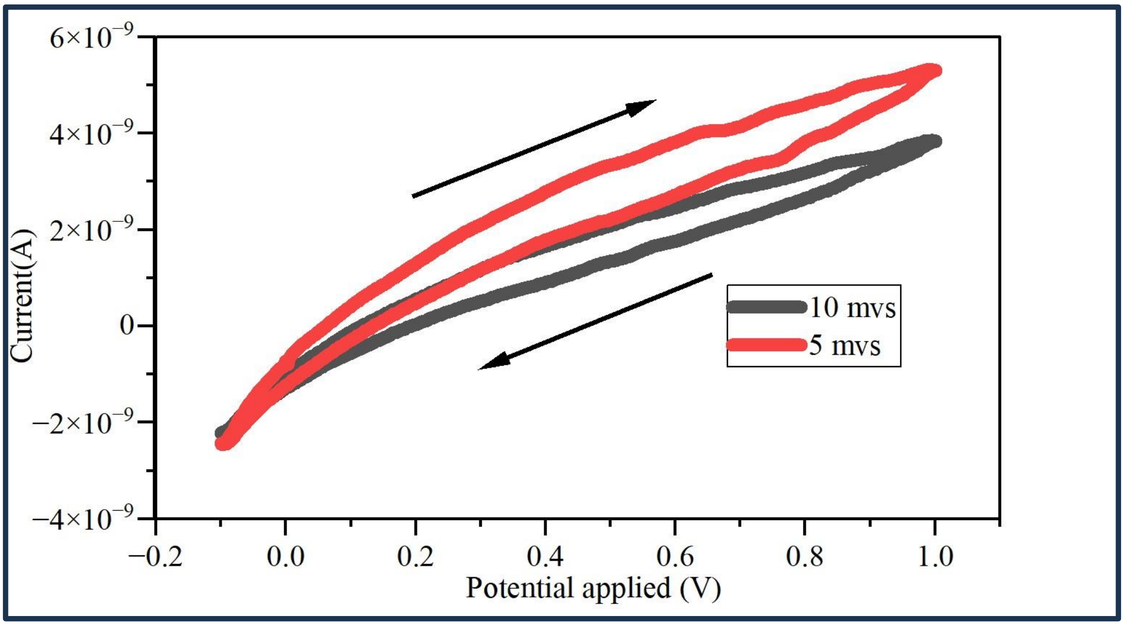

Figure 6.12: Cyclic voltammograms of multilayer MoS_2 (EtOH/H_2O) in aqueous 0.1 M PBS Buffer at scan rates: 5 mvs^{-1} and 10 mvs^{-1}. Potential window: -0.1 to 1.0 Vs Ag/AgCl.

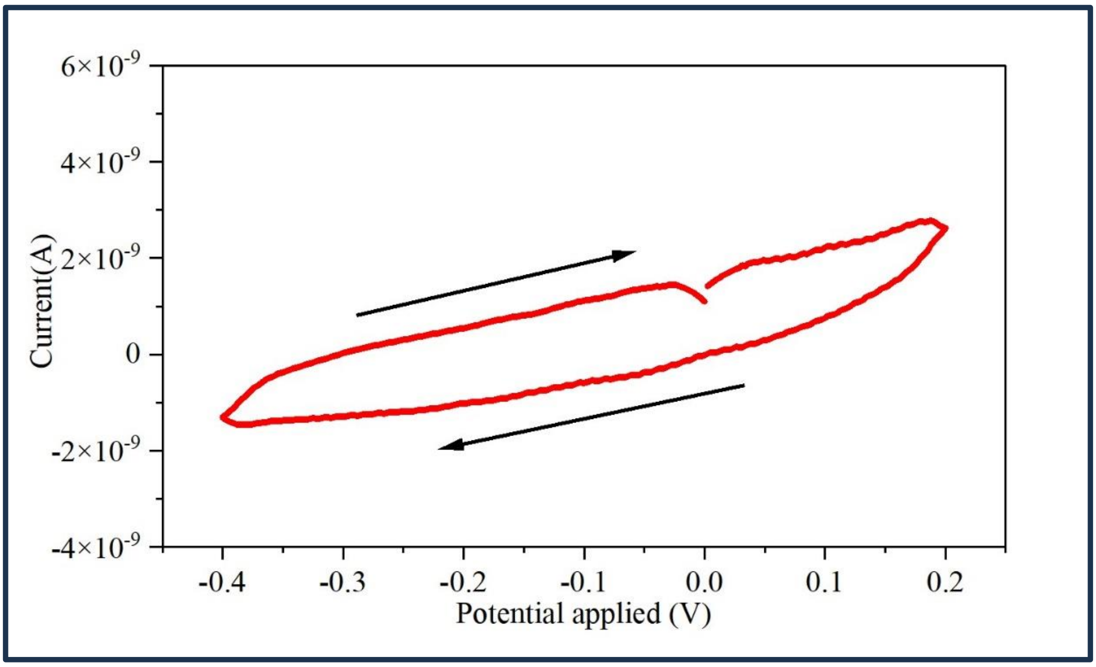

Figure 6.13: Cyclic voltammogram of multilayer MoS_2 ($EtOH/H_2O$) in aqueous 0.1 M PBS Buffer at scan rate: 10 mvs^{-1} and potential window: -0.4 to 0.2 Vs Ag/AgCl.

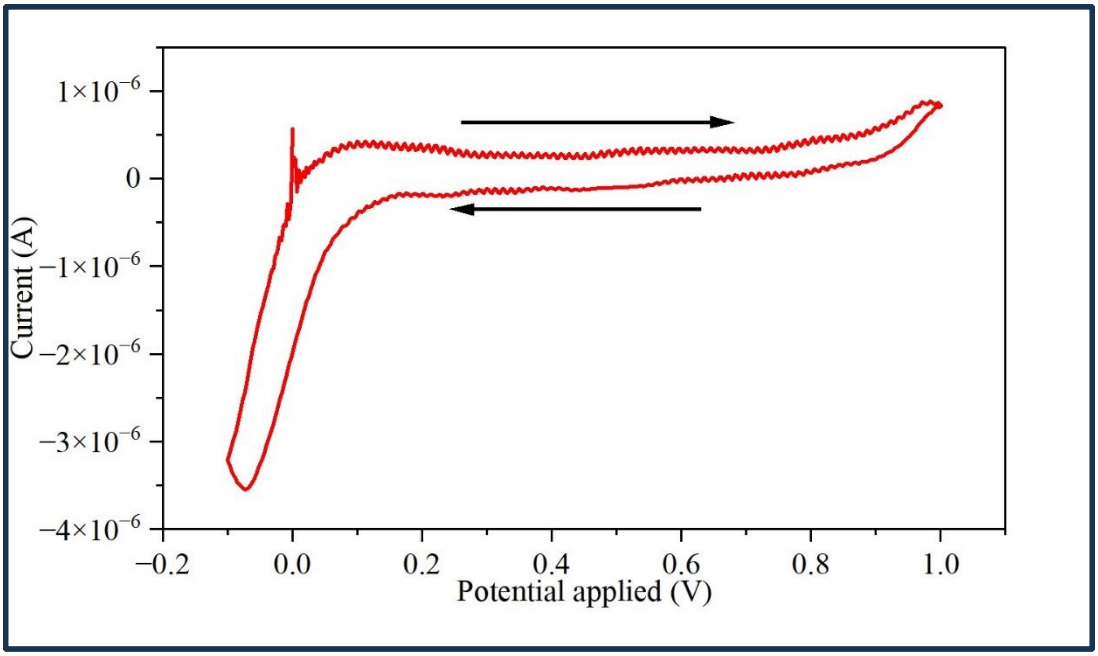

Figure 6.14: Cyclic voltammogram of monolayer MoS_2 TCD sample in aqueous 0.1 M PBS Buffer at scan rate: 10 mvs^{-1} and potential window: -0.1 to 1.0 Vs Ag/AgCl

As is evident from the CV curves for the MoS_2 (EtOH/H_2O) preparation in Figs 6.12 and 6.13, the CV curves are shown to be exhibiting more opening of the forward and reverse scans for an increase in scan rate for the multilayer MoS_2 (EtOH/H_2O) preparation. However, no redox peaks are observed due to the inner bulk flake thickness not allowing for any redox activity due to poor electron confinement and lack of electron transfer; therefore, not allowing the redox reactions to take place. The electron concentration on the surface of a monolayer is nearly four orders of magnitude higher than that in the inner bulk and a linear relationship is observed that when the thickness increases the conductivity decreases and vice versa.[225-227] The CV curve for the TCD sample in Fig. 6.14, however, does exhibit some small amount of redox activity due to its monolayer structure that allows for better electron confinement and electron transfer between the Mo states can now take place. However, in conclusion the CV curves are not reliable as it was not possible experimentally to cover the whole of the electrode surface with a uniform film of monolayer material to produce an authentic reliable CV curve. If successful exfoliation producing a high yield of monolayer had taken place this would have been possible as current is proportional to the surface coverage.[228] In addition to this, the current produced mainly comes from the working electrode, and only a small amount comes from the MoS_2 flake, again affecting the accuracy and reliability of the CV curve data. Fig. 6.15 shows the variation in current (I) with potential applied to the ITO substrate in the 0.01 M NaCl electrolyte solution to further emphasise this.

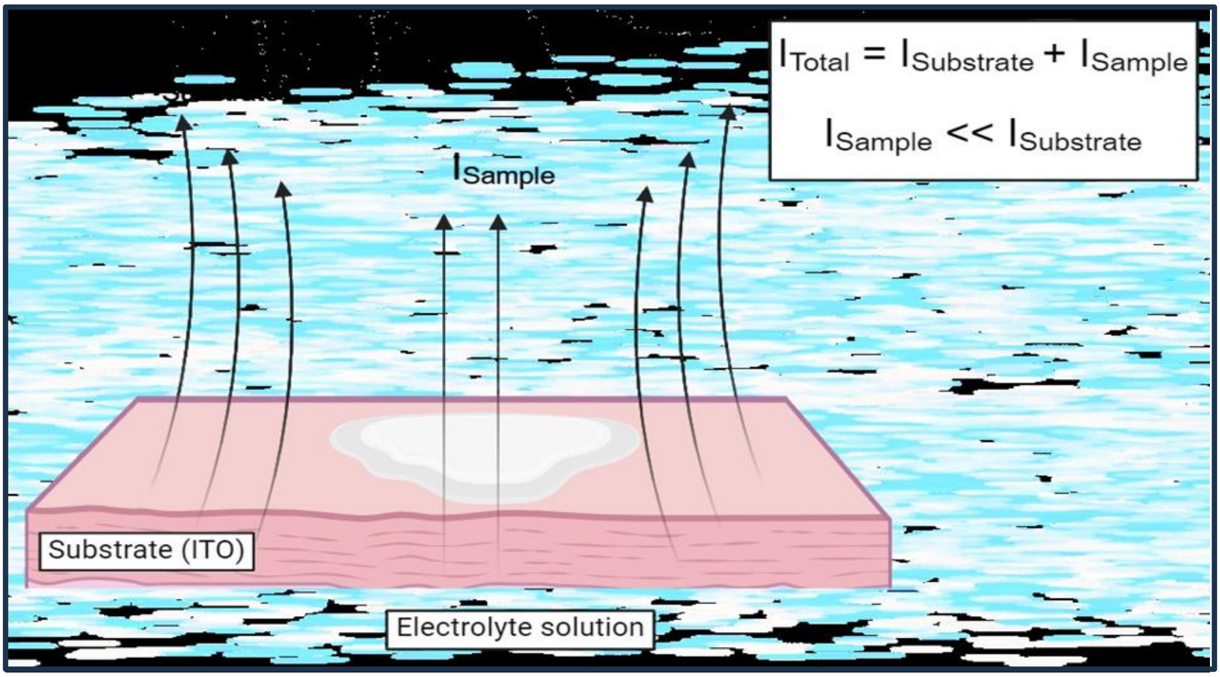

Figure 6.15: Diagram depicting the variation in current (I) for the ITO substrate and the sample inside the electrochemical cell in 0.01 M NaCl electrolyte solution.

Fig. 6.15 depicts conductivity is directly proportional to the area of cross-section and here the area of cross-section is decided by the much larger area of ITO substrate in comparison to the miniscule area of illuminated and conducting MoS_2 flake on it. Thus, total current would be largely decided by the ITO substrate (area of flake~100 sq. micron; area of ITO substrate > 1 sq.cm = 10^8 sq. micron) which is at least 10^6 times the area of illuminated flake. Thus, unless the conductivity of MoS_2 is enormous in comparison to ITO, contribution to current in the circuit by MoS_2 flake would be insignificant. Hence, the explanation for the poor redox activity in the CV curves produced in Figs. 6.12 to 6.14.

6.7 – Validation of Resonance Raman measurement of Ru complex at 457 nm excitation wavelength

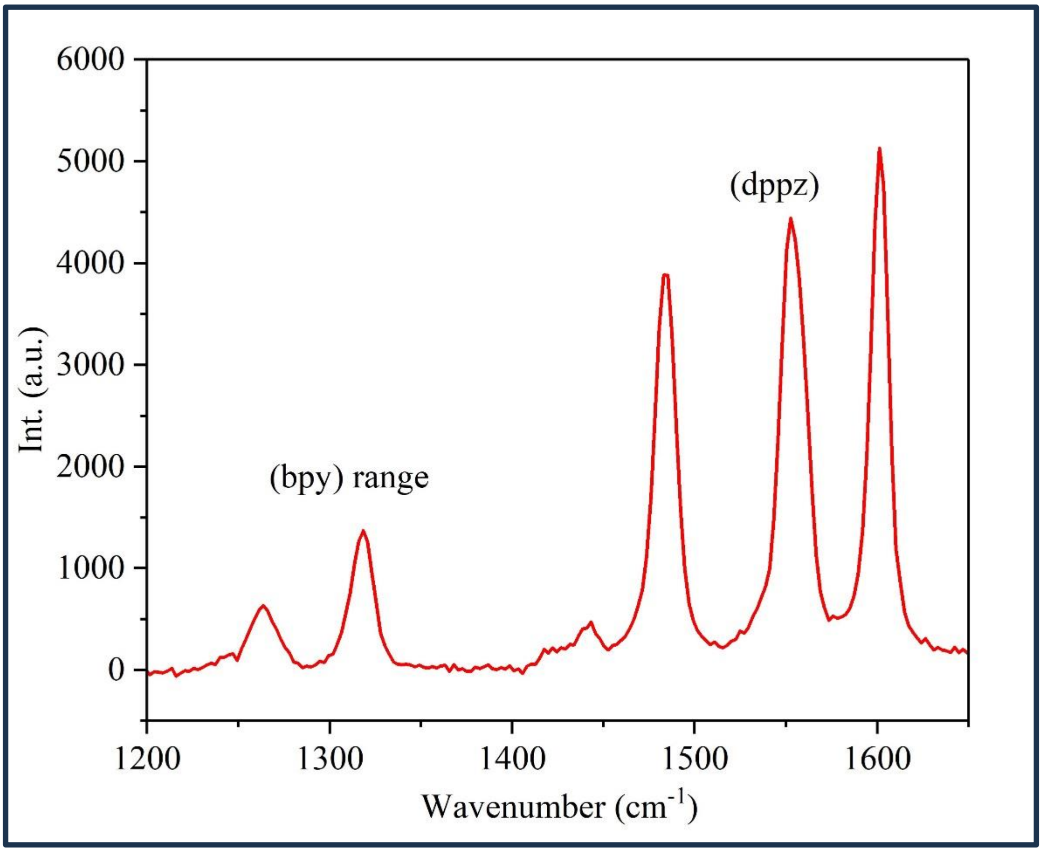

Figure 6.16: Validation of Resonance Raman spectra of Ru complex excited at 457 nm wavelength.

Figure 6.16 shows the validated Raman spectra of the ruthenium complex taken at an excitation wavelength of 457 nm. This was validated as electrochemical-Raman characterization is expected to be carried out on MoS_2, and so the Raman part is now validated for Ru as Raman bands are observed. The five larger peaks observed above 1250 cm^{-1} represent the presence of the ligands in the ruthenium complex. The three peaks between 1485 cm^{-1} and 1601 cm^{-1}

represent the (dppz) ligand, and the two peaks at 1266 cm^{-1} and 1318 cm^{-1} show the presence of the (bpy) ligand.[18, 20, 222, 223] The 457 nm excitation wavelength gives an improved Raman spectral signal and signal to noise ratio, causing the peaks to be fully visible and not be construed as noise, as observed at higher excitation wavelengths. Raman mode assignments for ruthenium complexes rely on several key factors. These include the complex's symmetry, the type of ligand, and resonance enhancement.[229-231] Raman spectroscopy provides insights into the vibrational modes of molecules, helping to identify different types of motions, including stretches, bends, and rotations.[230, 231] If the Ru complex is considered to have C2v symmetry for the coordinated bipyridine, including the ruthenium itself then we would expect 20 full symmetric modes. These symmetric modes are observed in the region below 1700 cm^{-1}, and are broken down into 12 stretching modes, 4 C–H's, 1 Ru–N, 4 C–C's, 2 C–N's and 1 inner – ring C–C stretch. There are also 4 C–H in plane deformations. The most intense peak at around 1601 cm^{-1} is assigned to the C–N stretch because of the rings being substituted in the 4' – ring position, the smaller peak at around 1260 cm^{-1} is assigned to the C–C inner – ring stretch.[210]

6.8 –Validation of electrochemical –Raman measurements on ruthenium complex

The validation measurements were carried out using the Nova software method which supplies the TTL trigger for the range of potentials, and the Wire software from the Renishaw Raman instrument receives the trigger to then produce the desired spectra at each potential value. The signal to noise ratio is increased as the noise was reduced by increasing the exposure time to twenty-five seconds on the Wire software. The current that is produced is used to identify the peak intensities with the potentials that are applied, the Raman spectrometer supplements this by producing the relevant changes in the peak intensities with the matched potentials that are coming from the cyclic voltammetry using the Nova software. The spectra are shown in Fig. 6.17.

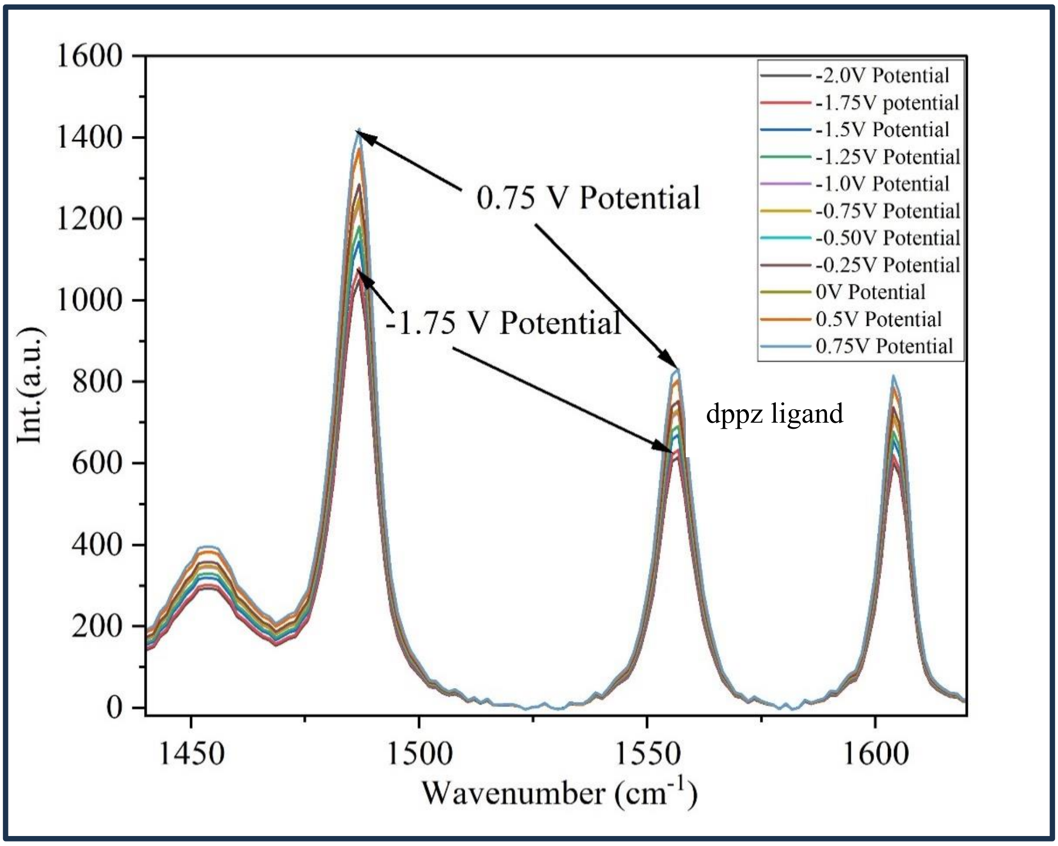

Figure 6.17: Validated Electrochemical-Raman spectra of Ru complex using the combination of cyclic voltammetry and Raman spectroscopy. The potential range is from -2 V to 0.75 V.

Figure 6.17 shows how the peaks of the (dppz) ligand change over the potential difference range applied of -2 V to 0.75 V. to confirm that there is a redox change occurring when a change in potential is applied to the Ru complex system. The ligand PL intensity is shown to increase for all peaks with increasing potential as expected as they undergo metal-to-ligand charge-transfer (MLCT) excitation and luminescence is associated with the MLCT bands as the ligand reduction and metal oxidation takes place. Density functional theory calculations carried out by Sun *et al*,[232] conclude that the electron density of lowest unoccupied molecular orbital (LUMO) was located on the distal portion of dppz. The electron densities of the LUMO+1, LUMO+2 and LUMO+3 states, are localised on the proximal section of the dppz ligand, which in this case should be emissive and would be consistent with electron transfer from the ^{3}dd Ru (II) states to the ^{3}MLCT bright excited state.

This demonstrates the electroluminescent properties of the Ru complex. [19, 233] The spectra produced highlight and confirm the validation of electrochemical-Raman technique to detect the redox changes that occur on the ruthenium centre when a change in potential is applied.

The potential range can also be varied accordingly depending on where redox reactions are likely to take place.
This could lead to lots of potential to explore and test other important metals and metal complexes that have practical use in medical (anti-cancer treatments) and in catalytic applications.

6.9–Electro-Spectrochemical PL on exfoliated MoS_2

6.9.1–Electrochemical PL using Single Channel Imaging

Although the TCD sample displayed a small flake size, but a higher yield in monolayer/few layers material, a decision was made to use the electrochemical exfoliated MoS_2 samples to perform the electrochemical PL measurements on, as they were found to be much larger in size. Some of the electrochemical flakes had sizes greater than 10 microns and thus variation of PL intensity could be measured and mapped more easily.

The electrochemical exfoliated MoS_2 flakes are transferred by micropipette onto 0.17 mm thick ITO coated coverslips to create a thin film inside the electrochemical cell setup. The prepared ITO substrate is then placed inside the two-electrode cell set-up and voltages ranging from +2 V to -2 V are applied across the two-electrode configuration via a DC power supply. The anode is connected to a copper plate, which is placed on top of the drop-casted ITO substrate. A Pt wire acted as the cathode and a 0.01 M NaCl aqueous solution is used as the electrolyte. Wide-Field imaging of electro-exfoliated MoS_2 flakes is carried out using a high-magnification 100x oil immersion lens and a 532 nm excitation laser source illuminates the sample that is focused on the back focal plane of the objective lens. Rayleigh scattering is removed by using a 540 nm long pass filter. Raman and PL spectra are firstly taken in air with the Horiba spectrometer for observation purposes before adding a suitable electrolyte such as 0.01 M NaCl to the cell to perform the electrochemical PL measurements over a certain potential range. The potentials are supplied using a DC voltage supply and the images are captured after each potential.

The obtained PL signal is passed through a birefringent crystal interferometer (model: Gemini from Nireos), and the interferograms generated by the interferometer at the camera (Hamamatsu). These are then Fourier transformed using a MATLAB code to generate the hyperspectral cubes and hence the images. HSImaging software is supplied with the camera to capture the images. The monolayer flakes had to be located using the number of intensity counts as a guide in identifying these types of flakes. As finding a monolayer flake over the whole sample can be time consuming, it is observed that by placing the laser spot on a flake with time can eventually thin it down to a few layer/monolayers as shown by the increase in PL intensity counts from the spectra extracted using MATLAB software. This process is similar to the thermal ablation process used in medicine to destroy tumours or abnormal tissue, and is a simple, efficient, and non-destructive way to control the thickness of MoS_2.[234] This burning effect on the flakes can produce flakes at 21 cm^{-1} MoS_2 peak separation (2-3 layers thickness).

The focus of the research on MoS_2 now becomes locating the distribution of trion-hotspots and their dynamics with the applied potential in an electrochemical environment. Based on previous work, it is known that excitons and trions exhibit distinct carrier dynamic behavior on ML MoS_2, characterized by different formation, dissociation times and decay processes.[70, 83, 235] The different formation and dissociation rates can influence the efficiency of light emission or PL, carrier transport, and other related phenomena.[235] Excitons exhibit a longer nonradiative decay lifetime of several tens of picoseconds and trions have a much shorter lifetime of only a few picoseconds, due to electron transfer.[70] A trion is formed when free electrons combine with the photogenerated excitons to create charged excitons (trions). Ultrafast study reveals that, photogenerated free carriers form excitons with a time scale ~500 fs and eventually turn into trions within ~1.2 ps.[235] Trions have been found to enhance the photocatalytic hydrogen evolution (PHE) efficiency in ReS_2 with monolayer-like structure.[60] Figure 6.18 shows the PL intensity of excitons and trions in an electrochemically exfoliated heterogeneous flake of MoS_2 under different applied voltages. It displays areas of intense PL signals as well as dark areas of weak signals at 0 V and ratios with Raman data. Upon shifting the voltage to +2 V as shown in Figure 6.18c, there are noticeable changes in the photoluminescence (PL) intensity as the counts are observed to increase with an increase in voltage as trions are formed. This should be expected as excitons can dissociate into free carriers and undergo recombination, thus dissociating faster than trions. It is also known that trions have a slower dissociation timescale compared to excitons.[235] Trions are a type of bound state where an exciton is coupled with an additional charge carrier (electron or hole). This interaction can lead to a redshift in the PL emission, and the intensity increase can be significant.[235] Finally, The thickness of material (MoS_2), and the presence of defects can influence the relative intensity of trions and excitons.[70]

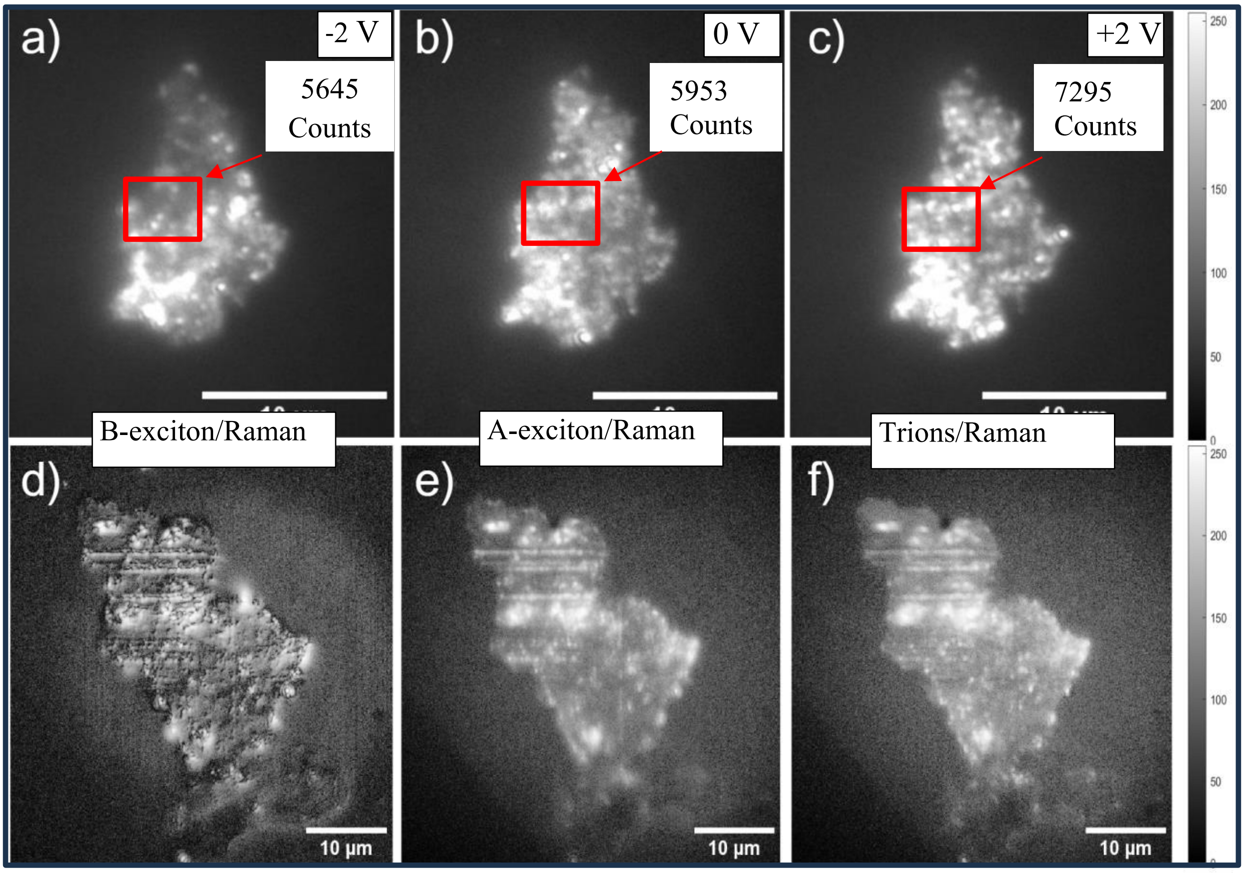

Figure 6.18: Electrochemically exfoliated different MoS_2 flake with heterogeneous structures including defects and combinations of single and few layers. PL emission is also highly heterogeneous: the bright areas show strong PL emission in 0.01M NaCl solution which depend on the applied voltage to the substrate: (a) applied voltage of -2V where the marked area shows weak PL, (b) at 0V the distribution of PL is stronger, (c) at +2V the PL increases further. These show voltage dependent intensity with high spatial heterogeneity, (d) the ratio of B-exciton band (610 m) to Raman ($A^1_g + E^1_{2g}$) band magnitude, (e) the ratio of A-exciton (650 nm) to Raman band magnitude and (f) ratio of the trion (680 nm) to Raman band magnitude.

Figures 6.18 (d-f) illustrate the ratio of PL from B-exciton, A-exciton, and trions with the corresponding total Raman signal from the A^1_g and E^1_{2g} peaks appearing between 400 and 500 cm^{-1}. The PL signals from MoS_2 are due to direct bandgap formation in few-layer MoS_2 (FL-MoS_2), which is absent in multilayer MoS_2. Typically, Raman signals are stronger from multilayer MoS_2, while PL signals are stronger from FL-MoS_2.[221,236] Therefore, the ratio can be used to map the FL-MoS_2 regions where a higher ratio signifies fewer layers. The ratio was calculated using a MATLAB coded script, which sums the PL intensity across all spectral bands for each pixel in the PL image. Similarly, the Raman signal is summed across the selected band range, and the script then computes the PL/Raman intensity ratio using median normalization. It is evident from Figures 6.18 (d-f) that an electrochemically exfoliated flake exhibits significant inhomogeneity due to its intrinsic structure. It should be mentioned that due to the poorer spectral resolution from the interferometer, total Raman signals from the A^1_g and E^1_{2g} peaks have been taken into consideration. Figure 6.19b shows the comparison of Raman spectra from the interferometer and the monochromator.

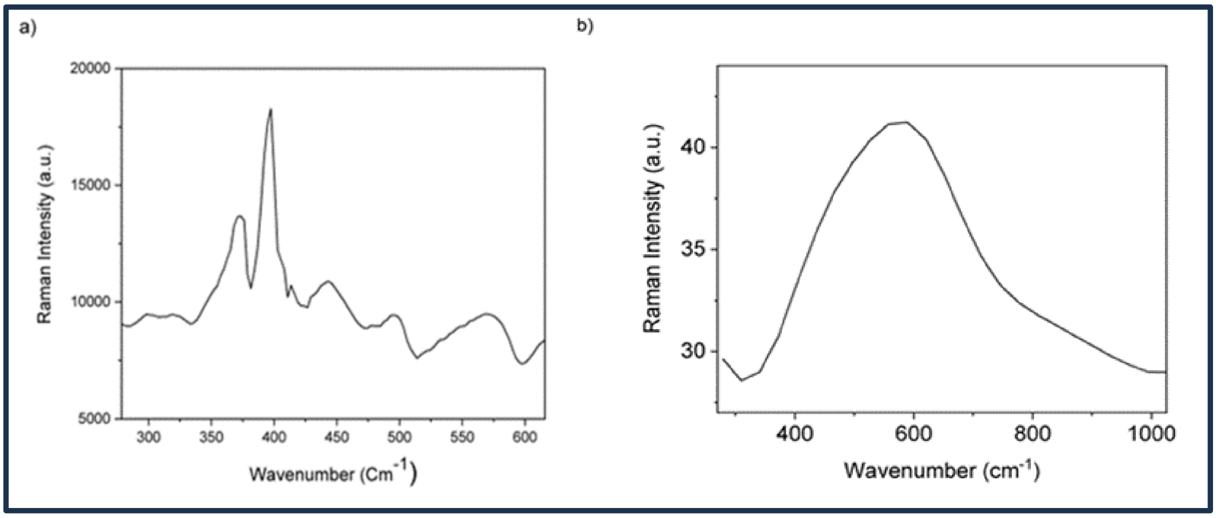

Figure 6.19: a) Typical Raman Spectra of MoS_2 using a monochromator with 1200 lines/mm grating, source Horiba Plc b) Raman spectra of MoS_2 extracted from a hyperspectral image using MATLAB software. The spectral resolution is 200 cm^{-1} (50 µm) which makes the A^1_g and the E^1_{2g} peaks hard to separate and quite indistinguishable. The total Raman signal intensities from the A^1_g and E^1_{2g} peaks was considered to prepare Figure 6.18 d-f.

The average PL intensity was measured across different regions of the flake, i.e. the edge and basal planes in 0.01M NaCl electrolyte solution, and the plot in Figure 6.20 displays the variation in intensity.

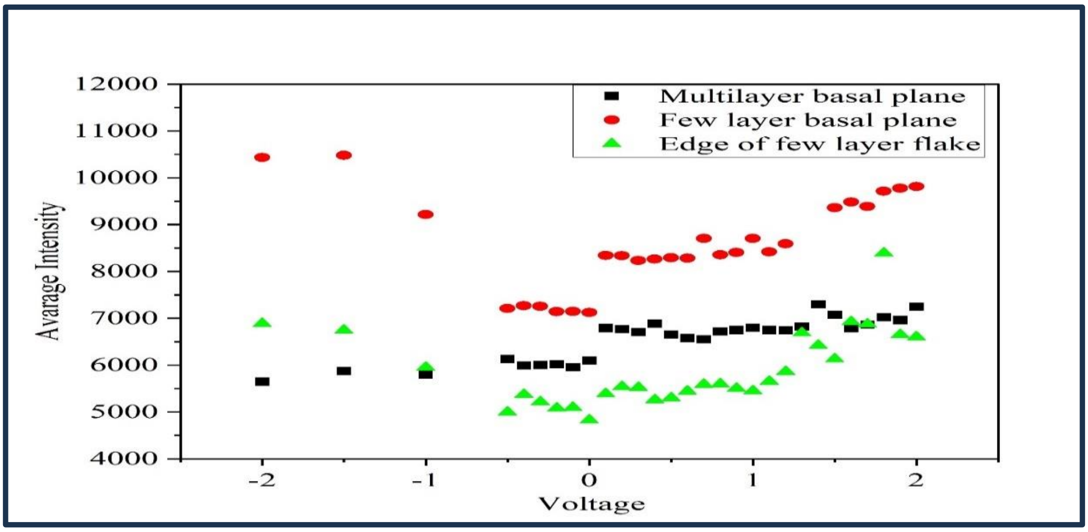

Figure 6.20: Plot of the average PL intensity across different regions of the MoS_2 flake. The few layer basal plane is shown to display the highest intensity PL signal on average. PL emission is also highly heterogeneous as the edge displays intensity signals between the few layer and multilayer basal planes with increasing voltage.

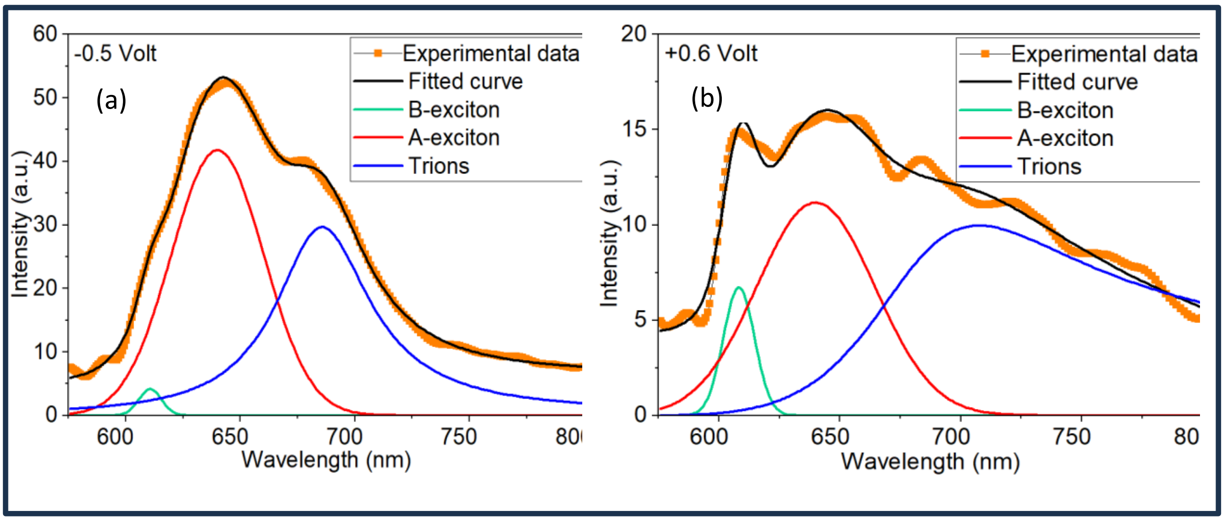

Figure 6.21: Plots extracted from the same region of the hyperspectral images acquired at (a) -0.5 V and (b) + 0.6 V. The signals were fitted with two symmetric functions (Gaussian function) to account for the B-exciton and A-exciton and an asymmetric function (Fano resonance function) to account for the slowly falling tail.

Figure 6.21 shows the plots of the PL from the marked locations at -0.5 V and +0.6 V, which are fitted with two symmetric Gaussian functions and one asymmetric function to account for the intensity tail on the low energy side. A Fano resonance function has been previously used to fit such asymmetric PL intensity from trions in $MoSe_2$. In this case, the combination of functions fits the spectra at different voltages with high accuracy. Although the spectra strongly depend on the location and circumstance of the scan, it can be seen from Figure 6.21 that the degree of asymmetry changes during the potential sweep from -0.5 V to +0.6 V, which relates to the width of the peak (plot (b) in Figure 6.21). This plot displays the presence of new peaks that are due to the presence of biexciton emission from a bound pair of two excitons (defect bound states), appearing at slightly higher energies than the single exciton peaks.[237, 238] The change in B-exciton (610 nm) intensity is minimal whereas there is strong variation in the A-exciton intensities. The centre of the trion peak exhibits a blue shift for positive potential and a red shift with negative potential. These observations are consistent with previously reported work using solid-state devices such as field-effect transistors where a back-gate voltage is applied.[79, 236, 239, 240]

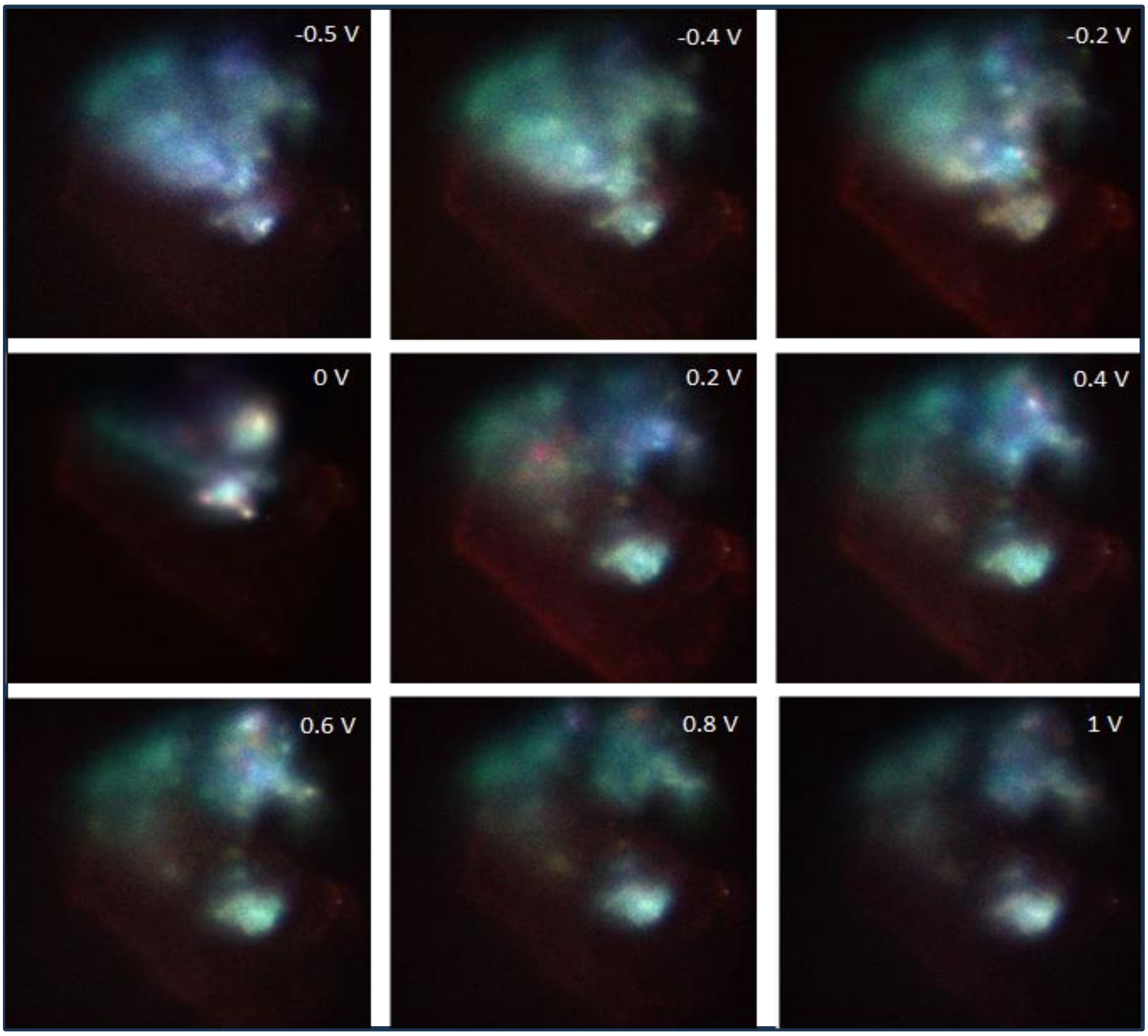

Figure 6.22: False colour representation of the hyperspectral images acquired at different voltages: blue colour corresponds to intensity at 610 nm (B-exciton), green colour corresponding to 650 nm (A-exciton) and red colour corresponding to trions (680 nm).

False colour representation of the hyperspectral images (Figure 6.22), show considerable variation across the MoS_2 flake. It is noted that due to the large size of the HSI data, it is only the three band intensities that are taken into consideration in this representation. As the images are generated using HSI MATLAB code, the bands are adjusted to correspond to specific wavelengths. In this case, the images were created by setting the bands at 610 nm, 650 nm, and 680 nm. Since this is a false-colour representation, the colours do not correspond to their actual wavelengths in the visible spectrum, and they are purely for visualization purposes. Fig. 6.23 displays selected region of MoS_2 flake (a) and the extracted HSI MATLAB plot (b).

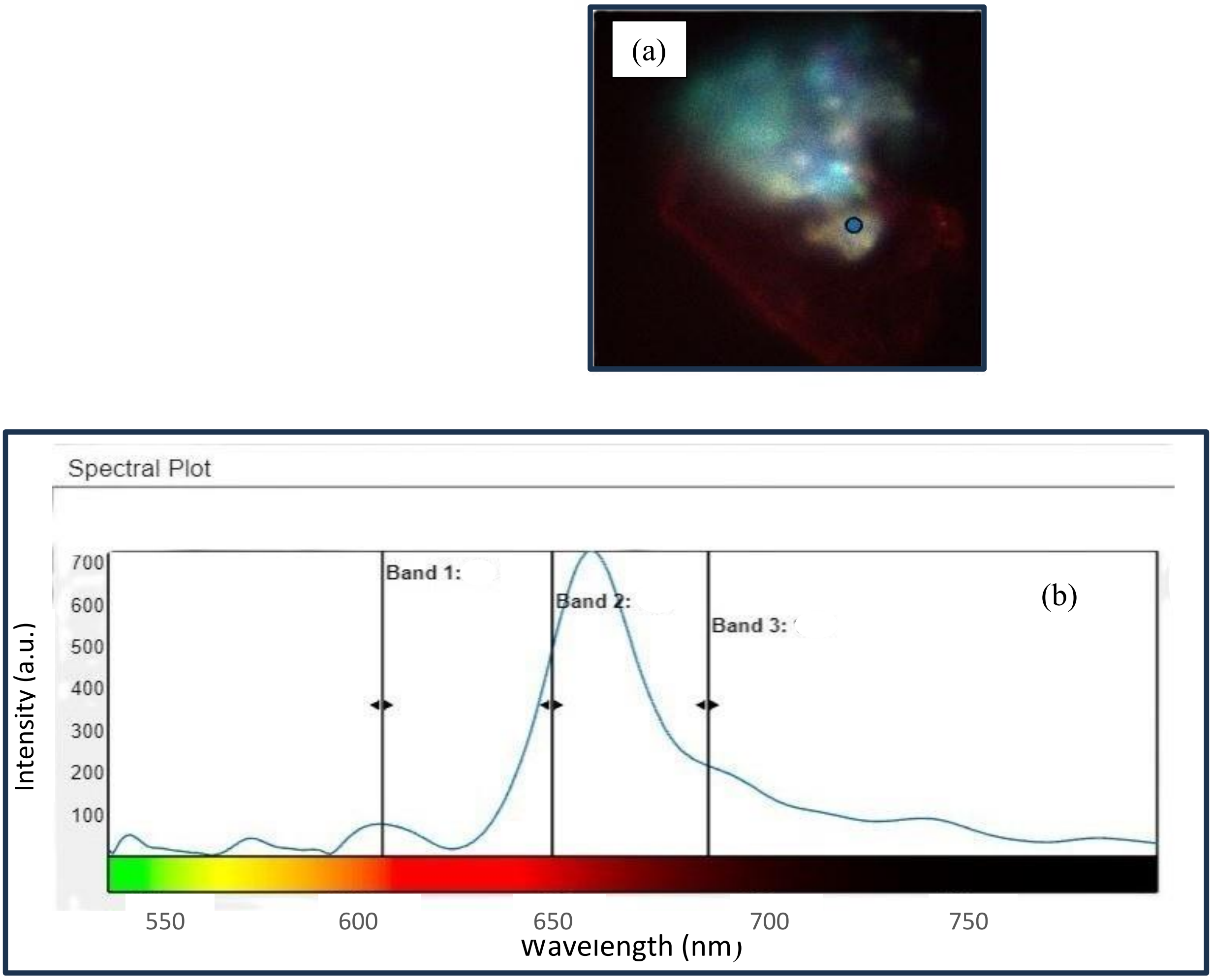

Figure 6.23: (a) Selected region from an image obtained on a FL-MoS_2 flake. (b) Plot of the extracted HSI MATLAB spectrum with the three bands adjusted to correspond to specific wavelengths. In this case, the images were created by setting the bands at 610 nm, 650 nm, and 680 nm.

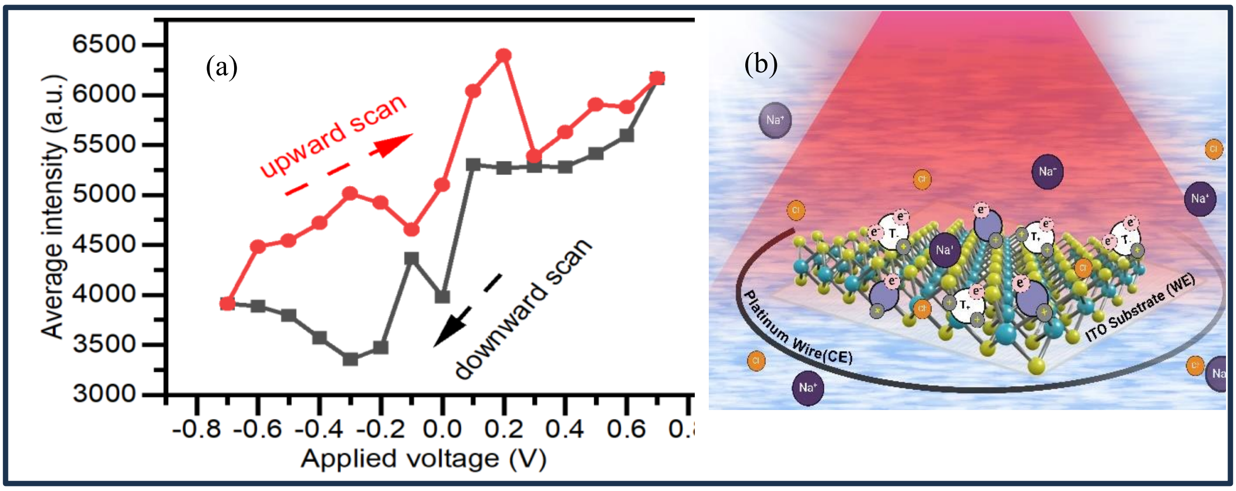

Figure 6.24: **(a)** Plot of intensity from a selected region from the images obtained on a different FL-MoS_2 flake acquired using a bandpass filter (680 ± 5 nm). The scan rate is 5 s/step. (b) A diagram depicting the electrochemical environment of the MoS_2 flake and influence of the electrolyte.

Figure 6.24a shows a PL intensity variation with voltage scan, which is analogous to a current-voltage (CV) curve. It is apparent that the PL intensity strongly depends on several factors, including the electrical layer formed during the scan.[69-71, 241] For example, at -0.3 V, the intensities show maximum difference during the upward and downward scans. This data is quite non-representative as other flakes were measured at the time, but due to instability of the flake, and the etching away during measurement, the exact trend was hard to determine. It is postulated from previous work that the electrolyte gating originating from the buildup of ions across the nanometer-scale electrochemical double layer (ECDL) may also result in the formation of excitons and trions at ML-MoS2 catalyst.[71] Figure 6.25 depicts the images obtained for both (a) the upward and (b) the downward scans in the range -0.7 V to +0.7 V.

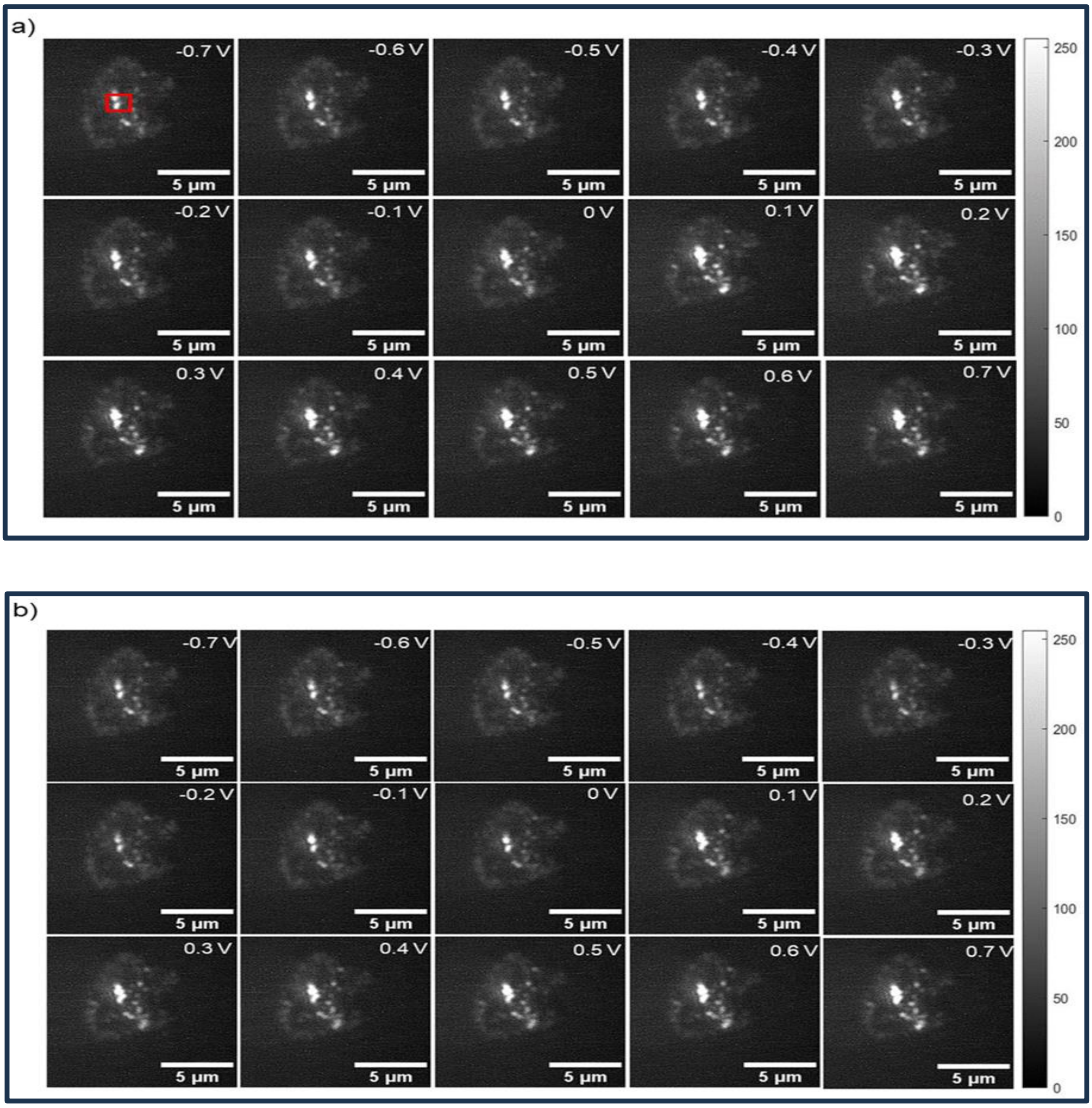

Figure 6.25: a) Upward voltage scan from -0.7 V to + 0.7 V b) Downward voltage scan from +0.7 V to -0.7 V

It is quite apparent from observations of both the forward and reverse scans that the PL intensity is increasing from the negative to the positive potentials in agreement with Figs. 6.18. and 6.20 that both show a higher concentration of trions observed at more positive potentials. The hydrogen evolution reaction (HER) is activated by these applied bias potentials. It is known from literature that the electrical layer formed during the voltage scan plays a key role in determining the Tafel plot and the overpotential in the HER using linear sweep voltammetry (LSV).[64, 70] However, as LSV could not be performed in this case due to insufficient monolayer yield of MoS_2, no such measurements could be made as no Tafel plot could be constructed in order for the Tafel slope to be calculated from the LSV data for HER. Therefore, this is something that could be done in future work when a sufficient monolayer yield of MoS_2 is obtained to produce an LSV curve.

CHAPTER−7

Stability of $MAPbBr_3$ perovskite in water−An investigation using Hyperspectral Imaging (HSI)

7.1. – Introduction

The objectives of the perovskite degradation study are to investigate and evaluate the stability of $MAPbBr_3$ (Methylammonium lead bromide) perovskite under various conditions. This will involve focusing on the mechanisms for degradation under different conditions for the $MAPbBr_3$ compound using various techniques and drawing a conclusion for this compound in terms of the mechanism and pathways involved in the degradation process The different conditions will consist of set relative humidity (RH) environments with PL measurements being made on the nanoplatelets (NPL) using a fluorescence microscope and a PL spectrometer that will determine if any degradation takes place in these environments. Induced water environments will also be investigated using *in-situ* Hyperspectral Imaging (HSI) techniques to image the NPL at varied timeframes. Water exposure is found to cause the onset of degradation, and this study will be extended to an investigation into different pH environments to determine if an alkaline or an acidic environment is required to retard and suppress the degradation process. From the results of this study, it is proposed that the mechanism of degradation can be made more transparent and understood and be of guidance and support in future studies of such compounds. It is concluded from this work that electrochemical-Raman techniques cannot be used to monitor the degradation process spectroscopically as well as microscopically.

7.2 – Perovskite synthesis

The synthesis of n>4 $MAPbBr_3$ nanosheets was carried out by the C. Klinke group at the University of Rostock in Germany. The standard synthesis is as follows: A three neck 50 mL flask was used with a condenser, septum and thermocouple. 6 mL of diphenyl ether (38.1 mmol), 0.08 mL of DDA (dodecylamine) (0.24 mmol) and 0.2 mL (0.44 mmol) of TOP (Tri-octyl phosphine) were heated to 80 °C in a nitrogen atmosphere, then vacuum was applied to dry the solution. After 1 hr the reaction apparatus was filled with nitrogen again, the temperature was increased at 120 °C and 0.8 mL of as prepared $PbBr_2$ nanosheets in toluene were added. The reaction temperature was reduced to 35 °C after all of the $PbBr_2$ dissolved. The synthesis was started with the injection of 0.06 mL of a 300 mg methylammonium bromide (2.68 mmol) in 6 mL dimethylformamide precursor; after the injection the temperature was increased to 120 °C. After 10 minutes the heat source was removed and the solution was left to cool down below 60 °C. Afterwards, it was centrifuged at 4000 rpm for 3 minutes. The particles were then washed two times in toluene before the product was finally suspended in toluene again and put into a freezer for storage.[128] The toluene dispersion is then sent to Swansea University Chemistry Dept for research purposes.

7.3 – *In-situ* Electrochemical-Raman

The setup for the in-situ electrochemical-Raman measurements involved the use of the 3-electrode PEEK electrochemical cell setup described in chapter 6. The measurements are made using the Raman Class 3B laser system interfaced with the Autolab potentiostat PGSTAT204 using .NET functionality triggering between the Wire and Nova software. The Class 3B laser using 488 nm excitation wavelength with a 2400-line mm^{-1} grating is used to produce spectra of the perovskite sample using an Olympus 40x 0.5NA objective and Wire version 5.1 software. Static scans are used to measure PL and exposure time, and laser power settings are optimised to produce a strong signal peak with low background noise.

7.4 – CV and Electrochemical-Raman PL measurements

The perovskite sample is applied to the ITO substrate by drop-casting a volume of 300 microlitres, this is then dried.at room temperature for 20-30 mins. A CV curve is produced using the Autolab potentiostat attached to the three-electrodes of the cell over a potential range of -0.1 to 1.0 V and is shown in Figure 7.1. Perovskites like $MAPbBr_3$ can undergo reversible redox reactions, meaning they can gain or lose electrons under certain electrochemical conditions. However, this was previously performed with $MAPbBr_3$ acting as an electrode (anode) in battery form hosting high Li-ion concentrations during the charging process.[242] The sample used for this research work was dispersed in toluene as nanoplatelets therefore, it was not known what to expect for the electrochemical response and CV curve produced in this case, as it was being carried out on a trial-and-error basis.

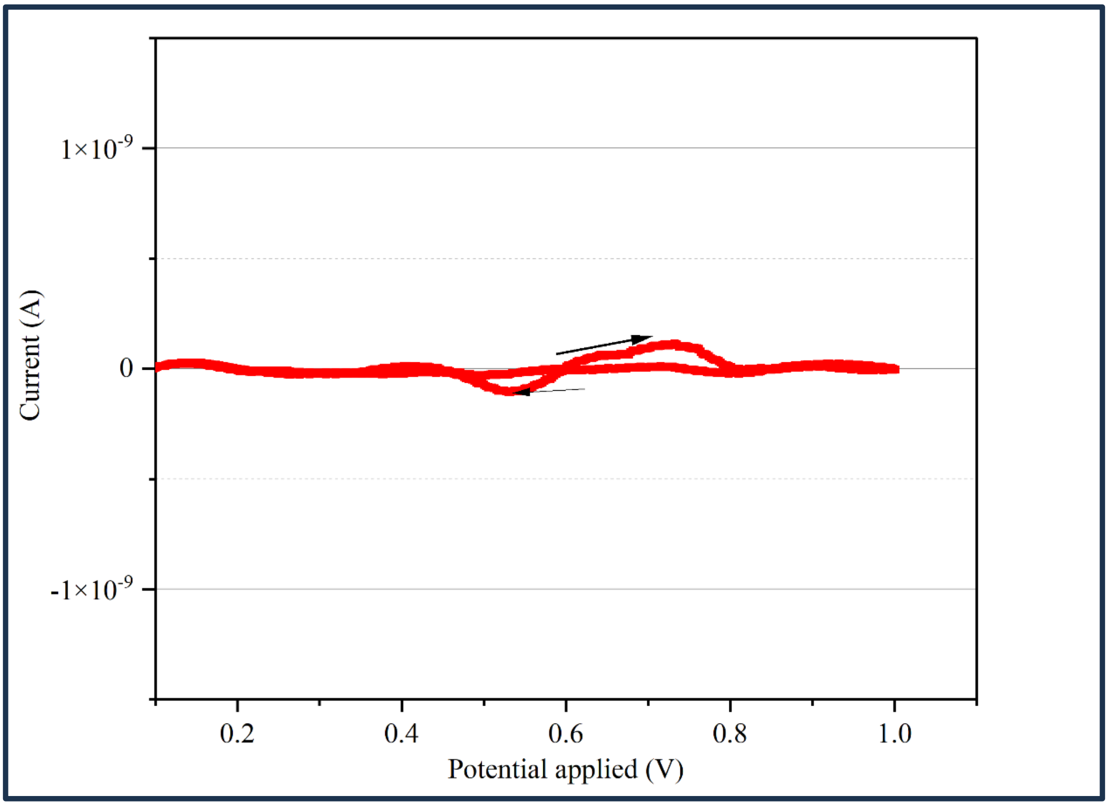

Figure 7.1: CV curve for $MAPbBr_3$ perovskite. Electrolyte: 0.1 M $TBAPF_6$ (Tetra-butyl ammonium hexafluorophosphate) in toluene. Scan rate 10 mv s^{-1}.

From the CV curve it can be inferred that it has not been successful in terms of redox activity. This can be explained by the lack of ions in the non-aqueous electrolyte as the 0.1 M $TBAPF_6$ is only partially soluble in toluene, and so very little electron transport is taking place due to this partial solubility. This gives an almost ohmic curve response and very weak signal in the nA range due to most of the signal coming from the ITO substrate and is therefore not reversible in this case. No other solvent system could be found other than toluene that did not dissolve and degrade the perovskite structure.

A Raman spectrum was then performed on the $MAPbBr_3$ perovskite at 457 nm excitation wavelength in the range 100 - 1500 cm^{-1} to determine if Raman bands are present. It was discovered that no Raman bands were observed and therefore subsequent measurements and degradation studies could only be made on the PL response from the perovskite as a strong PL signal is obtained ~ 525 nm at this excitation as shown in Figure 7.2. From literature on the $MAPbBr_3$ series, the main PL peak for all of the samples is centred between 515 and 525 nm when 457 nm excitation wavelength is used. This is at significantly lower energy than the exitonic absorption peaks arising from quantum confinement of the nanosheets.[128] UV-Vis spectroscopy is a versatile technique for characterizing perovskite materials, offering valuable information about their optical, electronic, and structural properties, which is essential for optimizing their performance in various applications. However, UV-Vis can only track changes in the absorption spectrum and not the PL signal over time and therefore cannot be used to study the degradation process.

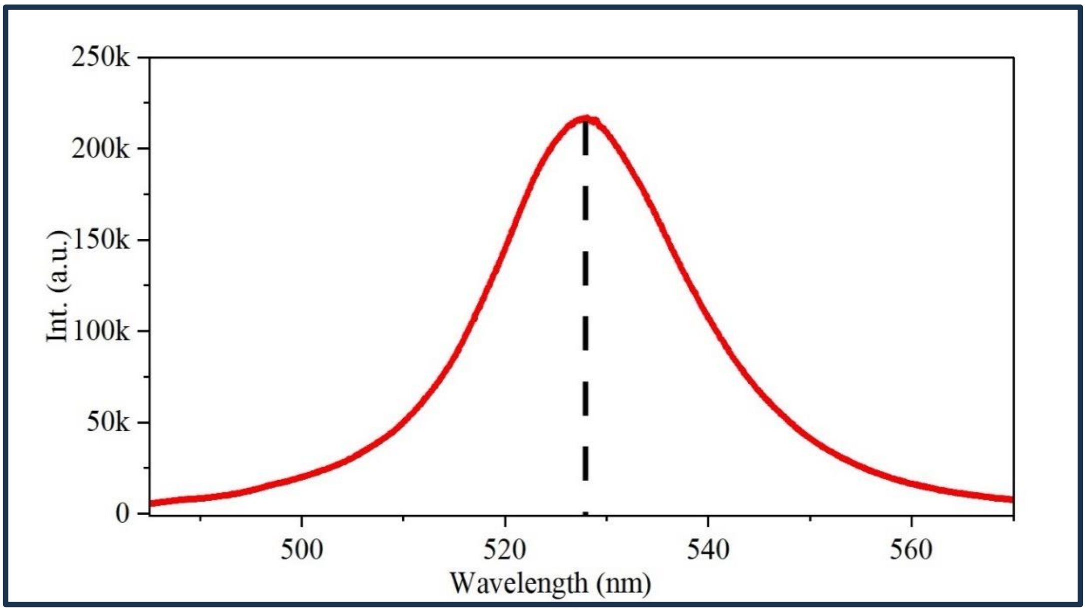

Figure 7.2: PL plot for $MAPbBr_3$ perovskite dispersed in toluene. Olympus 40x 0.5NA Objective, 1200-line mm^{-1} 457 nm Raman excitation used. (Renishaw plc).

As the sample is shown to be very emissive, the measurements were then carried out using HSI and fluorescence spectroscopy methods to utilise this response across the perovskite sample surface. To help improve our understanding of the behaviour of the perovskite structure, an in-situ degradation study was conducted on the $MAPbBr_3$ perovskite using fluorescence microscopy and HSI techniques to identify the spatial variations in degradation rates and to investigate the changes in the photoluminescence spectra during the degradation process. In situ techniques such as fluorescence microscopy and PL spectroscopy are powerful tools for this purpose, as they allow for structural, compositional, morphological, and optoelectronic changes to be tracked in real-time, and follow a single film or device over the course of the degradation process. The degradation of perovskites is a complex and multi-faceted process and involves changes in the crystal structure, composition, film morphology, and optoelectronic properties.[128]

7.5 – Moisture-induced degradation study using photoluminescence (PL) spectroscopy imaging techniques

A perovskite degradation study was undertaken in several different atmospheric environments as follows: 1: 36% moisture in saturated NaCl salt solution in a desiccator, 2: 77% moisture in saturated $MgCl_2$ salt solution in a desiccator, and 3: An ambient air non-controllable environment as a reference. Using a combination of a fluorescence microscope for imaging purposes and a fluorescence spectrometer for PL measurements, in-situ comparisons could then be drawn for measurements made every 2 hrs for up to 6 hrs, thus making 3 measurements on day 1 and then 1 measurement per day for up to 10 days on the six samples prepared.

7.5.1 – In-situ moisture-induced perovskite degradation study

100 microlitres of a 0.1x diluted $MAPbBr_3$ perovskite sample is deposited onto an FTO (fluorine-doped tin oxide) substrate and then placed on a hotplate to evaporate off the toluene solvent. This is repeated six more times, so as each experiment is carried out in duplicate for each environment. The Fluorescence Microscope and Fluorescence Spectrometer used to make the PL measurements are shown and described in Chapter 5, Fig 5.3 (a and b). The spectrometer averages the spectra taken from the sample giving a broad PL peak.

With respect to the imaging of the perovskite sample, it was observed that the sample was very emissive producing needle-like, and dot shaped nanoplatelets (NPLs). The PL is observed to show no decrease in intensity for up to the 6 hours and 10 days measurements at all for both moisture environments in air at ambient temperature. The samples were stored in the dark and proved to be quite resistant to the humidity conditions that were employed, and this is a testament of the capacity of the $MAPbBr_3$ crystalline structure to withstand humidity. This experiment demonstrated that moisture-induced atmospheres are not enough to enable the onset of degradation of the perovskite crystal lattice that is well protected with the hydrophobic long chain methylammonium ligand (MA) and bromide co-ligand that enhance the stability (Figs. 3.1 & 3.2).[243] To compare the intensities of the sample, images of the 6 hrs and 10 days samples at 36% and 77% RH at 160x magnification are shown to confirm the uniformity of intensity in

Figures 7.3 (a and b) and 7.4 (a and b) respectively. The measurements were not made in-situ as the samples had to be removed from the desiccator and transferred to the microscope stage at each time interval. Different points of the sample were used for each measurement immediately after transfer to the stage.

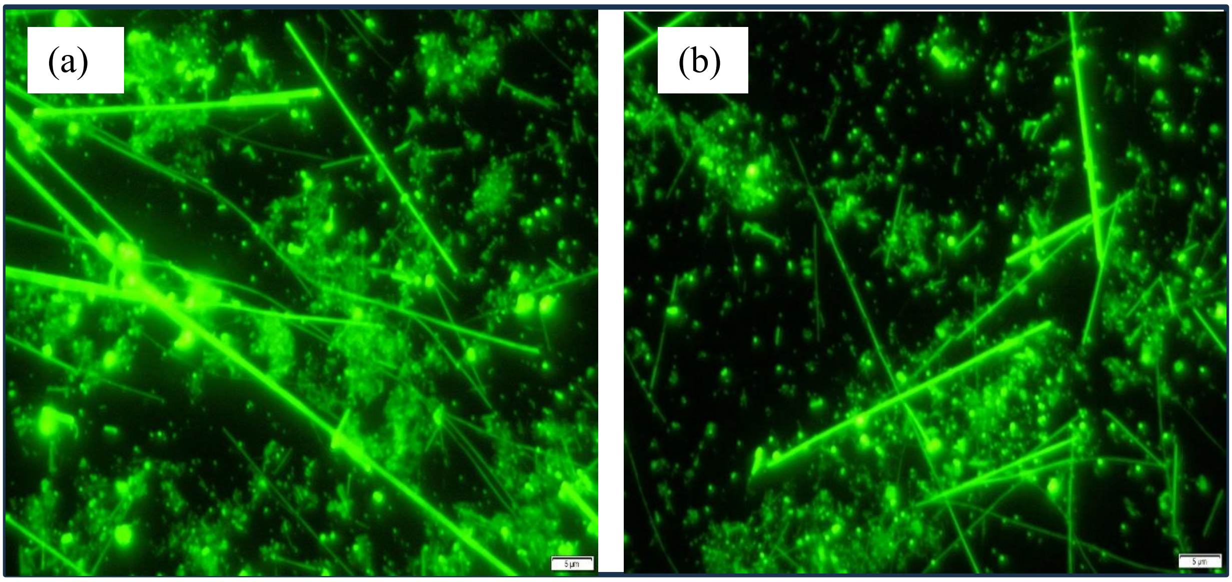

Figure 7.3: (a): Image of $MAPbBr_3$ sample taken at 6 hrs at 36% RH and 160x magnification. (b): Image of $MAPbBr_3$ sample taken at 10 days at 36% RH and 160x magnification. (Scale: 5 µm).

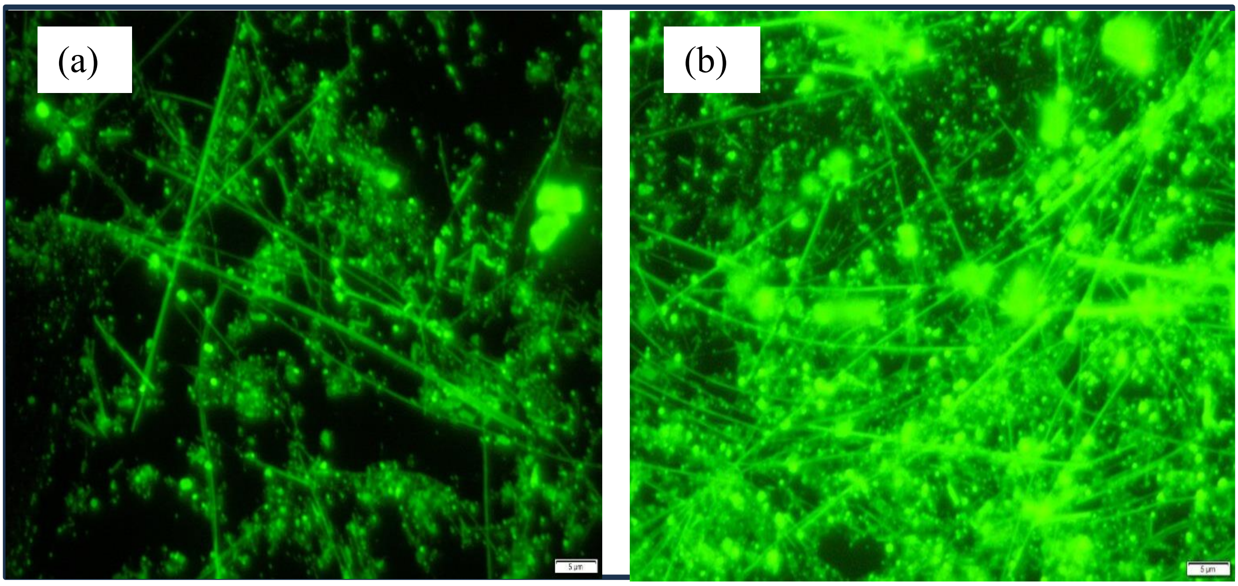

Figure 7.4: (a): Image of $MAPbBr_3$ sample taken at 6 hrs at 77% RH and 160x magnification. (b):Image of $MAPbBr_3$ sample taken at 10 days at 77% RH and 160x magnification. (Scale: 5 µm).

The images clearly show that there is no decrease in the PL intensity from these measurements, and it is observed to have increased for the 10 days measurement at 77% RH. PL intensity will usually only increase due to the contributions of nonradiative trapping and radiative exciton recombination. This is when moisture can interact with the perovskite, potentially filling or passivating surface trap states, which would then reduce the non-radiative recombination of excited electrons and holes, leading to an increase in PL intensity.[244] This may have happened over the 10-day period in Fig. 7.4 (b). This further confirms that the PL intensity has not decreased, and that degradation of the crystal lattice has not taken place. There are also no observable colour changes taking place over the course of the measurement in comparison to $MAPbI_3$ which undergoes a visually apparent colour change from black to yellow over a period of days due to the formation of PbI_2 after complete decomposition of the lattice structure.[126] The PL plots obtained from the fluorescence spectrometer would seem to support this as the PL emission peak at ~ 525 nm would appear to increase on day 10 at 36% RH as shown by the stacked plot in Figure 7.5. The straight line through the plots shows there is no change in peak position over time, further indicating no change in the crystal lattice over the time period measured. Figure 7.5 further highlights this at 77% RH, the PL intensity does not decrease over the same 10 days measurement period, and again no shift in the peak position at ~ 525 nm. The fluctuation in PL response could be due to the variation in light intensity from the instrument. It was stabilized each day for 30 mins before measurements with the same process used each day. As the data is a bit inconclusive, future work could involve studying the same sample point for each measurement, and for longer than a 10-day period until the PL signal disappears.

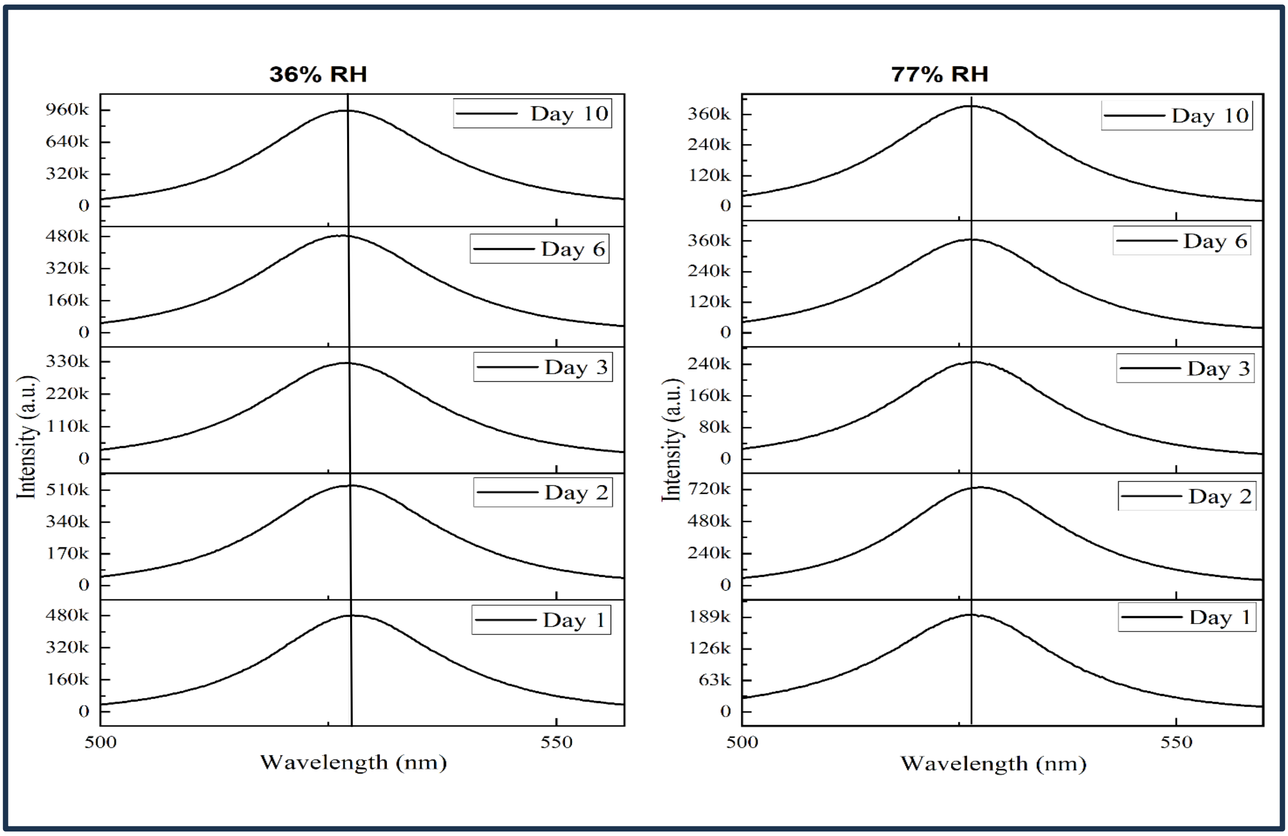

Figure 7.5: PL plots over the 10-day measurement period at 36% and 77% RH.

7.5.2 – In-situ water-induced degradation study using fluorescence microscopic imaging techniques

Water-induced degradation measurements are carried out using the Olympus fluorescence microscope as previously and the same settings used. The objective lens used in this case was the 50x. The software was setup to perform a time series measurement over 40 mins duration and images taken at 5-minute intervals. The sample is prepared by drop-casting 100 microlitres of the perovskite on to the surface of an FTO substrate with a micropipette, this is then left to dry at room temperature. The sample is then focused with the 50x objective lens, and an image taken before applying the water, this is the reference image. After this the water is applied by micro-pipetting 100 microlitres onto a coverslip and then placing the coverslip onto the sample to secure it in place during the measurement. The same location is imaged at each interval. The images are shown in Figures 7.6 to 7.9.

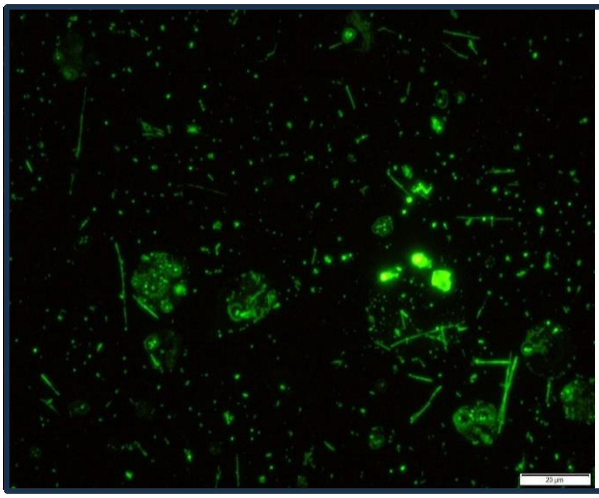

Figure 7.6: 1st image-Ref: No water.

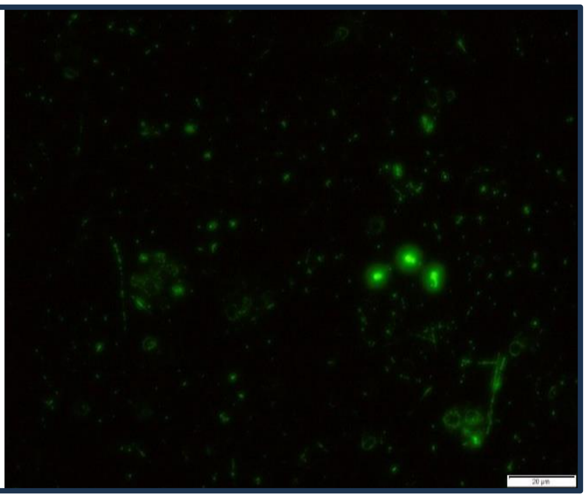

Figure 7.7: 2nd image after 5 mins water.

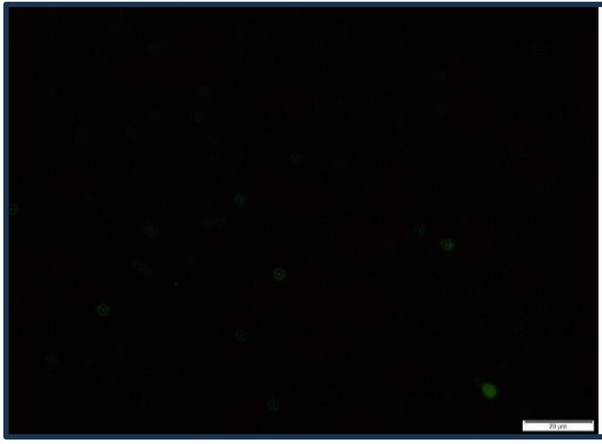

Figure 7.8: 3rd image after 10 mins water.

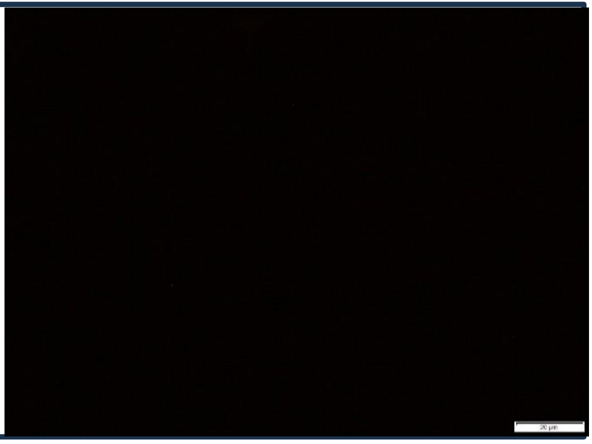

Figure 7.9: 4th image after 15 mins water.

(Scale: 50 mm).

As can be observed from Figures 7.6 to 7.9, complete degradation of the perovskite occurs after 15 mins water treatment, this is postulated as being due to the water molecule infiltrating the perovskite layer structure as they adsorb onto the crystallites through the gaps between grains. Mobile ions in the perovskite structure can migrate, leading to changes in the material's properties and potentially affecting PL.[127] This process occurred after just 15 mins and the 40 mins duration with images taken every 5 mins was deemed too long. The final image in Figure 7.10 highlights a colour change has taken place after 10 mins water application. This orange-brown colour could possibly indicate that the perovskite lattice has decomposed to lead bromide similar to the triiodide structure which undergoes decomposition to lead iodide under moisture ingress, forming a yellow colour.[7, 126, 127]

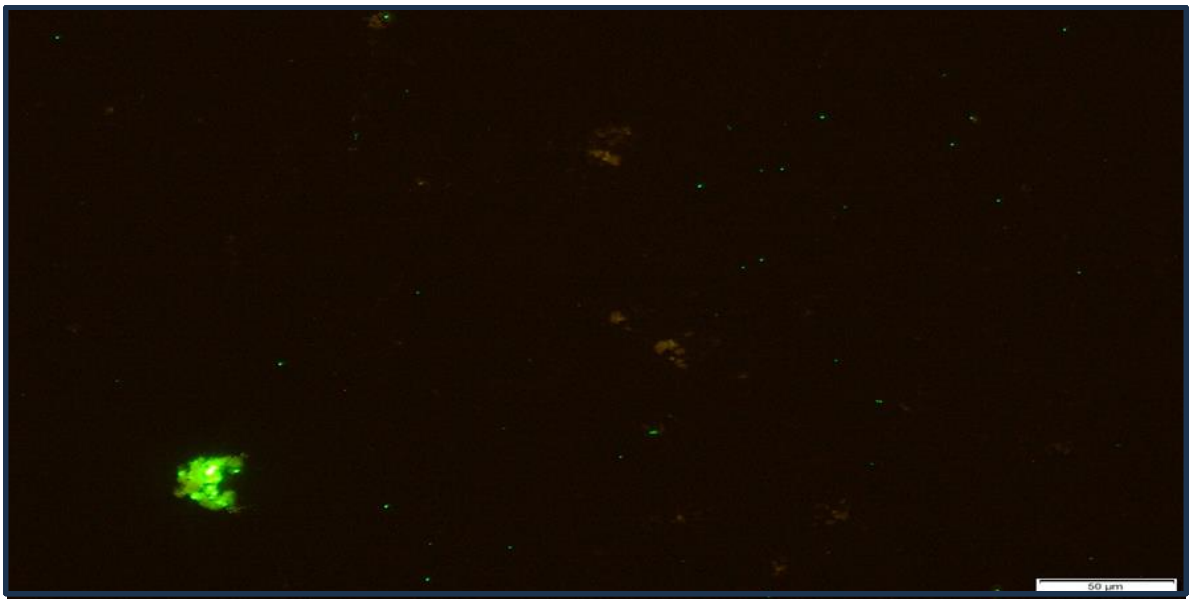

Figure 7.10: Image after 10 mins water treatment, taken at 20x magnification. (Scale: 60 µm).

It can be observed from the images that the degradation process is not fully captured and so a further measurement was carried out over 15 mins duration at 30 second intervals at 20x magnification.This time the measurement was carried out manually with a stopwatch to enable better control and improved focus between images. The images are shown in Figs 7.11 to 7.14.

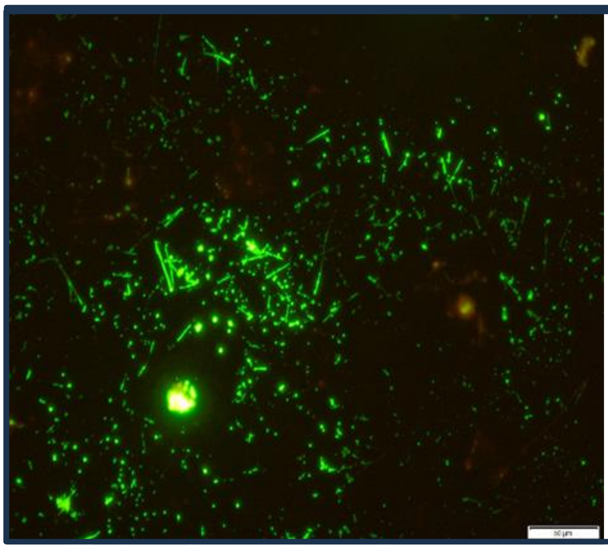

Figure 7.11: 1st image-Ref: No water.

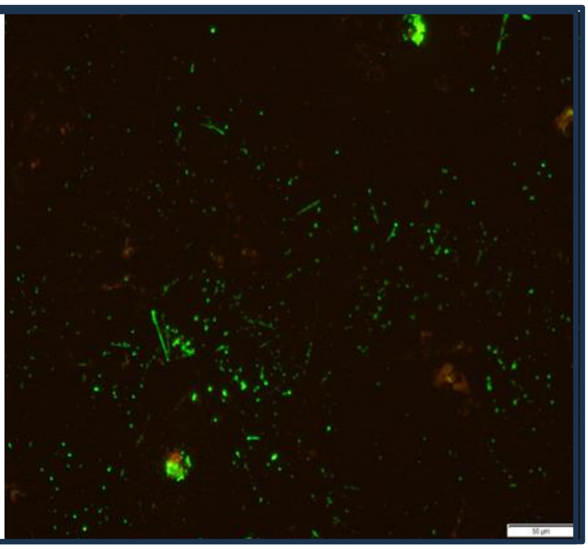

Figure 7.12: 10th image after 5 mins water.

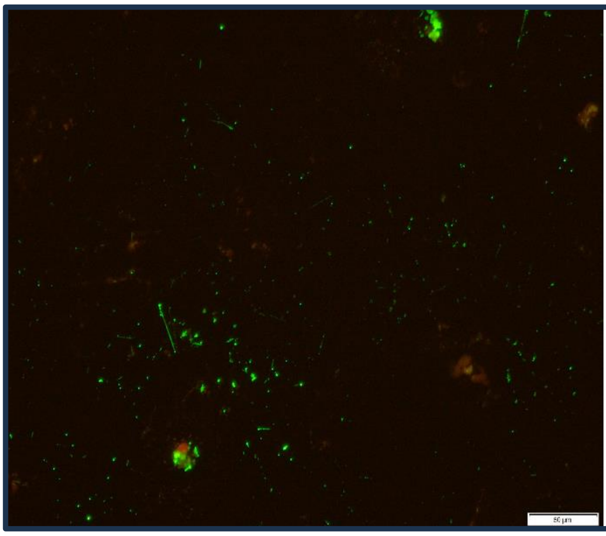

Figure 7.13: 20th image after 10 mins water.

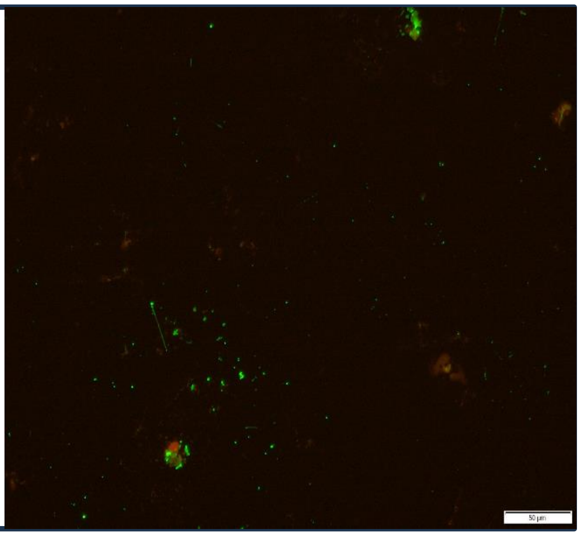

Figure 7.14: 30th image after 15 mins water.

(Scale: 50 mm)

The PL emission before and after water treatment was investigated for the perovskite sample over time and was calculated using the sum of intensities for grayscale images that are converted from false colour images produced using online software. Figure 7.15 displays the photoluminescence emission of the perovskite decreasing exponentially with time.

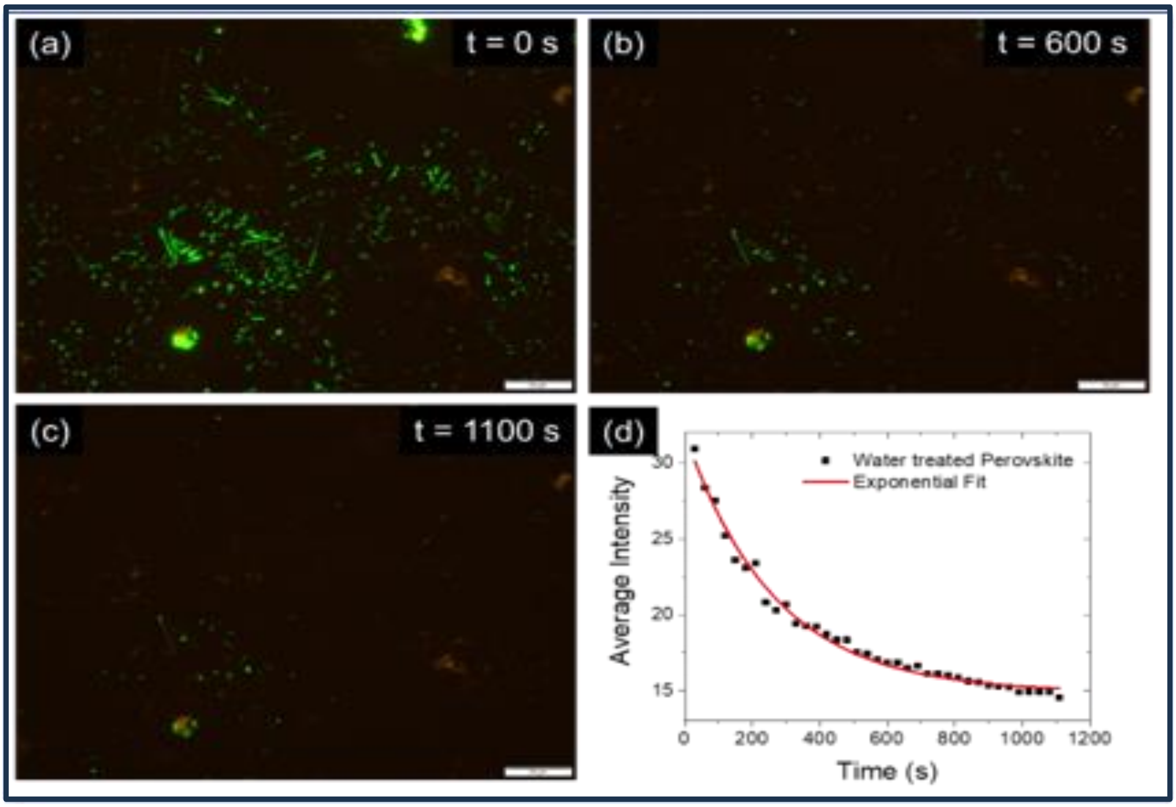

Figure 7.15: Images showing photoluminescence emission of perovskite (a) before water treatment and after (b) 600 s, (c) 1100 s of water treatment, respectively. (d) Variation of PL emission intensity of perovskite with time after water treatment. (Scale bars correspond to 50 mm)

From this further study it is again quite apparent that the needle and flake featured NPLs on the surface of the perovskite material are observed to gradually disappear over the course of 15 minutes. This suggests an overall homogeneous degradation could be taking place over the surface of the sample however, this does not indicate where the onset of degradation occurs. A video link of the degradation process was designed using ImageJ software to aid in determining the nature of the degradation process, and is available on Youtube at: https://youtu.be/NJomUZIVtKM. When viewed, the video of the image sequence clearly shows that degradation appears to initially take place externally from the outside of the needle-like structured NPL to the inside of the needle, the internal structure as the needles are observed to be getting thinner in appearance. This could suggest that degradation is starting at the edges and outer planes.The needles do appear to maintain their length but their width is decreasing over the measured timeframe indicating that the water is attacking the structure along a certain axial plane. This strongly suggests that the initial step of the decomposition process is hydration of the perovskite film on the surface as the water molecules permeate and percolate through the grain boundaries. The observed loss of PL intensity in $MAPbBr_3$ when added to water is likely a result of a combination of factors, including structural changes, surface modifications, and the introduction of nonradiative recombination centres, as defects or impurities are introduced by the interaction with water.[7, 126, 130] Future work should focus on understanding the specific degradation pathways, the role of water in these processes, and developing strategies to mitigate or prevent degradation. This could involve studying the effects of different water environments and the impact of other environmental factors like water and light combined.

7.6 – Water-induced degradation study using HSI techniques

HSI techniques were used to determine the PL intensity of the perovskite surface using LED 470 nm wavelength excitation. These measurements are carried out before and after water treatment and with and without light, to determine the effects of water and light on the degradation process. The experimental setup is shown in Chapter 5, Figure 5.9.

The sample preparation consisted of drop-casting 50 microlitres of a 0.1 x diluted perovskite sample dispersed in toluene using a micropipette onto a 0.17 mm thick coverslip and leaving to dry. Once dried the coverslip is then fixed onto the microscope stage and the sample is then focused with the lens, a reference image in air is acquired before administering 100 microlitres of deionised water on top of the perovskite sample. The same location is imaged at each interval during the water induced degradation as measurements are made.

Hyperspectral photoluminescence measurements were also made using LED light in between measurements to determine if the combination of light and water affected the degradation rate compared to just water alone. A schematic for the sample preparation is shown in Figure 7.16.

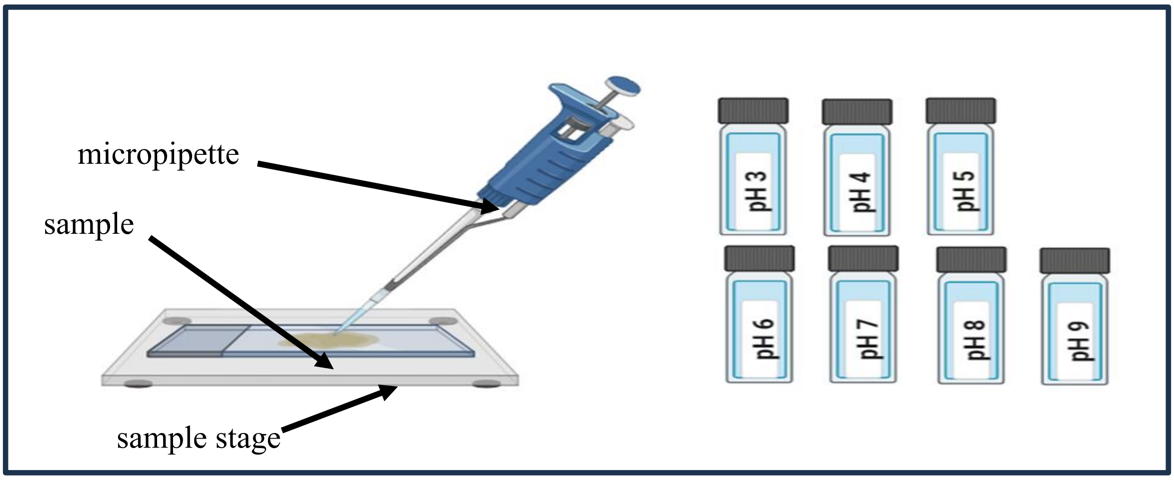

Figure 7.16: PL degradation measurement scheme using aqueous solutions of pH 3-9. pH 7 is used for this measurement.

The first measurements involved the application of light and the sample was focused on an NPL that displayed needle-like and dot shaped species. The water was applied to the sample in this instance and the measurements were taken over timeframes of 40 and 70 mins with no light being applied in between measurements to determine if light had any effect on degradation. 40 and 70 mins timeframes were used to show the effects of light over a longer timeframe. The images are shown for the sample at each timeframe after water treatment without light in Fig.7.17 (a-c).

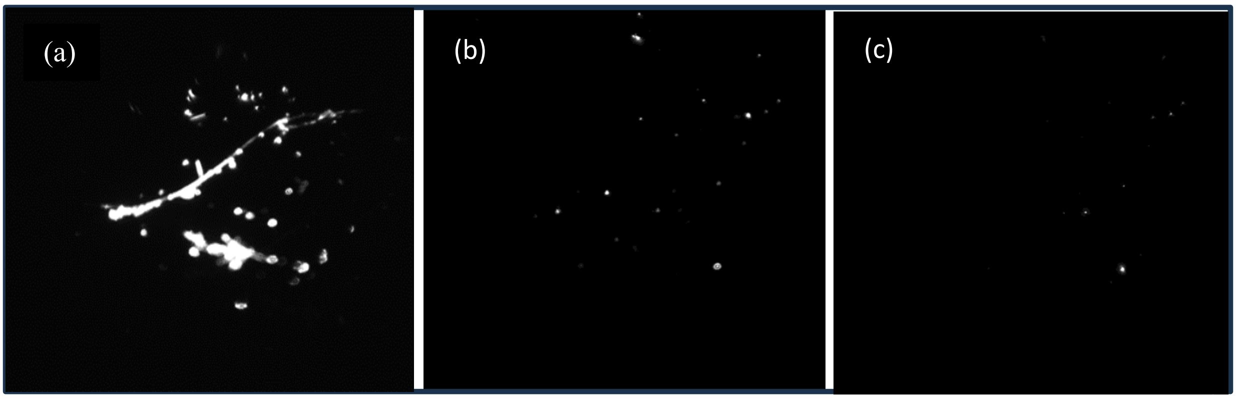

Figure 7.17: (a) Reference image without any water treatment. (b) After 40 mins water treatment and no light applied. (c) After 70 mins water treatment and no light applied. (Scale: 50 µm)

From the images shown, it can be observed that with no light applied, degradation still appears to take place, as the PL intensity has reduced significantly between each timeframe. This informs us that water alone is responsible for degradation to occur.

Following this a measurement with light now applied continuously between each measurement was carried out on a different NPL needle using the same number of images and the first and final images compared. The images are shown in Figure 7.18(a-c).

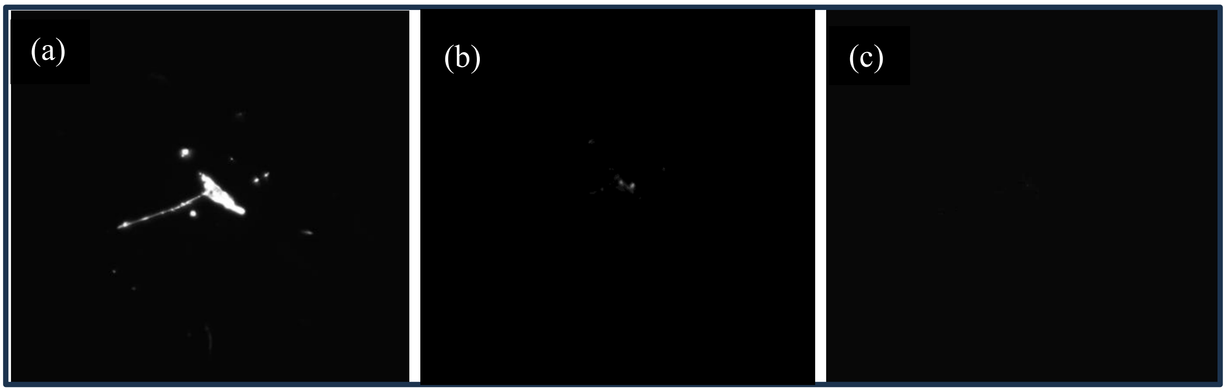

Figure 7.18: (a) Reference image without any water treatment. (b) After 40 mins water treatment and light applied. (c) After 70 mins water treatment and light applied. (Scale: 50 µm)

.

From the images shown, it can be observed that with light now applied, again degradation appears to take place, as the PL intensity is observed to reduce significantly between each time frame, and the needle-like NPL can no longer be observed in the final image. This confirms that the application of light does not appear to play any significant role in the degradation process.

Subjecting the perovskite sample to 40 mins and 70 mins water treatment with and without the application of light showed up very similar reductions in PL intensity as shown in Figs 7.17 and 7.18. Literature does propose that the addition of light can contribute to degradation of the perovskite lattice. This has been variously ascribed to certain processes such as the formation of light activated trap states, photoinduced ion segregation, photoinduced atom/ion migration, and photodecomposition.[71] In addition to this, continuous light illumination can lead to other changes, such as increased lattice strain and the generation of excess charge carriers, which in turn leads to defect generation.[71]

7.7 – Water-induced degradation study using wide-field HSI measurements

Wide-field HSI techniques are used to determine the PL intensity of the perovskite surface using the same LED 470 nm wavelength excitation over a larger area. The same setup is used as for the previous measurements on the degradation process however, this time an Olympus 40x 0.5 NA objective lens is used to cover a larger surface area of the sample that encompasses more flakes and needle-like species to verify the uniformity of the degradation process.

The sample preparation consisted of drop-casting 50 microlitres of a 0.1 x diluted perovskite sample onto a 0.17 mm thick coverslip and leaving to dry. Once dried the coverslip is then fixed onto the microscope stage and the sample then focused with the lens, when focused, 100 microlitres of deionised water is then placed on top of the perovskite sample and the water measurements then made. A reference spectra was taken before applying the water, and the measurements are made periodically every minute up to 75 minutes duration. The images are shown in figures 7.19 to 7.22. The wide-field HSI techniques offer not only multiple flake coverage but also improved spatial resolution of the flake areas down to approximately 300 nm depending on the NA of the objective lens used. This allows more detailed study of more localised degradation from needle and rod-like features to edges and basal plane regions of the flakes. In this case HSI achieved 50-micron spatial resolution with 40x magnification in comparison to the Olympus fluorescence microscope which achieved 5-micron spatial resolution with 160x magnification on the needle-like NPLs.

The HSI setup has the advantage of a camera connected to the interferometer that can produce a sequence of images spectroscopically in a very short timescale to generate a more accurate picture of the overall degradation process. The PL spectra can also be generated from this setup to show the variation of PL over time and under different conditions. The PL signal can also be an indicator for thick or thin layer regions as the emission peak is split giving more detailed information. The Olympus fluorescence microscope setup does not allow for any of these measurements and information.

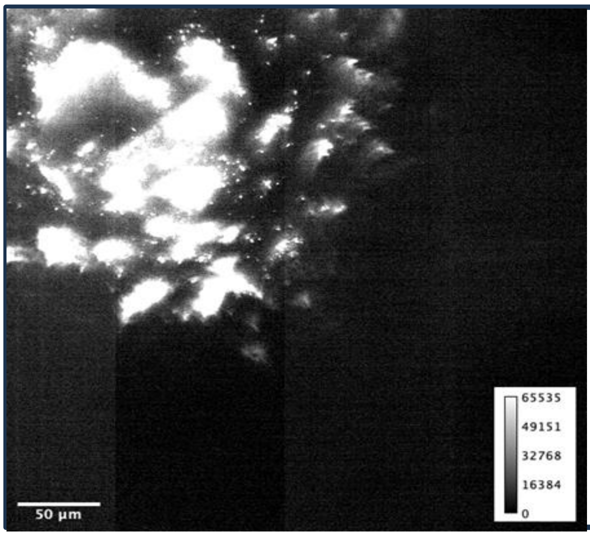

Figure 7.19: 1^{st}image-Ref: No water

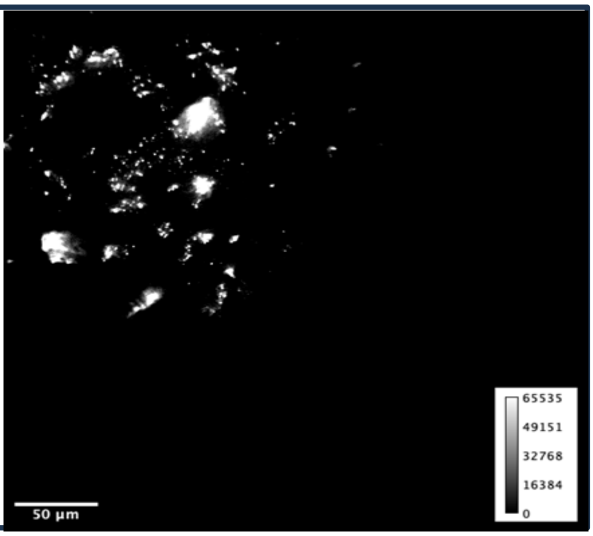

Figure 7.20: Image after 20 mins water

(Scale: 50 µm) (Intensity scale: 0 – 10,000 counts)

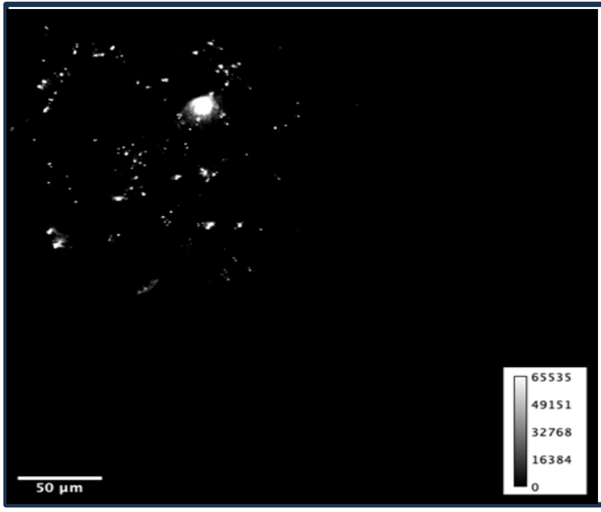

Figure 7.21: Image after 40 mins water

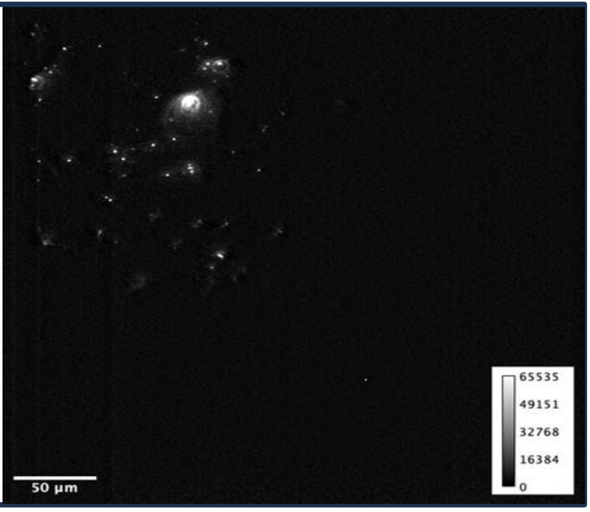

Figure: 7.22: Image after 75 mins water

It is apparent from experimental observations that the perovskite lattice is shown to be undergoing decomposition and therefore degradation as the flakes and needle NPLs show very little PL intensity after 75 minutes. This experiment further confirms that degradation is definitely taking place under water-induced conditions and appears to be happening uniformly over the whole sample.

7.8 –The effect on PL intensity before & after water treatment using wide-field HSI techniques

The PL spectra are collected over the wavelength range 400 to 700 nm and then extracted using the MatLab software using the same experimental setup as previously mentioned in section 7.7. Detailed analysis of the spectra was carried out using MATLAB code to identify the PL spectra arising from very thin layers, thick layers and intermediate layers as their PL spectral width and energy vary with the degree of their quantum confinement.

The region of sample to be investigated is the same as the needle NPL shown in Figure 7.18a. The images of the PL intensity before and after water treatment for 70 mins for this region are shown in Figures 7.23 and 7.24. A coverslip was placed on top of the sample to prevent flake movement during measurements.

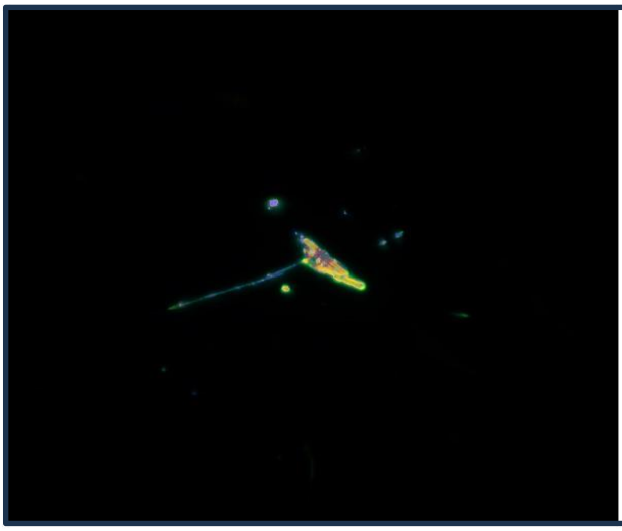

Figure 7.23: PL intensity before water treatment

Figure 7.24: PL intensity after water treatment

(Scale: 50 μm)

It is quite apparent from Figs 7.23 and 7.24 that the PL intensity decreases significantly after water treatment due to the process of degradation over the 70 minute timeframe. It was decided to investigate and explore different locations across the sample to compare the effects on PL intensity at the edges, the rod-like needle and basal plane sections. Five different location coordinates are selected using the MatLab program with the relevant PL plots extracted using the software. These are then imported into Origin software for plotting the graphs for each location before and after water treatment. The selected locations on the sample are shown in Figs. 7.25 and 7.26 with the corresponding PL plots before and after water treatment.

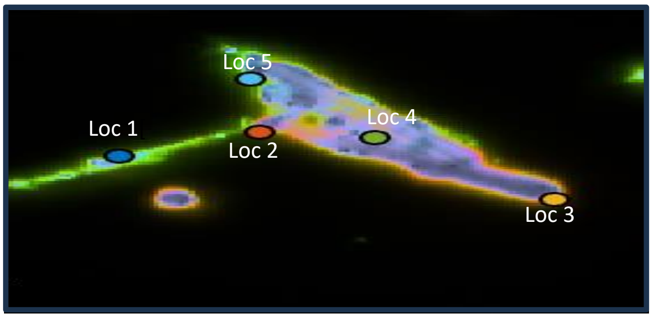

Figure 7.25: PL intensity locations before water treatment.

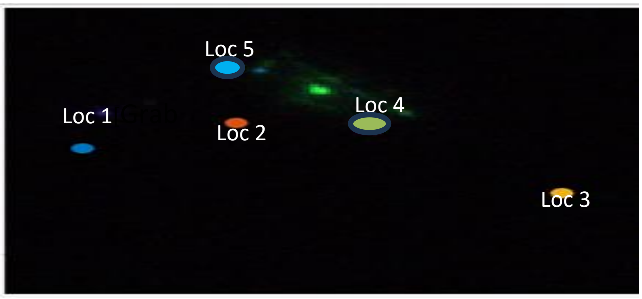

Figure 7.26: PL intensity locations after water treatment.

(Scale 50 μm)

It can be observed from the Figs 7.25 and 7.26 images that the PL intensity has decreased significantly at each location after water treatment. There is no significant peak shift for the prominent 525 nm PL peak however, the intensities have decreased significantly as the peaks have narrowed and become thinner thus indicating that the density of states (DOS) bands have decreased in size. This therefore increases the electron confinement and makes less energy levels available for electron transfer to the conduction band. In conclusion, this significant decrease in intensity indicates a change in DOS. The plots for the PL intensity across the five locations are shown in Figs 7.27 to 7.31 for a more accurate comparison of the bands before and after water treatment. Locations 4 and 5 appear to have the highest PL intensity before and after water treatment.

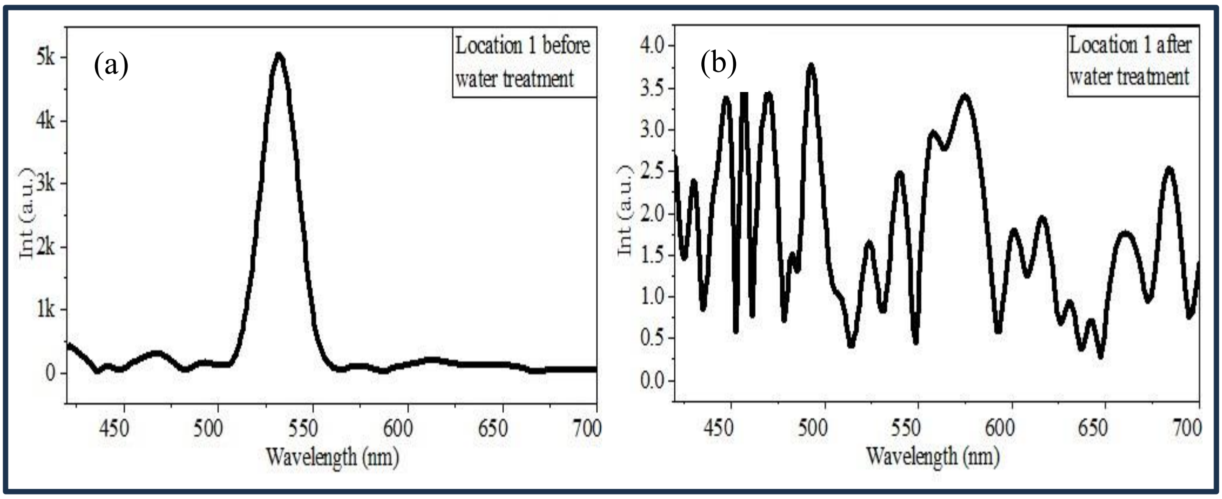

Figure 7.27: Location 1 (a) before and (b) after water treatment.

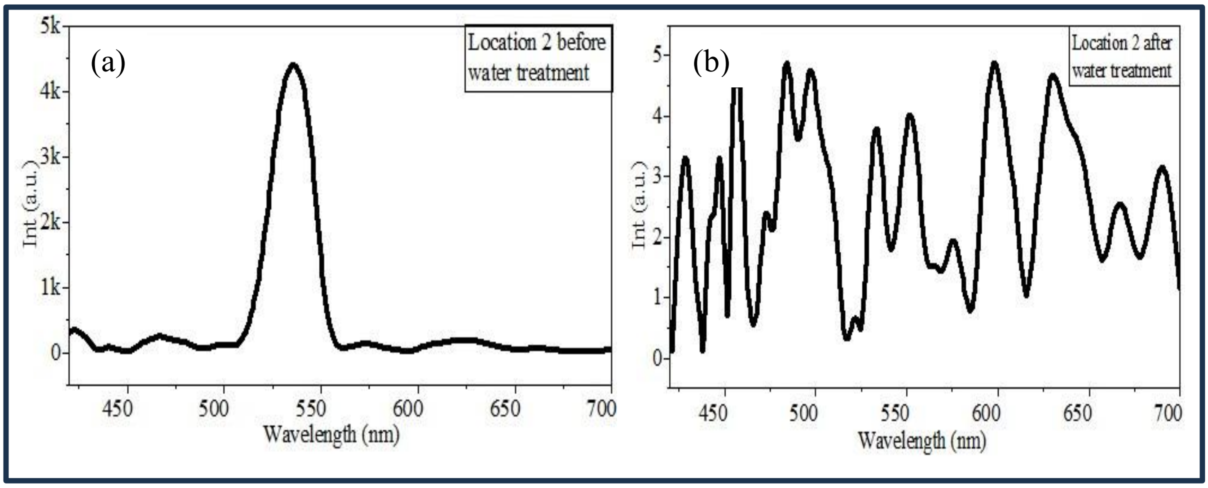

Figure 7.28: Location 2 (a) before and (b) after water treatment.

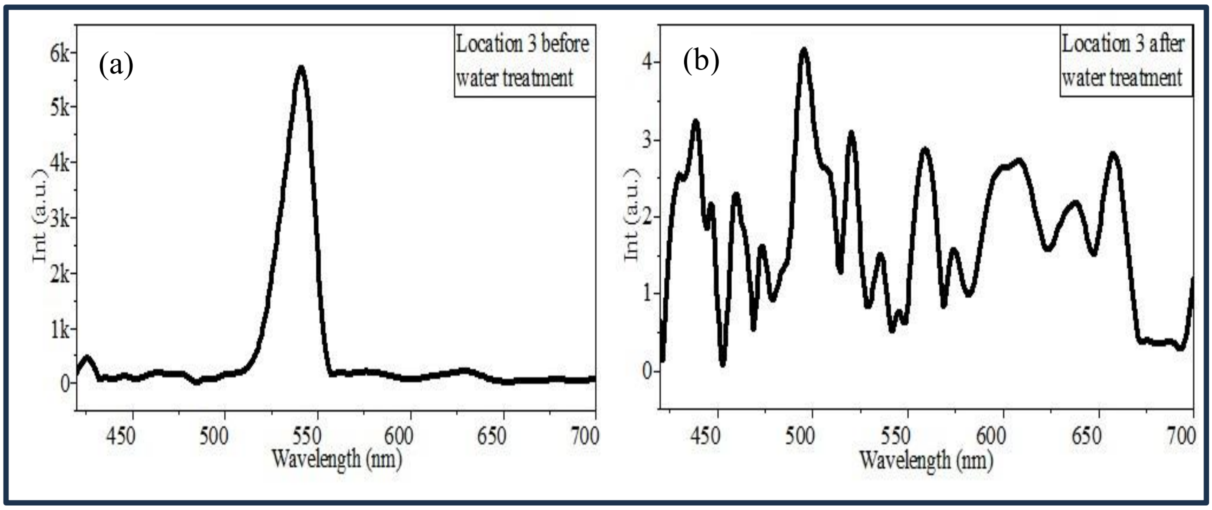

Figure 7.29: Location 3 (a) before and (b) after water treatment.

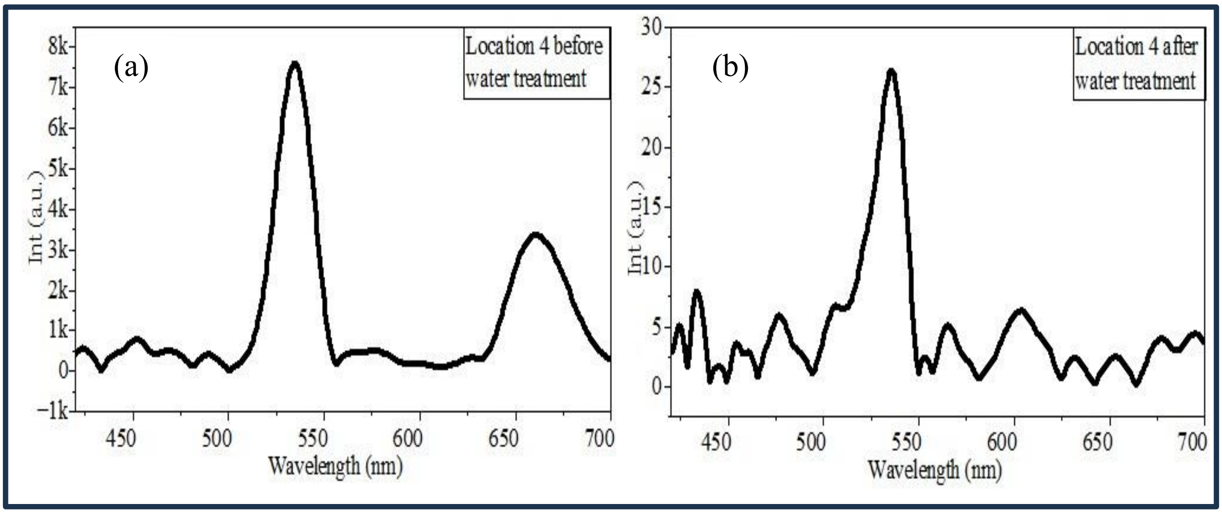

Figure 7.30: Location 4 (a) before and (b) after water treatment.

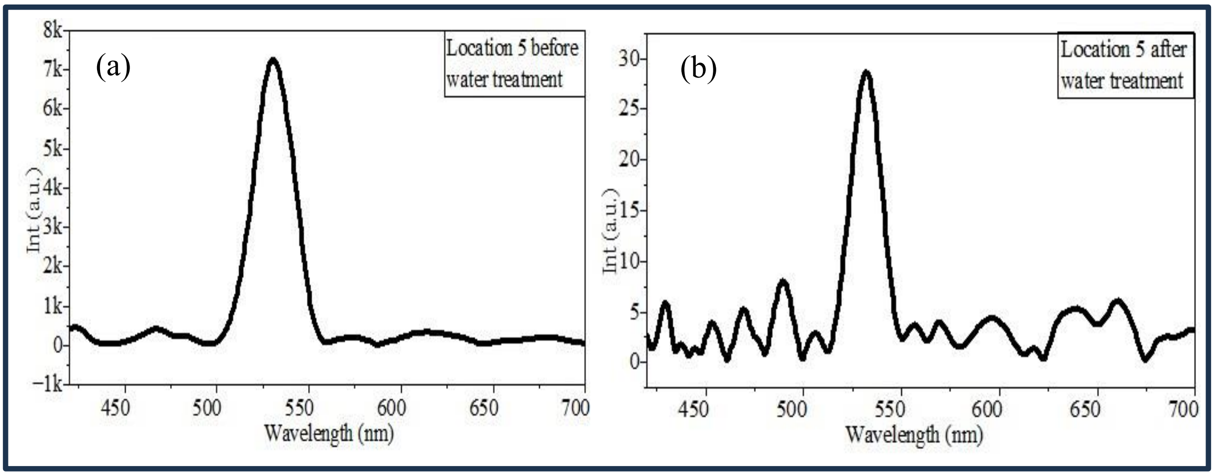

Figure 7.31: Location 5 (a) before and (b) after water treatment.

An investigation into how the bandgap correlates with the degradation process was conducted on the $MAPbBr_3$ perovskite sample to confirm the previous results. A UV-Vis absorption measurement was carried out using the Horiba Raman spectrometer to show the absorption for pristine perovskite and degraded perovskite on exposure to water. A Tauc plot was also constructed to show the effects of degradation by water on the bandgap. Figure 7.32 illustrates this phenomena.

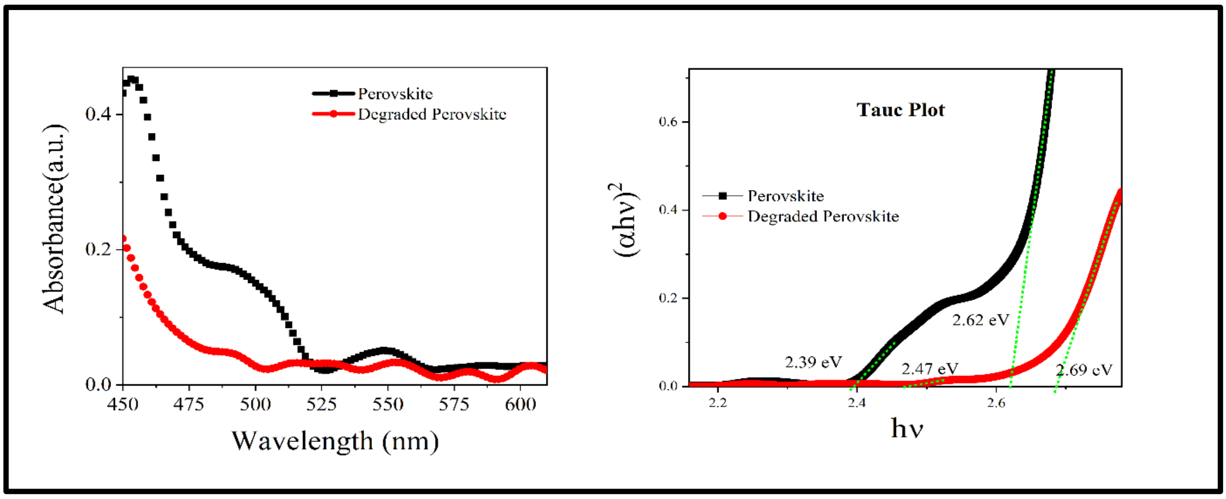

Figure 7.32: In situ UV/vis spectra and corresponding Tauc plot of a $MAPbBr_3$ film exposed to water (10 mins). The absorption spectra and bandgaps are shown for both pristine and degraded perovskite samples.

In Fig. 7.32, The Tauc plot shows the relationship between the absorption coefficient of the perovskite material and its photon energy and supplements the UV measurement in that it demonstrates that with an increase in absorption at 525 nm, the bandgap is increasing after 10 mins of degradation. The bandgap increases from 2.62 eV to 2.69 eV as the layers get thinner creating higher electron confinement. This is when the electrons and holes become more confined, and an increase in the energy difference occurs between filled and empty states, which widens the band gap. and hence giving a weaker PL emission response. This could be showing a correlation to the previous study on the locations and may indicate that the PL signal is decreasing due to a higher bandgap forming over the degradation process. The literature states that PL emission in this process consists of more confined, lower layer number regions with larger bandgap transferring their energy via resonant energy or charge-transfer processes to less confined, higher layer number regions with lower bandgap. The higher layer number regions is where radiative emission occurs as long-lived excitons in thin layers funnel into high *n* within 10–50 ps, which decreases their exciton binding energy and leads to the radiative recombination process.[128, 245] This is the reason why the degradation process starts in the thicker bulk regions and moves to the thinner regions.

7.9 – The effects of pH on PL intensity before & after water treatment using wide-field HSI techniques

From the previous measurements on the water degradation study of the perovskite and observing what seemed like uniform degradation, it was decided to conduct a further study to determine if the effect of pH could retard and slow down the onset of degradation and produce a stable state for the perovskite structure. When basic conditions were studied at pH's 8 and 9, the new perovskite sample NPL sent from Germany did not appear needle-like and was observed to be more flakey and crystalline in appearance. The synthesis does produce this shape and internal structure under different parameters, and in this case larger volumes of the solvent diphenyl ether (DPE) (10.5 ml), DDA (0.2 ml) and $PbBr_2$ (2.5 ml) precursors were added during synthesis. A frame of 138 images taken every 2 secs for 5 mins is set for pH 9 measurements using the Matlab software and the first and final images compared. These are shown in Figs 7.33 and 7.34.

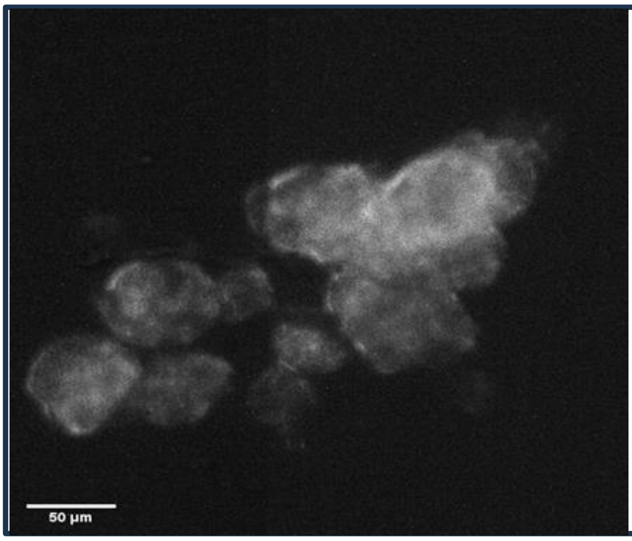

Figure 7.33: pH 9 1st image before 5 mins water treatment.

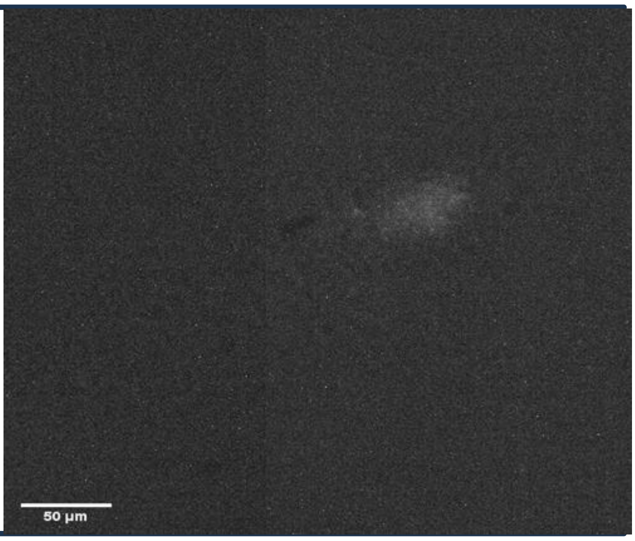

Figure 7.34: pH 9 final image after 5 mins water treatment.

(Scale: 50 µm)

At pH 9 the rate of degradation would appear to be very rapid as the flake/crystal NPL are observed to show either very little or no PL intensity after the 5 minute period, indicating instability in basic conditions. Shifting down the scale to pH 8, this was then investigated for comparison purposes to determine if the rate of degradation is being reduced. A frame of 138 images is again generated over 5 mins, and the first and final images at pH 8 are shown in Figs. 7.35 and 7.36. It is hypothesized that alkaline solutions of pH 8 and 9 contain hydroxyl ions

(OH-), which could potentially react with the lead and bromide ions within the $MAPbBr_3$ structure. This reaction can lead to the formation of lead hydroxide ($Pb(OH)_2$ and the release of bromide ions, essentially dissolving the perovskite material. The hydroscopic nature of the organic cation in $MAPbBr_3$, along with its interactions with water and oxygen, can contribute to decomposition in acidic environments. However, some studies suggest that specific acidic conditions, like those created by the formation of lead laurate shells, can actually enhance the luminescence and stability of $MAPbBr_3$.[127, 131, 246] At pH 8, the rate of degradation is again observed to be very rapid with the flake/crystal NPL showing little or no PL intensity after the 5 mins period, and further confirming that the perovskite crystal lattice is extremely unstable under basic conditions.

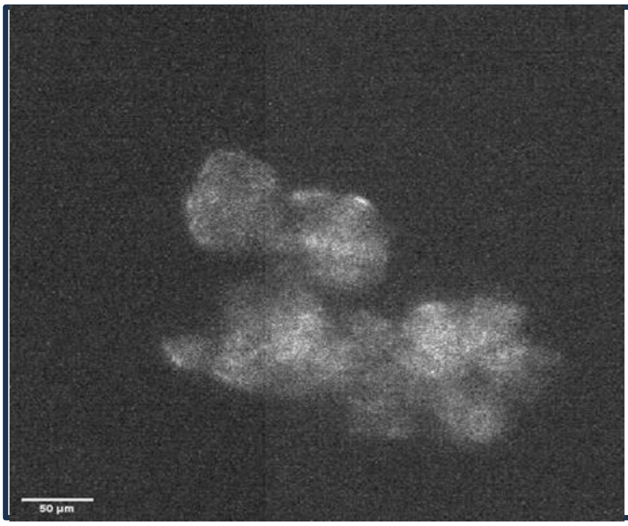

Figure 7.35*:* : pH 8 1st image before 5 mins water treatment. (Scale: 50 µm)

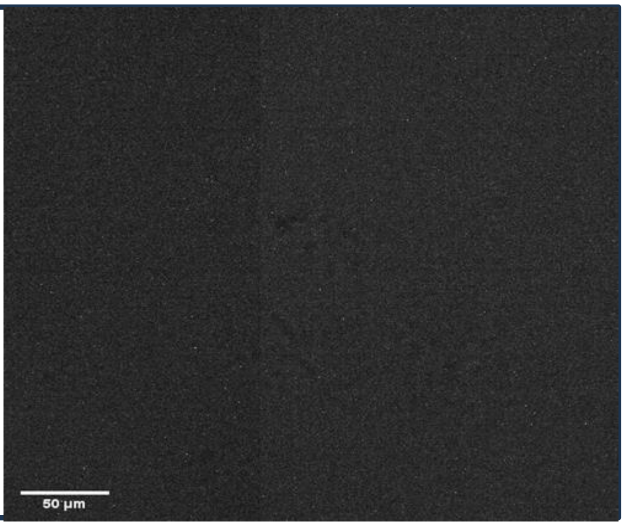

Figure 7.36: pH 8 final image after 5 mins water treatment. (Scale: 50 µm)

As is known from previous measurements, neutral pH 7 demonstrates complete degradation after 15 mins exposure to water. Hence it was decided to shift further down the scale from pH

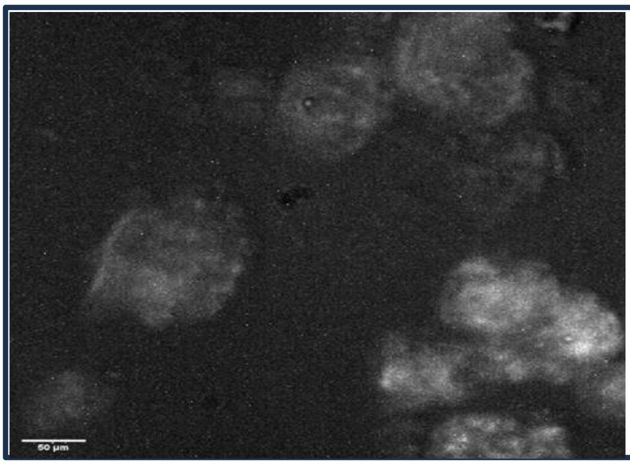

Figure 7.37: : pH 6 1st image before 20 mins water treatment. (Scale: 50 µm)

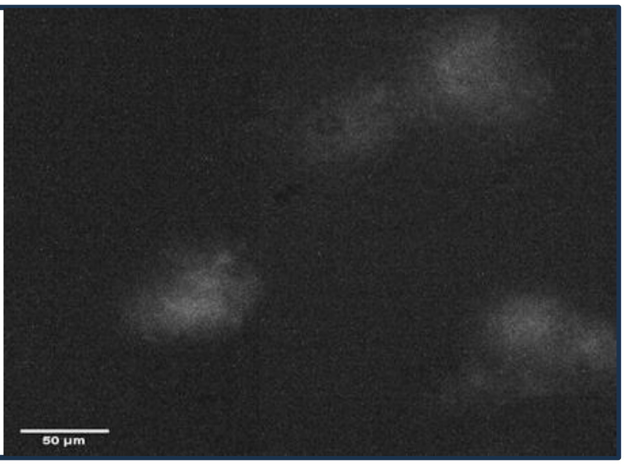

Figure 7.38: pH 6 final image after 20 mins water treatment. (Scale: 50 µm)

6 to pH 3 to create more acidic conditions and determine if the crystal lattice will be more stable under such conditions. The pH 6 solution is observed to degrade the perovskite after 20 minutes as Figures 7.37 and 7.38 display the first and final images of the HSI sequence.

The pH 5 aqueous solution displays complete degradation around 20 minutes and this demonstrates stability is not yet achieved. However, the degradation rate does appear to be slowing down. Figures 7.39 and 7.40 show the first and final images for the pH 5 solution.

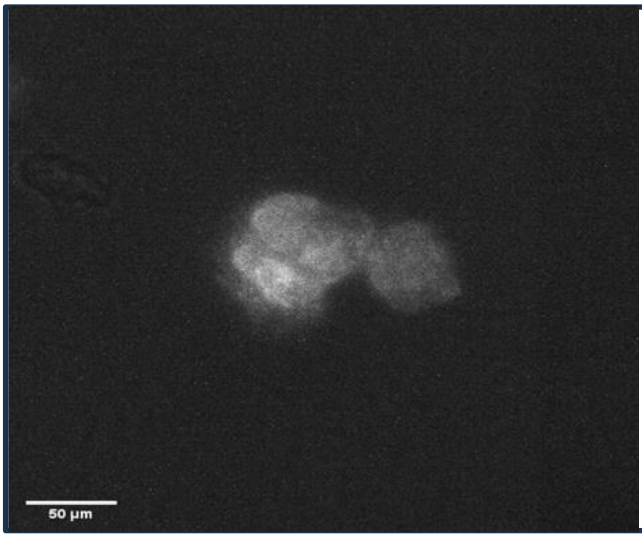

Figure: 7.39: pH 5 1st image before 20 mins water treatment.

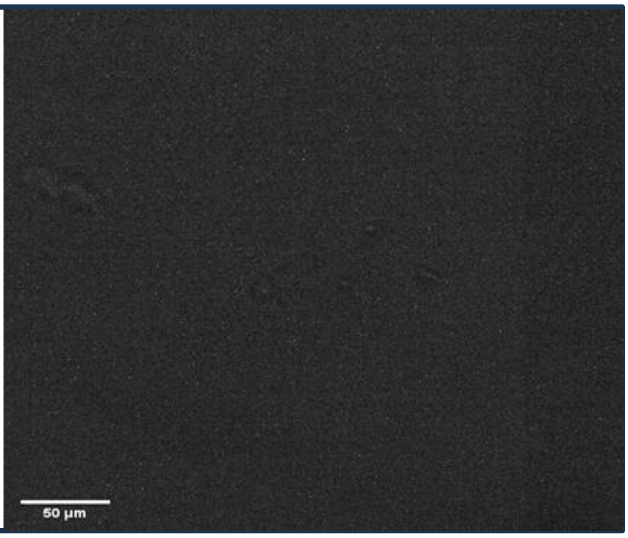

Figure: 7.40: pH 5 final image after 20 mins water treatment.

(Scale: 50 µm)

For the pH 5 aqueous solution, a PL study is undertaken on the effects of the degradation on the three PL emissions at different regions of the sample such as the edges and basal plane; and to determine where the most rapid rate of degradation is taking place and hence inform us on what is happening to the PL emissions of the perovskite sample before and after water treatment. Figures 7.41 and 7.42 display the graphical peak fitted plots for the basal planes and edges respectively. The HSI technique is observed to split the emission peak, unlike the PL spectrometer used in the moisture-induced degradation study that displays the entire area from spectral averaging and so does not show the detail of the emission peak splitting as shown previously in Fig. 7.5.

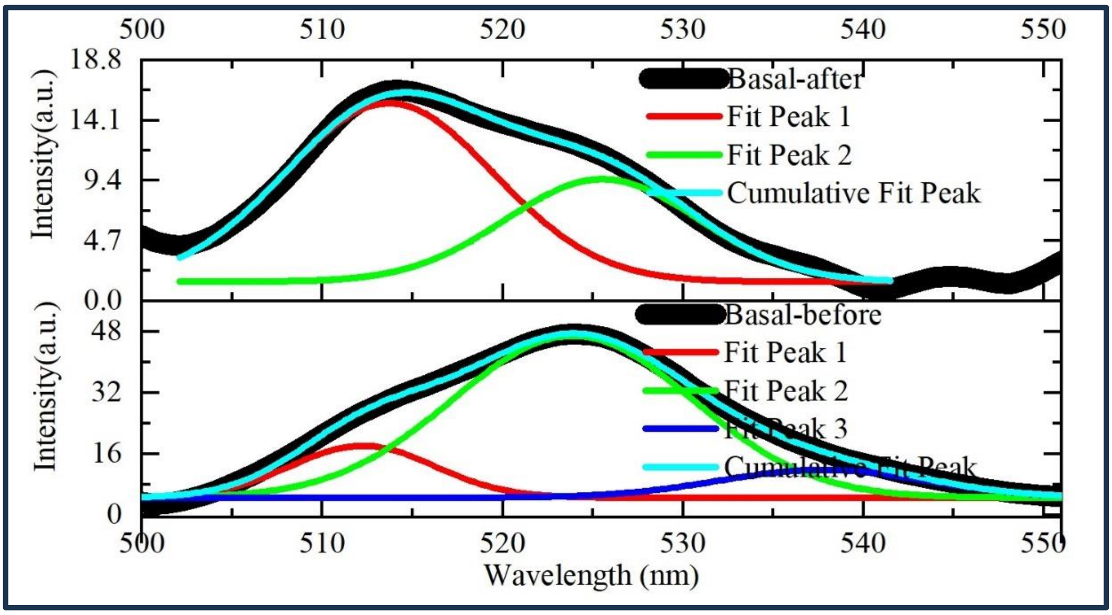

Figure 7.41: Plot of PL intensities from basal planes.

Before water treatment, the basal planes show emission peaks at 512 nm (red curve), 524 nm (green curve) and 538 nm (blue curve). The after-water treatment emissions show a slight blue-shift in the red and green emissions with the first component (red) sustaining after 20 mins of degradation., this could be indicative of thinner layers remaining and being sustained in the degradation process. The second component (green) suffers massive quenching with reduction in PL intensity. The third component blue emission disappears completely. The green and blue components could indicate that the thicker layers are being degraded faster than thinner layer.

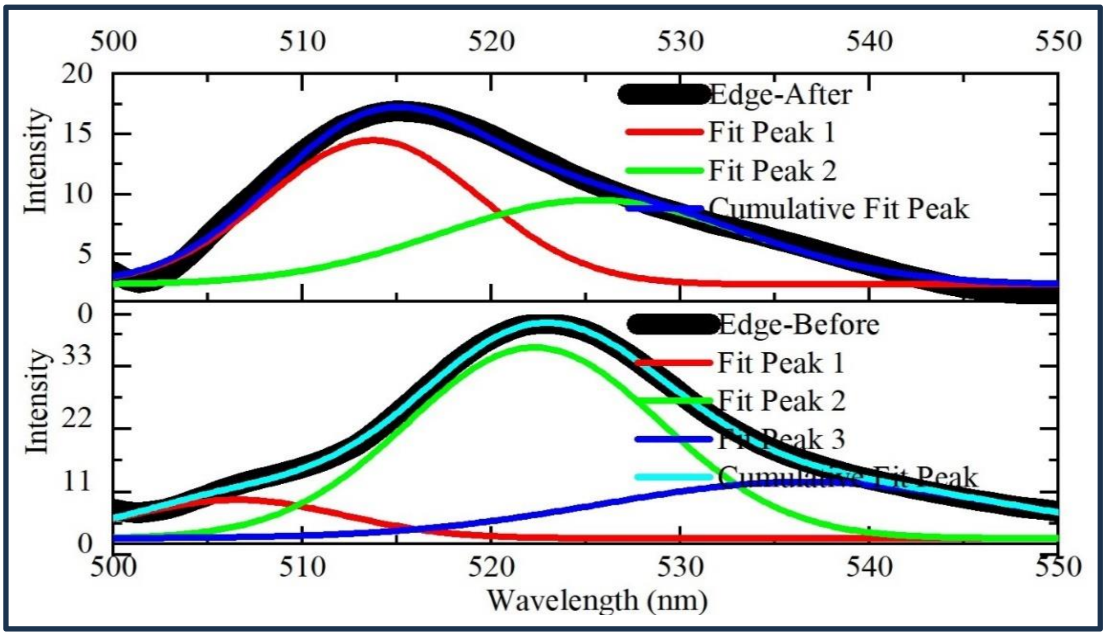

Figure 7.42: Plot of PL intensities from edges.

The edges show a similar pattern to the basal planes in terms of PL emission. Before water treatment the emissions show at 507, 522 and 537 nm. After water treatment, the emissions blue shift slightly again for the red and green components. The first red emission component again sustains after 20 mins of degradation. The second green emission component again suffers massive quenching with a significant reduction in the PL. The third blue emission component again vanishes. In addition to thinner layer and thicker layer rates of degradation, these data plots would appear to indicate that the degradation of the edges and basal planes are not of a similar rate and the degradation of the perovskite sample is demonstrating an inhomogeneous process. The Figures 7.43 and 7.44 display the PL emission and 2nd derivative PL emission images before and after water treatment for the three emission peaks 507, 522 and 537 nm.

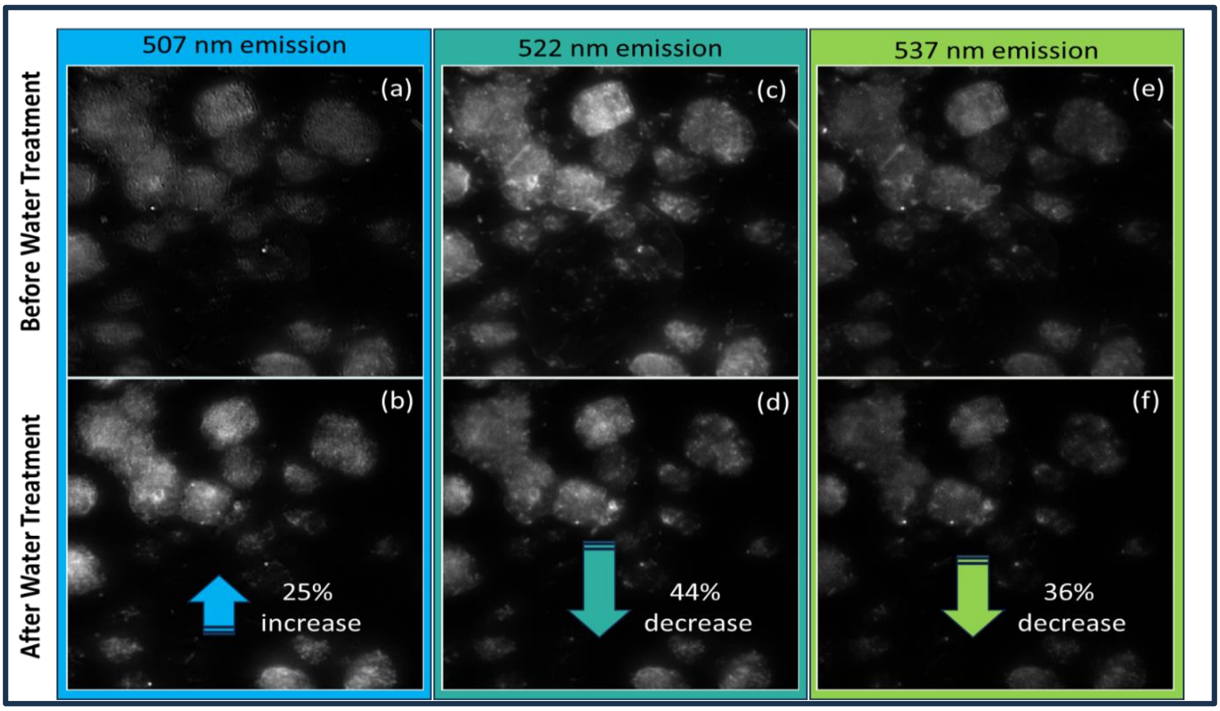

Figure 7.43: PL Emission image comparison before and after water treatment: 507 nm emission images (a) before, (b) after water treatment. 522 nm emission images (c) before, (d) after water treatment. 537 nm emission images (e) before and (f) after water treatment. (Scale: 50 µm)

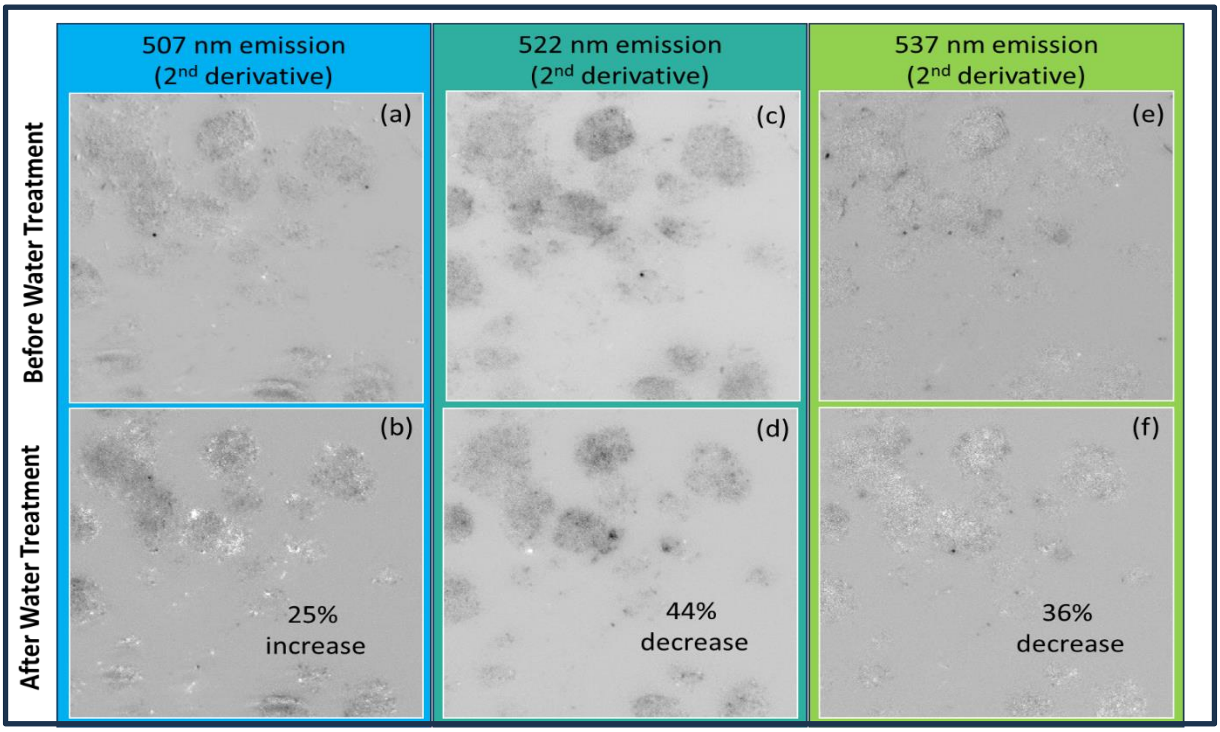

Figure 7.44: 2nd derivative images of PL Emission comparison for before and after water treatment: 507 nm emission images (a) before, (b) after water treatment. 522 nm emission images (c) before, (d) after water treatment. 537 nm emission images (e) before and (f) after water treatment. (Scale: 50 µm)

The images show a 25% increase in PL emission at 507 nm after water treatment that would appear to be in agreement with the red component sustainability after 20 mins of degradation previously shown for the basal planes and edges. The 522 nm and 537 nm emissions both display a decrease in PL emission from the grayscale images of 44% and 36% respectively, and this also supports the observations made on the green and blue components from figures 7.41 and 7.42 that underwent substantial quenching of the PL emission on both the basal planes and edges. Through detailed analysis of the PL spectra from the hyperspectral image, specifically from the pixels that survived and those that degraded (Figure-7.43). It can be observed that the spectral contibution from the thicker bulk regions with higher emissions (522 and 537 nm) reduced in PL, whereas that from the thinner layered region with lower emission (507 nm) PL remained unchanged which signifies preferential degradation of the thicker bulk region.

At pH 4, the perovskite material is starting to show some signs of increasing stability as the rate of degradation appears to be slowing down further and this can be observed from the first and last time lapse images shown in Figures 7.45 and 7.46. There is not much difference in the PL intensity at the end of the time lapse period of 20 mins. This is suggestive of getting closer to stability.

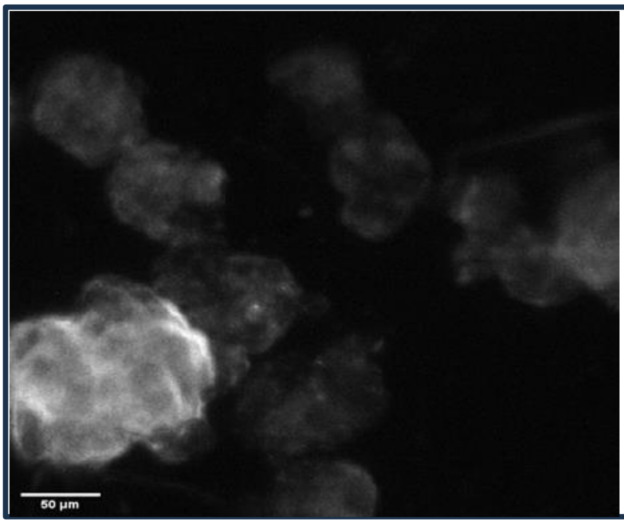

Figure 7.45: pH 4 1st image before 20 mins water treatment.

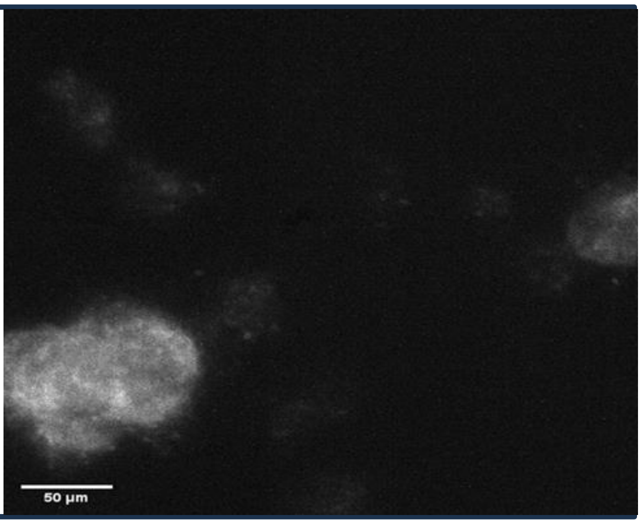

Figure 7.46: pH 4 final image after 20 mins water treatment.

(Scale: 50 µm)

The pH 3 aqueous solution measurement does demonstrate much greater stability of the perovskite lattice to water degradation as there is little sign of any degradation taking place over the timelapse periods of 20, 30, 75 and 105 minutes as shown in Figure 7.47 (a-d).

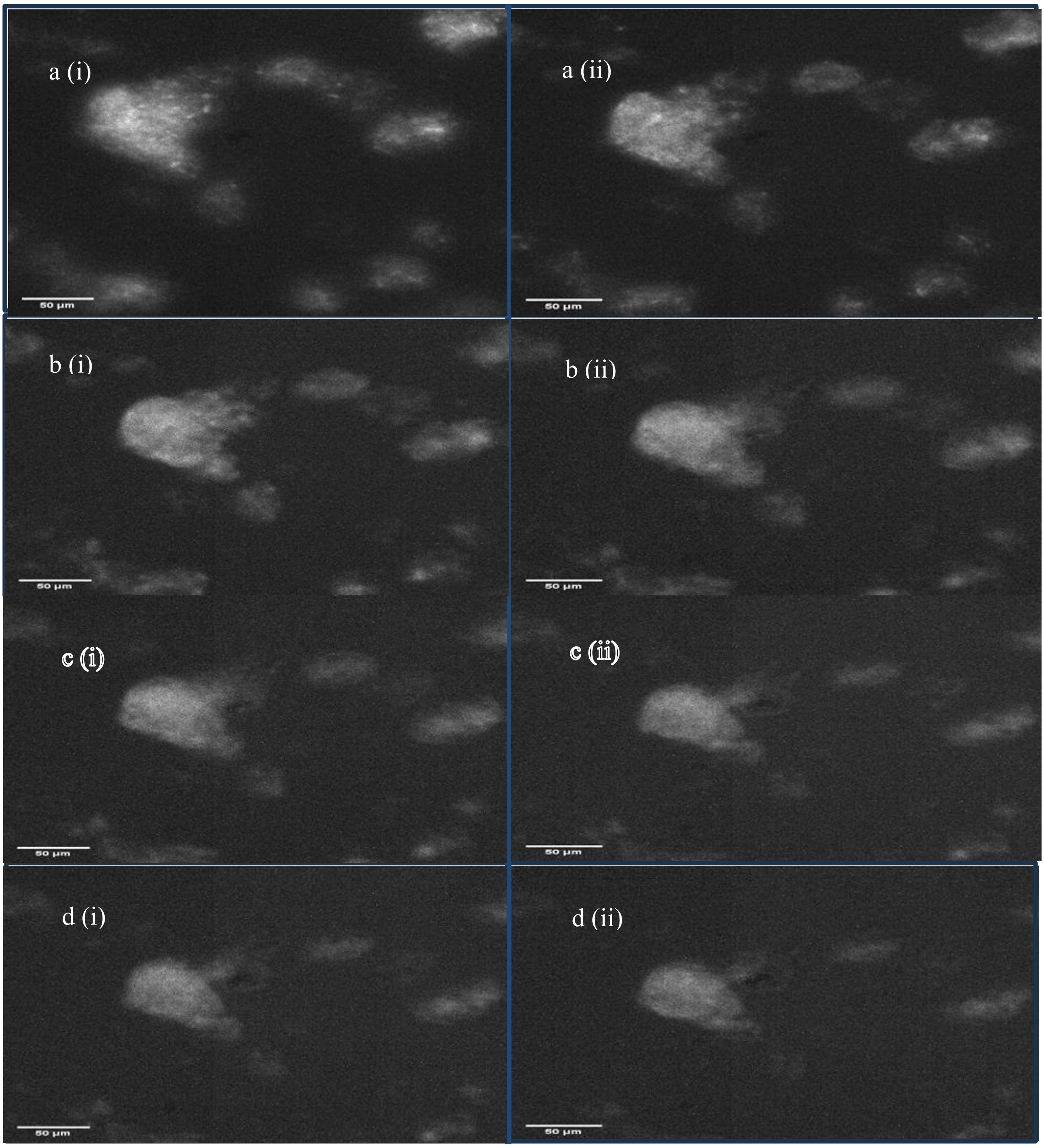

Figure 7.47: pH 3: a (i) 1st and a (ii) final images after 20 mins time period, b (i) 1st and b (ii) final images after 30 mins time period, c (i) 1st and c (ii) final images after 75 mins time period, d (i) 1st and d (ii) final images after 105 mins time period. (Scale: 50 µm)

The images in Figure 7.47 (a-d) for the four, time lapses of 20, 30 75 and 105 mins confirm that there is very minor degradation taking place for the pH 3 aqueous solution in comparison to the other pH time frames. Therefore, stability of the crystal lattice has been observed under acidic conditions and a lower pH value of 3. It is apparent from the images that higher pH's with high concentration of OH^- ion accelerate the degradation of NPL whereas the lower pH 3 with high concentration of H^+ ion suppresses it. It is hypothesised from the observations that the thick multilayered platelets are more prone to degradation in presence of OH^- than thinner layers. Additionally, it can be stated that single unit-cell layers capped with the long-chain methylammonium ligand and bromide co-ligand are the most stable due to this dense outer ligand shell protecting these layers from OH^- penetration; it is also plausible that the thicker platelets with multiple unit cells are degrading to thinner layers. This dense outer ligand shell shields the core perovskite structure, reducing the likelihood of degradation and enhancing overall stability. Such a possibility corroborates with the observations of Liu et al[131] and Xu et al[247] who propose the formation of PbBr(OH) that stabilises the perovskite structure, and has higher thermodynamic stability than $MAPbBr_3$, which can prevent the decomposition of internal $MAPbBr_3$. The studies by Xu have proved that PbBr(OH) is an excellent encapsulation material and claim there should be more development of applications for this material.

Variations of the PL intensities with time were extracted from the time-lapse images to calculate the degradation rate. The variation of the PL intensity (normalized) of the perovskite with time under different pH conditions is shown in Figure 7.48. When the data is denormalized, very similar trends were observed with pH's 3 and 4 showing higher stability.

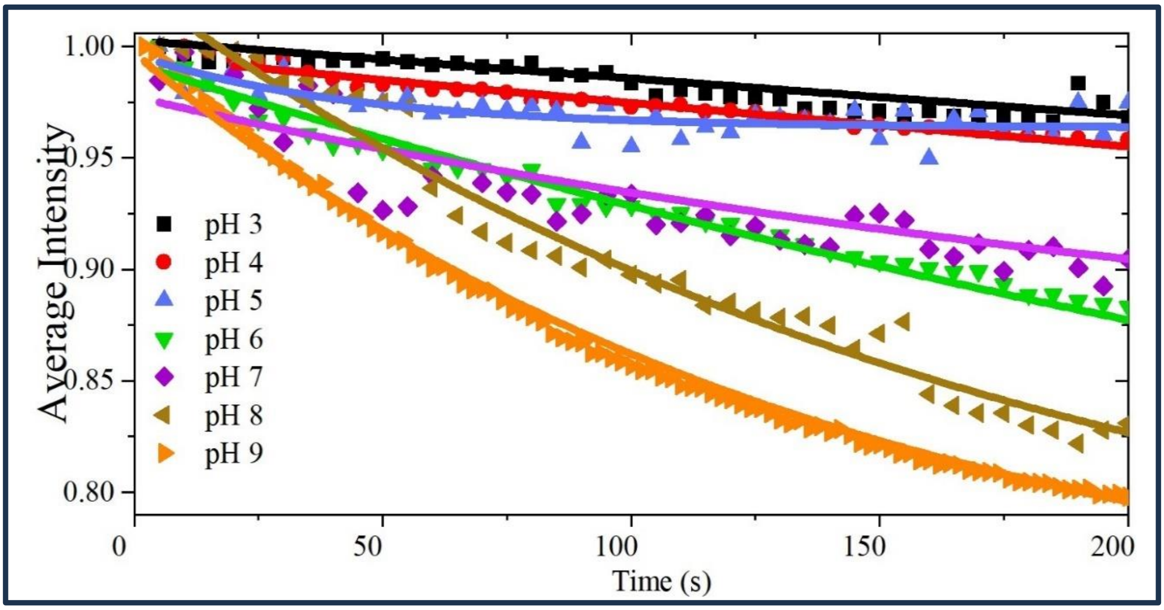

Figure 7.48: Variation of PL intensity with time.

The plot in Fig. 7.48 shows pH's 3 (black line) and 4 (red line) producing a more stable response for PL intensity in comparison to the higher pH values of 5-9. A table of the time constants against pH is shown in Table 7.1. Stability of pH and temperature is assumed. It is also assumed that the degradation rate has a linear dependence on light intensity as light was shown not to affect the degradation process.

Table 7.1: pH vs time constants

pH	**Time constant 't_0' (s)**
3	3810
4	1364
5	108
6	330
7	271
8	178
9	140

Table 7.1 of pH vs time constant t_0 shows that the time constant increases as the pH conditions decrease from pH 9 to pH 3. The exception being pH 5 where a decrease in the time constant (108) is observed to be lower than pH 9 (140). The experiment was not repeated, but this could have been caused by the crystallinity and surface area of the NPL that can affect the water diffusion rate into it. Other factors include the presence of surface defects, moisture exposure, or specific conditions during testing.[248] In conclusion, the degradation process is being slowed down or retarded at lower pH values and eventually reaching stability at pH 3 for the perovskite structure.

A video showing variation of PL emission intensity with time when the perovskite thin film undergoes aqueous treatment can be visited at the following youtube link: https://youtu.be/VW8owwzukXg.

The plots and peak fits in Figs 7.49 and 7.50 were produced from the Horiba spectrometer to verify accuracy of the results. Inherent detector noise is observed in both spectra. The spectra further confirm that the 524 nm (green curve) and 538 nm (blue curve) emission peaks undergo some quenching with a small reduction in PL intensity after pH 3 treatment. The 512 nm (red curve) is again shown to sustain and increases in PL intensity. This is in agreement with Figs. 7.41 and 7.42 HSI spectral measurements.

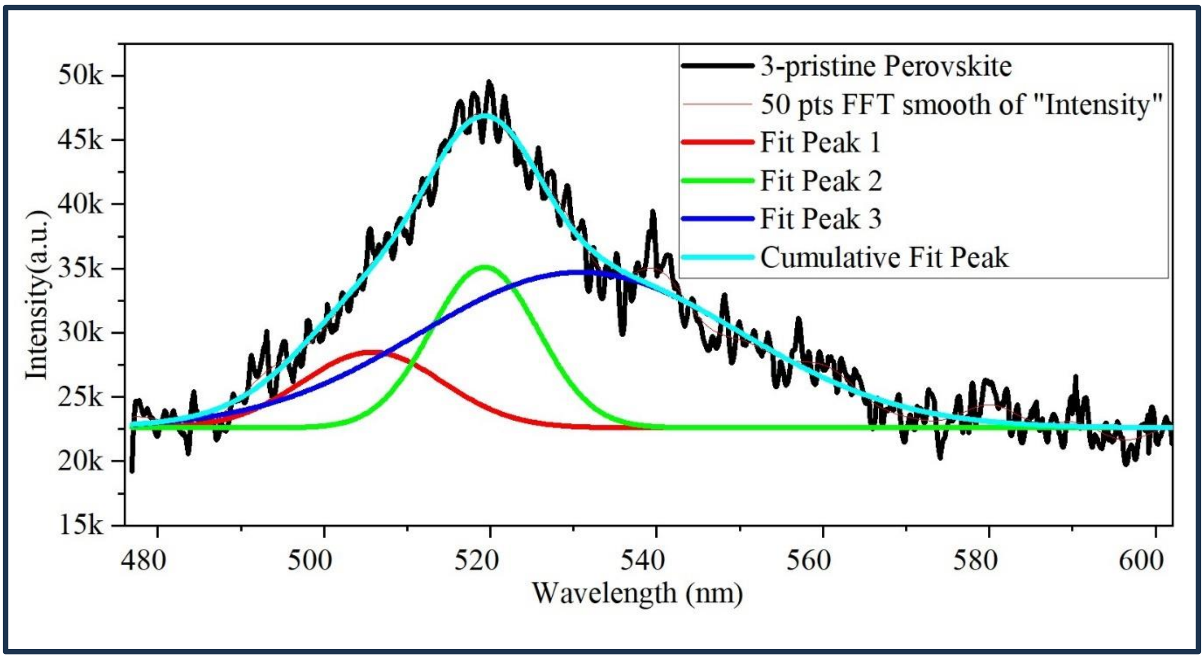

Figure 7.49: Plot of PL emission intensities before pH 3 treatment.

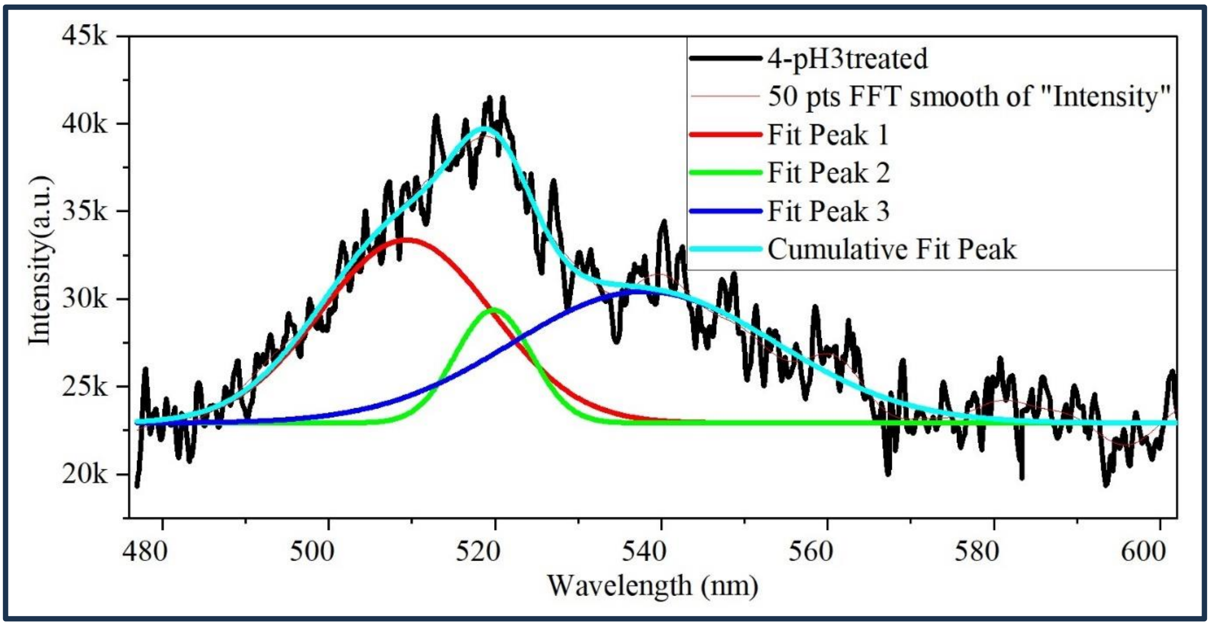

Figure 7.50: Plot of PL emission intensities after pH 3 treatment.

A Gaussian fitting function can be used as another way of determining the rate of degradation over different regions of the perovskite sample. Measurements on the height, centre and width of the PL peak produce an intensity map indicating regions of high or low rates of degradation at certain locations on the sample e.g. edges, basal plane etc. This is shown in Fig. 7.51 (a-d).

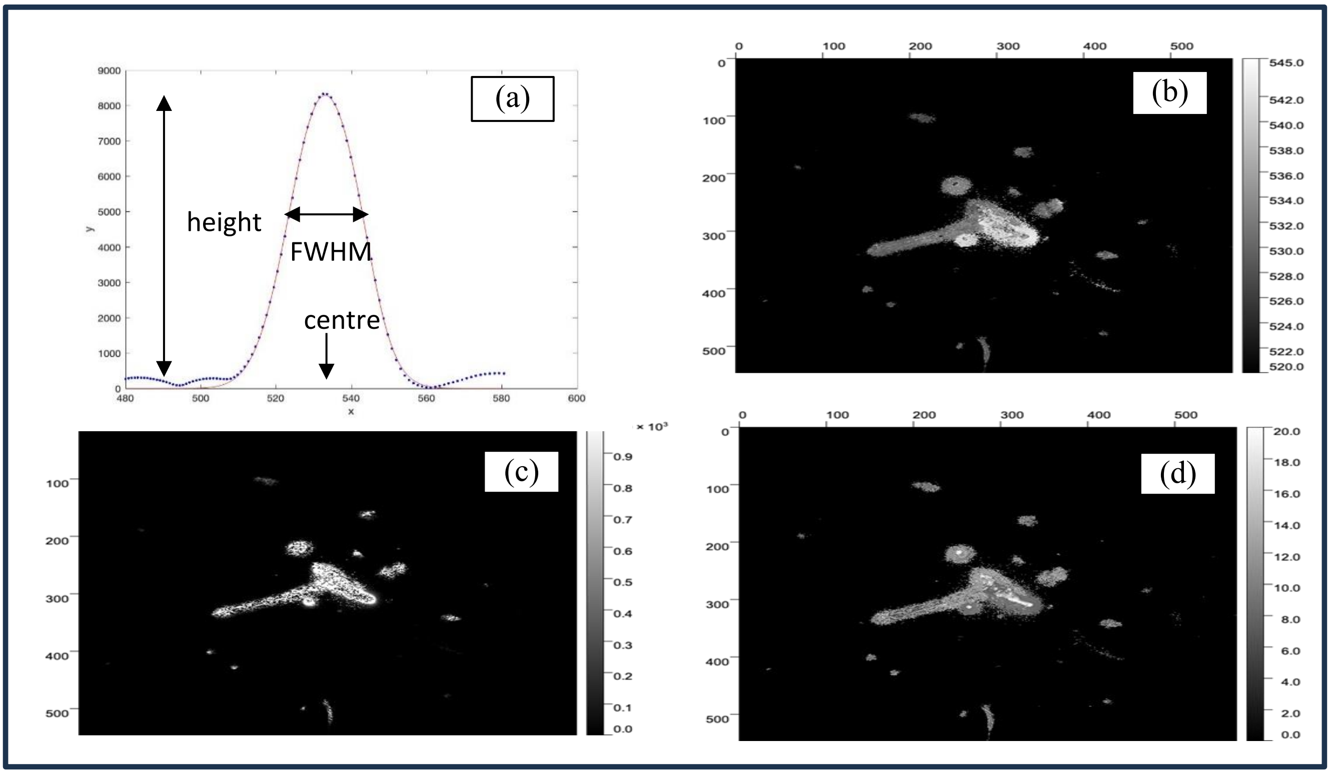

Figure 7.51: (a) Example PL spectrum of $MAPbBr_3$ perovskite exposed to water and fitted with a Gaussian function. (b) plot of the height values, (c) plot of the centre values, (d) plot of the width values.

7.10 – Discussion

It is evident from the PL spectra and their components that the thinner layer with highest confinement appears at lower energy emission with narrower spectral bandwidth in comparison to the thicker bulk crystals that possess higher energy emission, lower confinement and wider spectral bandwidth as shown in Figs. 7.41 and 7.42. It's plausible that a single crystalline layer (n=1) generates the highest energy PL spectrum and is blue shifted to this effect. In addition, we also observe that there are spatial variations of the PL spectra due to local confinement effects e.g. the spectrum from an edge appears at higher energy than the bulk, a narrow thin basal plane region of the NPL shows narrower spectral bandwidth than the wider basal plane region. The bulk fractions show higher intensity PL, that gets weaker with a decreasing layer number or thickness of the NPLs over the degradation process. The application of HSI techniques has shown capability in producing spectral plots and spatial resolution images down to about 50 μm with 40x magnification. The images are sufficient enough to determine the regions of the perovskite NPL where degradation occurs most rapidly whether it be from thinner or bulk regions or more locally from edges or basal planes. In future work, the HSI technique could be extended to the study of defects, vacancies and impurities on the surfaces of layers in halide perovskite compounds.

CHAPTER–8

In-situ monitoring of intermediates in the electrochemical N-nitrosation of secondary amines

8.1 – Introduction

The focus of this study is to determine if Electrochemical-Raman techniques can be used to study the intermediates formed during the course of the chemical reaction. In this study, we focus on the spectroscopic investigation of the electrochemical nitrosation of amines in an aqueous solution. Here we investigate the reaction between sodium nitrite and N-methylbenzylamine (**1**) as an exemplary secondary amine in 1:1 acetonitrile/water medium. A reaction scheme showing the reaction mechanism is shown in Scheme 1.

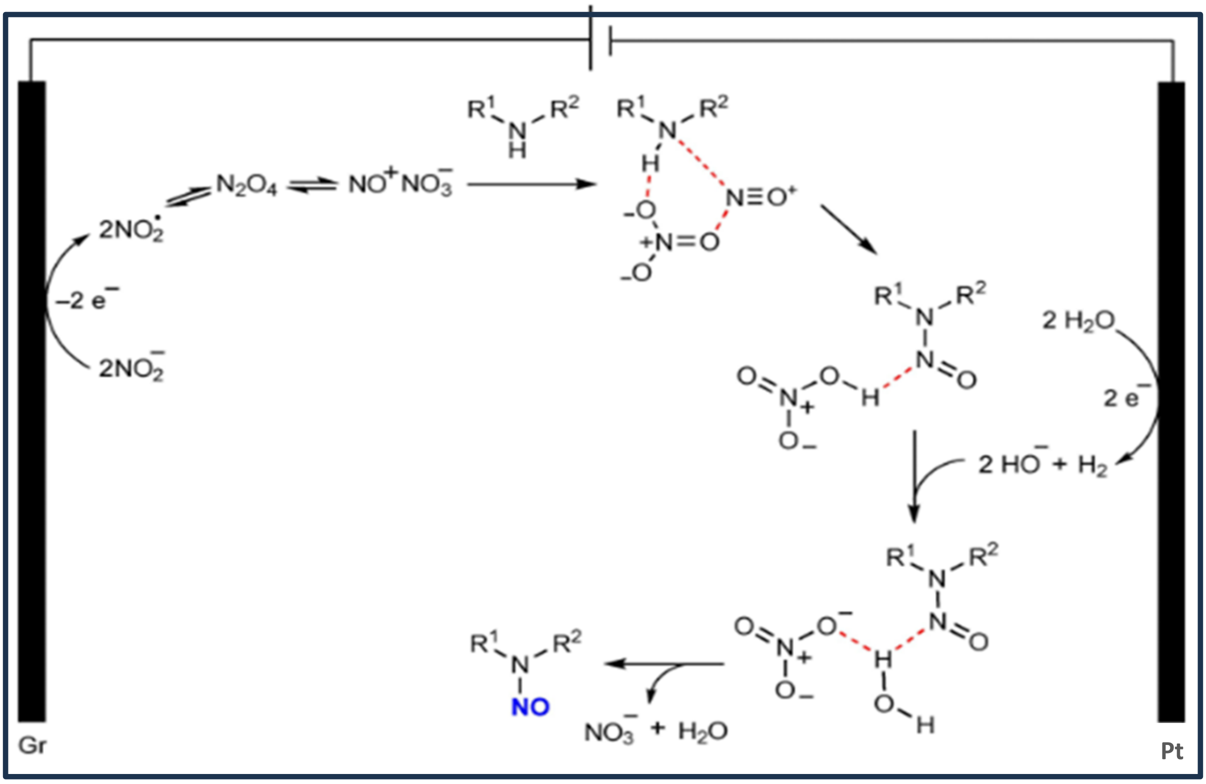

Scheme 1. Proposed reaction mechanism.[23]

Masui and coworkers used this electrochemical approach as a batch process towards the synthesis of N-nitrosamines using sodium nitrite as the nitrosating source.[145] While a flow electrochemical approach has been recently reported by Ali et al,[21] conventional routes used in the formation of N-nitrosamines involve the use of sodium nitrite in combination with a strong acid. [249-253] The experiment involved running a CV scan to identify the oxidation peaks and then applying potentials over the potential range of the scan until an optimum potential was found that accelerated the reaction and produced the highest intensity Raman peaks.

8.2 – Background and experimental setup

The experimental setup used for the Electrochemical-Raman measurements involved the use of the 3-electrode PEEK electrochemical cell setup described in Chapter 7, however this time a graphite electrode cross-section was used as working electrode in place of ITO glass plate to determine the effect of graphite surface area/topography on the reaction intermediates and products formed. A grubs screw and PTFE holder are used to hold the graphite strip in place. Figure 8.1 and Scheme 2 illustrates the cell design used for the experiment.

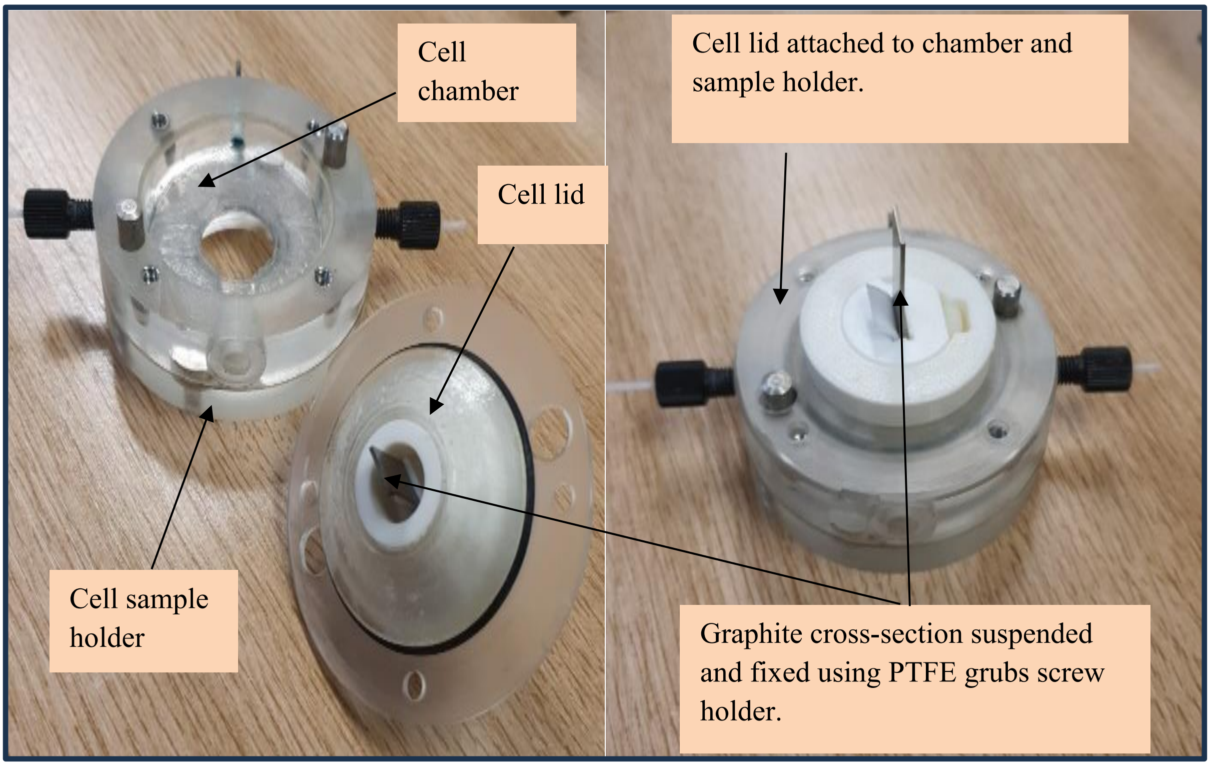

Figure 8.1: Labelled Illustration of the cell design used for the nitrosation reaction using a graphite electrode cross-section inserted through the top lid. Grubs screw and PTFE holder in white used to hold and suspend the graphite electrode cross-section.

With graphite acting as the anode and the platinum as the cathode in this setup, N-methylbenzylamine **1** (substrate **1)** is employed as the substrate for the determination of the optimal conditions required for the electrolysis towards N-nitrosamine **2** (product **2**). To conduct the experiment, the Autolab potentiostat PGSTAT204 is configured to the cell with the three-electrodes and the Nova software interfaced with the Wire software from the Renishaw Raman spectrometer using .NET functionality triggering between the Wire and Nova software. The potential value of 2.1 V was used throughout the reaction as it was found to be the optimum potential for driving the reaction and producing the highest intensity Raman peaks. The Raman microscope included a 488 nm excitation wavelength laser with 2.5mW of power to the sample. A grating of 2400 line mm^{-1}, an Olympus Objective lens of 40x magnification with 0.5 NA, and an exposure time of 40 seconds. The exposure time is used to minimise background noise interference from the liquid sample and produce optimum peak resolution. Lower exposure times produced noisy spectra with poor resolution. The electrochemical experiment was carried out at ambient temperature inside the cell.

Measurements for the current study were made using electrochemical-Raman methods to study and determine the intermediate/product formation over a range of potentials that produce simultaneously the relevant CV curve and Raman spectra. The peaks on the Raman spectra over the potential range provide evidence to support the proposed intermediates and products formed during the course of the reaction. The Raman spectra measured the composition of the mixture of reactants, intermediates and products depicting presence of the species. It is limited by the sensitivity of the Raman signal from a specific species as intermediate concentrations are expected to be low and short lived. It is also limited by the time resolution for the intermediates that are short lived. For this reason, a steady state was considered where all the species are expected to be observed.

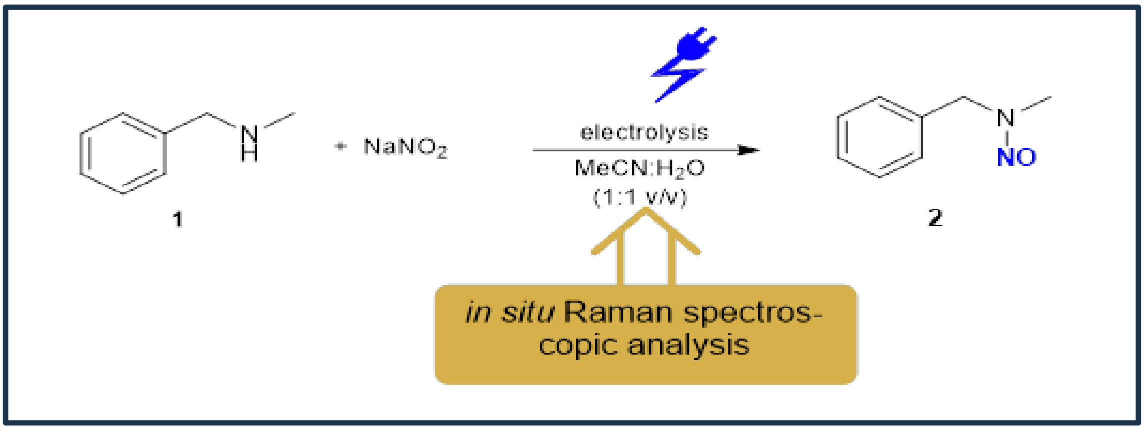

Scheme 2. Electrochemical synthesis of N-methyl N-nitrosobenzylamine **2**.

Water was used as the medium to dissolve sodium nitrite, as nitrite salts are insoluble in organic solvents, while the secondary amine is dissolved in acetonitrile owing to its miscibility with water.[21] A solution of 5 M $NaNO_2$ (5 eq.) and 1 M secondary amine (1 eq.) is necessary for the reaction to proceed efficiently, as the $NO_2\cdot$ radicals formed not only dimerise, but can also form various other species under the electrochemical conditions.[21] Both solutions are added to the cell by syringe (~ 2 ml), and quickly mixed to create a homogeneous solution and the electrochemical-Raman measurements started immediately. As the nitrite salt solution has sufficient conductivity, there is no need for any additional supporting electrolyte in the cell. In this setup, a one-electron anodic oxidation of the nitrite ion provides the $NO_2\cdot$ radicals, which exist in equilibrium with dinitrogen tetroxide (N_2O_4),[254] which is a known nitrosating agent for secondary amines under neutral or alkaline aqueous conditions and in organic media.[142] Raman spectra of the reagent solutions (a, b) and the spectrum of the N-nitrosamine**2** (c) are shown in Figure 8.2.

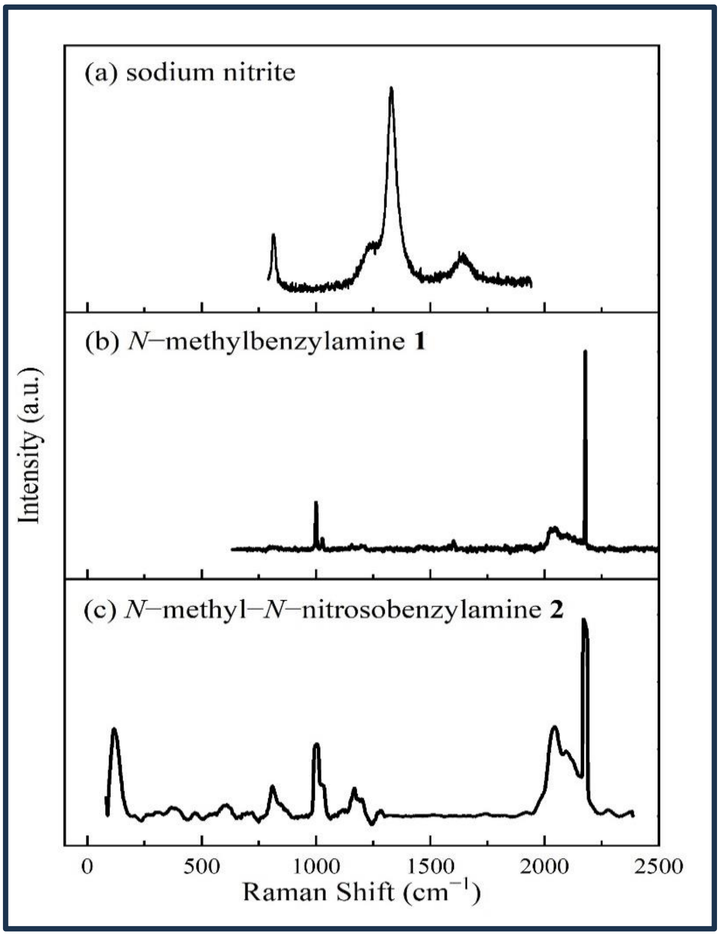

Figure 8.2: Raman spectra of a) sodium nitrite; b) N-methylbenzylamine **1**; c) N-methyl-N-nitrosobenzylamine **2**.

8.3 – Results and discussion

The reaction mechanism was investigated using a current-voltage CV measurement on the reaction mixture and an oxidation peak is observed around 0.4 V (vs Ag/AgCl). A smaller oxidation peak is observed around 1.4 V. This result, in combination with past literature reports,[146,255,256] suggests a possible reaction mechanism based on Figure 8.4. The CV curve shown in Figure 8.3 displays the plots for amine **1** and $NaNO_2$ + amine **1**.

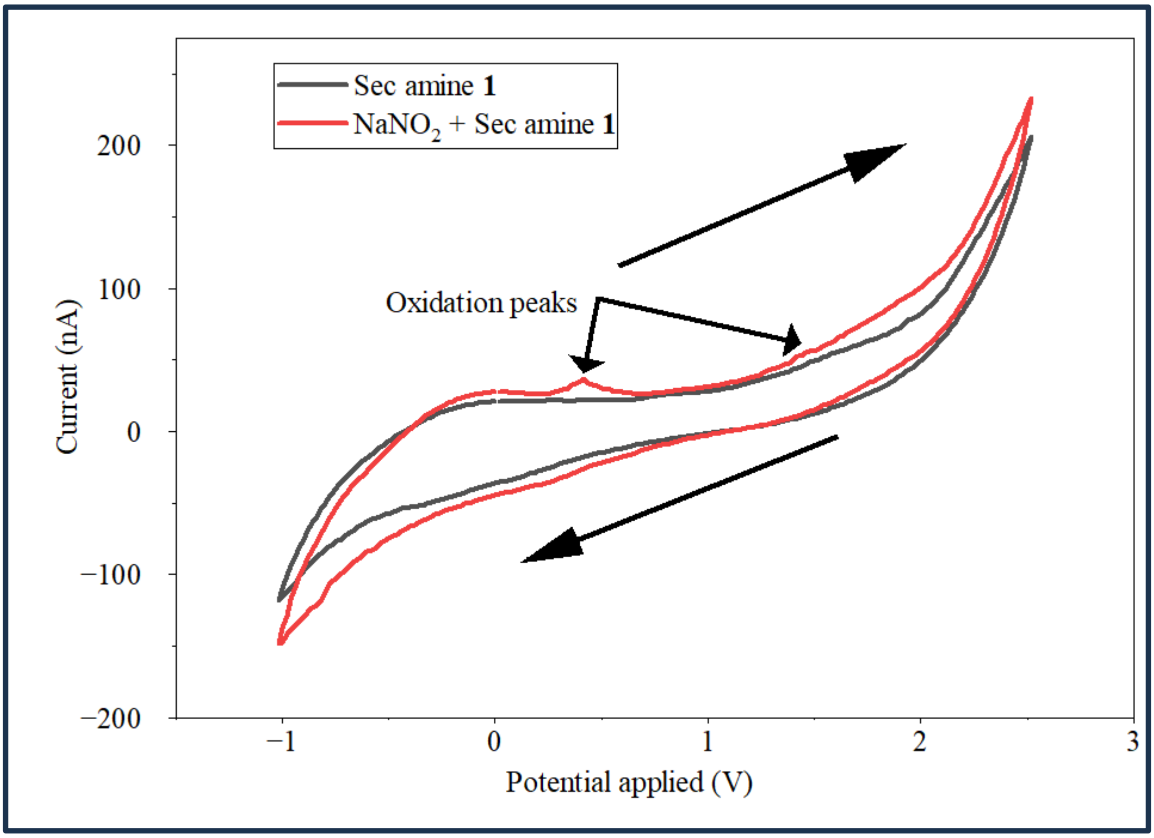

Figure 8.3: Cyclic voltammograms of the secondary amine (N-methylbenzylamine **1**), (5 mM, black) and secondary amine + $NaNO_2$ (5 mM, red). All CVs were taken in MeCN:H_2O = (1:1 v/v) with nBu_4NClO_4 (0.1 M) electrolyte, a graphite cross-section as working electrode, Pt wire counter electrode, 0.1 M Ag/AgCl reference and a scan rate of 100 mV s^{-1}

Initially, the NO_2^- anion undergoes a one electron oxidation to the $NO_2\cdot$ radical. This species can dimerise to form N_2O_4, which is in equilibrium with a NO^+ cation and NO_3^- anion in solution. They interact with the amine (**add-1**), which is followed by the nitrosation (**add-2**) and the introduction of a hydroxide anion, generated from the reduction of water at the cathode. This resulting intermediate (**add-3**) allows the formation of the desired N-nitrosamine **2**, with the release of one water molecule and a nitrate anion.[145] Investigation of the mechanism using density functional theory (DFT) calculations at the SMD/ωB97XD/def2tzvp//B3LYP-D3/6-31G(d) level, were carried out in collaboration by a team from The School of Chemistry at Cardiff University (Chapter 5, Section 5.14). Replacement was made for the current study of the symmetric secondary amine used in previous studies with the asymmetric secondary amine **1**.[21] The formation of int-cis and its conversion to int-trans as the active N_2O_4 isomers has already been discussed by Ali et al.[21] Figure 8.4 shows the calculated reaction pathway for the formation of N-nitrosamine product **2** from the reaction between int-trans and amine **1**.

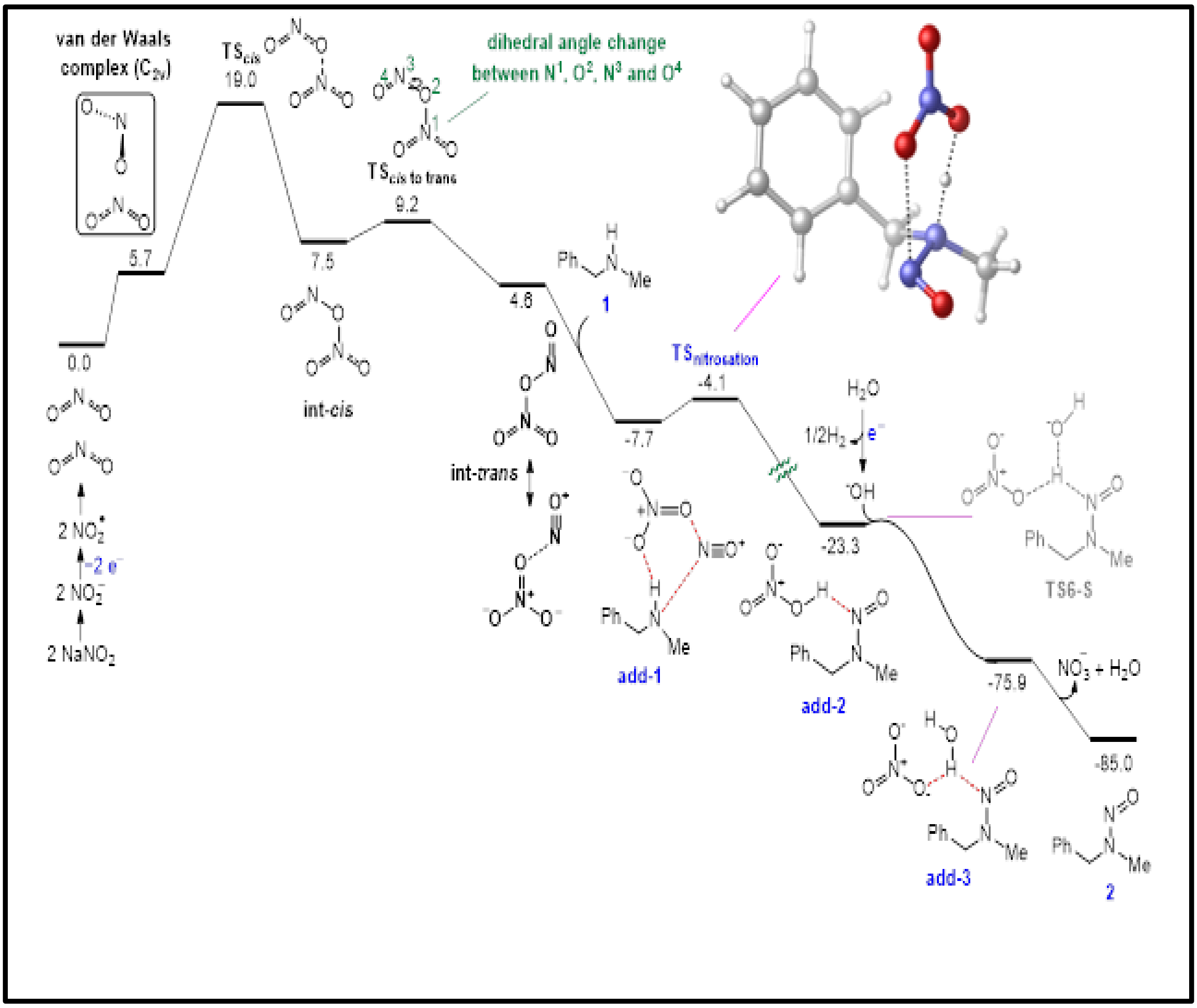

Figure 8.4: DFT reaction pathway for the formation of N-nitrosamine product **2** computed at the SMD/ωB97X-D/def2tzvp//B3LYP-D3/6-31G(d) level of theory. The relative free energies are given in kcalmol^{-1}.

The DFT calculated Raman spectra for each of the intermediate species formed during the course of the reaction are shown in Figure 8.5. The stacked plots show the calculated spectra for the intermediates against the experimental spectra produced at 2.1 V potential. Vertical dashed lines are given for guidance to relate the calculated species and the experimental spectra in order to identify the intermediates contributing to the reactants and products formed. The spectral range examined was from 500 to 2500 cm^{-1}. No peaks are observed above 2600 cm^{-1}.

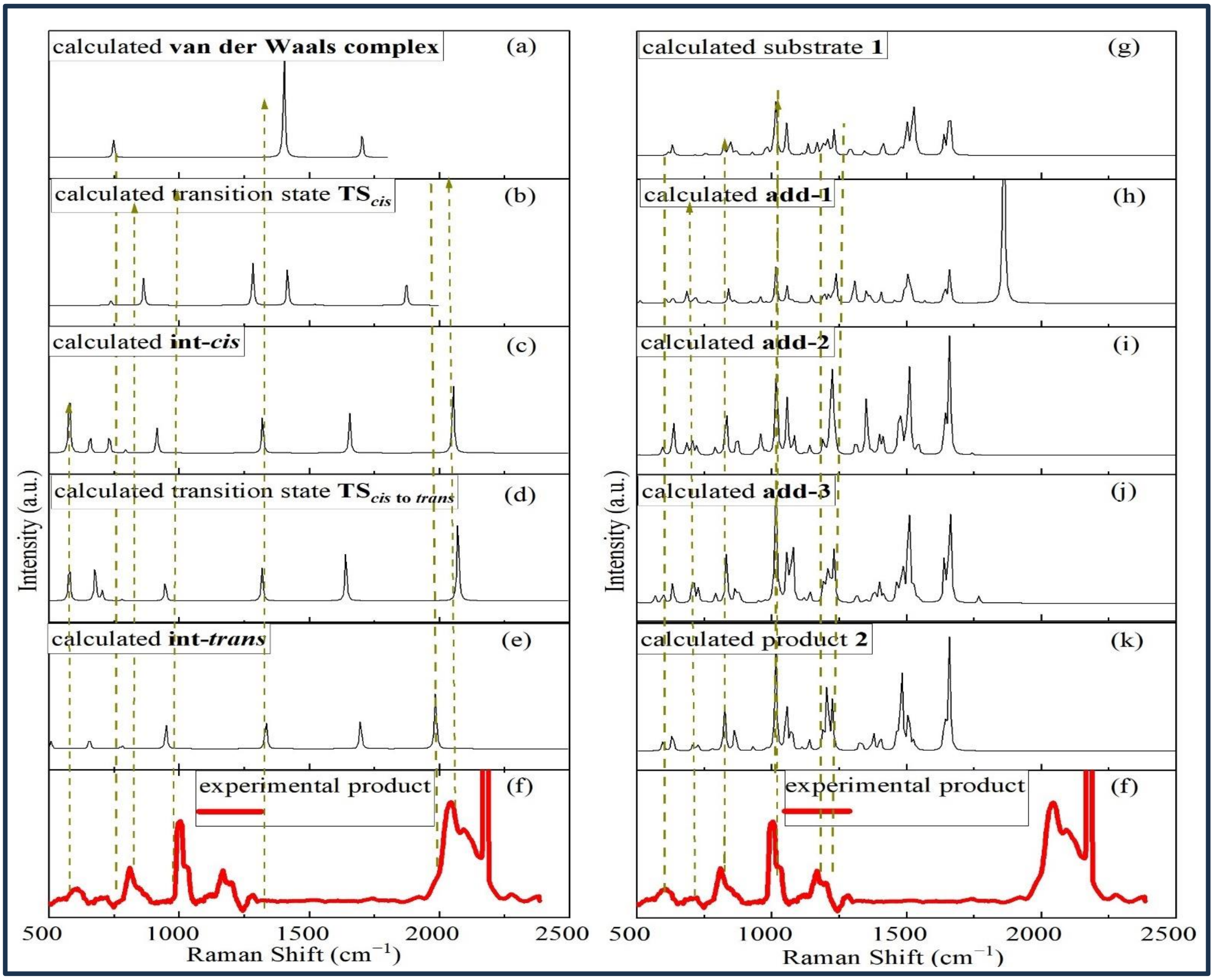

Figure 8.5: Raman spectra of the DFT calculated spectra (a-e, g-k) of the compounds detected and processed against the final experimental product spectra (f) taken at 2.1 V. Dashed lines are given as guidance to relate the intermediate species appearing in the reaction pathway.

The calculated Raman spectra should be treated as guidance only since the environment of the species are not the same in the experimental set up. It is expected that charge state of the molecule, laser wavelength dependence and the local environment influence the Raman spectra resulting in difference in relative intensities of the Raman peaks. Even with these limitations, it can be observed in Fig. 8.5 that all the intermediate species (van der Waals Complex, **TS$_{cis}$,** **int-cis**, **TS$_{cis\ to\ trans}$** and **int-trans**) are contributing to the product reaction pathway through the intermediates. The right-hand plot shows the detection of the intermediate species Substrate **1**,

add-1, **add-2**, **add-3** and Product **2** confirming them as contributors. The pathway for the formation of final product **2** is occurring through the **int-cis** route and **int-trans** formation. In the process of NO_2 isomerisation, the formation of **int-cis** is kinetically preferred, with an activation barrier of 19 kcal mol^{-1}. Subsequently, **int-*cis*** can be converted to **int-*trans*** via a dihedral angle rotation, requiring a low activation barrier of just 1.7 kcal mol^{-1}. After $\mathbf{TS_{cis\ to\ trans}}$ the intermolecular *N*-nitrosation of the secondary amine **1** progresses by forming adduct **add-1** and leading to the production of the final product *N*-nitrosamine **2**. The generation of adducts (**add-2** and **add-3**) also occurs through transition structure $\mathbf{TS_{nitrosation}}$, which has an energy barrier of 3.6 kcal mol^{-1}. When the theoretical spectra of **add-2** and **add-3** are plotted against the final product **2** and the secondary amine reagent **1**, there is clearly a signal overlap that suggests these intermediates are present and will be occuring during the course of the reaction. This is further illustrated in figure 8.5. The HNO_3 species is thought to be contributing to the reaction as nitric acid could be forming from the formation of the by-products NO_3^- and H_2O as part of the breakdown of **add-3** to the final product **2** in the reaction pathway. The assignment of the Raman peaks is summarised in Table 8.1.

Table 8.1. Assignment of Raman peaks from experimental and calculated Raman spectra.

Entry	Wavenumber (cm^{-1})	Peak Assignments
1	110	Van der Waals Complex
2	850	**TScis**
3	603	**int-cis**
4	603, 2062	**TScis to trans**
5	2022	**int-trans**
6	612, 820, 997, 1173, 1205	Substrate **1**
7	820, 997, 1173, 1205	**Add-1**
8	612, 820, 997, 1173, 1205	**Add-2**
9	612, 820, 997, 1173, 1205	**Add-3**
10	612, 820, 997, 1173, 1205	Product **2**

Table 8.1 further highlights the peak overlaps and intermediate detection between the experimental and calculated Raman spectra. Most of the assignments occur between entries 6-10 with mainly single assignments occurring between entries 1-5. This confirms that most of the intermediate detection occurred in the second half of the reaction pathway, from the introduction of substrate **1** to the formation of product **2**.

CHAPTER–9

9.1 – Conclusions

The HSI method used here in Chapter 6 provides an alternative to the current-voltage scan by probing the trion-PL intensity variation with voltage. Previous methods from literature have used various imaging techniques to study MoS_2. These include transmission electron microscopy (TEM) and scanning electron microscopy (SEM).[257] Raman microscopy and photoluminescence (PL) imaging have been used to image CVD-grown MoS_2 flakes.[258, 259] These techniques provide detailed information about the morphology, structure, and properties of MoS_2. However, the advantages of HSI are the capability of reaching <500 nm spatial image resolution depending on the objective lens used, whereas other techniques such as Raman and PL imaging have spatial resolution that is limited by the wavelength of light used and are typically in the micrometre to high nanometre spatial resolution range. HSI has also allowed image sequencing and the study of exciton and trion PL intensity in-situ and in real-time on an exfoliated MoS_2 flake, with the use of a back-gated voltage used to modulate the charge density within the MoS_2 layer. Previous work using a back-gated voltage involved controlling the Fermi level and modulating channel conductance in field-effect transistors (FETs). This technique is used to study MoS_2's electrical and optoelectronic properties, investigate hysteresis effects, and explore its potential for memory and sensing applications on CVD grown material.[260-262] The back-gated voltage used in this study was shown to influence the exciton/trion populations and the PL intensity with higher spatial resolution than other in-situ and real-time techniques such as mentioned above. This technique offers potential scalability in that the electrochemical exfoliation method used can be scaled up and the measurements are performed in an aqueous electrolyte in wide-field mode. A drawback of the HSI technique and a limitation of the instrument, is the poorer spectral resolution obtained from the interferometer which attains only 50 µm resolution and is unable to separate the two main signature peaks of MoS_2 as shown in Chapter 6. Previous methods have shown detail in trion size, temperature effects, trion lifetime, formation and decay processes in MoS_2. Doping methods and the effect of the surrounding solvent medium on trion emission properties, and PL intensity were also investigated.[57, 79, 84, 86, 174, 219, 239] These approaches, however, do not provide information on how efficient MoS_2 is as a catalyst toward the HER and are more useful for optoelectronic and valleytronics applications. The HSI approach is advantageous in that it provides images of trion populations on a MoS_2 flake in an electrochemical environment under varied potentials that indicate potential active sites where direct bandgap FL material is present. This then presents an opportunity for future work in maximizing these trion hotspots for catalysis purposes in HER.

The results show that PL intensity is observed to increase with increasing voltage, as there is a larger concentration of trions at higher positive voltages. The trions appear as a result of charged excitons, and these areas help in determining the regions of the flake that are potentially most active toward the HER. Excitons, in this case, are generated due to both optical excitation by the probing laser and the electrochemical pumping of electrons or holes. In addition, both positive and negatively charged trions can be present in the same monolayer due to heterogeneity arising from defects, electrical charge-induced doping, mechanical deformation and strain, and compositional heterogeneity.[75] These, together with the reacting species, make the electronic states of the excitons and trions highly complex and heterogeneous. This imaging study demonstrates that the HSI technique that has approximately 300 nm spatial resolution is able to resolve the trion hotspot sites; and has further enabled an in-situ investigation of the heterogeneity of an MoS_2 flake in wide-field mode, which provides us with information on the PL profile of the sample. Sufficient resolution is achieved as the imaging system resolved the relevant features of the reaction (spatial variations of PL exciton/trion intensity) without any excessive noise or other artifacts present. This would otherwise have been an unexplored area and gives a new perspective and insight into PL intensity properties on the surface of MoS_2 as the heterogeneity of the MoS_2 flake is important in electrochemical studies. The area of the hotspots determining the overall efficiency of a catalyst in terms of few-layer and multi-layer regions of the flake.

From Chapter 7 on the perovskite degradation study, it is probable from the experimental data that water alone without the application of light is responsible for degradation of the $MAPbBr_3$ perovskite; although further experimentation such as ligh versus dark exposure using separate samples is required to completely rule out the effect of light. A moisture-induced environment appears to have no effect at all on the structure, demonstrating the resistance and structural stability to withstand humid environments. A more acidic environment of pH 3 with a high concentration of H^+ ion is required to retard and delay the onset of the degradation process and create stability of the lattice, as higher pH's with high concentration of OH^- ion appear to accelerate the degradation of NPL, and breakdown of the lattice occurs quite rapidly. The thicker layers appear to degrade to thinner layers in the presence of OH^- ion, and the single unit-cell layers capped with the ligands are the most stable. The Youtube video link referred to in Chapter 7 (p 96) appears to confirm this as the degradation appears to be moving from the external to the internal section of the needles indicating the thinner layers are the last to being protected by the MA ligands. Reduction in PL intensity supports this claim in that pH 3 displays far less reduction in intensity than the higher pH values. Recent literature does propose the formation of PbBr(OH) that stabilises the internal perovskite structure, as PbBr(OH) has higher thermodynamic stability than $MAPbBr_3$.[131, 247]

The three PL emission peaks at 507, 522 and 537 nm would appear to support the degradation process of the basal planes and edges, with one sustaining or increasing in PL (507) and the other two (522 and 537) showing a reduction in PL emission intensity that concurs with the green and blue components both disappearing after 20 mins of exposure to water degradation. This would indicate that thicker layers (green and blue) are degrading faster than thinner layers (red).

It can also be concluded that the water-induced degradation process would appear to be quite non-uniform or inhomogeneous over the whole NPL in terms of thinner layered and thicker bulk regions. This is supported more locally as well as the basal plane and edges appear to show a difference in PL intensity reduction at different regions of the sample. The HSI technique has proved to be very efficient in measuring the in-situ degradation process over the time lapse periods required to observe the perovskite lattice breakdown. The imaging was able to capture the degradation process down to about 50 μm spatial resolution before and after water treatment for areas inside the perovskite NPLs without excessive noise or the presence of other artifacts.

From chapter 6, it can be concluded from the electrochemical-Raman studies on the Ru complex that the combination of Cyclic Voltammetry and Raman Spectroscopy can serve as a powerful tool as it enables the detection of the redox changes that occur on the Ruthenium centre when a change in potential is applied. The potential range can also be varied accordingly depending on where redox reactions are likely to occur. This combined technique could lead to potential applications in medicinal chemistry when metallo-insertion is used to displace mismatched base pairs in a DNA strand.[210] The spectra produced from the electrochemical-Raman measurements performed in this study confirm that the increase in potential applied has caused an increase in the dppz ligand intensity as a result of the redox changes that occur on the Ru centre.

The chapter 8 Raman study on the nitrosation reaction concluded from the experimental data that all ten intermediates were detected using the Electrochemical-Raman technique. This technique has never been used to study intermediate detection of nitroso species from previous studies where Raman spectroscopy was only used as an analytical quantification tool for N_2O_4 and N_2O_5 compounds.[23] The combination of potential applied, in this case 2.1 V for optimum reaction conditions, and the graphite electrode surface enabled the electron transfer to take place during the course of the DFT calculated chemical reaction pathway. This was achieved despite the limitations of the system in terms of species environment and the differences in relative intensities of the Raman peaks.

With sodium nitrite as the nitrosating source, it is a non-hazardous, straightforward, and simple experimental approach that avoids the use of any additional supporting electrolytes or other toxic reagents. Additionally, ambient temperatures and less hazardous solvents were employed for this reaction avoiding harsh reaction conditions. This all demonstrates a greener and more sustainable approach to the synthesis of organic molecules that has potential for scalability.

Finally, the ability of the technique to detect intermediate formation during the nitrosation reaction gives it further value and potential uses for other organic reactions in electrosynthesis applications when an electrochemical cell can be applied.

Overall, the three case studies demonstrate an electrochemical thread used throughout the thesis that has potential for scalability and more greener approaches adopted for in-situ reaction monitoring, whether it be for PL intensity, degradation processes and intermediate formation and detection.

9.2 – Future Work

Future work on MoS_2 could involve finding ways to refine the electrochemical exfoliation method, enabling the flakes to have narrower thickness, shape and lateral size distributions. This would lead to a more homogeneous PL response from the flake at higher voltages applied as there potentially would be a higher concentration of trions forming from the charged excitons, and efficient electron transfer facilitated by excitons and trions. The larger the FL-MoS_2 regions created the more active the surface is toward the HER., as reducing the layers can also promote HER activity, due to increased electron transfer facilitated by the excitons and trions, furthermore, this can increase the hopping of electrons from the working electrode to the MoS_2 surface. MoS_2 single layers are shown to display higher catalytic activity than their bulk crystals, and identification of FL/monolayer could be confirmed by atomic force microscopy (AFM) images [218] This is the ultimate aim of this research, to make the flake surface as active as possible at the basal planes and edges in order to increase the likelihood of the material to function in real catalytic applications such as water splitting for the HER. Reducing the heterogeneity arising from defects, electrical charge-induced doping, mechanical deformation and strain, and making the surface more homogeneous FL/monolayer in architecture is also key in developing a real catalytic material. The influence of the electrical layer formation on the photoluminescence from excitons and trions needs to be investigated further in terms of how it correlates with the voltage applied; and the voltage scan plays a key role in determining the Tafel plot and the overpotential in the HER. HSI imaging has proved to be a very useful tool in detecting higher PL intensities arising from the formation of trions in specific regions of a sample flake and this technique could be used in many other research areas including degradation studies where the decrease in PL intensity could be used as a measure of the rate of degradation. In addition to this, the measurement of hydrogen evolution rate and the current flowing through the hotspots can also be considered in future works.

Future work in the perovskite studies could involve further testing of other perovskite structures in moisture and water environments to compare degradation rates against the $MAPbBr_3$ compound and determine if any improvements can be made. This could involve pH testing again using HSI techniques and drawing comparisons with each structure investigated. Determining if the mechanism of degradation can be done under more neutral conditions would be a positive direction of investigation, to enable the avoidance and use of more acidic solutions that are not environmentally friendly. The results of these types of investigation could pave the way for different synthesis methods to alter the structure using different protecting ligands and protective coatings or layers that can further inhibit and prevent degradation. Controlling the thinness of the layers could be built in to synthesis methods and characterisation techniques such as XPS (X-ray Photoelectron Spectroscopy) and XRD (X-ray Diffraction) could be used to monitor the formation of hydrates and other species that could thicken the layers during a synthesis. This could therefore increasing the durability and lifetime of these materials, and enhance their potential to be used in commercial applications.

Future work for Electrochemical-Raman methods will be directed towards providing different technologies and complementary technologies without replacing conventional chemistry methods. Many industries such as medicine, food and pharmaceuticals could derive benefits from this technology. Many other organic chemistry reactions involving intermediate formation could be investigated using this electrochemical setup with optimising the electrode configurations in terms of working and counter electrodes. The disadvantages could be at a larger scale when the cost of electricity becomes expensive and this leads to everything having to be very efficient to minimise the costs. There is also the potential for waste supporting electrolyte at a larger scale, as these do not always contribute to anything in the reaction. However, it does offer an alternative way to drive a chemical reaction and will be another valuable tool in the industrial chemist's toolbox. The benefits are the potential to scale-up and provide greener more environmentally friendly processes, saving steps and toxic waste, making it a promising alternative that will contribute to the reduction in emissions and the carbon footprint.

The use of AI (Artificial Intelligence) and ML (Machine Learning) ststistical methods can be incorporated into catalysis, perovskite stability studies and electrosynthesis to better optimise processes and perovskite design. In the case of catalysis and electrosynthesis, running enough parallel reactions to create enough data points to train an AI system to identify electrochemically the best catalyst in terms of active sites or trions and product yield produced from the HER.. The best electrode material, solvent or electrolyte for any given reaction could also be determined, and whether both electrodes the anode and cathode can both produce products. In terms of perovskite stability studies, an AI system could be trained to identify the best perovskite when multiple perovskites are exposed to different conditions. This could aid in designing new processes and in the design of more stable perovskites. More recently, machine learning is being used to guide DFT calculations to find optimal electrocatalysts for CO_2 reduction and H_2 evolution through binding energy prediction. The DFT calculations are dedicated to optimizing models and finding optimal materials, respectively.[263]

References

1. D. Voiry, M. Salehi, R. Silva, T. Fujita, M. Chen, T. Asefa, V. B. Shenoy, G. Eda and M. Chhowalla, *Nano letters*, 2013, **13**, 6222-6227.
2. K. Novoselov, A. Mishchenko, A. Carvalho and A. C. Neto, *Science*, 2016, **353**, aac9439.
3. M. Mattinen, P. J. King, L. Khriachtchev, K. Meinander, J. T. Gibbon, V. R. Dhanak, J. Räisänen, M. Ritala and M. Leskelä, *Small*, 2018, **14**, 1800547.
4. G. Siegel, Y. Venkata Subbaiah, M. C. Prestgard and A. Tiwari, *APL materials*, 2015, **3**, 056103.
5. P. Tonndorf, R. Schmidt, P. Böttger, X. Zhang, J. Börner, A. Liebig, M. Albrecht, C. Kloc, O. Gordan and D. R. Zahn, *Optics express*, 2013, **21**, 4908-4916.
6. J.-R. Jacobo, O. F. Olea-Mejía, A. L. Martínez-Hernández and V.-S. Carlos, *FlatChem*, 2024, **45**, 100654.
7. S. Kundu and T. L. Kelly, *EcoMat*, 2020, **2**, e12025.
8. S. Jin, W. Hui, Y. Wang, K. Huang, Q. Shi, C. Ying, D. Liu, Q. Ye, W. Zhou and J. Tian, *Scientific reports*, 2017, **7**, 45209.
9. P. Pistor, *Scientific reports*, 2016.
10. S. T. Ha, X. Liu, Q. Zhang, D. Giovanni, T. C. Sum and Q. Xiong, *Adv. Opt. Mater*, 2014, **2**, 838-844.
11. M. Safdari, A. Fischer, B. Xu, L. Kloo and J. M. Gardner, *Journal of Materials Chemistry A*, 2015, **3**, 9201-9207.
12. W. M. Sears, M. Klein and J. Morrison, *Physical Review B*, 1979, **19**, 2305.
13. G. Grancini, S. Marras, M. Prato, C. Giannini, C. Quarti, F. De Angelis, M. De Bastiani, G. E. Eperon, H. J. Snaith and L. Manna, *The journal of physical chemistry letters*, 2014, **5**, 3836-3842.
14. S.-W. Lee, S. Kim, S. Bae, K. Cho, T. Chung, L. E. Mundt, S. Lee, S. Park, H. Park and M. C. Schubert, *Scientific reports*, 2016, **6**, 38150.
15. T. Chen, J. Xie and P. Gao, *Advanced Energy and Sustainability Research*, 2022, **3**, 2100218.
16. K. Schötz, A. M. Askar, W. Peng, D. Seeberger, T. P. Gujar, M. Thelakkat, A. Köhler, S. Huettner, O. M. Bakr and K. Shankar, *Journal of Materials Chemistry C*, 2020, **8**, 2289-2300.
17. J. B. Guttenplan, *Mutation Research/Reviews in Genetic Toxicology*, 1987, **186**, 81-134.
18. A. Basu, H. D. Gafney and T. C. Strekas, *Inorganic Chemistry*, 1982, **21**, 2231-2235.
19. J. S. Gardner, D. P. Strommen, W. S. Szulbinski, H. Su and J. R. Kincaid, *The Journal of Physical Chemistry A*, 2003, **107**, 351-357.
20. C. V. Kumar, J. K. Barton, N. J. Turro and I. R. Gould, *Inorganic chemistry*, 1987, **26**, 1455-1457.
21. R. Ali, R. Babaahmadi, M. Didsbury, R. Stephens, R. L. Melen and T. Wirth, *Chemistry–A European Journal*, 2023, e202300957.
22. M. A. Kamboures, W. van der Veer, R. B. Gerber and L. F. Phillips, *Physical Chemistry Chemical Physics*, 2008, **10**, 4748-4753.
23. J. E. Harrar, L. P. Rigdon and S. F. Rice, *Journal of Raman spectroscopy*, 1997, **28**, 891-899.
24. M. C. Leech, A. D. Garcia, A. Petti, A. P. Dobbs and K. Lam, *Reaction Chemistry & Engineering*, 2020, **5**, 977-990.
25. J. Utley, *Chemical Society Reviews*, 1997, **26**, 157-167.
26. M. C. Leech and K. Lam, *Nature Reviews Chemistry*, 2022, **6**, 275-286.
27. B. A. Frontana-Uribe, R. D. Little, J. G. Ibanez, A. Palma and R. Vasquez-Medrano, *Green Chemistry*, 2010, **12**, 2099-2119.
28. D. Pletcher, *Electrochemistry Communications*, 2018, **88**, 1-4.
29. F. Xia, H. Wang, D. Xiao, M. Dubey and A. Ramasubramaniam, *Nature Photonics*, 2014, **8**, 899.
30. Q. H. Wang, K. Kalantar-Zadeh, A. Kis, J. N. Coleman and M. S. Strano, *Nature nanotechnology*, 2012, **7**, 699.
31. A. Kokalj, *Computational Materials Science*, 2003, **28**, 155-168.

32. J. Xie, H. Zhang, S. Li, R. Wang, X. Sun, M. Zhou, J. Zhou, X. W. Lou and Y. Xie, *Advanced materials*, 2013, **25**, 5807-5813.
33. M. Chhowalla, H. S. Shin, G. Eda, L.-J. Li, K. P. Loh and H. Zhang, *Nature chemistry*, 2013, **5**, 263.
34. J. Přech, P. Pizarro, D. Serrano and J. Čejka, *Chemical Society Reviews*, 2018, **47**, 8263-8306.
35. H. Yin and Z. Tang, *Chemical Society Reviews*, 2016, **45**, 4873-4891.
36. A. J. Molina-Mendoza, E. Giovanelli, W. S. Paz, M. A. Niño, J. O. Island, C. Evangeli, L. Aballe, M. Foerster, H. S. Van Der Zant and G. Rubio-Bollinger, *Nature communications*, 2017, **8**, 1-9.
37. H. Fang, S. Chuang, T. C. Chang, K. Takei, T. Takahashi and A. Javey, *Nano letters*, 2012, **12**, 3788-3792.
38. E. Scalise, M. Houssa, G. Pourtois, V. Afanas'ev and A. Stesmans, *Nano Research*, 2012, **5**, 43-48.
39. D. Deng, K. Novoselov, Q. Fu, N. Zheng, Z. Tian and X. Bao, *Nature nanotechnology*, 2016, **11**, 218.
40. Z. Cai, B. Liu, X. Zou and H.-M. Cheng, *Chemical reviews*, 2018, **118**, 6091.
41. J. Xiong, J. Di, J. Xia, W. Zhu and H. Li, *Advanced Functional Materials*, 2018, **28**, 1801983.
42. D. Voiry, A. Mohite and M. Chhowalla, *Chemical Society Reviews*, 2015, **44**, 2702-2712.
43. J. H. Han, S. Lee and J. Cheon, *Chemical Society Reviews*, 2013, **42**, 2581-2591.
44. S. Dolai, P. Maiti, A. Ghorai, R. Bhunia, P. K. Paul and D. Ghosh, *ACS Applied Materials & Interfaces*, 2020, **13**, 438-448.
45. D. Kiriya, P. Lobaccaro, H. Y. Y. Nyein, P. Taheri, M. Hettick, H. Shiraki, C. M. Sutter-Fella, P. Zhao, W. Gao and R. Maboudian, *Nano letters*, 2016, **16**, 4047-4053.
46. Y. Xia, J. Huang, W. Wu, Y. Zhang, H. Wang, J. Zhu, J. Yao, L. Xu, Y. Sun and L. Zhang, *ChemCatChem*, 2018, **10**, 4424-4430.
47. S. Mouri, Y. Miyauchi and K. Matsuda, *Nano letters*, 2013, **13**, 5944-5948.
48. C. Meng, X. Chen, Y. Gao, Q. Zhao, D. Kong, M. Lin, X. Chen, Y. Li and Y. Zhou, *Molecules*, 2020, **25**, 1136.
49. S. Pak, J. Lim, J. Hong and S. Cha, *Catalysts*, 2021, **11**, 70.
50. C. Tsai, K. Chan, J. K. Nørskov and F. Abild-Pedersen, *Surface Science*, 2015, **640**, 133-140.
51. B. Kirubasankar, Y. S. Won, L. A. Adofo, S. H. Choi, S. M. Kim and K. K. Kim, *Chemical Science*, 2022, **13**, 7707-7738.
52. B. Ruqia, M. K. Kabiraz, J. W. Hong and S.-I. Choi, *Journal of Energy Chemistry*, 2022, **72**, 217-240.
53. J. Dong, W. Fang, H. Yuan, W. Xia, X. Zeng and W. Shangguan, *ACS Applied Energy Materials*, 2022, **5**, 4893-4902.
54. P. Ganguly, M. Harb, Z. Cao, L. Cavallo, A. Breen, S. Dervin, D. D. Dionysiou and S. C. Pillai, *ACS Energy Letters*, 2019, **4**, 1687-1709.
55. B. Balan, M. M. Xavier and S. Mathew, *ACS omega*, 2023, **8**, 25649-25673.
56. R. Kumar, V. Mishra, T. Dixit, P. K. Barman, P. K. Nayak and M. R. Rao, *Nanoscale*, 2023, **15**, 12358-12365.
57. K. F. Mak, K. He, C. Lee, G. H. Lee, J. Hone, T. F. Heinz and J. Shan, *Nature materials*, 2013, **12**, 207-211.
58. N. Mondal, N. Azam, Y. N. Gartstein, M. Mahjouri-Samani and A. V. Malko, *Advanced Materials*, 2022, **34**, 2110568.
59. M. Drüppel, T. Deilmann, P. Krüger and M. Rohlfing, *Nature communications*, 2017, **8**, 2117.
60. Q. Zhang, W. Wang, J. Zhang, X. Zhu, Q. Zhang, Y. Zhang, Z. Ren, S. Song, J. Wang and Z. Ying, *Advanced Materials*, 2018, **30**, 1707123.
61. D. P. Khatua, A. Singh, S. Gurung and J. Jayabalan, *Micro and Nanostructures*, 2022, **165**, 207205.
62. H. Wang, C. Zhang and F. Rana, *Nano letters*, 2015, **15**, 339-345.
63. T. Manyepedza, T. Auvray, T. Friščić and N. V. Rees, *Electrochemistry Communications*, 2024, **160**, 107678.

64. Z. He, R. Zhao, X. Chen, H. Chen, Y. Zhu, H. Su, S. Huang, J. Xue, J. Dai and S. Cheng, *ACS applied materials & interfaces*, 2018, **10**, 42524-42533.
65. P. HL, P. Mondal, A. Bid and J. K. Basu, *ACS Applied Nano Materials*, 2019, **3**, 641-647.
66. Y. He, Q. He, L. Wang, C. Zhu, P. Golani, A. D. Handoko, X. Yu, C. Gao, M. Ding and X. Wang, *Nature Materials*, 2019, **18**, 1098-1104.
67. S. H. Noh, J. Hwang, J. Kang, M. H. Seo, D. Choi and B. Han, *Journal of Materials Chemistry A*, 2018, **6**, 20005-20014.
68. D. Voiry, J. Yang and M. Chhowalla, *Advanced Materials*, 2016, **28**, 6197-6206.
69. Y. Cao, *ACS nano*, 2021, **15**, 11014-11039.
70. F.-H. Hsiao, C.-C. Chung, C.-H. Chiang, W.-N. Feng, W.-Y. Tzeng, H.-M. Lin, C.-M. Tu, H.-L. Wu, Y.-H. Wang and W.-Y. Woon, *ACS nano*, 2022, **16**, 4298-4307.
71. X. Liu, B. Li, X. Li, A. R. Harutyunyan, J. Hone and D. V. Esposito, *Nano letters*, 2019, **19**, 8118-8124.
72. C. Emmenegger, P. Mauron, P. Sudan, P. Wenger, V. Hermann, R. Gallay and A. Züttel, *Journal of Power Sources*, 2003, **124**, 321-329.
73. L. Diederich, E. Barborini, P. Piseri, A. Podesta, P. Milani, A. Schneuwly and R. Gallay, *Applied physics letters*, 1999, **75**, 2662-2664.
74. I. Hadjipaschalis, A. Poullikkas and V. Efthimiou, *Renewable and sustainable energy reviews*, 2009, **13**, 1513-1522.
75. A. Rufer and P. Barrade, *IEEE Transactions on industry applications*, 2002, **38**, 1151-1159.
76. S. C. Smith and P. Sen, 2008.
77. T.-X. Huang, X. Cong, S.-S. Wu, J.-B. Wu, Y.-F. Bao, M.-F. Cao, L. Wu, M.-L. Lin, X. Wang and P.-H. Tan, *Nature Catalysis*, 2024, 1-9.
78. S. Golovynskyi, I. Irfan, M. Bosi, L. Seravalli, O. I. Datsenko, I. Golovynska, B. Li, D. Lin and J. Qu, *Applied Surface Science*, 2020, **515**, 146033.
79. J. S. Ross, S. Wu, H. Yu, N. J. Ghimire, A. M. Jones, G. Aivazian, J. Yan, D. G. Mandrus, D. Xiao and W. Yao, *Nature communications*, 2013, **4**, 1474.
80. J. W. Christopher, B. B. Goldberg and A. K. Swan, *Scientific reports*, 2017, **7**, 14062.
81. C. Zhang, H. Wang, W. Chan, C. Manolatou and F. Rana, *Physical Review B*, 2014, **89**, 205436.
82. T. C. Berkelbach, M. S. Hybertsen and D. R. Reichman, *Physical Review B—Condensed Matter and Materials Physics*, 2013, **88**, 045318.
83. A. Genco, C. Trovatello, C. Louca, K. Watanabe, T. Taniguchi, A. I. Tartakovskii, G. Cerullo and S. Dal Conte, *physica status solidi (b)*, 2023, **260**, 2200376.
84. A. Singh, G. Moody, K. Tran, M. E. Scott, V. Overbeck, G. Berghäuser, J. Schaibley, E. J. Seifert, D. Pleskot and N. M. Gabor, *Physical Review B*, 2016, **93**, 041401.
85. W. Su, H. Dou, D. Huo, N. Dai and L. Yang, *Chemical Physics Letters*, 2015, **635**, 40-44.
86. A. Thomas and K. B. Jinesh, *ACS omega*, 2022, **7**, 6531-6538.
87. Y. Shi, H. Li and L.-J. Li, *Chemical Society Reviews*, 2015, **44**, 2744-2756.
88. H. Li, Y. Li, A. Aljarb, Y. Shi and L.-J. Li, *Chemical reviews*, 2017, **118**, 6134-6150.
89. M. Mattinen, P. J. King, G. Popov, J. Hämäläinen, M. J. Heikkilä, M. Leskelä and M. Ritala, *2D Materials*, 2019, **7**, 011003.
90. C. Backes, T. M. Higgins, A. Kelly, C. Boland, A. Harvey, D. Hanlon and J. N. Coleman, *Chemistry of materials*, 2017, **29**, 243-255.
91. A. P. Balan, S. Radhakrishnan, C. F. Woellner, S. K. Sinha, L. Deng, C. de los Reyes, B. M. Rao, M. Paulose, R. Neupane and A. Apte, *Nature nanotechnology*, 2018, **13**, 602-609.
92. J. N. Coleman, M. Lotya, A. O'Neill, S. D. Bergin, P. J. King, U. Khan, K. Young, A. Gaucher, S. De and R. J. Smith, *Science*, 2011, **331**, 568-571.
93. N. Higashitarumizu, H. Kawamoto, M. Nakamura, K. Shimamura, N. Ohashi, K. Ueno and K. Nagashio, *Nanoscale*, 2018, **10**, 22474-22483.
94. V. Nicolosi, M. Chhowalla, M. G. Kanatzidis, M. S. Strano and J. N. Coleman, *Science*, 2013, **340**, 1226419.
95. D. Wei, L. Peng, M. Li, H. Mao, T. Niu, C. Han, W. Chen and A. T. S. Wee, *ACS nano*, 2015, **9**, 164-171.

96. H. Kim, C. Ahn, G. Arabale, C. Lee and T. Kim, *ECS Transactions*, 2013, **58**, 47-50.
97. A.-Y. Lu, H. Zhu, J. Xiao, C.-P. Chuu, Y. Han, M.-H. Chiu, C.-C. Cheng, C.-W. Yang, K.-H. Wei and Y. Yang, *Nature nanotechnology*, 2017, **12**, 744-749.
98. K. Yi, D. Liu, X. Chen, J. Yang, D. Wei, Y. Liu and D. Wei, *Accounts of Chemical Research*, 2021, **54**, 1011-1022.
99. G. Lucovsky and D. Tsu, *Journal of Vacuum Science & Technology A: Vacuum, Surfaces, and Films*, 1987, **5**, 2231-2238.
100. T. H. Choudhury, X. Zhang, Z. Y. Al Balushi, M. Chubarov and J. M. Redwing, *Annual Review of Materials Research*, 2020, **50**, 155-177.
101. A. Koma, *Progress in crystal growth and characterization of materials*, 1995, **30**, 129-152.
102. M. Mattinen, G. Popov, M. Vehkamäki, P. J. King, K. Mizohata, P. Jalkanen, J. Räisänen, M. Leskelä and M. Ritala, *Chemistry of Materials*, 2019, **31**, 5713-5724.
103. M. Mattinen, T. Hatanpää, T. Sarnet, K. Mizohata, K. Meinander, P. J. King, L. Khriachtchev, J. Räisänen, M. Ritala and M. Leskelä, *Advanced Materials Interfaces*, 2017, **4**, 1700123.
104. J. Hämäläinen, M. Mattinen, K. Mizohata, K. Meinander, M. Vehkamäki, J. Räisänen, M. Ritala and M. Leskelä, *Advanced Materials*, 2018, **30**, 1703622.
105. G. Popov, M. Mattinen, T. Hatanpää, M. Vehkamäki, M. Kemell, K. Mizohata, J. Räisänen, M. Ritala and M. Leskelä, *Chemistry of Materials*, 2019, **31**, 1101-1109.
106. Z. Li, X. Zhao, S. Wu, M. Lu, X. Xie and J. Yan, *Crystal Growth & Design*, 2024, **24**, 1865-1879.
107. M. Yi and Z. Shen, *Journal of Materials Chemistry A*, 2015, **3**, 11700-11715.
108. K. S. Novoselov, A. K. Geim, S. V. Morozov, D. Jiang, Y. Zhang, S. V. Dubonos, I. V. Grigorieva and A. A. Firsov, *science*, 2004, **306**, 666-669.
109. M. Osada and T. Sasaki, *Journal of Materials Chemistry*, 2009, **19**, 2503-2511.
110. G. Abellan, C. Martí-Gastaldo, A. Ribera and E. Coronado, *Accounts of chemical research*, 2015, **48**, 1601-1611.
111. Y. Fang, X. Li, J. Li, C. Yao, H. Y. Hoh, X. Hai, J. Lu and C. Su, *Journal of Materials Chemistry A*, 2019, **7**, 25691-25711.
112. W. Wu, J. Xu, X. Tang, P. Xie, X. Liu, J. Xu, H. Zhou, D. Zhang and T. Fan, *Chemistry of Materials*, 2018, **30**, 5932-5940.
113. D. Voiry, J. Yang, J. Kupferberg, R. Fullon, C. Lee, H. Y. Jeong, H. S. Shin and M. Chhowalla, *Science*, 2016, **353**, 1413-1416.
114. Y.-J. Zhu and F. Chen, *Chemical reviews*, 2014, **114**, 6462-6555.
115. M. N. Nadagouda, T. F. Speth and R. S. Varma, *Accounts of Chemical Research*, 2011, **44**, 469-478.
116. S. Reshmi, M. Akshaya, B. Satpati, A. Roy, P. K. Basu and K. Bhattacharjee, *Materials Research Express*, 2017, **4**, 115012.
117. D. H. Cao, C. C. Stoumpos, O. K. Farha, J. T. Hupp and M. G. Kanatzidis, *Journal of the American Chemical Society*, 2015, **137**, 7843-7850.
118. P. Chen, Y. Bai, S. Wang, M. Lyu, J. H. Yun and L. Wang, *Advanced Functional Materials*, 2018, **28**, 1870113.
119. J. Hwang, R. R. Rao, L. Giordano, Y. Katayama, Y. Yu and Y. Shao-Horn, *Science*, 2017, **358**, 751-756.
120. G. Wu, R. Zhang, H. Wang, K. Ma, J. Xia, W. Lv, G. Xing and C. Runfeng, *Advanced Materials*, 2024, **36**.
121. B. Malani S, E. Klein, R. Lesyuk and C. Klinke, *Advanced Functional Materials*, 2025, **35**, 2416027.
122. Y. Wang, Y. Shi, G. Xin, J. Lian and J. Shi, *Crystal Growth & Design*, 2015, **15**, 4741-4749.
123. V. A. Hintermayr, A. F. Richter, F. Ehrat, M. Döblinger, W. Vanderlinden, J. A. Sichert, Y. Tong, L. Polavarapu, J. Feldmann and A. S. Urban, *Advanced materials*, 2016, **28**, 9478-9485.

124. J. A. Sichert, Y. Tong, N. Mutz, M. Vollmer, S. Fischer, K. Z. Milowska, R. García Cortadella, B. Nickel, C. Cardenas-Daw and J. K. Stolarczyk, *Nano letters*, 2015, **15**, 6521-6527.
125. E. Kim, K. Huang, S. Jegelka and E. Olivetti, *npj Computational Materials*, 2017, **3**, 1-9.
126. J. Yang, B. D. Siempelkamp, D. Liu and T. L. Kelly, *ACS nano*, 2015, **9**, 1955-1963.
127. A. M. Leguy, Y. Hu, M. Campoy-Quiles, M. I. Alonso, O. J. Weber, P. Azarhoosh, M. Van Schilfgaarde, M. T. Weller, T. Bein and J. Nelson, *Chemistry of Materials*, 2015, **27**, 3397-3407.
128. C. Klinke, *Journal*, 2019.
129. J. A. Christians, P. A. Miranda Herrera and P. V. Kamat, *Journal of the American Chemical Society*, 2015, **137**, 1530-1538.
130. D. Bryant, N. Aristidou, S. Pont, I. Sanchez-Molina, T. Chotchunangatchaval, S. Wheeler, J. R. Durrant and S. A. Haque, *Energy & Environmental Science*, 2016, **9**, 1655-1660.
131. K.-K. Liu, Q. Liu, D.-W. Yang, Y.-C. Liang, L.-Z. Sui, J.-Y. Wei, G.-W. Xue, W.-B. Zhao, X.-Y. Wu and L. Dong, *Light: Science & Applications*, 2020, **9**, 44.
132. R. Singh, S. R. Suranagi, M. Kumar and V. K. Shukla, *Journal of Applied Physics*, 2017, **122**.
133. E. Klein, R. Lesyuk and C. Klinke, *Small*, 2024, **20**, 2405758.
134. P. N. Magee and J. Barnes, *British journal of cancer*, 1956, **10**, 114.
135. W. Lijinsky, *Cancer and Metastasis Reviews*, 1987, **6**, 301-356.
136. Y. L. Kostyukovskii and D. B. Melamed, *Russian Chemical Reviews*, 1988, **57**, 350.
137. A. Tricker and R. Preussmann, *Mutation research/genetic toxicology*, 1991, **259**, 277-289.
138. W. Jin-Mei, L.-S. Shoei-Yn and L. Jen-Kun, *Biochemical pharmacology*, 1993, **45**, 819-825.
139. M. Nakajima, J. C. Warner and J.-P. Anselme, *Tetrahedron letters*, 1984, **25**, 2619-2622.
140. E. H. White and W. R. Feldman, *Journal of the American Chemical Society*, 1957, **79**, 5832-5833.
141. D. Lovejoy and A. Vosper, *Journal of the Chemical Society A: Inorganic, Physical, Theoretical*, 1968, 2325-2328.
142. B. C. Challis and S. A. Kyrtopoulos, *Journal of the Chemical Society, Chemical Communications*, 1976, 877-878.
143. B. C. Challis and S. A. Kyrtopoulos, *Journal of the Chemical Society, Perkin Transactions 2*, 1978, 1296-1302.
144. B. C. Challis and S. A. Kyrtopoulos, *Journal of the Chemical Society, Perkin Transactions 1*, 1979, 299-304.
145. M. Masui, N. Yamawaki and H. Ohmori, *Chemical and pharmaceutical bulletin*, 1988, **36**, 459-461.
146. Y. Wang, S. You, M. Ruan, F. Wang, C. Ma, C. Lu, G. Yang, Z. Chen and M. Gao, *European Journal of Organic Chemistry*, 2021, **2021**, 3289-3293.
147. S. F. Agnew, B. Swanson, L. Jones and R. Mills, *The Journal of Physical Chemistry*, 1985, **89**, 1678-1682.
148. L. Jones, B. Swanson and S. Agnew, *The Journal of chemical physics*, 1985, **82**, 4389-4390.
149. A. Givan and A. Loewenschuss, *The Journal of Chemical Physics*, 1989, **90**, 6135-6142.
150. A. Givan and A. Loewenschuss, *The Journal of chemical physics*, 1989, **91**, 5126-5127.
151. A. Givan and A. Loewenschuss, *The Journal of chemical physics*, 1991, **94**, 7562-7563.
152. W. G. Fateley, H. A. Bent and B. Crawford Jr, *The Journal of Chemical Physics*, 1959, **31**, 204-217.
153. I. Hisatsune, J. Devlin and Y. Wada, *The Journal of Chemical Physics*, 1960, **33**, 714-719.
154. R. V. St Louis and B. Crawford, *The Journal of Chemical Physics*, 1965, **42**, 857-864.
155. H. Beckers, X. Zeng and H. Willner, *Chemistry–A European Journal*, 2010, **16**, 1506-1520.
156. J. Harrar and R. Pearson, *Journal of the Electrochemical Society*, 1983, **130**, 108.
157. J. A. Happe and A. G. Whittaker, *The Journal of Chemical Physics*, 1959, **30**, 417-421.
158. C. C. Addison, *Chemical Reviews*, 1980, **80**, 21-39.
159. J. E. Harrar, R. Quong, L. P. Rigdon and R. McGuire, *Journal of the Electrochemical Society*, 1997, **144**, 2032.

160. P. A. Brooksby and A. J. McQuillan, *The Journal of Physical Chemistry C*, 2010, **114**, 17604-17609.
161. D. R. Lide, *Ann Arbor, Lodon, Tokyo*, 1992, **1993**.
162. M. W. Chase, *J. of Physical and Chemical Reffernce Data*, 1998, 1529-1564.
163. C. C. Addison, L. J. Blackwell, B. Harrison, D. H. Jones, N. Logan, E. K. Nunn and S. C. Wallwork, *Journal of the Chemical Society, Chemical Communications*, 1973, 347-348.
164. L. J. Blackwell, E. K. Nunn and S. C. Wallwork, *Journal of the Chemical Society, Dalton Transactions*, 1975, 2068-2072.
165. N. Logan, *Pure and applied chemistry*, 1986, **58**, 1147-1152.
166. H. H. Perkampus, H. C. Grinter and T. L. Threlfall, *UV-VIS Spectroscopy and Its Applications*, Springer Berlin Heidelberg, 2013.
167. K. Naresh, *J. Chem. Pharm. Sci*, 2014, **974**, 2115.
168. K. P. Goetz, A. D. Taylor, F. Paulus and Y. Vaynzof, *Advanced Functional Materials*, 2020, **30**, 1910004.
169. U. Alexiev and D. L. Farrens, *Biochimica et Biophysica Acta (BBA)-Bioenergetics*, 2014, **1837**, 694-709.
170. J. C. Del Valle and J. Catalán, *Physical Chemistry Chemical Physics*, 2019, **21**, 10061-10069.
171. N. P. Cook, M. Ozbil, C. Katsampes, R. Prabhakar and A. A. Martí, *Journal of the American Chemical Society*, 2013, **135**, 10810-10816.
172. H. H. Jaffé and A. L. Miller, *Journal of chemical education*, 1966, **43**, 469.
173. D. J. Vogel and D. S. Kilin, *The Journal of Physical Chemistry C*, 2015, **119**, 27954-27964.
174. J. Pei, J. Yang, R. Xu, Y. H. Zeng, Y. W. Myint, S. Zhang, J. C. Zheng, Q. Qin, X. Wang and W. Jiang, *Small*, 2015, **11**, 6384-6390.
175. M. Amani, D.-H. Lien, D. Kiriya, J. Xiao, A. Azcatl, J. Noh, S. R. Madhvapathy, R. Addou, S. Kc and M. Dubey, *Science*, 2015, **350**, 1065-1068.
176. A. C. Ferrari and D. M. Basko, *Nature nanotechnology*, 2013, **8**, 235.
177. J. R. Ferraro, *Introductory raman spectroscopy*, Elsevier, 2003.
178. X. Lu, X. Luo, J. Zhang, S. Y. Quek and Q. Xiong, *Nano Research*, 2016, **9**, 3559-3597.
179. C. Hess, *Chemical Society Reviews*, 2021, **50**, 3519-3564.
180. X. Zhao, Z. Li, S. Wu, M. Lu, X. Xie, D. Zhan and J. Yan, *Advanced Electronic Materials*, 2024, **10**, 2300610.
181. U. Sharma, B. Tyagi and R. V. Jasra, *Industrial & engineering chemistry research*, 2008, **47**, 9588-9595.
182. L. Lin, X. Bi, Y. Gu, F. Wang and J. Ye, *Journal of Applied Physics*, 2021, **129**.
183. F. Tumino, P. D'Agosta, V. Russo, A. Li Bassi and C. S. Casari, *Crystals*, 2023, **13**, 1271.
184. O. Samy, S. Zeng, M. D. Birowosuto and A. El Moutaouakil, *Crystals*, 2021, **11**, 355.
185. G. E. Shillito, C. B. Larsen, J. R. McLay, N. T. Lucas and K. C. Gordon, *Inorganic Chemistry*, 2016, **55**, 11170-11184.
186. J. Marotz, A. Siafliakis, A. Holmer, A. Kulcke and F. Siemers, *Wound Medicine*, 2015, **10**, 17-22.
187. B. Lu, P. D. Dao, J. Liu, Y. He and J. Shang, *Remote Sensing*, 2020, **12**, 2659.
188. R. A. Schultz, T. Nielsen, J. R. Zavaleta, R. Ruch, R. Wyatt and H. R. Garner, *Cytometry*, 2001, **43**, 239-247.
189. G. A. Mabbott, *Journal of Chemical education*, 1983, **60**, 697.
190. P. T. Kissinger and W. R. Heineman, *Journal of Chemical Education*, 1983, **60**, 702.
191. N. Elgrishi, *jchemeduc*, 2017.
192. A. Cranny and J. K. Atkinson, *Measurement Science and Technology*, 1998, **9**, 1557.
193. J. A. Rudd, M. K. Brennaman, K. E. Michaux, D. L. Ashford, R. W. Murray and T. J. Meyer, *The Journal of Physical Chemistry A*, 2016, **120**, 1845-1852.
194. J. H. Christie and P. J. Lingane, *Journal of Electroanalytical Chemistry (1959)*, 1965, **10**, 176-182.
195. M. Gama Sauaia and R. Santana da Silva, *Transition metal chemistry*, 2003, **28**, 254-259.
196. K. C. Kwon, S. Choi, K. Hong, C. W. Moon, Y.-S. Shim, T. Kim, W. Sohn, J.-M. Jeon, C.-H. Lee and K. T. Nam, *Energy & Environmental Science*, 2016, **9**, 2240-2248.

197. M. Frisch and F. Clemente, *Scalmani, V. Barone, B. Mennucci, GA Petersson, H. Nakatsuji, M. Caricato, X. Li, HP Hratchian, AF Izmaylov, J. Bloino and G. Zhe, Gaussian*, 2009, **9**.
198. M. Head-Gordon, J. A. Pople and M. J. Frisch, *Chemical physics letters*, 1988, **153**, 503-506.
199. A. D. Becke, *The Journal of chemical physics*, 1993, **98**, 5648-5652.
200. Q. Wu and W. Yang, *The Journal of chemical physics*, 2002, **116**, 515-524.
201. S. H. Vosko, L. Wilk and M. Nusair, *Canadian Journal of physics*, 1980, **58**, 1200-1211.
202. P. J. Stephens, F. J. Devlin, C. F. Chabalowski and M. J. Frisch, *The Journal of physical chemistry*, 1994, **98**, 11623-11627.
203. S. Grimme, J. Antony, S. Ehrlich and H. Krieg, *The Journal of chemical physics*, 2010, **132**.
204. A. V. Marenich, C. J. Cramer and D. G. Truhlar, *The Journal of Physical Chemistry B*, 2009, **113**, 6378-6396.
205. P. C. Hariharan and J. A. Pople, *Theoretica chimica acta*, 1973, **28**, 213-222.
206. C.-S. Wu and J.-D. Chai, *Journal of chemical theory and computation*, 2015, **11**, 2003-2011.
207. F. Weigend, F. Furche and R. Ahlrichs, *The Journal of chemical physics*, 2003, **119**, 12753-12762.
208. L. Lu, H. Hu, H. Hou and B. Wang, *Computational and Theoretical Chemistry*, 2013, **1015**, 64-71.
209. C. Legault, *Journal*, 2009.
210. F.-I. Lu, C. B. Gilks, A.-M. Mulligan, P. Ryan, G. Allo, K. Sy, P. A. Shaw, A. Pollett and B. A. Clarke, *International journal of gynecological pathology*, 2012, **31**, 524-531.
211. S. A. Magee, S. Sproules, A.-L. Barra, G. F. Whitehead, D. Collison, R. E. Winpenny and E. McInnes, *Magnetic Properties of Heterometallic Ruthenium-based Clusters*, **1001**, 128.
212. C.-Z. Zhao, N. Egashira, Y. Kurauchi and K. Ohga, *Electrochimica acta*, 1998, **43**, 2167-2173.
213. W.-Y. Lee, *Microchimica Acta*, 1997, **127**, 19-39.
214. R. J. Smith, P. J. King, M. Lotya, C. Wirtz, U. Khan, S. De, A. O'Neill, G. S. Duesberg, J. C. Grunlan and G. Moriarty, *Advanced materials*, 2011, **23**, 3944-3948.
215. C. Backes, D. Hanlon, B. M. Szydlowska, A. Harvey, R. J. Smith, T. M. Higgins and J. N. Coleman, *JoVE (Journal of Visualized Experiments)*, 2016, e54806.
216. Q. Chen, C. Dwyer, G. Sheng, C. Zhu, X. Li, C. Zheng and Y. Zhu, *Advanced Materials*, 2020, **32**, 1907619.
217. M. Agrawal, V. Prasad, G. Nijhawan, S. S. Jalal, B. Rajalakshmi and S. P. Dwivedi, 2024.
218. A. Splendiani, L. Sun, Y. Zhang, T. Li, J. Kim, C.-Y. Chim, G. Galli and F. Wang, *Nano letters*, 2010, **10**, 1271-1275.
219. K. M. McCreary, A. T. Hanbicki, S. V. Sivaram and B. T. Jonker, *Apl Materials*, 2018, **6**.
220. Y. Liu, T. Shen, S. Linghu, R. Zhu and F. Gu, *Nanoscale Advances*, 2022, **4**, 2484-2493.
221. N. Liu, P. Kim, J. H. Kim, J. H. Ye, S. Kim and C. J. Lee, *ACS nano*, 2014, **8**, 6902-6910.
222. D. W. Thompson, A. Ito and T. J. Meyer, *Pure and Applied Chemistry*, 2013, **85**, 1257-1305.
223. M. N. Ackermann and L. V. Interrante, *Inorganic Chemistry*, 1984, **23**, 3904-3911.
224. J. V. Caspar and T. J. Meyer, *Inorganic Chemistry*, 1983, **22**, 2444-2453.
225. M. Siao, W. Shen, R. Chen, Z. Chang, M. Shih, Y. Chiu and C.-M. Cheng, *Nature communications*, 2018, **9**, 1442.
226. D. Lembke, A. Allain and A. Kis, *Nanoscale*, 2015, **7**, 6255-6260.
227. M.-W. Lin, I. I. Kravchenko, J. Fowlkes, X. Li, A. A. Puretzky, C. M. Rouleau, D. B. Geohegan and K. Xiao, *Nanotechnology*, 2016, **27**, 165203.
228. M. I. Prodromidis, A. B. Florou, S. M. Tzouwara-Karayanni and M. I. Karayannis, *Electroanalysis: An International Journal Devoted to Fundamental and Practical Aspects of Electroanalysis*, 2000, **12**, 1498-1501.
229. R. Beaulac, A. Lever and C. Reber, *Journal*, 2007.
230. J. Wu, 2007.
231. S. F. Parker and I. R. Butler, *European Journal of Inorganic Chemistry*, 2019, **2019**, 1142-1146.
232. Q. Sun, B. Dereka, E. Vauthey, L. M. L. Daku and A. Hauser, *Chemical science*, 2017, **8**, 223-230.

233. S. Das and B. Pradhan, *RSC Advances*, 2015, **5**, 73726-73731.
234. Y. Liu, H. Nan, X. Wu, W. Pan, W. Wang, J. Bai, W. Zhao, L. Sun, X. Wang and Z. Ni, *ACS nano*, 2013, **7**, 4202-4209.
235. T. Goswami, R. Rani, K. Hazra and H. Ghosh, *The Journal of Physical Chemistry Letters*, 2019, **10**, 3057-3063.
236. R. Hu, Z. Huang, B. Wang, H. Qiao and X. Qi, *Journal of Materials Science: Materials in Electronics*, 2021, **32**, 7237-7248.
237. J. Pandey and A. Soni, *Applied Surface Science*, 2019, **463**, 52-57.
238. W. Wang, N. Sui, M. Ni, X. Chi, L. Pan, H. Zhang, Z. Kang, Q. Zhou and Y. Wang, *The Journal of Physical Chemistry C*, 2019, **124**, 1749-1754.
239. G. D. Shepard, J. V. Ardelean, O. A. Ajayi, D. Rhodes, X. Zhu, J. C. Hone and S. Strauf, *ACS nano*, 2017, **11**, 11550-11558.
240. Y. Wang and C. D. Frisbie, *The Journal of Physical Chemistry C*, 2024, **128**, 1819-1826.
241. H. Fei, R. Liu, Y. Zhang, H. Wang, M. Wang, S. Wang, M. Ni, Z. Wu and J. Wang, *Materials Futures*, 2023, **2**, 022103.
242. N. Vicente and G. Garcia-Belmonte, *The journal of physical chemistry letters*, 2017, **8**, 1371-1374.
243. A. Jancik Prochazkova, M. C. Scharber, C. Yumusak, J. Jančík, J. Másilko, O. Brüggemann, M. Weiter, N. S. Sariciftci, J. Krajcovic and Y. Salinas, *Scientific reports*, 2020, **10**, 15720.
244. N. Droseros, G. Longo, J. C. Brauer, M. Sessolo, H. J. Bolink and N. Banerji, *ACS energy letters*, 2018, **3**, 1458-1466.
245. A. Niebur, E. Klein, R. Lesyuk, C. Klinke and J. Lauth, *arXiv preprint arXiv:2408.04571*, 2024.
246. T. Song, X. Feng, H. Ju, T. Fang, F. Zhu, W. Liu and W. Huang, *Journal of Alloys and Compounds*, 2020, **816**, 152558.
247. T. Xu, G. Liu, S. Zhou, W. Cao, J. Li and Z. Liu, *Nanotechnology*, 2023, **34**, 455601.
248. L. McGovern, M. H. Futscher, L. A. Muscarella and B. Ehrler, *The journal of physical chemistry letters*, 2020, **11**, 7127-7132.
249. A. b. L. Fridman, F. Mukhametshin and S. S. Novikov, *Russian Chemical Reviews*, 1971, **40**, 34.
250. K. Kano and J. P. Anselme, *Bulletin des Sociétés Chimiques Belges*, 1983, **92**, 229-232.
251. V. E. Platonov, A. Haas, M. Schelvis, M. Lieb, K. V. Dvornikova, O. I. Osina, T. V. Rybalova and Y. V. Gatilov, *Journal of fluorine chemistry*, 2002, **114**, 55-61.
252. K. Laihia, A. Puszko, E. Kolehmainen and J. Lorenc, *Journal of molecular structure*, 2007, **831**, 203-208.
253. A. Klasek, A. Lyčka, F. Křemen, A. Růžička and M. Rouchal, *Helvetica Chimica Acta*, 2016, **99**, 50-62.
254. C. E. Castellano, A. J. Calandra and A. J. Arvia, *Electrochimica Acta*, 1974, **19**, 701-712.
255. C. Castellano, J. Wargon and A. Arvia, *Journal of Electroanalytical Chemistry and Interfacial Electrochemistry*, 1973, **47**, 371-372.
256. N. Tanaka and K. Kato, *Bulletin of the Chemical Society of Japan*, 1956, **29**, 837-842.
257. Q. Sun, H. Miao, X. Hu, G. Zhang, D. Zhang, E. Liu, Y. Hao, X. Liu and J. Fan, *Journal of Materials Science: Materials in Electronics*, 2016, **27**.
258. H. M. Oh, G. H. Han, H. Kim, J. J. Bae, M. S. Jeong and Y. H. Lee, *ACS nano*, 2016, **10**, 5230-5236.
259. D. Tuschel, 2015.
260. C. Marquez, N. Salazar, F. Gity, J. C. Galdon, C. Navarro, R. Duffy, P. Hurley and F. Gamiz, *Solid-State Electronics*, 2021, **186**, 108173.
261. Q. Gao, C. Zhang, P. Liu, Y. Hu, K. Yang, Z. Yi, L. Liu, X. Pan, Z. Zhang and J. Yang, *Nanomaterials*, 2021, **11**, 1594.
262. C. Marquez, N. Salazar, F. Gity, J. C. Galdon, C. Navarro, C. Sampedro, P. K. Hurley, E. Y. Chang and F. Gamiz, *Micromachines*, 2021, **12**, 646.
263. K. A. Brown, S. Brittman, N. Maccaferri, D. Jariwala and U. Celano, *Nano Letters*, 2019, **20**, 2-10.